High-latitude dust as a potential source of ice-nucleating particles in the Arctic

Zur Erlangung des akademischen Grades eines
DOKTORS DER NATURWISSENSCHAFTEN (Dr. rer. nat.)
von der KIT-Fakultät für Physik des
Karlsruher Instituts für Technologie (KIT)
angenommene

DISSERTATION

von

M. Sc. Alexander Böhmländer

Tag der mündlichen Prüfung:	01. August 2025
Referent:	Prof. Dr. Thomas Leisner
Koreferentin:	Prof. Dr. Corinna Hoose

Preface

This thesis contains results, which are connected to the following publications:

A. Böhmländer, L. Lacher, D. Brus, K.-M. Doulgeris, Z. Brasseur, M. Boyer, J. Kuula, T. Leisner and O. Möhler (2024). 'A novel aerosol filter sampler for measuring the vertical distribution of ice-nucleating particles via fixed-wing uncrewed aerial vehicles'. In: *Atmospheric Measurement Techniques* 18 (16), pp. 3959–3971. ISSN: 1867-8548. DOI: 10.5194/amt-18-3959-2025.

A. Böhmländer, L. Lacher, R. Fösig, N. Büttner, J. Nadolny, D. Brus, K.-M. Doulgeris and O. Möhler (2025a). 'Measurement of the ice-nucleating particle concentration with the Portable Ice Nucleation Experiment during the Pallas Cloud Experiment 2022 [dataset]'. In: *Earth System Science Data* 17 (11), pp. 6165–6171. ISSN: 1866-3516. DOI: 10.5194/essd-17-6165-2025.

A. Böhmländer, L. Lacher, K. Höhler, D. Brus, K.-M. Doulgeris, J. Girdwood, T. Leisner and O. Möhler (2025b). 'Measurement of the ice-nucleating particle concentration using a mobile filter-based sampler on-board of a fixed-wing uncrewed aerial vehicle during the Pallas Cloud Experiment 2022 [dataset]'. In: *Earth System Science Data* 17 (11), pp. 6157–6164. ISSN: 1866-3516. DOI: 10.5194/essd-17-6157-2025.

The publications do not contain text or figures of this thesis, but discuss results that are also discussed within this thesis.

Abstract

Ice-nucleating particles (INPs) play a key role in the climate and weather systems on the Earth. They are a small subset of atmospheric aerosol particles and are able to facilitate primary ice nucleation in mixed-phase clouds above 235 K. Through this process, they can control the occurence of ice crystals in mixed-phase clouds, which, in turn, determines their radiative properties as well as their lifetime via the formation of precipitation. This mechanism is part of aerosol-cloud interactions and results in an overall net negative radiative forcing, although it is associated with significant uncertainties. Improving the representation of clouds in current weather and climate models requires a better understanding of the types of INPs and their spatiotemporal distribution in the atmosphere.

Different types of aerosol particles are able to act as INPs, which vary in their abundance and ice nucleation ability with temperature. The INP concentration in the atmosphere typically follows an exponential increase towards lower temperatures, with only about one in a million of ice-active aerosol particles at about 268 K, but about one in a thousand ice-active aerosol particles at about 240 K. Mineral dust often dominates the INP concentration at lower temperatures, while biogenic aerosol particles dominate the INP concentration at temperatures above around 258 K.

The climate is changing faster in the Arctic compared to the rest of the world, a phenomena knows as Arctic amplification, which is not yet fully understood, partly due to missing knowledge on the primary ice formation in clouds. This study aims at better capturing the concentration and types of INPs in the Arctic and sub-Arctic region. Mineral dust in the Arctic was found to be an important type of INP in the Arctic, as well as biogenic aerosol particles. One often overlooked source of mineral dust is high-latitude dust, which can be defined as all mineral dust that originates from dust sources located above 60° N. In this work, I conducted measurements at Svalbard at 79° N, as well as in Northern Finland (68° N). Longterm studies were conducted using the Portable Ice Nucleation Experiment to measure the INP concentration at different nucleation temperatures at a high temporal resolution of minutes. Together, these measurements were used to assess the impact of local emission of aerosol on the INP concentration as well as the contribution from long-range transport. In addition, vertical measurements of the INP concentration were conducted utilizing a lightweight filter-based aerosol sampler onboard of a uncrewed aerial vehicle to assess the distribution of INPs in the sub-Arctic. This sampler was developed and characterized during this work and offered a novel approach in measuring the vertical distribution of INPs.

Additional modelling results from the FLEXible PARTicle dispersion model model were used to investigate the source and age of mineral dust arriving at the high Arctic. To understand the INP population, the INP concentration was normalized with the aerosol surface concentration to obtain the ice nucleation active site density. During periods, where a low ice nucleation active site density was observed, mineral dust was typically originating from sources in Russia. Higher ice nucleation active site densities were observed for sources in Africa, indicating that high-latitude dust might have a lower ice nucleation ability compared to other mineral dust. Furthermore, dust

that travelled through the atmosphere for longer time periods, generally was connected to an increase in ice nucleation active site density, which might hint to possible aging effect enhancing the ice nucleation ability. The reason for this behaviour remains unclear.

The vertical measurements using the newly developed uncrewed aerial vehicle based setup often showed either similar INP concentrations between the ground and higher altitudes (<600 m above ground level), or even higher INP concentrations at higher altitudes. Given that ground-based measurements are more impacted by local emission, this finding suggests that either the atmospheric layers are well-mixed and ground-based measurements are also representative for the INP concentration at higher altitudes, or that the air masses arriving at elevated levels contain air masses with aerosol particles that are more efficient INPs. The dataset is still too small to draw a conclusive picture, but it is clear, that more vertical measurements of the INP concentration are needed to understand this behaviour.

Contents

List of Figures

List of Tables

List of Acronyms

AA	Arctic amplification.
ACTRIS	Aerosols, Clouds, and Trace gases Research Infrastructure.
agl	above ground level.
AH	Arctic haze.
AIDA	Aerosol Interaction and Dynamics in the Atmosphere.
AMOC	Atlantic meridional overturning circulation.
APS	Aerodynamic Particle Spectrometer.
AS	active site.
asl	above sea level.
AWI	Alfred Wegener Institute Helmholtz Centre for Polar and Marine Research.
BC	black carbon.
BVOC	biogenic volatile organic compound.
CCN	cloud condensation nucleus.
CCNC	cloud condensation nuclei counter.
CDF	cumulative distribution function.
CF	Climate and Forecast.
CHL	Chlorophyll *a*.
CMIP6	Coupled Model Intercomparison Project 6th Assessment Report.
CNR	Consiglio Nazionale delle Ricerche.
CNT	Classical Nucleation Theory.
CPC	Condensation Particle Counter.
CSU-IS	Colorado State University - Ice Spectrometer.
DMA	Differential Mobility Analyzer.
DMS	dimethyl sulfate.
ECMWF	European Centre for Medium-Range Weather Forecasts.
EPFL	École Polytechnique Fédérale de Lausanne.
ERA5	European Centre for Medium-Range Weather Forecasts Reanalysis v5.

ESSD	Earth System Science Data.
ExINP_GVB	Examining ice-nucleating particles at Gruvebadet Atmosphere Laboratory.
ExINP_ZEP	Examining ice-nucleating particles at Zeppelin Observatory.
FLEXPART	FLEXible PARTicle dispersion model.
FMI	Finnish Meteorological Institute.
GAW	Global Atmosphere Watch.
GCVI	ground-based counterflow virtual impactor.
GDAS	Global Data Assimilation System.
GNSS	global navigation satellite system.
GVB	Gruvebadet Atmosphere Laboratory.
HEPA	high efficiency particulate air.
HYSPLIT	Hybrid Single-Particle Lagrangian Integrated Trajectory model.
IMKAAF	Institute of Meteorology and Climate Research Atmospheric Aerosol Research.
INAS	ice nucleation active site.
INDA	Ice Nucleation Droplet Array.
INP	ice-nucleating particle.
INSEKT	Ice Nucleation Spectrometer of the Karlsruhe Institute of Technology.
IPCC	Intergovernmental Panel on Climate Change.
IPEV	French Polar Institute Paul Emile Victor.
IR-CS	infrared cold stage.
IUPAC	International Union of Pure and Applied Chemistry.
Kb3	Kingsbay 3.
KIT	Karlsruhe Institute of Technology.
LiIon	Lithium-Ion.
LINA	Leipzig Ice Nucleation Array.
LPDM	Lagrangian particle dispersion model.
MIZ	marginal ice zone.
MOSAiC	Multidisciplinary drifting Observatory for the Study of Arctic Climate.
MPC	mixed-phase cloud.
MPCK$^+$	Advanced Max Planck CloudKite.
MPIDS	Max Planck Institute for Dynamics and Self-Organization.

MSA methanesulfonic acid.

NAC Norwegian Atlantic Current.
netCDF Network Common Data Format.
NILU formerly Norwegian Institute for Air Research.
NPI Norwegian Polar Institute.

OC organic carbon.
ODR orthogonal distance regression.
odv optical detection volume.
OPC Optical Particle Counter.

PaCE Pallas Cloud Experiment.
PCF pore condensation and freezing.
PCR polymerase chain reaction.
PDF probability density function.
PIA Portable Ice Nucleation Experiment ice-nucleating particle AnalDraxler1998ysis.
PIMAV PINE ice-nucleating particle analysis for Manual and Automatic Versioning.
PINE Portable Ice Nucleation Experiment.
PM particulate matter.
PMA photo multiplier amplification.
PVC polyvinyl chloride.

RF radiative forcing.

SaQC System for automated Quality Control.
SML sea surface microlayer.
SMPS Scanning Mobility Particle Spectrometer.
SOA secondary organic aerosol.
SQL Structure Query Language.
SSA sea spray aerosol.
SU Stockholm University.

TBS tethered balloon system.
TOF time-of-flight.
TSP total suspended particulate.
TUV Vienna University of Technology.

UAS uncrewed aerial system.
UAV uncrewed aerial vehicle.
UH University of Hertfordshire.

WELAS white light aerosol spectrometer.

WIBS	Wideband Integrate Bioaerosol Sensor.
WMO	World Meteorological Organisation.
WSC	West Spitsbergen Current.
WT-CRAFT	West Texas Cryogenic Refrigerator Applied to Freezing Test system.
WTAMU	West Texas A&M University.
ZEP	Zeppelin Observatory.

Chapter 1.

Introduction

The Earth and its atmosphere are a complex system, containing a mixture of gases, liquids and solids. Aristotle (2006) discussed theses elements as the four bodies of 'fire, air, water, earth'. The interplay of these constituents as well as the related short-term and the long-term effects are subject of natural sciences for millenia. Since the industrial revolution and the related ever-increasing emissions of greenhouse gases into the atmosphere, humankind is changing the climate, a fact that became more apparent in the second half of the 20th century. In the 1970s a group of scientists conducted a 'Study of Man's impact on climate' and found an 'inadvertent climate modification', which they subsequently proposed as 'authoritative guidance' to the 1972 United Nations Conference on the Human Environment (MIT 1972). Back then there was no consensus in the scientific community what the consequences of modification could be, the modification itself was however clear. A few years later, Broecker (1975) first introduced the term 'Climate Change', discussing the inverse impact of an increase in 'man-made dust' and the exponential rise in the carbon dioxide content in the atmosphere. Neglecting the impact of dust aerosol, they concluded that by the beginning of the 21st century, the mean planetary temperature will have increased 'beyond the limits experienced in the last 1000 years'.

The climatic impact of aerosol particles, such as mineral dust, is still subject of discussion in the scientific community 50 years later. In these 50 years, the Intergovernmental Panel on Climate Change (IPCC) was founded in 1988 and published six assessment reports, the latest published in three parts in 2021 and 2022 (IPCC 2021, 2022a,b). The three parts focus on (1) the physical science basis, (2) impacts, adaption and vulnerability and (3) mitigation of climate change and target policymakers. The latest report discusses the emission of aerosols and the following radiative forcing due to absorption, scatter and albedo changes (IPCC 2021, p. 823). The anthropogenic influence on the global dust emission is very uncertain, spanning from less than 10 % to over 60 % (Ginoux et al. 2012; Stanelle et al. 2014; Xi and Sokolik 2016). In summary, IPCC (2021) state that the atmospheric dust source and loading are sensitive to climate change (*high confidence*), but there is *low confidence* in the quantitative estimates of dust emission. In addition, the effective radiative forcing of dust on the Earth is highly heterogeneous (*high confidence*) in time and location (IPCC 2021, p. 853). The largest change in temperature due to climate change is occuring in the Arctic, which warms up nearly four times faster than the rest of the Earth (Rantanen et al. 2022). This enhanced warming is part of various phenomena occuring in the Arctic, which are summarized under the term Arctic amplification (AA) (e.g., Serreze and Francis 2006). Local and remote aerosol is influencing the warming of the Arctic especially (Stjern et al. 2017; Westervelt et al. 2018).

The effective radiative forcing of aerosol-cloud interactions and aerosol-radiation interactions are shown in figure 1.1 as calculated by the sixth assessment report based on energy balance

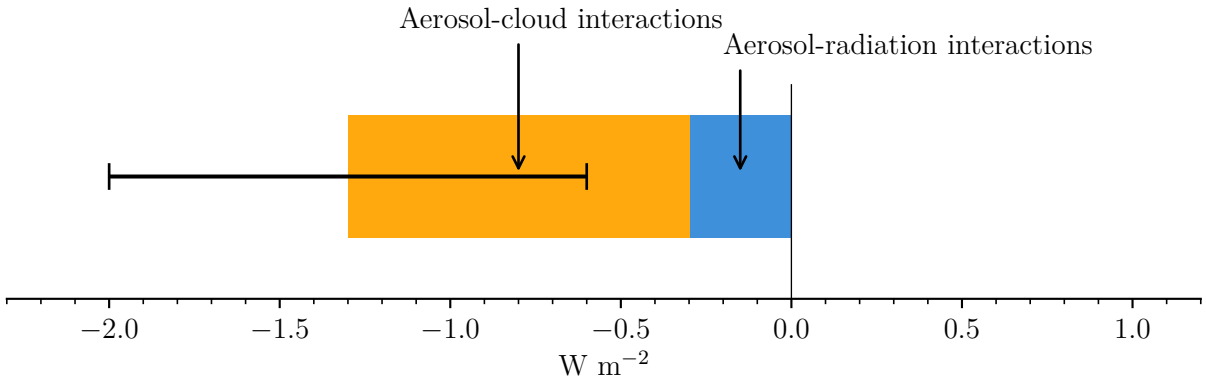

Figure 1.1.: **Net aerosol effective radiative forcing due to aerosol-cloud interactions and aerosol-radiation interactions.** Figure adapted from (IPCC 2021, figure 7.5 therein).

constraints, observational evidence and combined model evidence (IPCC 2021, figure 7.5 therein). The evidence for a negative total aerosol effective radiative forcing is clear, but the associated uncertainties are large, especially in regard to aerosol effects on mixed-phase, ice and convective clouds (IPCC 2021, p. 955). Mixed-phase clouds (MPCs) contain liquid cloud droplets as well as ice crystals. The influence on the phase of clouds, alters their lifetime (e.g., Wendisch et al. 2019), radiative effect (e.g., Bellouin et al. 2020; Boucher et al. 2013; Vergara-Temprado et al. 2018) and precipitation (e.g., Field and Heymsfield 2015; Heymsfield et al. 2020; Mülmenstädt et al. 2015). The primary formation of these ice crystals involves a small subset of aerosols: INPs.

INPs facilitate heterogeneous freezing of liquid cloud droplets in MPCs at subzero temperatures above 235 K (e.g., Kanji et al. 2017). Their abundance and properties are highly variable and depend on the temperature at which they are able to initiate the freezing of liquid cloud droplets. This ice nucleation ability of INPs depends on their chemical composition and size, although other factors may also play a role (e.g., Kanji et al. 2017; Kiselev et al. 2017; Pruppacher and Klett 1997). The measurement of INPs is challenging, since the prerequisites that aerosol particles need to fulfil are not fully understood (e.g., Kanji et al. 2017). To determine whether an aerosol particle is active as an INP, it needs to be subjected to subzero temperatures in sufficiently humid air and freezing needs to be observed. These measurements have been conducted in various field- and lab-based campaigns (e.g., DeMott et al. 2025, (field); DeMott et al. 2018, (lab)). Generally, two temperature regions can be loosely defined, where different aerosol particles contribute mostly to the INP population active at:

- temperatures above 258 K, often dominated by biogenic aerosol particles (e.g., Kanji et al. 2017),
- temperatures below 258 K, often dominated by mineral dust particles (e.g., Hoose and Möhler 2012).

Mineral dust particles are effective INPs, especially at lower temperatures (e.g., Atkinson et al. 2013; Barr et al. 2023; Broadley et al. 2012; DeMott et al. 2015; Marcolli et al. 2007; Möhler et al. 2006; Salam et al. 2006; Wiacek et al. 2010). Mineral dust and sea spray aerosol (SSA) are the two most common aerosols in the Earth's atmosphere by mass (Kok et al. 2021; Weng et al. 2020). The largest source of mineral dust is the Sahara (e.g., Prospero et al. 2002), but higher latitudes have been shown to contribute to mineral dust emission (Baddock et al. 2017; Bullard et al. 2016; Groot Zwaaftink et al. 2016; Meinander et al. 2022; Prospero et al. 2012). Potential

dust sources in higher latitudes are confined to ice-free areas, especially from glacial outwash plains (Bullard et al. 2016). The deposition of locally emitted dust on snow has been observed as well on the greenlandic ice sheets (Wientjes et al. 2011). Iceland is the most studied area for high-latitude dust emission (Bullard et al. 2016), featuring an average of 34 dust days per year (Dagsson-Waldhauserova et al. 2013). These regions might play an increased role in mineral dust emission, especially considering AA and the thawing of permafrost, which might increase snow- and ice-free areas (Creamean et al. 2020). To identify high-latitude dust sources, Meinander et al. (2022) used a global dust database and quantified the potential of dust emission based on the source intensity. Above 60° N, 5.5 % of the land mass had a source intensity larger than 0.5, amounting to around 1 % of global dust emission (Meinander et al. 2022). However, high-latitude dust deposition on snow- and ice-covered areas in the Arctic contributes 57 % to the total amount of deposited dust in these areas (Meinander et al. 2022). High-latitude dust might play a more important role in the Arctic compared to dust from other sources. Shi et al. (2022) modelling the total dust burden for the Arctic and found a 30.7 % contribution from high-latitude dust sources. Using a parameterization to estimate the INP population of high-latitude dust, Shi et al. (2022) find a net cooling effect of $-0.24\,\mathrm{W\,m^{-2}}$ resulting from faciliated primary ice nucleation due to high-latitude dust.

Measurements of the INP concentration are still sparse in the Arctic and typically rely on filter-based methods, which have a low temporal resolution of days to weeks (e.g., Wex et al. 2019). In addition, most of these measurements are ground-based and therefore cannot provide a vertical assessment of the INP concentration (e.g., Wex et al. 2019). Vertical measurements of the INP concentration might be crucial to understand aerosol-cloud interactions in the Arctic better (Creamean et al. 2021, 2018b; Schmale et al. 2021). During this work, a novel lightweight and filter-based method was developed and deployed during a measurement campaign in northern Finland to assess the vertical distribution of the INP concentration in the Arctic (Böhmländer et al. 2024, 2025b). During four field campaigns in northern Finland and Svalbard, the Portable Ice Nucleation Experiment (PINE) instrument was used to measure the INP concentration at a high temporal resolution of minutes (Böhmländer et al. 2025a). Together, these measurements aimed at measuring the vertical distribution and the short- and long-term variability of the INP concentration to assess - together with other instrumentation and modelling - the impact of high-latitude dust on the Arctic INP population. Meteorological aspects as well as snow and ocean as potential sources are taken into account to assess their potential impact on the INP population.

Chapter 2.

Scientific Background

This chapter provides the scientific background to understand and follow the methods used for data analysis and interpretation. Section 2.1 introduces aerosol particles and their properties, while section 2.2 discusses the processes and interaction of aerosol particles in the atmosphere. Finally, INPs are introduced in section 2.3 and put into the context of the Arctic in section 2.4.

2.1. Aerosol particles

The Earth's atmosphere mainly contains the three gases N_2 (78 %), O_2 (21 %) and Ar (1 %) (e.g., Emmert et al. 2021). Another important major constituent is water vapour, most abundant in the lower atmosphere and highly variable < 3 % (e.g., Emmert et al. 2021). This mixture of gases and water vapor was already proposed by Aristotle around 300 BCE (Aristotle 2006), and nowadays the concentrations of other rare gases are known down to a mixing ratio of 1 part per trillion by volume (Seinfeld and Pandis 2016, p. xxiii). With the increase of human activities on Earth, the concentration of certain gases (e.g., CO_2) has increased over the past 200 years (IPCC 2021), leading Earth into a new era, termed the Anthropocene (Lewis and Maslin 2015). In addition to these gases, particles are suspended in the atmosphere. These airborne particles are relevant to the Earth's climate, but can also lead to harmful impacts on human health and plants (IPCC 2021).

2.1.1. Definition

An aerosol is defined as solid or liquid particles suspended in a gaseous medium (e.g., Kulkarni 2011, p. 3). Aerosol particles consist of these suspended particles, interact with each other and the gaseous medium and can originate from various sources. They are created from gas particles as well as from the disintegration of larger particles into smaller particles which are then able to be suspended in the air.

Aerosol particles can be described via various properties, such as their size and shape, the morphology of their surface, their composition as well as their refractive index. The size and shape of aerosol particles are most important for their physical behaviour and are governed by different physical forces. For spherical aerosol particles, their size can directly be described by their diameter, which ranges from about 1 nm up to 100 µm (Kulkarni 2011, p. 4). For non-spherical aerosol particles, different diameters can be defined to ultimately refer to an equivalent diameter. The aerosol particle concentration is used to quantify the abundance of

aerosol particles, being normalized to different parameters, depending on their use case. An aerosol particle number concentration refers to the number of aerosol particles per unit volume of gas. For the significance to the human respiratory system, the abundance of aerosol particles is related to the aerosol particle mass (e.g., Oh et al. 2020), although smaller particles have been found to be more dangerous, since they are able to penetrate deeply into the lungs (e.g., Shiraiwa et al. 2017). The surface area concentration is important whenever the aerosol particles interact primarily due to their surface properties (e.g., Noël et al. 2016).

The size and the abundance of aerosol particles in the atmosphere can be described by a continuous distribution (Seinfeld and Pandis 2016, eq. 8.1 therein)

$$N_{\text{total}} = \int_0^\infty n_N(d_\text{p})\,\mathrm{d}d_\text{p}\ , \tag{2.1}$$

where: N_{total} – total number of aerosol particles (cm^{-3}),
$n_N(d_\text{p})$ – number of aerosol particles with a particle diameter of d_p ($\text{cm}^{-3}\,\mu\text{m}^{-1}$).

Assuming spherical aerosol particles, this consquently leads to the surface area (n_S), volume (n_V) and mass (n_M) distributions (Seinfeld and Pandis 2016, eqs. 8.4, 8.6 and 8.8 therein):

$$n_\text{S}(d_\text{p}) = \pi d_\text{p}^2 n_N(d_\text{p}) \quad (\mu\text{m}^2_\text{aer}\,\text{cm}^{-3})\ , \tag{2.2}$$

$$n_\text{V}(d_\text{p}) = \frac{\pi}{6} d_\text{p}^3 n_N(d_\text{p}) \quad (\mu\text{m}^3_\text{aer}\,\text{cm}^{-3})\ , \tag{2.3}$$

$$n_\text{M}(d_\text{p}) = \frac{\rho_\text{p}}{10^{12}} \frac{\pi}{6} d_\text{p}^3 n_N(d_\text{p}) \quad (\mu\text{g}\,\text{m}^{-3})\ , \tag{2.4}$$

where: ρ_p – aerosol particle density ($\text{kg}\,\text{m}^{-3}_\text{aer}$).

In the Earth's atmosphere, aerosol particles typically can span multiple orders of magnitude in size and concentration, which makes their distribution cumbersome to handle. Taking the logarithm of the distribution provides a distribution that can be handled more easily. Equation (2.1) can be expressed as (Seinfeld and Pandis 2016, eq. 8.9 therein)

$$N_{\text{total}} = \int_{-\infty}^\infty n_N^\text{dec}\left(\log\frac{d_\text{p}}{\mu\text{m}}\right)\mathrm{d}\log d_\text{p}\ , \tag{2.5}$$

where: $n_N^\text{dec}\left(\log\frac{d_\text{p}}{\mu\text{m}}\right)$ – aerosol size distribution as a function of the decadal logarithm of the aerosol particle diameter (cm^{-3}).

Here the aerosol particle diameter d_p is given in µm[1] and the limits of integration have been adjusted according to the logarithm. One can also define the same according to the natural logarithm and according to equations (2.2) to (2.4) for the surface, volume and mass distributions, respectively. The atmospheric aerosol size distribution is often found to be close to the sum of multiple lognormal distributions (e.g., Whitby et al. 1975). This means the logarithm of the atmospheric aerosol size distribution is normally distributed for a single mode (Seinfeld and Pandis 2016, eq. 8.33 therein)

$$n_N^\text{dec}(\log d_\text{p}) = \frac{\mathrm{d}N}{\mathrm{d}\log d_\text{p}} = \frac{N_{\text{total}}\log 10}{(2\pi)^{(1/2)}\log\sigma_\text{g}}\exp\left(-\frac{\log d_\text{p} - \log\overline{d_\text{pg}}}{2\log^2\sigma_\text{g}}\right)\ , \tag{2.6}$$

[1]The argument of a transcendental function, such a the logarithm, needs to be unitless. Therefore, wherever present inside a logarithm, the aerosol particle diameter is implicitedly divided by its unit (see also Matta et al. 2010).

where: σ_g – geometric standard deviation (µm),
$\overline{d_{pg}}$ – median of the aerosol particle diameter (µm).

The median $\overline{d_{pg}}$ is here defined as the aerosol particle diameter, where exactly half of the aerosol particles are smaller and the other half is larger. The geometric standard deviation can be understood as a scale to the width of the distribution. Accordingly, one can calculate the mean of the size distribution $\overline{d_p}$, which depends on the geometric standard deviation and the median (Seinfeld and Pandis 2016, eq. 8.44 therein)

$$\overline{d_p} = \overline{d_{pg}} \exp\left(\frac{\ln^2 \sigma_g}{2}\right) . \tag{2.7}$$

The mean and median of the distribution are equal for a geometric standard deviation of 1. Such a distribution is called monodisperse. Atmospheric aerosol size distributions typically contain multiple different aerosol types with different sizes and properties. Therefore, they are typically described as a mixture of multiple aerosol particle size distributions n_N^{dec}. A polydisperse aerosol particle size distribution is therefore defined as (Seinfeld and Pandis 2016, eq. 8.54 therein)

$$n_N^{dec}(\log d_p) = \sum_{i=1}^{n} \frac{N_{total,i} \log 10}{(2\pi)^{(1/2)} \log \sigma_{g,i}} \exp\left(-\frac{\log d_p - \log \overline{d_{pg,i}}}{2 \log^2 \sigma_{g,i}}\right) , \tag{2.8}$$

where: n – number of individual modes.

The aerosol number size distribution is dominated by small particles smaller than about 0.1 µm, whereas the surface and volume distributions are dominated by larger aerosol particles larger than about 1 µm. One can define a number of different modes that can be differentiated by their size, source and emission (Seinfeld and Pandis 2016, pp. 342–343): The *Nucleation mode* contains ultrafine particles with an aerosol particle diameter smaller than about 20 nm, created from precursor gases via nucleation. *Aitken mode* are ultrafine particles with aerosol particle diameter between around 20 and 100 nm. Aitken mode aerosol particles originate from the nucleation mode, but grow due to condensation of secondary material during their lifetime in the atmosphere. *Condensation submode* forms the *accumulation mode* together with the *droplet submode*, featuring aerosol particles from primary emissions, condensation of secondary material onto the primary aerosol as well as the coagulation of smaller particles. *Coarse mode* aerosol particles have aerosol particle diameters around 2.5 µm and originate from mechanical processes, for example soil dust and sea salt aerosol (Seinfeld and Pandis 2016, p. 343). Depending on the source, the different modes can show slightly different aerosol particle diameters, in some locations they might not even be present at all. An example for the different modes is shown in figure 2.1.

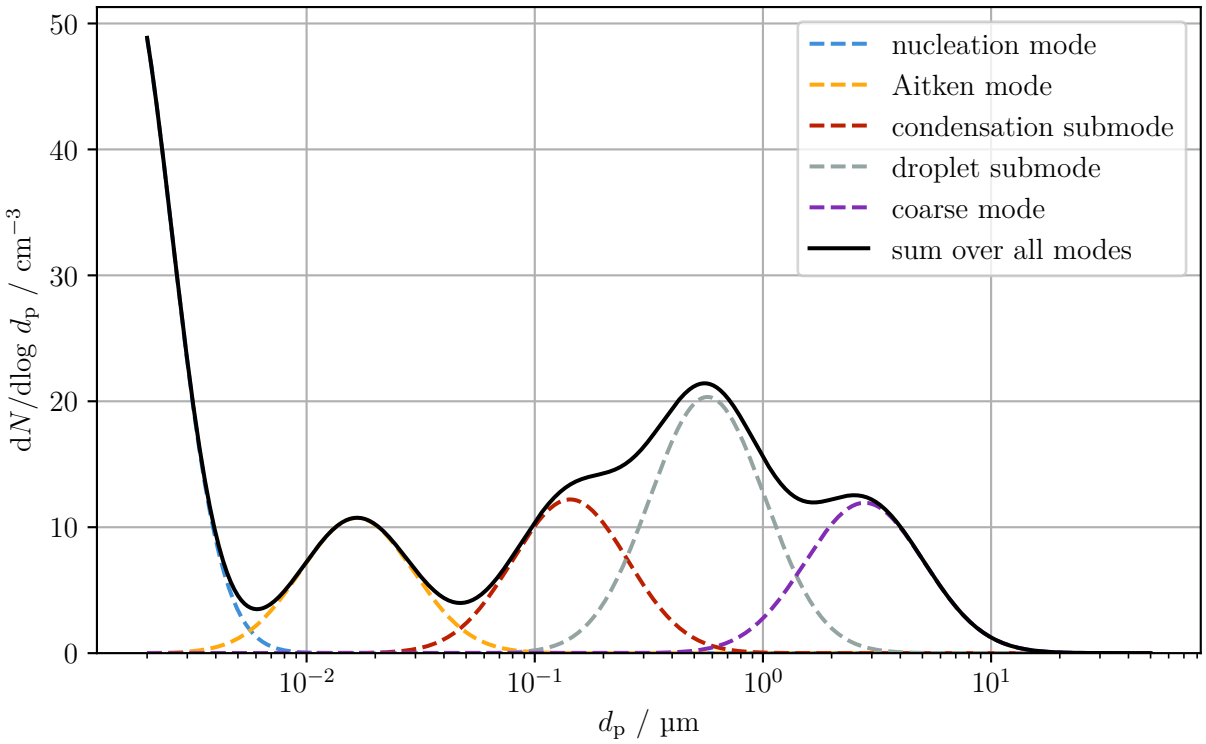

Figure 2.1.: **An example of an aerosol size distribution with different modes.** The nucleation and Aitken mode are scaled by three orders of magnitude to fit inside the same graph as the other modes.

2.1.2. Measurement

Aerosol size distributions are most commonly measured in situ with two instruments. The Scanning Mobility Particle Spectrometer (SMPS) measures the size distribution of particles with diameters up to 800 nm, whereas the Aerodynamic Particle Spectrometer (APS) measures the size distribution of larger particles with diameters from about 0.5 µm to 20 µm. Both instruments measure different aerosol particles diameters due to their measurement principle. To combine the aerosol size distributions measured by these two instruments, one needs to equalize the size reference frame. The volume equivalent diameter is equal to its physical diameter for spherical particles, therefore it is the preferred size reference frame.

2.1.2.1. Electrical mobility particle diameter

The SMPS consists of two instruments, where at first the aerosol particles are charged and separated through an electric field inside the Differential Mobility Analyzer (DMA). The measured aerosol particle diameter is called the electrical mobility equivalent diameter d_{em} and is related to the volume equivalent diameter d_{ve} (Seinfeld and Pandis 2016, eq. 9.114 therein)

$$d_{em} = d_{ve}\chi\frac{C_c(d_{em})}{C_c(d_{ve})} \ , \tag{2.9}$$

where: χ – dynamic shape factor
C_c – slip correction factor .

The dynamic shape factor χ is a measure to account for the different behaviour of non-spherical particles and is defined as the fraction of the drag force F_{drag} on the particle to the drag force $F^{\text{ve}}_{\text{drag}}$ of a spherical particle of its volume equivalent diameter (Seinfeld and Pandis 2016, eq. 9.103 therein)

$$\chi = \frac{F_{\text{drag}}}{F^{\text{ve}}_{\text{drag}}} \geq 1 \ . \tag{2.10}$$

The slip correction factor becomes relevant, when aerosol particle diameters become close to the mean free path of the aerosol particles inside the medium. For these noncontinuum effects the drag force of is reduced by the slip correction factor since $F_{\text{drag}} \propto C_{\text{c}}^{-1}$ where (Seinfeld and Pandis 2016, eq. 9.34 therein)

$$C_{\text{c}} = 1 + \frac{2\lambda}{d_{\text{p}}} \left[1.257 + 0.4 \exp\left(-\frac{1.1 d_{\text{p}}}{2\lambda} \right) \right] \ , \tag{2.11}$$

where: λ – mean free path (m).

The slip correction factor is close to 1 for spherical aerosol particles with diameters above 5 µm, but increases fast for smaller aerosol particles, reaching about 100 for spherical aerosol particles with a diameter of 20 nm at standard conditions. Equation (2.9) needs to be evaluated iteratively, but converges fast.

2.1.2.2. Aerodynamic particle diameter

The aerodynamic diameter of aerosol particles is related to the volume equivalent diameter via the aerosol particle density (Seinfeld and Pandis 2016, eq. 9.110 therein)

$$d_{\text{ae}} = d_{\text{ve}} \left(\frac{\rho_{\text{p}}}{\rho^{\circ}_{\text{p}}} \right) \left(\frac{C_{\text{c}}(d_{\text{ve}})}{C_{\text{c}}(d_{\text{ae}})} \right)^{\frac{1}{2}} \ , \tag{2.12}$$

where: ρ_{p} – aerosol particle density (kg m^{-3}),
ρ°_{p} – standard aerosol particle density ($1\,\text{kg m}^{-3}$).

This function needs to be evaluated iteratively, but converges fast.

2.1.3. Types and sources

Aerosol particles originate from different sources and can vary in their respective abundance (see table 2.1). One of the largest contributions to the total aerosol mass in the Earth's atmosphere is mineral dust. Mineral dust contributes around 3500 Tg annually (Kok et al. 2021). The main sources of mineral dust are the large deserts of the Earth (e.g., Sahara, Prospero et al. 2002, see also figure 2.2) but can also be emitted in higher latitudes (e.g., Iceland, Dagsson-Waldhauserova et al. 2013, 2017). Mineral dust consists of a wide range of elements with varying composition, dependent on the source region. Some tracers can be found that can help in sourcing the mineral dust; but in general a combination of different techniques is required to obtain a robust source attribution scheme (Scheuvens et al. 2013). Sea salt aerosols are the second major contribution to the total aerosol mass in the Earth's atmosphere, with a similar contribution to the total aerosol mass as mineral dust. Sea salt aerosol is produced from the oceans via bubble bursting (e.g., Lv et al. 2020), where the wind speed is used in the best source functions to predict its abundance (Grythe et al. 2014; Song et al. 2023). Secondary aerosols are sulfates from dimethyl sulfate (DMS)

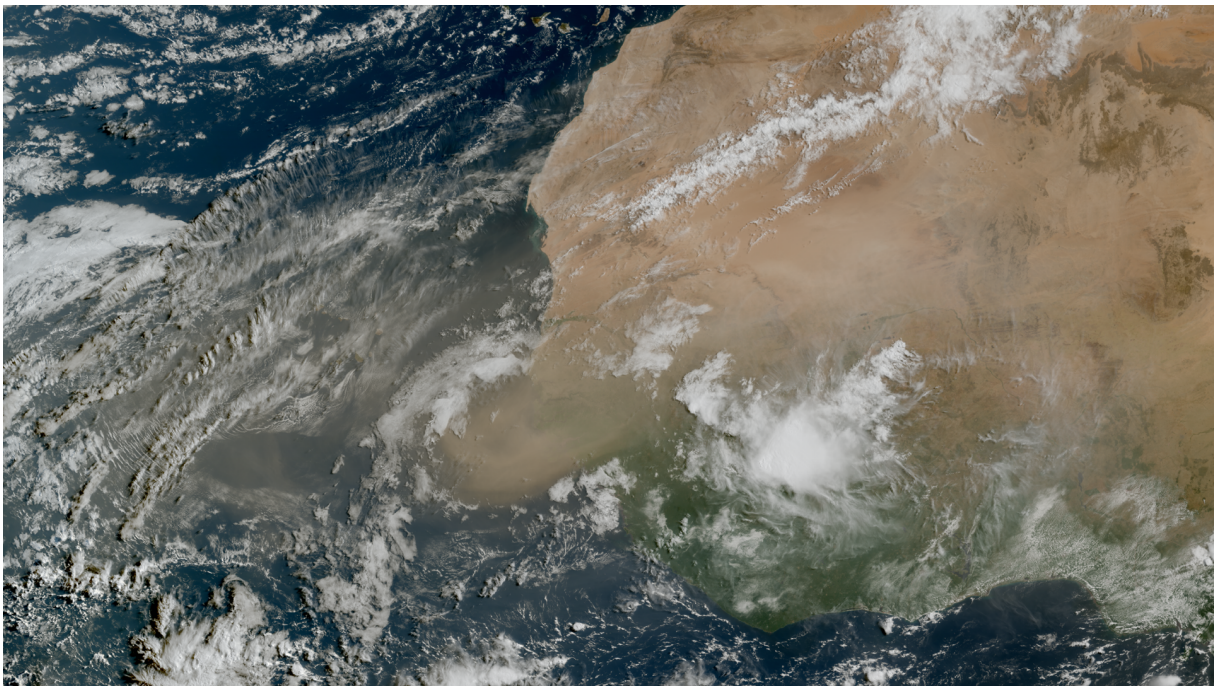

Figure 2.2.: **Satellite picture of Saharan dust emission into the atmosphere and transport westwards.** The image was captured by the FCI instrument onboard Meteosat-12 on 7th May 2025. Figure from https://www.eumetsat.int/saharan-dust-space, last access: 12th May 2025.

and volcanic SO_2 as well as biogenic volatile organic compounds (BVOCs). Anthrophogenic aerosol sources, i.e. industry or agriculture, lead to the emission of black carbon (BC) and organic aerosols. Secondary products are sulfates and nitrates from SO_2 and NO_x. In the following section, the interaction between these aerosols and the water in the atmosphere is described in detail.

Table 2.1.: **Estimated global aerosol fluxes for different sources.** The values for the estimated flux are given with uncertainties covering one standard deviation if available.

Source				Estimated flux / $\mathrm{Tg\,yr^{-1}}$	Reference
Natural	Primary	Mineral dust		3500	Kok et al. (2021)
		Sea salt	Accumulation mode	57.9 ± 2.6	Weng et al. (2020)
			Coarse mode	3502 ± 157	Weng et al. (2020)
	Secondary	Sulfates from DMS		28 ± 4	Brodowsky et al. (2024)
		Sulfates from volcanic SO_2		27 ± 2	Fischer et al. (2019)
		BVOC		563	Weng et al. (2020)
Anthrophogenic	Primary	Black carbon		6.2 ± 2.1	Xu et al. (2021)
		Organic aerosol		44.4	Tsigaridis et al. (2006)
	Secondary	Sulfates from SO_2		65 ± 4	Brodowsky et al. (2024)
		Nitrates from NO_x		9.5 ± 0.4	Weng et al. (2020)

2.2. Aerosol-cloud interactions

The Earth's energy balance is determined by the incoming solar radiation and the outgoing terrestrial radiation (Stephens and L'Ecuyer 2015; Stephens et al. 2012). The atmosphere with its constituents is responsible for this balance and in determining the temperatures on Earth (Hansen et al. 2011). Aerosol particles take part in interaction with other constituents of Earth's atmosphere. These interactions can range from chemical reactions of precursor gases that lead to the formation of primary aerosol particles and subsequent growth through condensation (Wagner 1982; Yoshida et al. 1976) or aggregation (DallaValle et al. 1954; Matsoukas and Friedlander 1991), to the effect on the incoming solar radiation (Satheesh and Moorthy 2005; Yu et al. 2006). This section focuses on the effect of aerosol particles on the radiative budget of Earth and the interaction between aerosol particles and the water suspended in Earth's atmosphere.

2.2.1. Direct aerosol effect

Aerosol particles have an immediate and direct effect on the radiative budget of Earth that is related to their absorption and scattering (Li et al. 2022b).

In electromagnetic terms, electromagnetic radiation can transfer energy onto aerosol particles via absorption and scattering (Mishchenko et al. 2002, p. 3). The energy can induce oscillating dipoles in the target molecules, which are contained in a single aerosol particle. Due to the movement of a charge, a certain radiation is emitted. For multiple molecules this leads to emission of radiation into all directions, which is called scattering (Mishchenko et al. 2002, p. 4). Some of the radiation can be absorped as thermal energy. The amount of scattering and absorption depends on the incident energy of the electromagnetic radiation. The factor between incoming and scattered or absorbed radiation is called the single-particle scattering cross section C. The sum of both effects is called extinction and the single-scattering albedo ω is given by the fraction between scattering (C_{scat}) and extinction cross section (C_{ext})

$$\omega = \frac{C_{\text{scat}}}{C_{\text{ext}}} \ . \tag{2.13}$$

The type of scattering depends on the wavelength of incoming and outgoing radiation. *Elastic scattering* occurs when the wavelength of the incident radiation is the same as that of the scattered beam. When *inelastic scattering* occurs, the two wavelengths are not the same. Elastic scattering on spherical aerosol particles is described by *Mie theory* and is dependent on three main parameters (Wriedt 2012):

1. the incident wavelength,
2. the aerosol particle size,
3. the optical properties of the aerosol particle in relation to the surrounding medium.

The optical properties of aerosol particles can be described by the complex refractive index[2] (Sokolik et al. 1993):

$$m = n + ik \ , \tag{2.14}$$

[2]The refractive index is given in relation to the surrounding medium. Since the refractive index of air is for all practical purposes unity, the refractive index described here is not explicitly calculated with a refractive index of air unequal to unity.

where: m – complex refractive index,
n – real part of the complex refractive index,
k – imaginary part of the complex refractive index.

The real part n describes the scattering effect, while the imaginary part k is used to describe the absorption effect. Both values depend on the wavelength of the incident light. At a wavelength of 589 nm pure water droplets have a complex refractive index of $1.33 + \mathrm{i}0$ (Rowe et al. 2020), incoming solar radiation is therefore only scattered and practically not absorbed. At a wavelength of 10 µm of the incident radiation, this changes to around $1.218 + \mathrm{i}0.0508$ (Rowe et al. 2020). The outgoing terrestrial radiation of Earth with a peak around 10 µm is therefore partly absorbed by the pure water droplets in the atmosphere. Mineral dust shows a slight absorption at an incident wavelength of visible light and a slightly higher scattering value compared to water ($1.59 + \mathrm{i}0.009$, Kandler et al. 2007).

The total effect on the radiative budget of Earth is described as the radiative forcing (RF) and given in dimensions of energy per time per area. The RF of the direct aerosol effect has been the subject of various studies of the last decades (e.g., Bauer et al. 2010; Charlson et al. 1991; Chin et al. 2009; Hauglustaine et al. 2014; Loeb and Su 2010; Schulz et al. 2006; Seland et al. 2008; Stier et al. 2005; Takemura et al. 2002; Terrenoire et al. 2022; Wall et al. 2022). Improvements on individual processes have increased the confidence in the output of models, while also decreasing uncertainty. Myhre et al. (2013) reported the global RF from the intercomparison of 16 global aerosol models during AeroCom Phase II with one standard deviation. The direct aerosol effect leads to an overall negative RF of $(-0.3 \pm 0.1)\,\mathrm{W\,m^{-2}}$ (Myhre et al. 2013). The two largest contributions to the global RF are sulphates ($-0.34\,\mathrm{W\,m^{-2}}$) and BC from fossil fuel ($0.23\,\mathrm{W\,m^{-2}}$, Myhre et al. 2013). In comparison to that, the Coupled Model Intercomparison Project 6th Assessment Report (CMIP6) reports an average of $(-0.3 \pm 0.4)\,\mathrm{W\,m^{-2}}$ (with a 95 % confidence level, IPCC 2021). According to IPCC (2021) is is very likely that the global RF of the direct aerosol effect is negative.

2.2.2. Indirect aerosol effect

Aerosol particles can not only interact with the electromagnetic radiation in the atmosphere, but also with the water. The following sections describe the interaction of aerosols with atmospheric water, detailing the processes involved and their effect on the radiative budget of Earth and the role of clouds in Earth's atmosphere.

2.2.2.1. Homogeneous and heterogeneous nucleation

The atmosphere contains a water vapour concentration of up to 3 % (Seinfeld and Pandis 2016, p. 4). The formation of pure liquid water droplets in the atmosphere can only happen in a supersaturated water vapour phase. The extent of supersaturation of water vapour is described by the saturation ratio S

$$S = \frac{p_\mathrm{w}}{p_\mathrm{w}^\mathrm{s}(T)}\ , \tag{2.15}$$

where the partial pressure of water vapour p_w is divided by the saturation vapour pressure p_w^s at equilibrium with liquid water at the temperature T. If $S > 1$, the formation of liquid water droplets can happen in two main ways: homogeneously, i.e. pure water with no other material involved, and heterogeneously, i.e. pure water nucleating onto a different substance. A concise

overview of homogeneous nucleation is initially presented, followed by a subsequent discussion on heterogeneous nucleation involving aerosol particles.

The Gibbs free energy is a thermodynamic potential, which is used to describe the equilibrium state of a thermodynamic system, which is at constant temperature and pressure. The change in the Gibbs free energy is negative or equal to zero, when the thermodynamic system is at constant temperature and pressure, which follows directly from the second law of thermodynamics (Denbigh 1981). Classical Nucleation Theory (CNT) is used to describe the formation of a new phase from a parent metastable phase (e.g., Murray et al. 2012). The nucleation of water vapour into its liquid phase does not occur instantaneously upon reaching a saturation ratio above 1, but is rather a stochastic process, which has a probability of occuring. The individual nuclei form clusters, increasing in size until a critical cluster size is reached, at which point the phase transition takes place. This nucleation happens via four distinct pathways:

Homogeneous-homomolecular: self-nucleation of a single species

Homogeneous-heteromolecular: self-nucleation of more than one species

Heterogeneous-homomolecular: nucleation of a single species on a foreign substance

Heterogeneous-hetermolecular: nucleation of more than one species on a foreign substance

The following discussion focuses on the homomolecular pathways for illustration purposes (for a detailed discussion of the heteromolecular nucleation see Seinfeld and Pandis 2016).

Clusters of monomers[3] grow and shrink by the addition and subtraction of single monomers. The number concentration of clusters containing i monomers is therefore given by (Seinfeld and Pandis 2016, eq. 11.2 therein)

$$\frac{\mathrm{d}N_i}{\mathrm{d}t} = \beta_{i-1}N_{i-1}(t) - \gamma_i N_i(t) - \beta_i N_i(t) + \gamma_{i+1}N_{i+1}(t) \ , \tag{2.16}$$

where: N_i – number concentration of clusters of size i,
β_i – collision rate of monomers of size i,
γ_i – evaporation rate of monomers of size i.

The characteristic time to form a steady-state is relatively short in comparison to the concentration changes in the atmosphere, therefore the left hand site of equation (2.16) can be set to zero. The growth of a single cluster by one monomer can thus simply be described with a constant flux J (Seinfeld and Pandis 2016, eqs. 11.3 and 11.4 therein)

$$J = J_{\mathrm{i+1/2}} = \beta_i N_i(t) - \gamma_{i+1}N_{i+1}(t) \ . \tag{2.17}$$

The collision and evaporation rates can be linked by a quantity f_i (Seinfeld and Pandis 2016, eq. 11.9 therein)

$$f_i = \prod_{j=1}^{i-1} \frac{\beta_j}{\gamma_{j+1}} \ . \tag{2.18}$$

In the case of a saturation ratio $S > 1$, this function needs to increase for large i with the increase in i by more than 1 to lead to a growth of a critical cluster. Even at supersaturated conditions, the concentration of monomers far exceeds the concentration of clusters of size i. Consequently, the reduction in monomer concentration due to cluster growth can be neglected. From this a

[3] A monomer in this context denotes a single molecule or nucleus, depending on the species.

nucleation rate as a function of collision and evaporation rate and monomer concentration is found (Seinfeld and Pandis 2016, eq. 11.11 therein)

$$J = N_1 \left(\sum_{i=1}^{\infty} \frac{1}{\beta_i f_i} \right)^{-1} \quad . \tag{2.19}$$

Equation (2.18) can also be written slightly different for saturated conditions with the saturation ratio S (Seinfeld and Pandis 2016, eq. 11.23 therein)

$$f_i = S^{i-1} \prod_{j=1}^{i-1} \frac{\beta_j^S}{\gamma_{j+1}^S} \ , \tag{2.20}$$

where the collision and evaporation parameters are given in regard to a saturation ratio S as $\beta_i = S\beta_i^S$ and $\gamma_i = \gamma_i^S$. The evaporation rate γ_i is only dependent on the size of the cluster and the temperature as long as the number of monomers is smaller than the number of monomers of the carrier gas (i.e. air). The Gibbs free energy change ΔG_i can be considered for the creation of a cluster of size i by factoring in that the collision happens one at a time and at the same constant as described by f_i. This means, a cluster growing from size 1 to 2 and a cluster growing from size 1 to 3, still both contain the constant f_2 of the cluster size increasing from 1 to 2. For a physical reaction of i monomers A_1 at saturated conditions with $i\,\mathrm{A}_1 \rightleftharpoons \mathrm{A}_i$ an Arrhenius form follows (Seinfeld and Pandis 2016, eq. 11.24 therein)

$$f_i = S^{i-1} \exp\left(-\frac{\Delta G_i}{k_\mathrm{B} T} \right) \quad . \tag{2.21}$$

where: k_B – Boltzmann constant ($1.380\,649 \times 10^{-23}\,\mathrm{J\,K^{-1}}$),
T – temperature (K).

So far, all equations are exact and no major approximation was performed. To connect CNT with macroscopic values, it is assumed that the surface tension of a small number of molecules is the same as the one of the bulk liquid. From this *capillarity approximation*, the formation of an interface between the surface of the cluster and the gas is associated with a change in the Gibbs free energy (Seinfeld and Pandis 2016, eq. 11.25 therein)

$$\Delta G_i = \sigma a_i \ , \tag{2.22}$$

where: σ – surface tension ($\mathrm{N\,m^{-1}}$),
a_i – surface area of a cluster of size i ($\mathrm{m^2}$).

In addition to this, energy is released by the formation of the bonds between the monomers, leading to a formulation of the Gibbs free energy change in dependence of macroscopic variables in line with the CNT (Seinfeld and Pandis 2016, eq. 10.83 therein)

$$\Delta G = -\frac{4}{3}\pi R_\mathrm{p}^3 \frac{k_\mathrm{B} T}{v_\mathrm{l}} \ln S + 4\pi R_\mathrm{p}^2 \sigma \ , \tag{2.23}$$

where: R_p – radius of the droplet (m),
v_l – volume of one molecule in the liquid phase ($\mathrm{m^3}$),
S – saturation ratio,
σ – surface tension of the water-air interface ($\mathrm{N\,m^{-1}}$).

The saturation ratio S is given here as the ratio of the vapour pressure of the actual equilibrium

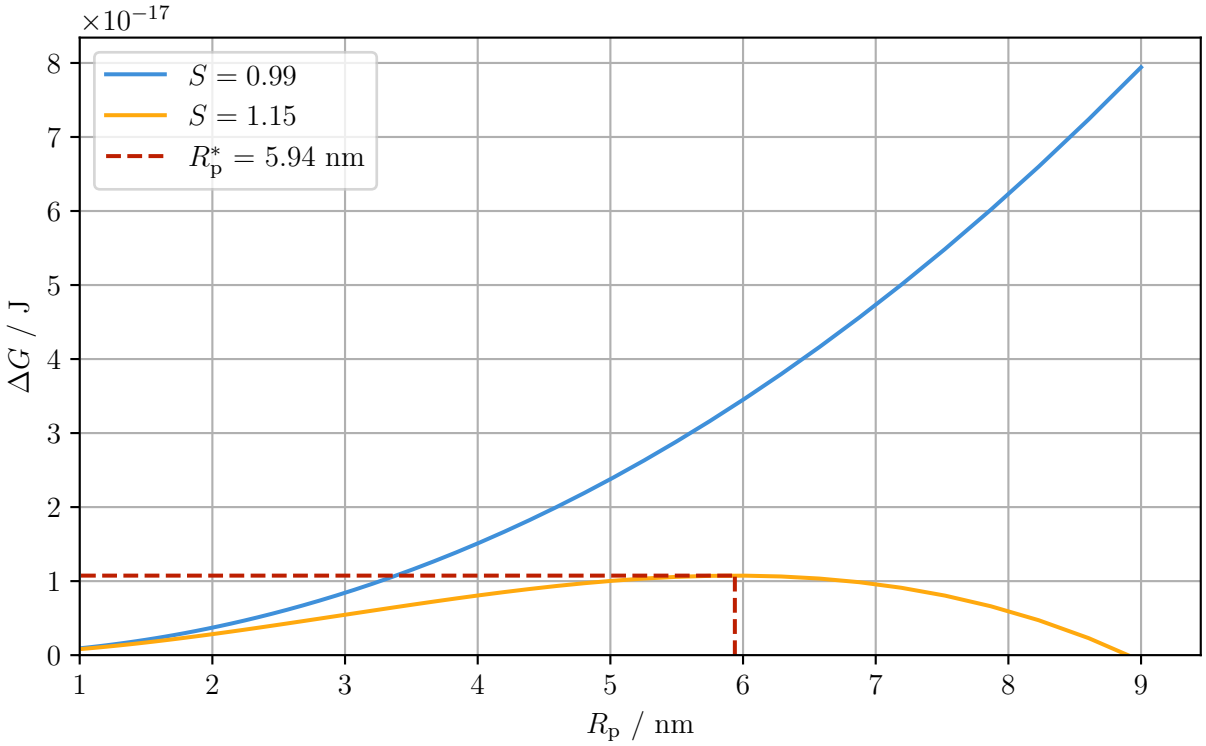

Figure 2.3.: **Gibbs free energy change ΔG as a function of the droplet radius R_p for the formation of a water droplet from air with the saturation ratio S.** The calculation is done with a temperature of 293.15 K.

partial pressure over water (p_v) and the vapour pressure of water over a flat surface (p_v°, Seinfeld and Pandis 2016, p. 420)

$$S = \frac{p_\mathrm{v}}{p_\mathrm{v}^\circ} \ . \tag{2.24}$$

The maximal value of the Gibbs free energy change can be calculated as a function of the vapour pressures by setting the derivative of equation (2.23) to zero, resulting in the *Kelvin equation* (Seinfeld and Pandis 2016, eq. 10.85 therein)

$$p_\mathrm{v} = p_\mathrm{v}^\circ \exp\left(\frac{2\sigma v_\mathrm{l}}{k_\mathrm{B} T R_\mathrm{p}}\right) \ . \tag{2.25}$$

The vapour pressure over a curved interface always exceeds the vapour pressure over a flat surface, since the exponential function is always ≥ 1. The Gibbs free energy is shown as a function of the droplet radius for two different saturation ratios S in figure 2.3. The critical radius can only be attained if the saturation ratio exceeds unity. For water molecules to reach the critical radius, a critical number of molecules need to agglomerate. The rate of which these molecule nucleate can be found using CNT. CNT predicts a homogeneous nucleation rate J_hom as (Seinfeld and Pandis 2016, eq. 11.47 therein)

$$J_\mathrm{hom} = \left(\frac{2\sigma}{\pi m_1}\right)^{1/2} \frac{v_\mathrm{l} N_1^2}{S} \exp\left(-\frac{16\pi}{3} \frac{v_\mathrm{l}^2 \sigma^3}{(k_\mathrm{B} T)^3 (\ln S)^2}\right) \ , \tag{2.26}$$

where: m_1 – mass of one monomer ($\approx 2.99 \times 10^{-23}$ kg),
N_1 – concentration of monomers (m^{-3}).

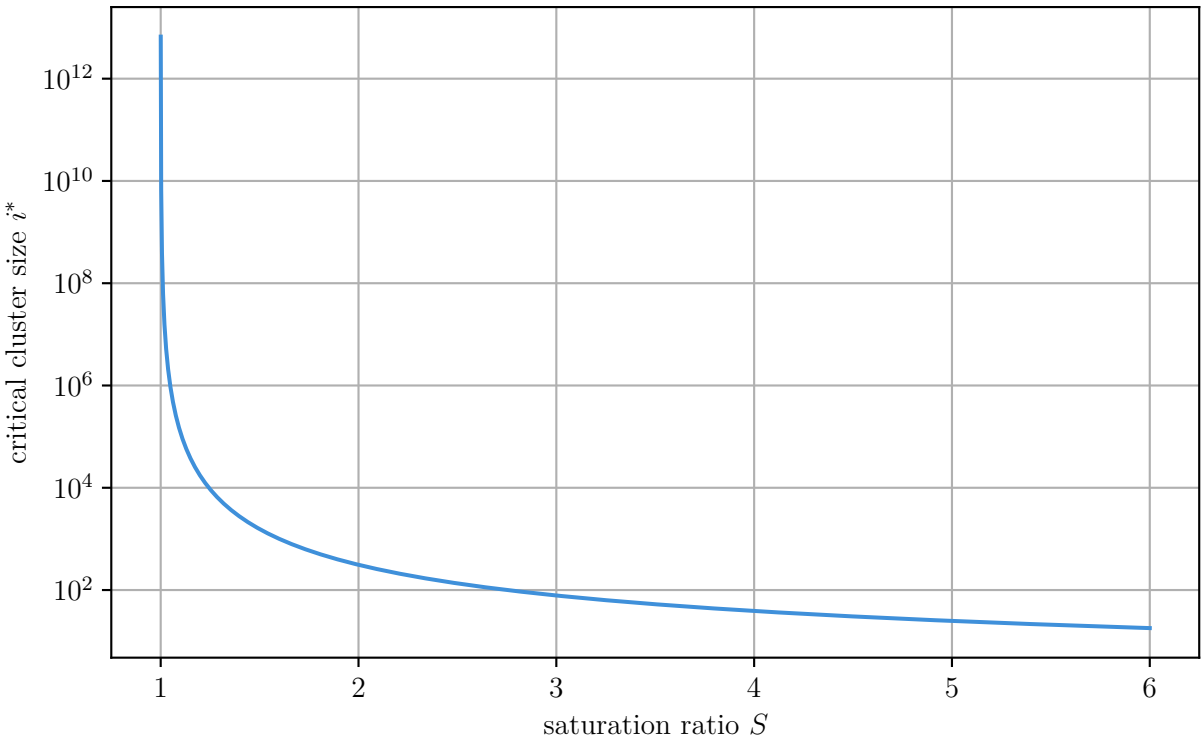

Figure 2.4.: **The critical cluster size i^* required for homogeneous-homomolecular nucleation to occur at $T = 293.15\,\mathrm{K}$ as a function of the saturation ratio S.**

The nucleation rate is defined as the number of clusters that exceed a critical size, and it varies around 28 orders of magnitude, with a saturation ratio ranging from 2 to 3. One can take a look at the size of the critical cluster, i.e. the number of molecules i^* that need to form a cluster to trigger nucleation, which is visualized for different saturation ratios and temperatures in figure 2.4 (Seinfeld and Pandis 2016, eq. 11.35 therein):

$$i^* = \frac{32\pi}{3} \frac{v_\mathrm{l}^2 \sigma^3}{(k_\mathrm{B} T)^3 (\ln S)^3} \,. \tag{2.27}$$

Homogeneous nucleation does not occur for water droplet formation in the Earth's atmosphere, during which the saturation ratio typically does not exceed 1.02 (e.g., Hudson 1992). Heterogeneous nucleation is possible at lower saturation ratios, enabling the formation of clouds in the Earth's atmosphere (e.g., Hudson 1992; Sun and Ariya 2006; Twomey 1959).

2.2.2.2. Cloud condensation nuclei (CCNs)

As a soluble or hydrophilic aerosol particle is lifted up in the atmosphere within an air parcel with a constant absolute humidity, the reduction in temperature leads to an increase in relative humidity and the particle grows via condensation (e.g., Lohmann et al. 2016, p. 155).[4] This uptake of water leads to the depletion of water vapour in the air parcel, but as the water saturation vapour pressure of the cooling air parcel decreases, it will become supersaturated. When a critical supersaturation in the air parcel is exceeded, the growing particle will reach its activation point. This activation point is determined by the size and the chemical composition of

[4]This is the simple case, considering only water vapour and no other soluble vapour compounds in the atmosphere.

the particle (e.g., Seinfeld and Pandis 2016, p. 719). The activated particles are called cloud condensation nuclei (CCNs). Once activated, the droplets increase in size until the water vapour is depleted and a steady state condition is realized (e.g., Seinfeld and Pandis 2016, p. 720). In principle, all aerosol particles in a given population can ast as CCNs when the saturation ratio is sufficienctly high.The concentration of CCNs is usually expressed as a function of the supersaturation s, which is defined as $s = S - 1$. The critical supersaturation is a characteristic property of CCNs and depends on their size and chemical composition (e.g., Twomey 1959).

Most CCNs are soluble, which means that, in general, there are no pure water droplets in the atmosphere, but the effects of solutes must be considered (Seinfeld and Pandis 2016, p. 712; Lohmann et al. 2016, p. 167). In the idealized case, where the solute has a low concentration, the vapour pressure of water containing a solute is given by Raoult's law (Seinfeld and Pandis 2016, eq. 17.9 therein)

$$e_{\mathrm{s,sol}} = x_w e_{\mathrm{s}}^{\circ} \tag{2.28}$$

where: $e_{\mathrm{s,sol}}$ – water vapour partial pressure over the solution (Pa),
x_{w} – mole fraction of water in the solution,
e_{s}° – saturation vapour pressure of pure water (Pa).

Therefore, by increasing the mole fraction of the solute and thereby decreasing the mole fraction of water in the solution x_{w}, the water vapour partial pressure over the solution decreases. By substituting Raoult's law (see (2.28)) into the Kelvin equation (see (2.25)), one arrives at a modified Kelvin equation, which is defined by Köhler theory (Seinfeld and Pandis 2016, eq. 17.19 therein)

$$\ln\left(\frac{e_{\mathrm{s}}(d_{\mathrm{p}})}{e_{\mathrm{s}}}\right) = \frac{A}{d_{\mathrm{p}}} - \frac{B}{d_{\mathrm{p}}^3} \ . \tag{2.29}$$

Here, the coefficients A and B are dependent on the temperature and the number of solute moles for a given solution, respectively (Seinfeld and Pandis 2016, p. 713). The first term represents the Kelvin effect, while the second term describes the effect of the solute, which leads to a decrease of the vapour pressure. For diameters below the critical diameter, the solute effect dominates, while above the critical diameter the equation approaches the Kelvin equation. In thermodynamic equilibrium, the critical droplet diameter is equivalent to a critical supersaturation. Upon reaching this activation point, a growing particle acts as a CCN and ultimately makes cloud formation in the Earth's atmosphere possible (see also Fletcher 1958; Köhler 1936). Extensions to classic Köhler theory exist to describe the case for partially soluble particles or soluble gases, which have the ability of deliquescence (e.g., Chen 1994; Hings et al. 2008; Seinfeld and Pandis 2016, app. 17 therein). While the formation of a cloud droplet in the Earth's atmosphere does not require a nucleation process, a short introduction into the phase transition for homogeneous and heterogeneous nucleation is given as an analogue process to describe heterogeneous ice nucleation using a contact angle in section 2.3.1.

A simple model is to consider heterogeneous nucleation of pure water onto a planar insoluble surface which reduces the energy barrier $\Delta G_{\mathrm{hom}}^{*}$ by a certain factor. This factor is a function of the contact angle θ, which can be understood as a proxy for the wettability of a surface (McDonald 1964; Pruppacher and Klett 1997, p. 301). The Gibbs free energy barrier is lowered as the contact angle decreases (Seinfeld and Pandis 2016, eq. 11.103 therein)

$$\Delta G_{\mathrm{het}}^{*} = \Delta G_{\mathrm{hom}}^{*} f(\cos\theta) \ , \tag{2.30}$$

where: $\Delta G_{\mathrm{het}}^{*}$ – maximum of the Gibbs free energy for heterogeneous nucleation (J),
$\Delta G_{\mathrm{hom}}^{*}$ – maximum of the Gibbs free energy for homogeneous nucleation (J, see equation (2.23)),
$f(\cos\theta)$ – function of a contact angle that varies between zero and one ($\theta \in [0°, 180°]$).

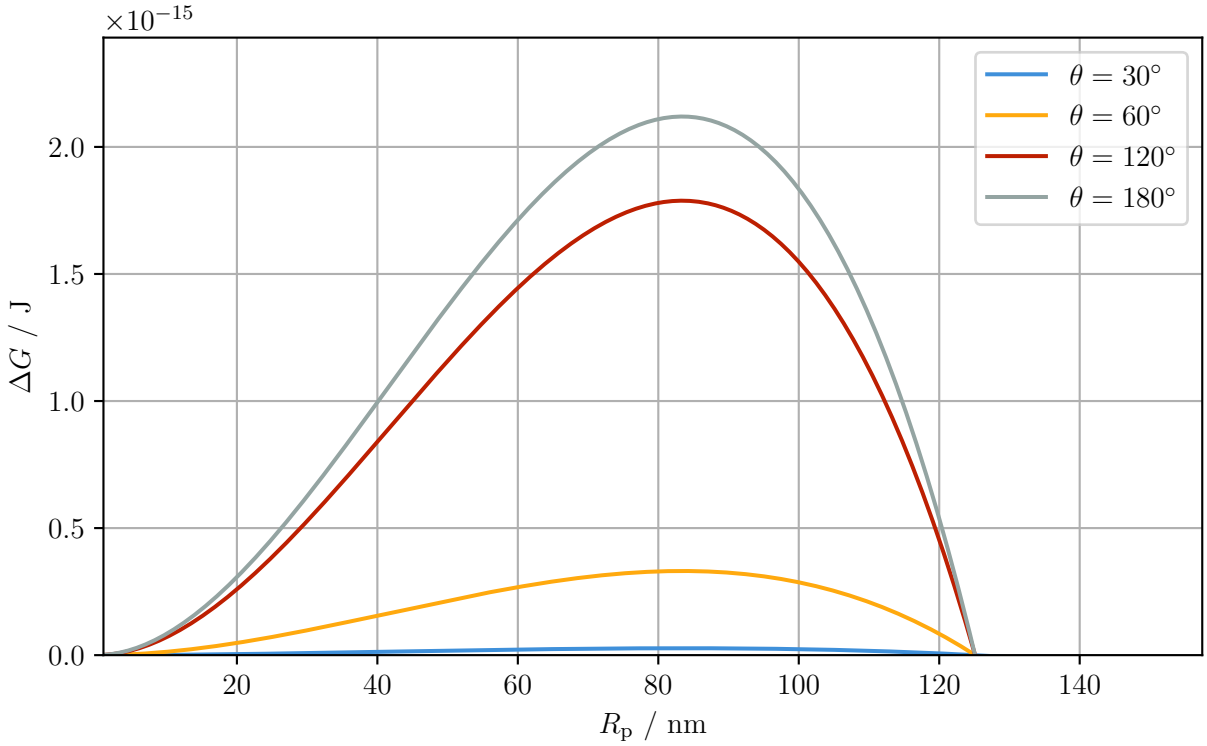

Figure 2.5.: **The Gibbs free energy change ΔG as a function of the droplet radius R_p for the formation of a water droplet on an aerosol particle with different contact angles θ at $T = 293.15\,\mathrm{K}$ and $S = 1.01$.**

The function f can be written as (Seinfeld and Pandis 2016, eq. 11.105 therein)

$$f(\cos\theta) = \frac{1}{4}(2 + \cos\theta)(1 - \cos\theta)^2 \ , \tag{2.31}$$

and the Gibbs free energy barrier for heterogeneous nucleation for different contact angles θ is visualized in figure 2.5. The function f does always satisfy $0 \leq f \leq 1$ (since $\theta \in [0°, 180°]$), thereby showing that the insoluble surface always decreases the Gibbs free energy barrier (e.g., Pruppacher and Klett 1997, p. 301). Dusek et al. (2006) report contact angles between 4 to 6° for carbon black particles, although they note that this contact angle is dependent on their definition of a size for irregularly shaped particles and not necessarily characteristic for the material. Different CCN are reported to have higher contact angles, with Chernoff and Bertram (2010) reporting a contact angle of 15° for Illite and similar values for other mineral dusts. For CCN of bacterial origin, contact angles have been found to be higher than 70°, making those able to nucleate water at very low supersaturation (Sharma and Hanumantha Rao 2002). CCN are responsible for all liquid cloud formation in Earth's atmosphere.

The above calculations were done at a standard temperature of $T = 293.15\,\mathrm{K}$, where pure water droplets always exist in their liquid form. In the Earth's atmosphere temperatures down to 100 K can be measured (e.g., ISO 2533:1975 1975), while above 235 K clouds can exist as a mixture of liquid and solid water (e.g., Kanji et al. 2017). The following section discusses the effect of different atmospheric temperatures on the activation of aerosol particles as INPs in detail.

2.2.2.3. INPs

MPCs exist for subzero temperatures above 235 K (e.g., Kanji et al. 2017). This is related to the same effect already mentioned in section 2.2.2.2, where the change in Gibbs free energy needs to be overcome for freezing to occur. Homogeneous ice nucleation of aqueous droplets in the Earth's atmosphere occurs only at temperatures below 235 K (e.g., Kanji et al. 2017). Above this temperature ice nucleation can only occur heterogeneously. Primary heterogeneous ice nucleation is initiated by INPs, a rare subset of aerosol particles. The concentration of INPs is heavily dependent on the ambient temperature. The efficiency of an INP is primarily related to its chemical composition and the size of the INP (e.g., Kanji et al. 2017).

The freezing of cloud droplets can occur via different pathways. Heterogeneous ice nucleation can be split into the following pathways:

Immersion freezing denotes the most prominent pathway for atmospheric conditions. An aerosol particle acts as a CCN, leading to the nucleation of a liquid water droplet at temperatures $T > 273.15\,\mathrm{K}$. The droplet is then cooled down, i.e. by vertical lifting in the atmosphere, and primary ice nucleation is initiated at the nucleation temperature T_{nuc}, that is distinct for each aerosol particle.

Deposition ice nucleation occurs in the absence of a macroscopic liquid phase. From the supersatured vapour phase, ice can directly form on the surface of the INP (Knopf and Alpert 2023). This pathway occurs for subsaturation in regard to water. Pore condensation and freezing (PCF) is a specific mechanism, where liquid water can exist inside nanometre-sized pores even below water saturation (David et al. 2019; Marcolli et al. 2021), leading to subsequent freezing. David et al. (2019) suggest that PCF is much more likely to occur compared to deposition ice nucleation, rendering this pathway not relevant for the formation of ice clouds in the Earth's atmosphere. Wagner et al. (2016) demonstrated the ability to pre-activate an aerosol particle by cooling it down below 228 K inside a cloud chamber and enhancing its ice-nucleating ability via the PCF mechanism.

Contact ice nucleation occurs when an INP collides with a supercooled liquid droplet. Cooper (1974) described contact freezing using CNT, where the critical ice embryo size must be equal or larger than the one required by immersion freezing. Niehaus et al. (2014) show that contact freezing can also enhance the ice nucleation ability of the bacteria *Pseudomonas syringae* by two orders of magnitude at 270 K. Contrary, Diehl and Mitra (1998) and Hoffmann et al. (2013) show a reverse effect, where contact ice nucleation happens at lower temperatures than immersion freezing. Ladino et al. (2011) reports no significant difference between the activation temperatures for both modes using kaolinite particles. A review of experimental field studies on this pathway can be found by Ladino Moreno et al. (2013). This pathway and its molecular mechanisms are still not understood fully (e.g., Hussain and Haji-Akbari 2021; Knopf and Alpert 2023).

Inside-out ice nucleation can be understood as a combination of immersion and contact freezing. A droplet contains an aerosol particle, which is not completely immersed inside the droplet, but is connected to the surface of the droplet. Due to this connection, an enhancement factor can be introduced to favor ice nucleation (Hussain and Haji-Akbari 2021). Bieber and Borduas-Dedekind (2024) utilized high-speed cryo-microscopy to measured the ice nucleation trigger location, revealing that some samples predominately initiate ice nucleation on the outer

shell of the droplet.

In addition, secondary ice production processes lead to a multiplication of ice crystals inside MPCs with the prerequisite of primary ice formation (e.g., Field et al. 2017; Hallett and Mossop 1974; Korolev et al. 2020; Korolev and Leisner 2020; Mossop 1976; Sullivan et al. 2017; Sullivan et al. 2018).

Looking at heterogeneous ice nucleation, two approaches to described it are used: the deterministic and the stochastic approach (Lohmann et al. 2016, pp. 229–230). The deterministic approach is shown by the CNT with a fixed energy barrier that needs to be overcome to facilitate ice nucleation heterogeneously (e.g., Lohmann et al. 2016). Knopf and Alpert (2023) suggest that the stochastic approach is sufficient to describe heterogeneous ice nucleation at mixed-phase temperatures, stating that their computational studies show that this approach can describe heterogeneous ice nucleation at temperature higher than about 240 K.

There are some requirements that seem to be required for aerosol particles to act as an INP. INPs are not water-soluble and a solid surface is required for ice nucleation to occur (e.g., Pruppacher and Klett 1997). Since the ice nucleation is triggered by the surface of the INP, the size of the aerosol particle matters. The ice nucleation ability increases for larger INPs (e.g., Pruppacher and Klett 1997). Aerosol particles are typically more efficient for ice nucleation, if the material contains chemical bonds similar to hydrogen bonds, available inside the ice crystal lattice (e.g., Pruppacher and Klett 1997). In addition, Fukuta (1966) reports an enhanced ice nucleation ability, if the molecule on the surface of the aerosol particle possesses a rotational symmetry, allowing a further reduction of the Gibbs free energy. A similar feature is observed for the structure of the lattice of the surface of an INP. The closer it is to the lattice formed by the ice crystals, the higher its ice nucleation ability (e.g., Evans 1965; Pruppacher and Klett 1997). The last requirement is related to the surface of the aerosol particles. Ice nucleation does not happen over the whole surface, but at certain sites, called active sites (AS) (e.g., Connolly et al. 2009; Holden et al. 2019; Hoose and Möhler 2012; Kiselev et al. 2017; Pruppacher and Klett 1997). Recent investigations have shown that immersion freezing and deposition nucleation start at surface defects (Friddle and Thürmer 2019; Holden et al. 2019; Pach and Verdaguer 2019), although the AS are different for the different heterogeneous freezing pathways (Holden et al. 2021).

The assumed structure of the ice lattice that forms during nucleation is not trivial. There are 15 known polymorphs of ice, albeit only Ih[5] ice is a stable phase at ambient pressure (Salzmann et al. 2011). The transition into a stable phase occurs over one or more metastable phases (Ostwald 1897; Van Santen 1984). This phenomenon is known as *Ostwald's rule* and was also observed for pure water droplets of 0.9 µm in diameter at 232 K (Malkin et al. 2012). Malkin et al. (2012) report that homogeneous freezing leads to a metastable phase, consisting of randomly stacked layers of the metastable cubic ice Ic and the stable Ih ice polymorphs. Since cubic ice Ic has lower interstitial energy, CNT and its derivation of the change in the Gibbs free energy is dependent on the lattice structure of the ice that forms. Contrary to homogeneous freezing, where the phase transition follows Ostwald's rule, heterogeneous ice nucleation can happen without the prerequisite of the metastable phase (Pruppacher and Klett 1997, p. 314).

[5] h denotes the hexagonal structure of Ih ice.

2.3. INP representation in models

Describing the detailed microphysics of different heterogeneous ice nucleation pathways is often not possible for global or even large scale models. Therefore, simplifications are used to calculate the concentration of INPs in relation to other parameters or to describe the microphysics using the contact angle approach. The present section describes several of these methodologies. The fundamental process of ice nucleation can be categorised into two distinct groups of representations. Various parameterizations exist to describe the stochastic nature of ice nucleation, in which ice nucleation is time-dependent and a very low probability will lead to ice nucleation if given enough time (e.g., Alpert and Knopf 2016; Hoose et al. 2010; Khvorostyanov and Curry 2000, 2005; Murray et al. 2011; Niedermeier et al. 2010). Conversely, the deterministic approach, in which a surface is associated with a characteristic nucleation temperature[6], is frequently cited in the literature (e.g., Holden et al. 2021; Hoose and Möhler 2012; Kiselev et al. 2017; Ullrich et al. 2017; Wheeler et al. 2014; Zolles et al. 2015). The subsequent sections will provide a concise overview of both representations, in addition to the methodologies that aim to combine them (e.g., Ervens and Feingold 2013; Marcolli et al. 2007; Murray et al. 2012; Niedermeier et al. 2011; Vali 1994; Welti et al. 2012).

2.3.1. Contact angle

Contact angles were already discussed in section 2.2.2.2 in regard to CCN. The principle of contact angles can also be used to describe heterogeneous ice formation. For cloud droplet formation the contact angle is a representation of the wettability of a surface, while for primary ice formation the contact angle does not directly relate to a physical quantity, but rather is understood as a model parameter (Chen et al. 2008; Murray et al. 2012; Savre and Ekman 2015). Chen et al. (2008) uses CNT with a shape factor to described the nucleation rates for different ice nucleation pathways

$$J_\mathrm{m} = A_\mathrm{m} \exp\left(\frac{-\Delta G_\mathrm{act,m} - \Delta G_\mathrm{g,m} f}{k_\mathrm{B} T}\right) , \tag{2.32}$$

where:
- J_m – nucleation rate for a given mode ($\mathrm{m^{-2}\,s^{-1}}$)
- A_m – pre-exponential factor for a given mode ($\mathrm{m^{-2}\,s^{-1}}$)
- $\Delta G_\mathrm{act,m}$ – activation Gibbs free energy for a given mode (J)
- $\Delta G_\mathrm{g,m}$ – critical Gibbs free energy required for a given mode (J)
- f – shape factor (see also equation (2.31)).

Each relevant pathway discussed in section 2.2.2.3 is further on described by its own expression, which are often a mixture of CNT and experimentally-derived functions. Barahona (2012) provides a parameterization for deposition ice nucleation, which is used by Savre and Ekman (2015) in combination to a temperature-dependent formulation of the Gibbs free energy of desorption of water molecules on the surface to suppress deposition ice nucleation at higher temperatures (see also Hoose and Möhler 2012; Wang et al. 2011; Welti et al. 2014, 2009). The change in Gibbs free energy for the immersion ice nucleation pathway is given as a function of the water saturation with the parameterizations by Chen et al. (2008), Ervens and Feingold (2013) and Khvorostyanov and Curry (2004). Contact ice nucleation is not considered since it occurs for equal or higher supersaturations compared to immersion freezing (Cooper 1974)

[6] Here it is assumed, that the surface already is in contact to water, i.e. sufficient saturation ratios in regard to ice S_ice are available.

and also is not understood fully (Hussain and Haji-Akbari 2021; Knopf and Alpert 2023, see also section 2.2.2.3). Ervens and Feingold (2013) show that using CNT and a single contact angle θ (denoted as single-α model) for an entire aerosol population is not feasible, leading to a vast overestimation of the ice crystal production. The single-α model has been used in many parameterizations, but more complex models are more prevalent nowadays due to better and more accurate results (Lüönd et al. 2010; Marcolli et al. 2007; Niedermeier et al. 2011; Niedermeier et al. 2015, 2014; Peckhaus et al. 2016; Welti et al. 2014). As discussed in section 2.1 an aerosol population is characterized by a multitude of different factors, predominantly their size and shape as well as their concentration. For estimating the ice nucleation ability of the aerosol population, the contact angle can be described by a probability density function (PDF) (e.g., Wheeler and Bertram 2012). By integrating over the PDF $p_{\mathrm{x,m}}(\Theta)$, one can estimate the average freezing probability $\overline{\mathcal{P}_{\mathrm{x,m}}}$ of the aerosol population characterized by its size distribution $f_x(D)$ as

$$\overline{\mathcal{P}_{\mathrm{x,m}}} = \int_{\theta_{\min}}^{\theta_{\max}} \int_{d_{\mathrm{p,min}}}^{d_{\mathrm{p,max}}} \mathcal{P}_{\mathrm{x,m}}(\Theta, D) p_{\mathrm{x,m}}(\Theta) f_x(D)\, \mathrm{d}D\, \mathrm{d}\Theta \ . \tag{2.33}$$

Savre and Ekman (2015) use a normal distribution for the contact angle PDF given as a function of the mean contact angle $\overline{\theta_{\mathrm{x,m}}}$ and its standard deviation $\sigma_{\theta_{\mathrm{x,m}}}$

$$p_{\mathrm{x,m}}(\theta) = \frac{1}{\sqrt{2\pi}\sigma_{\theta_{\mathrm{x,m}}}} \exp\left(-\frac{\theta - \overline{\theta_{\mathrm{x,m}}}}{2\sigma^2_{\theta_{\mathrm{x,m}}}}\right) \ . \tag{2.34}$$

This is known as the α-PDF model (Lüönd et al. 2010; Marcolli et al. 2007; Welti et al. 2014, α denoting the contact angle θ). A different modification of the single-α model is the soccer-ball model, which aims to describe the surface of aerosol particles covered with surface sites with different nucleation barriers (Niedermeier et al. 2011; Niedermeier et al. 2015, 2014; Peckhaus et al. 2016). Both methods are used to account for the inter-sample variability often observed in freezing events (Consiglio et al. 2023; Kulkarni et al. 2012; Wheeler and Bertram 2012). Experimental data is then used to fit these two parameters for a given aerosol species, with a nucleation temperature defined at the point where half of the droplets are frozen (Savre and Ekman 2015). Barahona (2012) use a similar approach, but use a differen nucleation temperature, which is defined at the temperature, where ten percent of the droplets are frozen, which might introduce a certain bias for highly active nucleation pathways into the fitting of the contact angle. In general, there is usually a relatively high spread of the experimental results as well as the model results, which is also in part related to the capillary approximation used in CNT (see section 2.2.2.2).

2.3.2. Ice nucleation active site (INAS) density

CNT is a fundamentally stochastic theory that describes the nucleation in regard to the surface of the aerosol, which is assumed to be uniform (Fletcher 1958). The introduction of a surface angle (see section 2.3.1) introduces a deterministic approach to describe ice nucleation. A similar approach is the definition of AS, which represent surface areas that are able to nucleate ice below a certain nucleation temperature. Surface-based parameterizations use the INAS densities to describe the size-dependency of an aerosol particle to act as an INP (e.g., Connolly et al. 2009; DeMott 1995; Ullrich et al. 2017). Hoose and Möhler (2012) define the INAS density by normalizing the ice nucleation active fraction with the surface area per particle (see section 2.1.1)

$$n_{\mathrm{s}}(T, S_{\mathrm{i}}) = -\frac{1}{A_{\mathrm{aer}}} \ln(1 - f_{\mathrm{IN}}(T, S_{\mathrm{i}}))) \tag{2.35}$$

Table 2.2.: **Fit parameters for the frozen fractions of different aerosol species.** The uncertainties are given with a coverage value determined for a 95 % confidence interval considering an underlying Student's t distribution (Student 1908).

Material	mass fraction / %	B / K^{-1}	M / K	residual variance
BiI_3	0.1	-2.9 ± 0.1	263.48 ± 0.02	0.1
Snomax	0.0001	-5.8 ± 0.6	265.15 ± 0.03	0.1
NX illite		$-10.0 \pm 31\,493.9$	252.36 ± 377.57	3 769 197.4

where: T – temperature (K),
S_i – saturation ratio in regard to ice,
A_aer – aerosol surface per particle ($\mathrm{m}^2_\mathrm{aer}$),
f_IN – ice nucleation active fraction.

The intrinsic variability in size of a given aerosol sample is taken into account by normalizing the ice nucleation ability of aerosols to their surface area. This way an aerosol is characterized by its AS and not as a function of its size, resulting in a dependency only on the temperature T and the saturation ratio in respect to ice S_i. Equation (2.35) can also be written for the general case of polydisperse aerosol distribution by taking the integral over the different particle diameters d_p

$$n_\mathrm{s}(T, S_\mathrm{i}) = -\int_0^\infty \frac{1}{A_\mathrm{aer}(d_\mathrm{p})} \ln(1 - f_\mathrm{IN}(T, S_\mathrm{i}, d_\mathrm{p}))\, \mathrm{d}d_\mathrm{p} \ . \tag{2.36}$$

The frozen fraction is shown in figure 2.6 for different types of aerosol particles measured with a freezing assay for immersion freezing (Schneider et al. 2021). It is therefore only dependent on the temperature when considering a monodisperse aerosol distribution. The frozen fraction is fit using orthogonal distance regression (ODR), considering only upper uncertainties (Boggs and Rogers 1990) using a generalized version of the logistic function, described by

$$f_\mathrm{IN}(T) = \frac{1}{1 + \exp\left(-B(T - M)\right)} \ , \tag{2.37}$$

where: B – fit parameter describing the slope (K^{-1}),
M – fit parameter describing the location where the slope has its maxima (K).

Bismuth(III) iodide is an inorganic compound that has a crystal structure, wherein iodide centers a hexagonally closest-packed lattice, while bismuth occupies octahedral holes in an alternating fashion (Smart et al. 2005, p. 40; MacKay 2017, pp. 122–126; see also Vonnegut 1947). Snomax is a commercially available product used in the production of artifical snow, which is based on the proteins of the *Pseudonomas syringae* bacteria, known to nucleate ice at high temperatures (Maki et al. 1974; Wex et al. 2015; Wieber et al. 2024). Illite is a group of clay materials known for its ice-nucleating ability (e.g., Hiranuma et al. 2015). Defining the freezing onset temperature as the temperature where the ice nucleation active fraction is 0.5, results in the values shown in table 2.2. The difference between the three samples is evident in the different qualities of the fits. The fit assumes a single contact angle, i.e. a characteristic nucleation temperature, whereas NX illite shows a low quality fit, indicating that a single contact angle is unable to describe the mixture of slightly different materials. Eidhammer et al. (2009) report that a contact angle distribution also leads to better results when predicting the frozen fraction of atmospheric INPs.

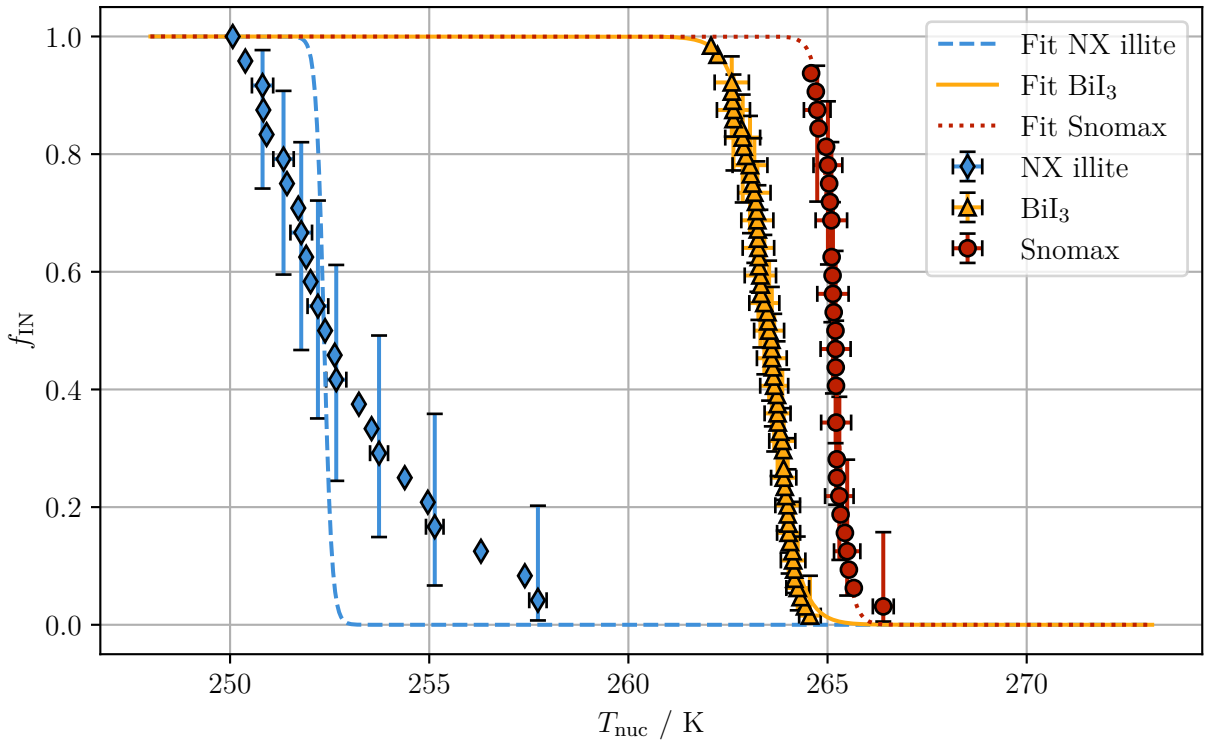

Figure 2.6.: **The ice nucleation active fraction f_{IN} for immersion freezing is shown as a function of the nucleation temperature T_{nuc} for three different materials: NX illite (mixture of illite, kaolinite, quartz, calcite and feldspar), Bismuth(III) iodide (BiI_3) and Snomax.** The fit is shown for each dataset considering a single contact angle.

2.3.3. Parameterization

Previous sections discussed work focusing on a single aerosol sample, with its properties measured in the lab. Other efforts focus on the measurement of aerosols in the atmosphere without an *a priori* knowledge on the nature of aerosols. Efforts in this direction try to estimate the INP concentration at a certain temperature by using variables that are already used in models, such as the ambient surface temperature or the aerosol particle size distribution.

2.3.3.1. Deterministic parameterizations

Meyers et al. (1992) predict the INP concentration as a function of the supersaturation s, while Cotton et al. (1986) and Fletcher (1962) provide parameterizations that are related to the nucleation temperature T_{nuc}. They, however, often fail to account for the INP concentration at different locations and seasons (e.g., DeMott et al. 2010).

A popular and measurement-based parameterization is given by DeMott et al. (2010). Combining measurements of multiple aircraft-based field campaigns, results in a parameterization that is based on the number of aerosol particles above an aerodynamic particle diameter of 0.5 µm:

$$c_{INP} = a \left(273.16 - \frac{T_{nuc}}{K}\right)^{b} \left(\frac{n_{aer,0.5}}{cm_{std}^{-3}}\right)^{c\left(273.16 - \frac{T_{nuc}}{K}\right)+d}, \tag{2.38}$$

where: a – fit parameter ($5.94 \times 10^{-5}\,\mathrm{l}_{\mathrm{std}}^{-1}$),
T_{nuc} – nucleation temperature (K),
b – fit parameter (3.33),
$n_{\mathrm{aer},0.5}$ – number concentration of aerosol particles with diameters larger than 0.5 µm ($\mathrm{cm}_{\mathrm{std}}^{-3}$),
c – fit parameter (0.0264),
d – fit parameter (0.0033).

The measured INP concentration was limited to aerosol particle diameters below 1.6 µm, therefore the parameterization might introduce a bias for temperatures above −15 °C (DeMott et al. 2010). Aerosol particles, that are active as INP at higher temperatures (>−13 °C), are generally larger (Santachiara et al. 2010). Furthermore, Berezinski et al. (1988) report the highest influence to the total number concentration of INPs for aerosol particles with a particle diameter above 10 µm. Mason et al. (2016) report size-resolved measurements of the INP concentration at six sites in North America and one in Europe, where (91 ± 9) % of INP active at −15 °C have an aeroynamic particle diameter above 1 µm. Consequently, for a nucleation temperature of −25 °C this percentage decreases to (60 ± 20) %, while the same behaviour is seen also for coarse mode particles (>2.5 µm, Mason et al. 2016).

A similar parameterization was developed by Murray et al. (2012) focusing on INPs of agricultural soil origin with a dependence on the surface area

$$c_{\mathrm{INP}} = N_{\mathrm{tot}}(1 - \exp(-n_{\mathrm{s}}(T_{\mathrm{nuc}})A_{\mathrm{aer}})) \ , \tag{2.39}$$

where: N_{tot} – total aerosol number concentration (cm^{-3}),
n_{s} – INAS density ($\mathrm{m}_{\mathrm{aer}}^{-2}$, see equation (2.35)),
A_{tot} – total aerosol surface area ($\mathrm{m}_{\mathrm{aer}}^{2}$).

All three of these types of parameterization lack a dependence on the type and nature of the different INP populations. By performing measurements of known aerosol species, one can evaluate different parameterizations that are related to the aerosol species to predict a representative INP population.

To predict the ice nucleation ability of aerosol, one can also predict not the INP concentration per volume of air, but the INAS density directly. These parameterizations can be found for different lab-based studies, following a polynomial fit as a function of the nucleation temperature T_{nuc}

$$n_{\mathrm{s}} = a \times \exp\left(\sum_{i=0}^{N} a_i T_{\mathrm{nuc}}^{i}\right) \ . \tag{2.40}$$

Different parameterizations that predict the INAS density are shown in Murray et al. (2012) and table 2.3. The fitted parameterizations are visualized together with a field-based parameterization of boreal forest aerosol over different seasons (Schneider et al. 2021; Ullrich et al. 2017, figure 2.7). Higher temperatures are dominated by ice-nucleation-active bacteria. In this instance, *Pseudonomas Syringae* is used as a model bacteria due to its extensive application as a high-temperature INP in intercomparison studies (Wex et al. 2015). The highest INAS density is shown for soot aerosol with dust slightly below and volcanic ash showing one of the lowest INAS densities at lower temperatures. Aerosol of biogenic origin, such as birch pollen show a high INAS density and a relatively high nucleation temperature, while *Cladosporidium* spores (i.e. fungal spores) show an ice-nucleating ability only at lower temperatures and at low INAS densities. NX illite is a mixture of different minerals (illite, kaolinite, quartz, carbonate, and feldspar) that is commercially available and has been used in recent intercomparison campaigns

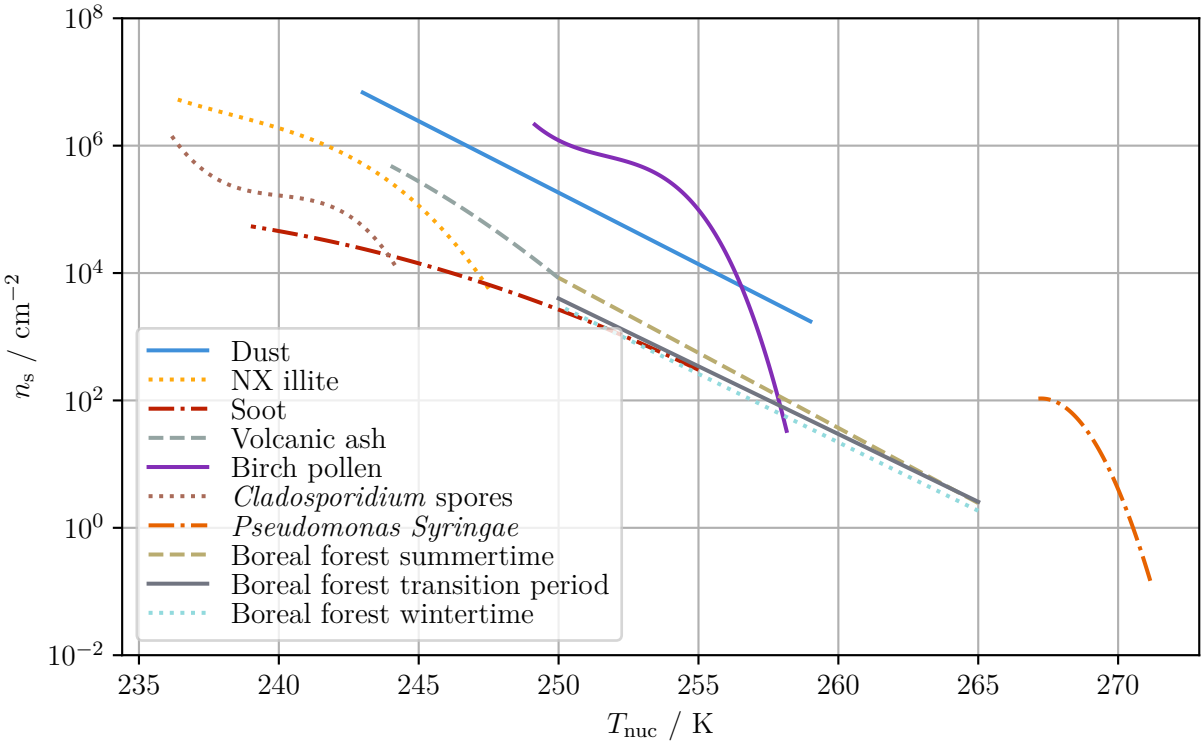

Figure 2.7.: **INAS parameterizations for various aerosol samples.** The data and fitting are detailed further in table 2.3.

for lower temperatures (Hiranuma et al. 2015), Broadley et al. (2012) report that this mixture is a good proxy for transported natural dust. In addition to parameterizations that are focused on single aerosols or on a mixture of similar aerosols, longer termed field campaigns are used to predict the INAS density of aerosols too. Schneider et al. (2021) measured the INP concentration in southern Finland, located inside the boreal forest and defined three different periods based on snow height. At lower temperatures, the INAS density for the summertime shows good agreement with the INAS density of volcanic ash, while the other two periods show slightly lower INAS densities. For higher temperatures, Schneider et al. (2021) find a high influence from local aerosols that are of biogenic origin. Such local emissions are hard to quantify in global models and might also play a relatively small role, when comparing to the most prevalent aerosol sources such as mineral dust (see also table 2.1).

Koop and Zobrist (2009) provides a water-activity-based approach to predict heterogeneous ice nucleation in the case of droplets that do not contain pure water, where the heterogeneous ice nucleation depression is calculated as a function of the solute and the type of the INP

$$\Delta T_{\text{het}} = \lambda_{\text{het}}(\text{s}, \text{INP}) \Delta T_{\text{m}} \ , \tag{2.41}$$

where:
- ΔT_{het} – heterogeneous ice nucleation depression (K),
- $\lambda_{\text{het}}(\text{s}, \text{INP})$ – proportionality constant,
- s – solute,
- INP – INP type,
- ΔT_{m} – equilibrium ice melting point depression for the solution (K).

This approach was originally developed by Mackenzie (1977) and Rasmussen (1982) for homogeneous ice nucleation. This approach might be vital, since the coating of aerosol particles can have

Table 2.3.: **INAS parameterizations for various aerosol samples.** The corresponding formulas are described in chapter E.

Name	Temperature range	Parameterization	Reference
Dust	243.0 to 259.0 K	(E.1)	Ullrich et al. (2017)
NX Illite	236.2 to 247.5 K	(E.2)	Broadley et al. (2012)
Soot	239.0 to 255.0 K	(E.3)	Ullrich et al. (2017)
Volcanic ash	251.4 to 258.0 K	(E.4)	Fornea et al. (2009), Hoyle et al. (2011), Murray et al. (2012) and Steinke et al. (2011)
Birch pollen		(E.5)	Murray et al. (2012)
Cladosporidium spores	236.2 to 244.2 K	(E.6)	Iannone et al. (2011) and Murray et al. (2012)
Pseudomonas Syringae	264.2 to 271.2 K	(E.7)	Murray et al. (2012) and Yankofsky et al. (1981)
Boreal forest summertime	250.0 to 265.0 K	(E.8)	Schneider et al. (2021)
Boreal forest transition period	250.0 to 265.0 K	(E.9)	Schneider et al. (2021)
Boreal forest wintertime	250.0 to 265.0 K	(E.10)	Schneider et al. (2021)

large effects on their ice nucleation ability (e.g., Bertozzi et al. 2021; Friedman et al. 2011; Kanji et al. 2019; Knopf et al. 2018; Kulkarni et al. 2014; Möhler et al. 2005; Möhler et al. 2008).

2.3.3.2. Stochastic parameterizations

Stochastic parameterizations are based on CNT, which describes heterogeneous nucleation as a purely stochastic process by predicting a freezing rate for a given set of conditions. A set of different parameterization of this type are given by e.g. Hoose et al. (2010) for two nucleations modes (immersion freezing and deposition nucleation, see also section 2.2.2.3) and four different aerosol species (soot, dust, *Pseudonomas syringae* for bacteria, birch pollen for pollen). Hoose et al. (2010) note that some results from CNT are in conflict with measurements, especially in regard to a freezing rate that is constant in time. Knopf and Alpert (2023) on the other hand report that the heterogeneous nucleation observed in freezing events of illite particles at a constant surface area can be completely explained by CNT.

Steinke and Burrows (2022) use a Monte Carlo approach and simulated freezing spectra to assess the different aspects of experimental uncertainty, aerosol surface area variability and particle-to-particle differences. The Monte Carlo approach is used on differently-shaped distributions of the heterogeneous freezing rate J_{het}. They find that the choice of distribution is not impacting the frozen fraction, unless the underlying distribution spans at least on order of magnitude, impacting especially low values of the frozen fraction (i.e., at higher temperatures and/or less effective INPs). They further advocate that a large statistic is needed to reduce uncertainties in droplet freezing experiments and that the particle-to-particle variability even for well-studied aerosol types is virtually unknown.

In general, the literature agrees, that ice formation inside clouds needs to be assessed better and in more detail to achieve a unifying theory that describes heterogeneous nucleation for different aerosol types and under different ambient conditions.

2.4. Arctic environment

Global climate change is most strongly felt in the Arctic, where temperatures have increased much faster than in the rest of the world. This phenomenon is known as AA. Recently, Rantanen et al. (2022) showed that the Arctic has warmed nearly four times faster than the rest of the world since 1979. The factors influencing this increased warming effect are manifold, but thought to be: increase of oceanic heating and ice-albedo feedback due to diminishing sea ice (Dai and Jenkins 2023; Dai et al. 2019; Jenkins and Dai 2021; Screen and Simmonds 2010; Thackeray and Hall 2019), Planck feedback (Pithan and Mauritsen 2014), lapse-rate feedback (Dai and Jenkins 2023; Stuecker et al. 2018), near-surface air temperature inversion (Bintanja et al. 2011), cloud feedback (Taylor et al. 2013), ocean heat transport (Beer et al. 2020), meridional atmospheric moisture transport (Graversen and Burtu 2016; Kim et al. 2017; Woods and Caballero 2016) and reduced air pollution in Europe (Acosta Navarro et al. 2016; Krishnan et al. 2020). The changes associated with this have global relevancy, for example Dai (2022) reports that AA is the main cause of the weakening of the Atlantic meridional overturning circulation (AMOC) under high emission scenarios. The collapse of the AMOC will have large and global effects (e.g., amazon rainforest, Ciemer et al. 2021; monsoon, Ben-Yami et al. 2024).

2.4.1. Arctic aerosols

This section aims to provide a short description of relevant aerosols in the Arctic and transport pathways of those. In the Arctic, natural aerosol sources are limited. The two main sources

being the oceans for sea salt aerosol and bare soil for dust (Kokhanovsky and Tomasi 2020). Sea salt aerosol consist of primary SSA and secondary organic aerosol (SOA) produced by DMS and other BVOCs. Increasing temperatures will lead to an increase in the emission of these, mostly due to an increase in biological activity. In addition, the phenomenon known as Arctic haze (AH) leads to increased anthropogenic aerosol transport into the Arctic from mid latitudes. AH was first observed in the 1950s from personell on weather reconnaissance missions into the high Arctic. Data from these flights were later analysed by Raatz (1984), who discovered that it is most prevalent 'during anticyclone conditions when mechanical turbulence is lowered and rain or snowfall is slight' (Shaw 1995, p. 2404). AH has a strong seasonal frequency, reaching its maximum occurence between February and April (Shaw 1995). The reasons for the occurence of AH can be grouped into three different aspects:

Strong temperature inversions: during polar night, the polar atmosphere is very stable and stagnant due to the strong and sustained cooling of the lower atmosphere. Strong temperature inversions cause the atmosphere to stabilize, leading to inhibition of turbulent transfer between the atmospheric layers. The removal of aerosol from the atmosphere is therefore inhibited.

Low water amount: the cold air is very dry, leading to almost no precipitation during polar night and therefore also to small scavenging rates for aerosol particles.

Low turbulence: wind systems on Earth are driven by gradients in the heat budget. Tropical regions have large vertical mixing due to deep convection, while mid latitudes show strong frontal systems related to subtropical jet streams. The Arctic does not show these gradients of energy, therefore during winter months the stable atmosphere remains calm. A calm atmosphere suppresses the removal of aerosol and trace gases.

AH is a phenomenon that exists due to the formation of this polar dome, whose extent is smallest during summer. Different transport mechanisms for BC into the polar dome are depicted in figure 2.8 based on Stohl (2006). Aerosols from emission sources outside the polar dome can reach the Arctic by following isentropic surface, which are surfaces of constant potential temperature. These surface increase in altitude towards the north (pathway 1 in figure 2.8). This typically leads to the formation of clouds (see section 2.2.2.2), precipitation and subsequent deposition of aerosols on snow (pathway 2). At its largest extent, the polar dome can stretch as far south as 40° N, allowing low-level transport directly into the Arctic (pathway 3). Aerosols can also enter the Arctic from the upper troposphere by slowly descending into the polar dome (pathway 4) or by mixing of extra-Arctic air into the polar dome (pathway 5). Both processes require radiative cooling which takes several weeks (typically around $1\,\mathrm{K\,d^{-1}}$). The aerosol that slowly descends into the polar dome can originate from anthropogenic and biomass burning pollution plumes (pathway 6). Agricultural fires can inject aerosols into the free troposphere, reducing the impact of dry and wet deposition (pathway 7). The aerosol from agricultural fires can also get injected into the stratosphere if sufficient convection exists, leading to even longer residence times of the aerosol plume (pathway 8). Pathway 9 is related to the high altitude of the Greenland ice sheet, which is more susceptible to mid latitude transport. Due to the highly vertically stable atmosphere during polar night, AH is highly stratified. This means that different atmospheric layers are affected by different source regions (see also Quinn et al. 2011, figure 5.2 therein for different emission sensitivities of stations at different altitudes inside the Arctic).

The current knowledge on the vertical distribution of AH is mostly based on sporadic aircraft campaigns, mostly conducted during late spring and summer (e.g., Bozem et al. 2019; Jurányi et al. 2023). While aircraft campaigns provided sparse *in situ* measurements of AH during late spring and early summer, remote sensing observations allowed prolonged characterization of AH

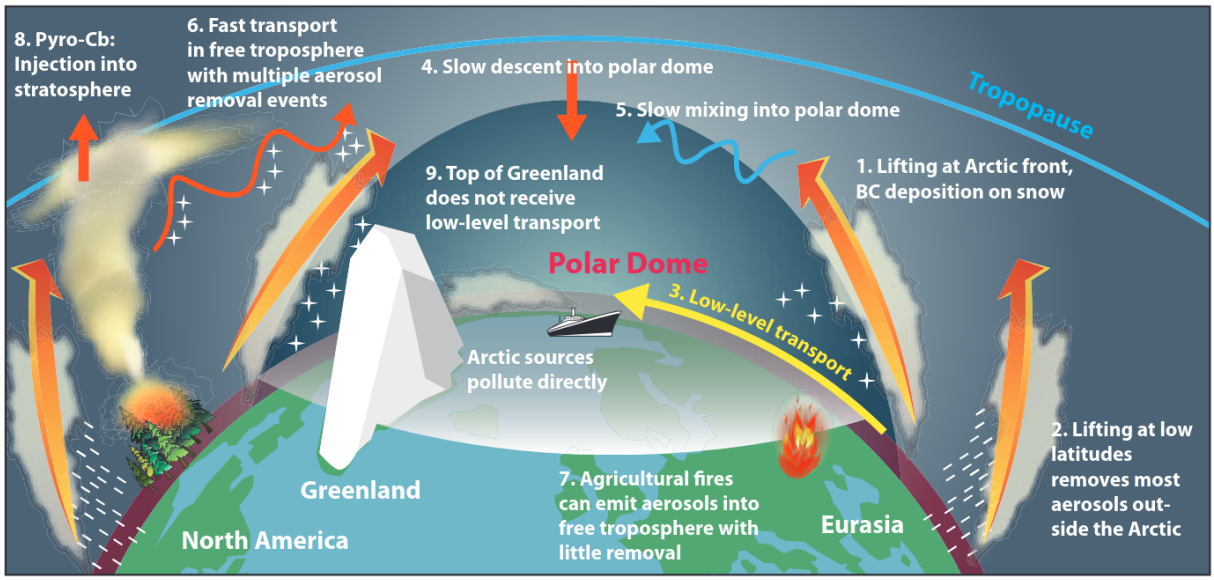

Figure 2.8.: **Schematic illustration of the transport process of BC into the Arctic based on Stohl (2006).** The extent of the polar dome is not symmetric in reality, having its greatest extent over Eurasia. In addition, its extent varies over the different seasons. Figure from Quinn et al. (2011).

during the peak in winter. Remote sensing data from Multidisciplinary drifting Observatory for the Study of Arctic Climate (MOSAiC) are shown for two cases of AH in figure 2.9 (Engelmann et al. 2021; for a general overview of the atmospheric measurements during MOSAiC see also Shupe et al. 2022). Both cases show a near surface layer (<2.5 km altitude) and a second aloft layer reaching to 5 km and 7 km, respectively. Together with local emissions of aerosol particles these long-range transported aerosol particles form the background arctic aerosol population.

As described in section 2.1 aerosol can be emitted from multiple sources, both anthropogenic and natural. These aerosols can be characterized by their size, forming different modes. The aerosol particle size distribution is characterized by three distinct modes: (i) the nucleation mode (5×10^{-3} to 10^{-1} µm); (ii) the accumulation mode (0.1 to 1 µm); and (iii) the coarse mode (>1 µm). The largest aerosols are typically of sizes between 5 µm and 8 µm. The aerosol populations and their properties are spatially and temporally varied throughout the Arctic. In Ny-Ålesund, on Svalbard, a Norwegian archipelago extending from 74°N to 81°N in the Arctic Ocean, measurements of the arctic aerosol population have been carried out since 1997 with *in situ* instrumentation. Measurements of the chemical composition of aerosol particles smaller than 10 µm during the period 2011-2015 show a higher mass concentration during spring[7] (2.82 µg m^{-3}) compared to summer (1.40 µg m^{-3} Kokhanovsky and Tomasi 2020).

Table 2.4 shows the data split into three size ranges: PM10 for all particles smaller than 10 µm, sub-micrometric (<1 µm) and super-micrometric (>1 µm) particles. Focusing on the change in the chemical composition, sea salt aerosol and mineral dust are especially relevant at larger size ranges, where they make up most of the aerosol mass in the atmosphere (e.g., Kok et al. 2021; Weng et al. 2020, see also table 2.1). Sub-micrometric particles are dominated by sulfate and nitrate aerosol during spring with a slight decrease in summer, when mineral dust dominates in the aerosol mass concentration. The reasons for this are manifold: transported aerosol has

[7] Spring denotes the months March, April and May; whereas summer denotes the months June, July, August and September.

Table 2.4.: **Aerosol mass concentrations and aerosol chemical composition for spring and summer for three different size categories.** Total of mass percentage can be above 100 % due to rounding. Data collected at GVB and taken from Kokhanovsky and Tomasi (2020).

Aerosol subset	Chemical composition	Spring	Mass percentage %	Summer	Mass percentage %
PM10	sea salt	$2.82\,\mu g\,m^{-3}$	42.3	$1.40\,\mu g\,m^{-3}$	28.5
	mineral dust		27.6		23.1
	sulfate / nitrate		12.5		36.1
	OC[a]		12.5		7.1
	MSA[b]		3.6		3.6
	BC[c]		1.6		2.4
<1 µm	sea salt	$1.66\,\mu g\,m^{-3}$	12.6	$0.70\,\mu g\,m^{-3}$	6.7
	mineral dust		23.4		33.1
	sulfate / nitrate		42.9		25.2
	OC[a]		12.5		24.8
	MSA[b]		5.8		5.4
	BC[c]		2.8		4.8
>1 µm	sea salt	$0.96\,\mu g\,m^{-3}$	50.6	$0.89\,\mu g\,m^{-3}$	48.7
	mineral dust		39.5		42.8
	sulfate / nitrate		9.4		8.3
	OC[a]		0.0		0.0
	MSA[b]		0.5		0.2
	BC[c]		0.0		0.0

[a] organic carbon;
[b] methanesulfonic acid;
[c] black carbon

different residence times in the atmosphere in relation to its size (e.g., Williams et al. 2002) and wet and dry deposition is more effective for larger aerosol particles (e.g., Hertel et al. 1995; Kyrö et al. 2009; Laakso et al. 2003). Consequently, larger aerosol particles tend do travel shorter distances, while smaller aerosol particles can travel further. Sea salt aerosol accounts for around half of the aerosol mass concentration for spring and summer for super-micrometric particles, highlighting the local sources from the Arctic Ocean. In addition, the diameter of sea salt aerosol is in general larger with a global emission that is around 60 times more abundant in the coarse mode compared to the accumulation mode (Weng et al. 2020, see also table 2.1). The difference between spring and summer is especially pronounced for the sub-micrometric aerosol particles, aerosol particles that have longer residence times in the atmosphere and therefore might also be originating at sources outside of the Arctic.

Seasonal changes in the Arctic lead to the shift in Arctic aerosol composition and abundance, which in turn alter the radiative budget and influence clouds in the Arctic. The vertical distribution of Arctic aerosols also changes during the different seasons. Aircraft-based measurements during April 2015 show a clear dependence between the mean potential temperature and the mass fractions of sulfate, organic aerosol, refractory BC and ammonium (Willis et al. 2019). In addition, by splitting the polar dome vertically, the different aerosols also spend a varying fraction of time

in the different vertical layers (Willis et al. 2019). Air masses inside the lower polar dome had the longest lifetimes of ten days or longer, largely dominated by SSA and sulfate. This increased age might indicate a travel into the lower level of the Arctic dome, which may alter the transported aerosol via chemical processing. This could indicate that the dominant contribution of SSA observed during Arctic spring by ground-based stations might not represent the full vertical column, increasing the need for additional vertical measurements (Willis et al. 2019).

The need for vertically resolved measurements in the Arctic cannot be filled solely by remote sensing instrumentation. While some parameters can be measured and estimated, others are out of reach (e.g., Silva et al. 2022). Accurately measuring for example the ice nucleation ability of aerosols requires *in situ* instrumentation. Such *in situ* instrumentation needs to be mounted on a platform. Three such platforms are currently being used: aircraft, balloon and uncrewed aerial system (UAS). Aircraft campaigns have been used extensively in the Arctic (e.g., Aliabadi et al. 2016; Jacob et al. 2010; Jones et al. 2018; Roiger et al. 2015; Sanchez-Marroquin et al. 2023; Schulz et al. 2019; Willis et al. 2019; Xu et al. 2017; Zamora et al. 2016), but they are limited in their spatial and temporal coverage and altitude (e.g., Schmale et al. 2021) and also require increased personell and associated costs (e.g., Shupe et al. 2005). Balloon-borne *in situ* instrumentation has been used recently to assess the INP concentration in the Arctic (Creamean et al. 2021). Balloon-borne setups can carry larger loads (multiple kilograms) and therefore offer the opportunity of using well-established instrumentation on-board (e.g., Pilz et al. 2023). On the other hand, the precise altitude is hard to control and a ground-based tether needs to be secured and controlled. UAS are able to offer an additional platform, but are restricted more in size and weight of the used instrumentation (Altstädter et al. 2018).

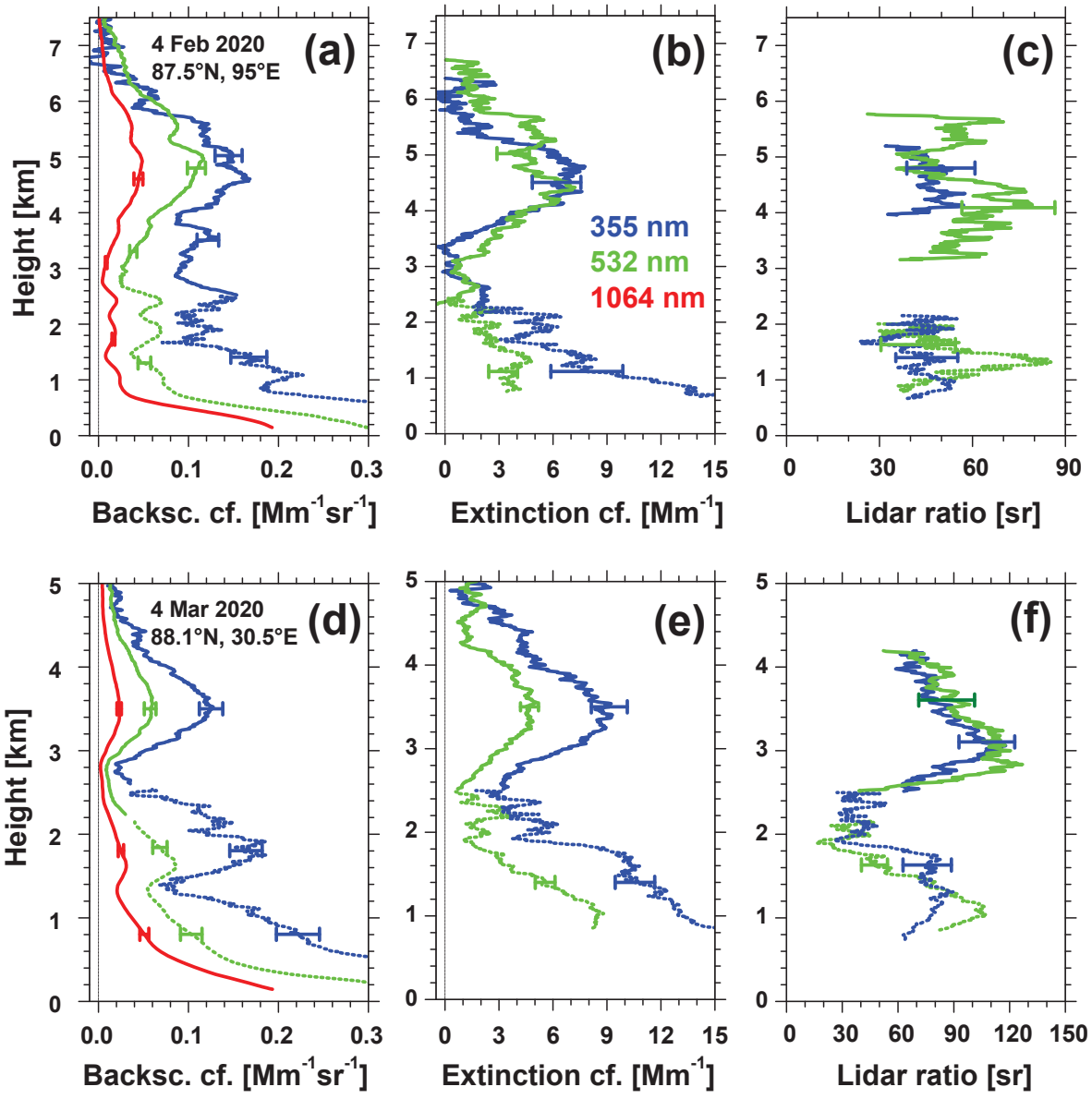

Figure 2.9.: **Remote sensing data from two AH events observed during MOSAiC.** The backscatter and extinction coefficient are shown in the left and middle panels, respectively. The lidar ratio (extinction-to-backscatter ratio) is shown on the right panels. Data is shown for three different wavelengths (355 nm, 532 nm and 1064 nm). The error bars represent one standard deviation. Figure from Engelmann et al. (2021).

2.4.2. Arctic clouds

The focus of this work is on INPs in the Arctic, therefore this section focuses on the cloud feedback and the role of aerosols for the direct aerosol effect as well as indirect aerosol effect via aerosol-cloud interactions (see also section 2.2 Shupe 2011). Dietel et al. (2024) analysed data from satellite measurements over a two year-period and classified different single-layer clouds by their vertical extent and their phase:

vertical extent:

low level: $0.5\,\mathrm{km} < z < 2.0\,\mathrm{km}$,

mid-low level: $0.5\,\mathrm{km} < z < z_{\mathrm{max}}$,

high-mid-low level: $0.5\,\mathrm{km} < z > 2.0\,\mathrm{km}$,

mid level: $2.0\,\mathrm{km} < z < z_{\mathrm{max}}$,

high-mid level: $2.0\,\mathrm{km} < z > z_{\mathrm{max}}$,

phase:

liquid: liquid fraction $f_{\mathrm{liquid}} = 1$,

mixed-phased: liquid fraction $0 < f_{\mathrm{liquid}} < 1$,

solid: liquid fraction $f_{\mathrm{liquid}} = 0$.

This classification leads to low-level clouds to be the most frequent cloud with 8.6 %, while mid-to-low level clouds occur less at a frequency of 5.5 %. Around 19.9 % of the time period was considered clear-sky. Around half of the low-level clouds are mixed-phase clouds (52 %), with around 40 % being liquid clouds. The balance shifts towards ice clouds for high-mid-low and high-mid level clouds were 60 % and 64 % are ice clouds, respectively. Across all vertical extents of clouds observed, the occurence of mixed-phased clouds is ≥24 % (Dietel et al. 2024). These mixed-phase clouds generally show a high vertical and horizontal extent, while liquid clouds are vertically thinner. Looking at the liquid fraction as a function of the cloud top temperature, they find two local minima around −15 °C and −5 °C, which could be associated with freezing events. The phase of low-level clouds is increasingly liquid over sea ice compared to open sea. This has already been investigated by Carlsen and David (2022), who calculated a transition temperature T^*, which denotes the temperatures where the ice phase is larger than the liquid phase. They find little difference for the transition temperature during summer time between ocean ($T^* = -13\,^\circ\mathrm{C}$) and land ($T^* = -14\,^\circ\mathrm{C}$), while during winter there is a larger difference between sea ice ($T^* = -24\,^\circ\mathrm{C}$) and land ($T^* = -23\,^\circ\mathrm{C}$) compared to open ocean ($T^* = -17\,^\circ\mathrm{C}$). This could indicate that during summer local aerosol of biological origin is especially important for primary ice nucleation (Kanji et al. 2017), an effect that has also been observed by *in situ* instrumentation (Creamean et al. 2018a; Tobo et al. 2019). Hartmann et al. (2020) report measurements from an aircraft campaign measuring the INP concentration during winter 2018, which suggest that the marine boundary layer is a reservoir of aerosol particles that show ice-nucleating abilities at relatively high temperatures up to −7.5 °C during winter.

The effect of Arctic clouds is different in comparison to the global effect mainly due to the low and absent sun and the highly reflective surface consisting of sea ice and snow (e.g., Wendisch et al. 2019). They also play an important role in AA and still represent a gap in current knowledge (Wendisch et al. 2019). While low-level clouds globally have a cooling effect (Raschke et al. 2015;

$(-1.0 \pm 0.7)\,\mathrm{W\,m^{-2}}$, IPCC 2021, p. 7-40), in the Arctic they generally[8] have a warming effect ($(30 \pm 4)\,\mathrm{W\,m^{-2}}$, Intrieri et al. 2002; $33\,\mathrm{W\,m^{-2}}$, Miller et al. 2015). The radiative effect of clouds is mainly controlled by its phase and lifetime (Morrison et al. 2011). Various observations have shown that mixed-phase clouds are prevalent in the Arctic, providing the largest contribution of the radiative effect of clouds (Shupe and Intrieri 2004; Stramler et al. 2011). The lifetime of these clouds has been shown to extend to multiple days (Morrison et al. 2011; Shupe et al. 2006), an observation that is not captured by current models (Wendisch et al. 2019). One key part that is not well-represented is the role of aerosols in the formation and persistence of Arctic clouds (Wendisch et al. 2019). The following section gives an overview of these aerosol particles, specifically aerosol particles that are able to act as INPs.

2.4.3. INP sources in the Arctic

Arctic INPs are dominated by mineral and biological aerosol particles emitted by land and ocean (e.g., Creamean et al. 2020, 2018a; Gabric et al. 2018; Irish et al. 2017; Jensen et al. 2025; Tobo et al. 2019, 2024; Wilson et al. 2015; Xi et al. 2022). Glacial outwash sediments on Svalbard show a high ice-nucleating ability, substantially higher than illite NX (see also figure 2.7) at temperatures above $-25\,^{\circ}\mathrm{C}$ and with an activation in the immersion mode at temperatures as high as $-5\,^{\circ}\mathrm{C}$ (Tobo et al. 2019, 2024). These sediments contain substantial amounts of organic material, which influences its ice nucleation ability (Tobo et al. 2019). Creamean et al. (2018a) report size-resolved INP measurements, where larger aerosol particles were more efficient INPs, but also showed a larger spread between the INP spectra, the highest INP concentrations at temperature above $-10\,^{\circ}\mathrm{C}$ were observed during late May. The large spread for the larger aerosols might indicate different sources for the larger INP (Creamean et al. 2018a). The higher INP concentration in late May indicates a local source of biological aerosol particles (e.g., Kanji et al. 2017). One potential source could be the marginal ice zone (MIZ), a source of aerosol particles that was also observed during other studies (Gabric et al. 2018; Irish et al. 2017; Wilson et al. 2015), resulting from bubble bursting and of biogenic origin (Creamean et al. 2018a). Decaying leaves have been identified as an important terrestrial source of INPs at $-15\,^{\circ}\mathrm{C}$, with their ice nucleation ability orginating from microorganisms (Conen et al. 2016). Oceans emitt SSA, which have been suggested to contain aerosol particle capable of nucleating ice (Burrows et al. 2013; Creamean et al. 2013; DeMott et al. 2010). DeMott et al. (2016) simulated the formulation of SSA and obtained similar INP concentrations as observed from SSA in field-based campaigns.

The production of SSA via bubble bursting can be grouped into three different modes of production: (1) film drops produce particles of particle diameter below 1 µm (Gong et al. 1997; Leeuw et al. 2011; Mårtensson et al. 2003; Woolf et al. 1987), (2) jet drops produce particles of particle diameter 1 to 100 µm (Hoppel et al. 2002; Leeuw et al. 2011; Lewis and Schwartz 2004; Wu 1992) , and (3) spume drops from wave tearing at higher wind speeds produce particles of particle diameter around 100 µm (Andreas et al. 2010; Andreas 1992, 1998; Anguelova et al. 1999; Fairall et al. 2009; Monahan et al. 2017; Smith et al. 1993; Veron 2015; Wu 1993). The formation of SSA over open ocean is generally a source function of the wind speed, with a threshold around $4\,\mathrm{m\,s^{-1}}$ (May et al. 2016; Monahan et al. 1986). McCluskey et al. (2018a) measured the INP concentration in the Southern Ocean and found an organic population of ice active aerosol particles associated with phytoplankton blooms (see also McCluskey et al. 2017, 2018b). Other measurements of the INP concentration of marine air have been conducted by

[8] Only during early July, the clouds effectively cooled the surface ($(-4 \pm 4)\,\mathrm{W\,m^{-2}}$, Intrieri et al. 2002). Uncertainty determined by adding uncertainties in quadrature.

DeMott et al. (2016) and of the sea surface microlayer (SML) by Irish et al. (2017) and Wilson et al. (2015).

Measurements of the INP concentration from four different arctic locations (Alert, Utqiagvik, Villum and Ny-Ålesund) show large seasonal variance, with the highest INP concentrations observed during summer (Wex et al. 2019). The INP concentration generally follows an exponential increase with a decrease in temperature, with different samples most often not intersecting. Aerosol particles sampled were active as INP at temperatures up to −5 °C, with those highly ice-active INPs observed from April onwards for Utqiagvik and Villum. As mentioned before, these INP are likely of biogenic origin, although tests on the chemical composition have not been performed by Wex et al. (2019). An additional analysis with backward trajectories and ground type analysis, showed that coastal regions may be important sources of highly ice-active INPs (Irish et al. 2017; Wex et al. 2019; Wilson et al. 2015). The INP concentration in Ny-Ålesund was especially high during times where the local surface was not covered by snow, indicating that local soil also can influence the local INP population (Creamean et al. 2018a; Irish et al. 2019; Wex et al. 2019). A collection of INP concentration measurements is given in section 2.4.3.

Creamean et al. (2022) report size-resolved INP concentration measurements during the year-long MOSAiC campaign (October 2019 – October 2020). Lowest INP concentrations were measured in winter, with an increase during June, July, and August especially at $T_{\mathrm{nuc}} > -15\,^{\circ}\mathrm{C}$. At colder nucleation temperatures (−20.0 °C and −22.5 °C), a peak was seen during late summer and winter, influenced by dust from continental sources (Creamean et al. 2022, 2018a; Hartmann et al. 2021; Kokhanovsky and Tomasi 2020). Onset freezing temperatures reached a maximum during June and July with −6 °C, which coincided with an increase in Chlorophyll *a* (CHL) concentration and increased open water and melt pond occurence. The opening up of the ice might also expose sea ice algae to increased wind speeds, favouring an increased emission of biogenic material (Ardyna et al. 2020; Creamean et al. 2022; Leu et al. 2015).

Current data on the INP concentration in the Arctic is still sparse, especially for temperatures above −10 °C and temperatures below −20 °C. This is in part due to the used measurement principles and the generally relatively low INP concentrations in the Arctic. There is also a lack of data during winter, where especially AH might have a significant effect on the INP population. In addition, due to the nature of the highly stratified arctic atmosphere, vertical measurements of aerosol parameters such as INPs are needed to understand the complex interplay of aerosol-cloud interactions in the Arctic. The following chapter describes different measurement methods used during this work that are able to provide new insights, specifically for the temperature range below −20 °C and methods to assess the INP population on different vertical levels.

Table 2.5.: **Collection of mean INP concentrations of previous studies in the Arctic.** Previous compiled data is taken from Creamean et al. (2018a) and additional data is taken from the references listed. The data from Hartmann et al. (2020) is given for two different instruments, details are available in Chen et al. (2018) and references therein.

Reference	Location	Dates	Max volume air	N_{INP}^{-5}	N_{INP}^{-10}	N_{INP}^{-15}	N_{INP}^{-20}	N_{INP}^{-25}
			l	l^{-1}	l^{-1}	l^{-1}	l^{-1}	l^{-1}
Bigg (1996)	High Arctic	early 1991	3000			1×10^{-2}		
		Aug-Oct 1991				3×10^{-3}		
Borys (1989)	Alaska, Canada, Greenland	Apr 1986	1400			2×10^{-2}		5×10^{-1}
Conen et al. (2016)	Norway	Jul 2015	24 000		6×10^{-4}	7×10^{-3}		
DeMott et al. (2015)	Bering Sea	Summer 2012	13 500			3×10^{-3}	3×10^{-2}	
Fountain and Ohtake (1985)	Alaska	Aug 1978-Apr 1979	250				1×10^{-1}	
Mason et al. (2016)	Canada	Mar-Jul 2014	32 400			5×10^{-2}	2×10^{-1}	1
Prenni et al. (2009)	Alaska	Oct 2004	1		2×10^{-1}		4×10^{-1}	
Radke et al. (1976)	Alaska	Mar 1970	3000				2×10^{-2}	
Creamean et al. (2018a)	Alaska	Mar-May 2017	38 428		8×10^{-4}	5×10^{-3}	2×10^{-2}	4×10^{-2}
Wex et al. (2019)	Alert	Apr 2015 - Apr 2016	564	2.9×10^{-6}	3.2×10^{-3}	1.1×10^{-2}	1.5×10^{-2}	
	Ny-Ålesund	Apr 2012 - Sep 2012	145		4.1×10^{-4}	1.1×10^{-3}	2.8×10^{-3}	
	Villum	Dec 2013 - Dec 2015	255		4.8×10^{-4}			
	Utqiagvik	Jul 2012 - Jun 2013	1002		2.9×10^{-3}	2.8×10^{-3}	7.7×10^{-3}	
Li et al. (2022a)	Ny-Ålesund	Spring 2020	18 000		4.7×10^{-2}	1.7×10^{-1}	5.9×10^{-1}	
		Autumn 2019	18 000		6×10^{-2}	2.3×10^{-1}	2.6×10^{-1}	
Rinaldi et al. (2021)	Ny-Ålesund[a]	Apr - August 2018	16 255[*]		1.6×10^{-3}	8.8×10^{-3}	1.3×10^{-3}	
Tobo et al. (2019)	Ny-Ålesund	July 2016 / March 2017	15 609		1.0×10^{-3}	1.4×10^{-2}	5.7×10^{-2}	3.3×10^{-1}
Hartmann et al. (2020)	High Arctic[b]	March 2018	4347			1.5×10^{-2}	7.4×10^{-2}	1.6
	High Arctic[c]		4347		2.2×10^{-3}	1.0×10^{-2}	5.1×10^{-2}	2.0×10^{-1}

[a] West Texas Cryogenic Refrigerator Applied to Freezing Test system;
[b] Leipzig Ice Nucleation Array;
[c] Ice Nucleation Droplet Array;
[*] One filter sample was sampled for two periods, resulting in a max volume of air for one filter of 32 883 l.

Chapter 3.

Methodology

The present chapter describes the different instrumentation, model and experimental data used for this work. It also provides an overview of the different campaign locations. Section 3.1 details the methods used to measure the aerosol particle diameter, while section 3.2 details the methods to measure the ice nucleation ability of aerosol particles. Following that, section 3.3 describes the UAV setup and instrumentation. Reanalysis and model data is described in section 3.4 and lastly section 3.5 lists the different measurement locations and their associated campaigns.

3.1. Aerosol sizing instrumentation

One of the key properties of atmospheric aerosol particles is their size. Two instruments are commonly used to measure the size of aerosol particles *in situ*: the Aerodynamic Particle Spectrometer and the Scanning Mobility Particle Spectrometer. Both are described in section 3.1.1 and section 3.1.2, respectively. In addition, aerosols can also be measured optically by measuring their scattering intensity to obtain a light-scattering equivalent diameter (e.g., Welker 2012). One Optical Particle Counter (OPC) used during this work is described in section 3.1.3.

3.1.1. APS

The APS measures the aerodynamic particle diameter of aerosol particles (see also section 2.1.2.2, Kulkarni 2011, p. 326). The sampled air is accelerated through a nozzle, which constricts the air flow and therefore increases its velocity according to Bernoulli's principle. The accelerated aerosol particles within the sample flow pass two beams of light. The time difference between the two beams is calculated, providing a transit time. This is also known as time-of-flight (TOF). Smaller particles have a similar velocity to the surrounding air, whereas progressively larger aerosol particles have a higher inertia and therefore are associated with a larger TOF. From the TOF, an aerodynamical particle size can be inferred from a calibration table that is specific to the nozzle size and the optical arrangement. A schematic of the measurement principle and an example of a light scattering signal is shown in figure 3.1. Typically an APS measures aerodynamic particle diameters between 500 to 20 000 nm. An intercomparison campaign utilizing 15 APS (model 3321, TSI Inc.) has been performed by Pfeifer et al. (2016) within the framework of Aerosols, Clouds, and Trace gases Research Infrastructure (ACTRIS). Three key parameters were checked: flow rate, sizing accuracy and particle number concentration. All instruments show a good agreement for the flow rate (within a few percent) and the sizing accuracy ($< 10\,\%$). The aerosol particle number concentration was within 10 to 20 % in the size range 0.9 to 3.0 µm. For smaller

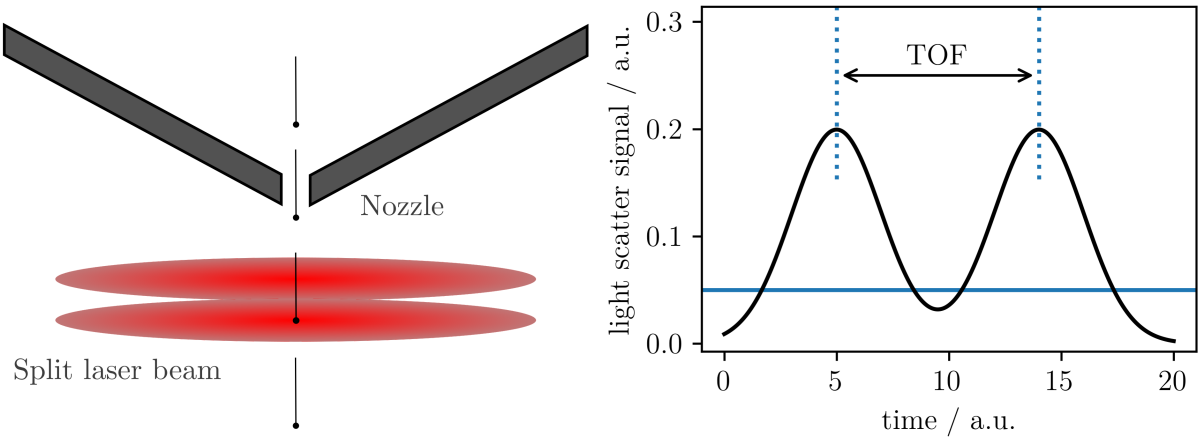

Figure 3.1.: **Schematic of the APS and an example of a typical light scattering signal.** The measured TOF is used to determine the aerodynamic particle diameter.

aerodynamic particle diameters, the unit-to-unit variability increased up to 60 %, likely caused by different counting efficiencies for smaller particles (Karg et al. 1991). The larger size range above 3.0 µm also shows increased variability, which is especially important when using higher modes of particle number size distribution, such as aerosol surface and volume distributions (see also section 2.1.1).

3.1.2. SMPS

The SMPS is the combination of two instruments that work in tandem to measure the electrical mobility diameter of aerosol particles. It consists of a DMA and a Condensation Particle Counter (CPC). Aerosol particles are artificially charged and subsequently enter the DMA. The air flow containing the charged aerosol is sampled through an electrical field, nowadays typically in a column-like structure (e.g., Knutson and Whitby 1975). The charged aerosol particle is affected by the electric field, the affecting force being proportional to the electric field strength ($F = qE$). The electric field strength is proportional to the voltage difference (V) between the electrodes and depends on the inner (R_1) and outer diameter (R_2) of the cylindrical electrodes (Kulkarni 2011, eq. 15-6 therein)

$$E(r) = \frac{V}{r \ln \frac{R_2}{R_1}} \ . \tag{3.1}$$

A charged particle will migrate relative to the surrounding gas motion with a steady-state migration velocity (Kulkarni 2011, eqs. 15-1–15.2 therein)

$$v_\mathrm{e} = ZE = \frac{ieC_\mathrm{c}(d_\mathrm{p})}{3\pi\eta d_\mathrm{p}} \tag{3.2}$$

where: v_e – migration velocity ($\mathrm{m\,s^{-1}}$),
Z – electrical mobility ($\mathrm{m^2\,s^{-1}\,V^{-1}}$),
i – number of charges,
e – elementary charge (1.602 176 634 C),
η – gas viscosity ($\mathrm{kg\,m^{-1}\,s^{-1}}$).

By scanning over a range of voltages, aerosol particles of different electrical mobilities can be selected and can then be further analyzed with the CPC. The high voltage used for the size

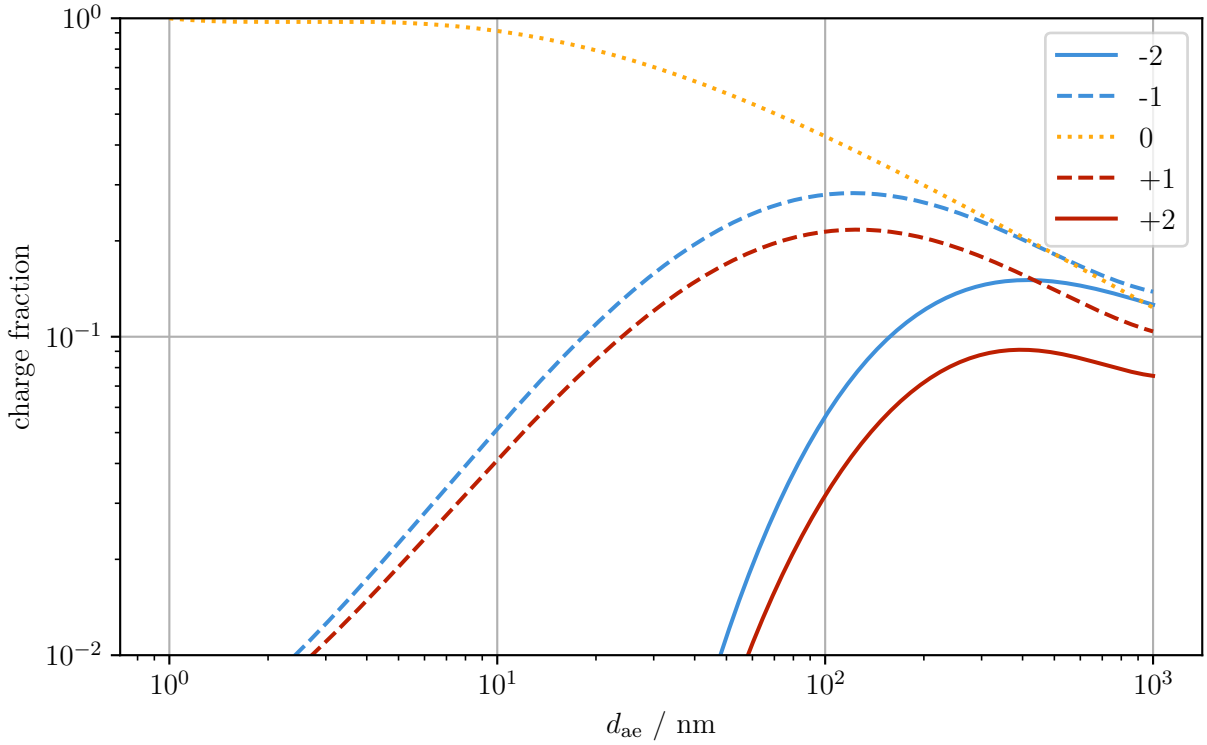

Figure 3.2.: **Steady-state charge fraction as a function of the particle size for different number of electric charges.** Zero charge is the most common for aerosol particles, but single (positive and negative) and double (positive and negative) charges increase in frequency for larger particles sizes. Difference between positive and negative electric charges is related to differences in the ion mobilities. Data from Wiedensohler (1988) for an approximation of the corrected Fuchs charge distribution (Fuchs 1963).

classification improves sizing resolution, but is limited to around $10^6\,\mathrm{V\,m^{-1}}$, where electrostatic breakdown increases in likelihood at ambient conditions (Kulkarni 2011, p. 347). At a typical setup, the distance between the two electrodes is around 10 mm, resulting in a maximum voltage of around 10 kV. Increasing the size resolution further, leads to diffusional broadening, which in turn reduces the number of aerosol particles selected for a selected size. For larger aerosol particles the probability of multiple charges per aerosol particles increases, which leads to a potential bias, where larger particles are counted as smaller particles due to their increased electrical mobility, which is proportional to the number of charges. The determination of the number of charges per aerosol particle is important for accurate sizing using the SMPS. Ideally each particle possesses one charge, but this assumption is not valid in ambient air. An approximation of the steady-state charge fraction of an aerosol particle as a function of its particle diameter is shown in figure 3.2 (Kulkarni 2011, p. 352; Wiedensohler 1988). This shows that larger particles have a higher probability of possessing one or even two electric charges, compared to smaller particles, that are mostly electronically neutral. The same behaviour can be seen when using a charger to charge the aerosol particles before they enter the electrical field of a DMA. For this reason, a charge correction is typically used to accurately determine the number of charges of aerosol particles passing through the DMA (e.g., He and Dhaniyala 2013).

After size selection of the DMA, the aerosol particles pass to a CPC to measure their concentration. A CPC uses condensation to grow small aerosol particles to larger sizes, that are subsequently detected optically (Kulkarni 2011, pp. 385–386). To achieve condensational growth, the aerosol

particles pass through a region of vapor supersaturation. The growth rate is dependent on the vapor properties and the particle diameter, whereas the lower limit of detection, i.e. the smallest aerosol particle that can grow through condensation is given by the Kelvin diameter (see also equation (2.25)). Butanol is a typical working fluid used in CPCs to achieve condensational growth for particles down to a few nm due to its favourable properties (Kulkarni 2011, pp. 382–383). The CPC alone only provides a concentration of the aerosol population, but is unable to determine their size. Together with the DMA, the CPC is able to measure the concentration of differently sized aerosol particles, providing a size distribution over a certain time frame. SMPS are commonly used for smaller particle sizes between 10 to 800 nm and with a temporal resolution of minutes.

3.1.3. OPC

OPCs are used to measure the light-scattering equivalent diameter *in situ*. They can cover sizes down to around 60 nm (Cai et al. 2008; Moore et al. 2021; Uin 2024) and are able to provide a higher temporal resolution, which is needed in the case of a fast changing aerosol population. There are many different types of OPCs, differentiated by the wavelength of the light source and the collection angle of the scattered light. The principle is generally the same. Aerosol particles pass through a light beam and from the scattered signal the optical particle diameter is calculated. The optical size of an aerosol particle is dependent on its physical size, its shape, its orientation and its refractive index (Kulkarni (2011, p. 471), see also section 2.2.1). A full-flow OPC (fidas-PINE, Pallas GmbH) is integrated into the PINE (see also section 3.2.2).

The fidas-PINE collects the scattered light at an angle of 90°. The sampling air flow passes through a nozzle which restricts the width of sampling air to 1.5 mm. About 2 mm behind the nozzle, the aerosol sample passes the optical detection volume (odv), which is 300 µm in height with a width of 1.5 mm. A schematic view of the setup is shown in figure 3.3[1]. The odv is smaller than the volume of the aerosol stream (denoted by aer) by a factor η

$$\eta = 1 - \frac{s_{\text{odv}}}{s_{\text{aer}}} \approx 0.841 \ . \tag{3.3}$$

Of course one needs to consider that the aerosol is not evenly distributed across the axis, therefore the amount of aerosol particles actually detected optically is somewhere between η and 1. The sensor detects single particle scattering signals. From the signal, the time, the width and the height is reported. From the height of the signal, the size of the aerosol particle is estimated according to a calibration table. From the width of the signal, called the pulse length, the aerosol flow rate can be estimated. This sensor has two important properties, which make it ideal for measuring low number concentrations of ice crystals. The odv is generally much larger compared to similar sensors which are designed to measure the aerosol concentration and therefore have a small odv (i.e., 1 % of the aerosol sample cross section) and scale the measured concentration to achieve the total aerosol concentration (e.g., Kulkarni 2011, p. 296). The second part is related to the scattering phase function of a droplet and an ice crystal. A spherical water droplet shows a stronger scattering signal in the forward direction (10 to 60°) and in the backward direction ($> 160°$), while ice crystals show an increased scattering signal for angles between 60 to 130°. Measuring at 90° therefore enhances the optical size of ice crystals and lessens the optical size of water droplets (Sassen and Liou 1979). This allows the discrimination between ice crystals and cloud droplets, which is crucial for INP concentration measurements with PINE in the MPC regime.

[1] Personal communication with Dr. Sergej Sel, Head of Department Optics, Pallas GmbH.

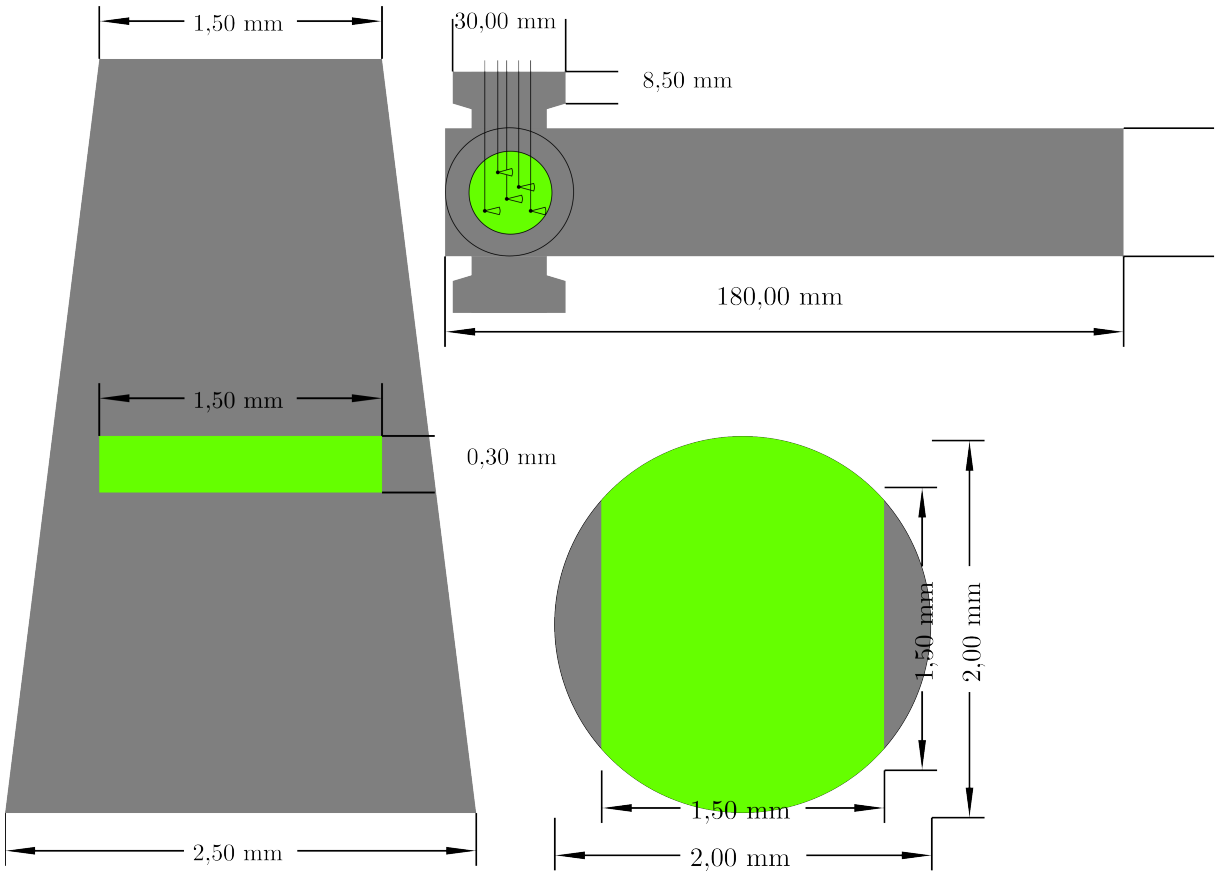

Figure 3.3.: **Schematic view of the fidas-PINE.** On the left, the view is shown for the aerosol sample area in grey with the odv specified in green. The view from above is shown at the lower right panel in the same colors. The upper right panel shows the side view of the fidas-PINE sensor with the aerosol entering from above and producing a scattering signal which is measured at an angle of 90°.

3.2. INP instrumentation

3.2.1. Ice Nucleation Spectrometer of the Karlsruhe Institute of Technology (INSEKT)

INSEKT is an instrument that mimics the immersion freezing mode to investigate the ice nucleation ability of aerosol particles. It is an offline-based instrument, i.e., the aerosol particles are collected, e.g., via filter collection, and subsequently suspended in clean and particle free water. 50 µl aliquots of this suspension are then filled into wells and cooled down to measure a temperature dependent INP concentration, henceforth called INP temperature spectra. INSEKT is based on the Colorado State University - Ice Spectrometer (CSU-IS) (Creamean et al. 2024; Hill et al. 2016; Schneider et al. 2021). The following section describes the components of the instrument as well as a typical experiment; more information on the instrument characteristics is available in chapter B.

3.2.1.1. Main components

INSEKT consists of an aluminium incubation block for two 96-well polymerase chain reaction (PCR) plates (Brand, Cat. No. 781368) that are temperature controlled by a cooling liquid from a cryostats (Lauda®, ProLine RP 855 for INSEKT1, Pro RP 245 E for INSEKT2[2]). The whole setup is enclosed inside a polyvinyl chloride (PVC) box and isolated by 2 cm thick ArmaFlex® insulation material. The PVC box is topped by a removable anti-reflection coated glass pane. This ensures that no external contamination influences the mimicked droplets. To prevent condensation on the glass pane, a constant flow (80 l m^{-3}) of cooled and filtered synthetic air passes over it. Figure 3.4 shows a schematic view of the setup from above, including the eight PT100 temperature sensors (PT100A 20/050 (NB), class A, Electronic Sensor GmbH). The temperature sensors are located in drilled holes inside the aluminium blocks and their data is recorded with a custom-made LabVIEW® program. The temperature sensors are calibrated against a temperature standard at −40 °C, −30 °C, −25 °C, −20 °C, −15 °C, −10 °C, −5 °C, 0 °C and 5 °C (see also chapter B and Schiebel 2017). A camera, located above the PCR plates, films the freezing arrays through a polarization filter. The LabVIEW® program uses a mask to identify the sample aliquots on the PCR plates and calculates a greyscale value[3] for each well. The temperature and greyscale value data is saved at a temporal resolution of 1 Hz to an Structure Query Language (SQL) database. Once the suspension inside a well freezes, the greyscale value changes abruptly and from the number of frozen droplets the INP concentration is calculated (see sec. 3.2.1.2). For a full list of materials used in the filter loading and filter analysis see table 3.1. Consistent results can only be obtained, when each analysis and handling step is documented and a clear protocol is established. The following protocol is used for all filters analysed during this work, unless otherwise noted. Every Nuclepore™ filter is pre-cleaned with 10 % H_2O_2 and afterwards rinsed with deionized water that was passed through a 0.1 µm syringe filter (Whatman®, 6784-2501). These cleaned filters are then dried on aluminium foil under a constant clean air flow and afterwards packaged as pairs inside aluminium foil. During handling of these filters, forceps, that are pre-cleaned the same way and packaged in aluminium foil before each use, are used. The aluminium foil bags where sterilized by heating. After collecting aerosols onto the filter, they are stored in sterile Petri dishes (Pall® Analyside™ Petri Dish), packed inside aluminium and stored - if possible - in a freezer at −20 °C until analysed by INSEKT. Even with these measures aimed at decreasing the amount of INPs that are collected on the filter during handling (i.e. from water, from surfaces, from plastic ware, etc.), there is an INP background, which inhibits the INSEKT freezing array to measure INP concentrations at temperatures lower about −25 °C. This threshold is mainly due to the Nanopure™ water background freezing at this temperature. For higher temperatures the limiting factor is the amount of sample analysed, i.e. the low INP concentration. For more information on the different methods and their impact on the background see Barry et al. (2021).

[2] At the Institute of Meteorology and Climate Research Atmospheric Aerosol Research (IMKAAF), two INSEKT freezing arrays are used, both featuring the same setup and components, except for the used cryostat.

[3] The greyscale value can be understood as the amount of light reflected from the mimicked droplet.

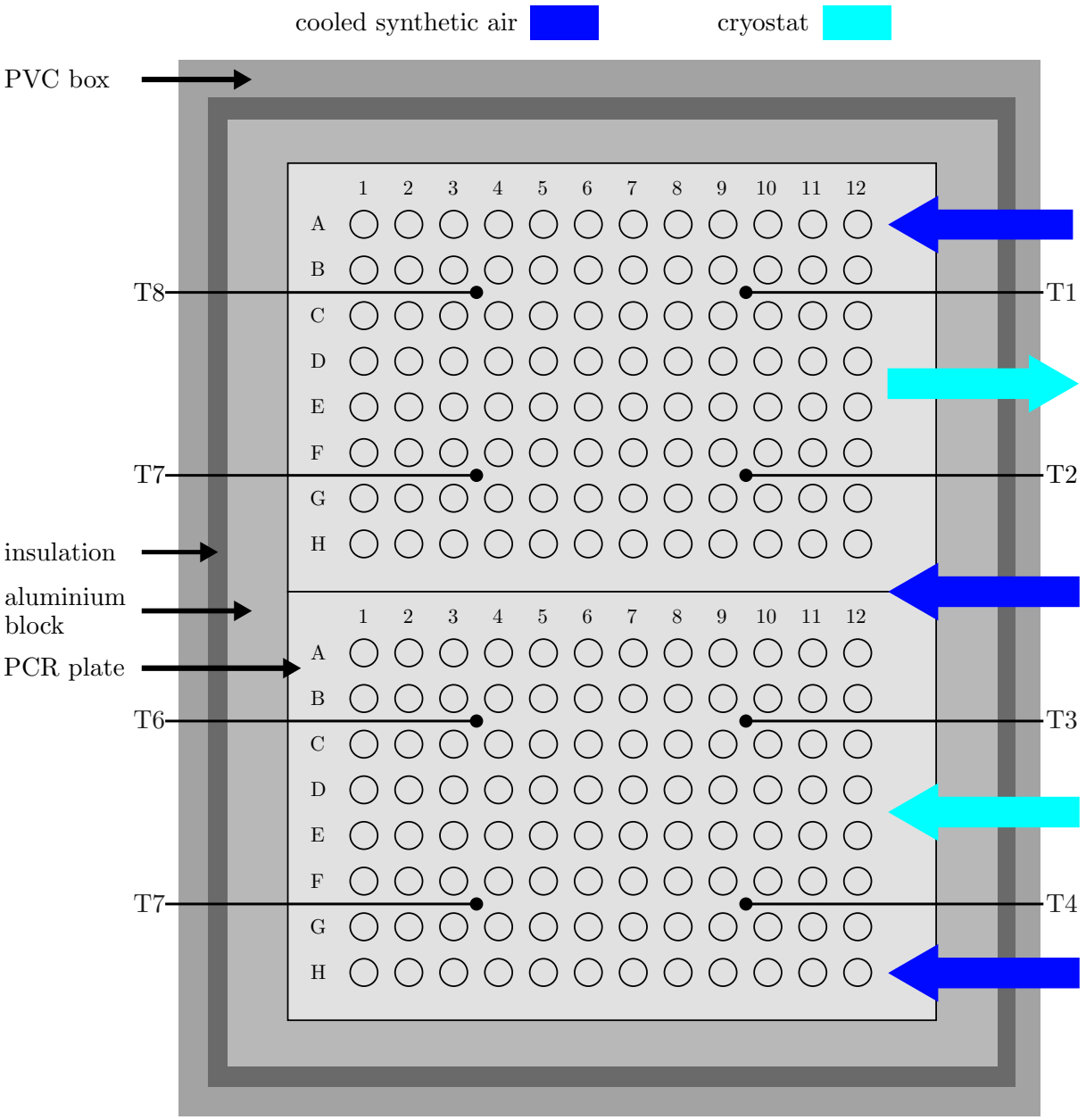

Figure 3.4.: **Schematic of INSEKT (top view).** Adapted from Böhmländer (2021) and Schiebel (2017).

Table 3.1.: **INSEKT material list.** Description of the used materials during filter taking and filter analysis.

Name	Description	Function
Gloves	Hartmann Peha-soft® syntex powder-free	used during all steps
Forceps	VITLAB GmbH Pinzetten, polymethylpenten, cleaned with H_2O_2 before use	used to handle filters
Petri dishes	Pall® Analyslide™ Petri Dish	holds filter between sampling and analysis
Aluminium foil	Aluminium foil is baked out before use	provided a clean surface to work on, encapsulates Petri dishes between sampling and analysis
Plastic bags	Aromata® Allzweck-/Gefrierbeutel mit Gleitverschluss 3L	used to store multiple Petri dishes encapsulated by aluminium foil in a fridge and to store filter solutions for re-analysis
Disinfectant	Bacillol® AF	used to clean surfaces, forceps and gloves
Nanopure™ water	generated by Barnstead™ GenPure™ Pro UV	water used for making filter solutions
Centrifuge tubes	50 ml CELLSTAR® polypropylene tube	used for filter washing and for the different solutions
Pipette tips (0.1 to 5 ml)	Eppendorf epT.I.P.S.® 0.1 to 5 ml	used for filling the centrifuge tubes with Nanopure™ water for filter washing
Pipette tips (50 to 1000 µl)	Eppendorf epT.I.P.S.® 50 to 1000 µl	used for filling the wells with 50 µl of Nanopure™ water
Syringe (20 ml)	Braun Injekt® LL 20 ml	used in conjunction with the 0.1 µm syringe filter for further filtration of Nanopure™ water
Syringe (12 ml)	HSW NORM-JECT® 10 (12) ml	used to activate 0.1 µm syringe filters with alcohol before use
Syringe filter (0.1 µm)	Whatman® Puradisc 25 syringe filter 0.1 µm	used to filter Nanopure™ water further in combination with the 20 ml syringe, used up to 10 times before replaced
PCR plate 96-well	Brand GmbH & Co. KG	used for the aliquots

3.2.1.2. Calculation of INP concentration

INSEKT calculations are based on the equations described by Vali (1971), who calculates the INP concentration in a suspension $c_{\mathrm{INP,\,sus}}$ according to:

$$c_{\mathrm{INP,\,sus}} = -\frac{d}{V_{\mathrm{well}}} \cdot \ln\left(f_{\mathrm{l}}\right) \ , \tag{3.4}$$

where d is the dilution scale, V_{well} the volume of one PCR well and f_{l} the liquid fraction of the given aerosol suspension. One important assumption is that a single well only contains one aerosol particle that is active as an INP at the same temperature, since the measurement produces a cumulative INP temperature spectra.

Cleanliness is very important for accurate measurements, especially since the liquid volumes mimicking the droplets are comparatively large ($V_{\mathrm{well}} = 50\,\mu\mathrm{l}$). Therefore, in each experiment a part of the PCR wells is filled with filtered Nanopure$^{\mathrm{TM}}$ water (see tab. 3.1) to provide the INP background for the freezing of the suspensions. The other major background source stems from the handling during sampling, which is why a handling blank filter is taken regularly next to the sample filters. A handling blank filter goes through the very same procedure as sample filters, but is not subjected to an active air flow. Every sample filter and every handling blank filter has a water background that can be subtracted:

$$\begin{aligned} c_{\mathrm{INP,\,sus}}^{\mathrm{water,\,corr}} &= c_{\mathrm{INP,\,sus}} - c_{\mathrm{INP,\,sol}}^{\mathrm{water}} \\ &= -\frac{d}{V_{\mathrm{well}}} \cdot \ln\left(f_{\mathrm{l}}\right) \\ &\quad + \frac{d}{V_{\mathrm{well}}} \cdot \ln\left(f_{\mathrm{l}}^{\mathrm{water}}\right) \\ &= -\frac{d}{V_{\mathrm{well}}} \cdot \ln\left(\frac{f_{\mathrm{l}}}{f_{\mathrm{l}}^{\mathrm{water}}}\right) \ . \end{aligned} \tag{3.5}$$

The subscript notation is related to the aerosol sample suspension (INP, sus) and the filtered Nanopure$^{\mathrm{TM}}$ water solution (INP, sol), whereas the superscript notation refers to the solution media, i.e., Nanopure$^{\mathrm{TM}}$ water and the corresponding corrected (corr) INP concentration. This is true for any aerosol suspension, regardless of the handling. For this work, the handling blank filter aerosol suspension was used to assess the handling procedure and correspondingly flag aerosol samples that might have been contaminated during handling. No subtraction of the handling blank aerosol suspension INP concentration has been performed. The main reason for this is the issue of subtracting a cumulative spectra from a second cumulative spectra. This is already an issue with the subtraction of the INP concentration of the Nanopure$^{\mathrm{TM}}$ water solution, although to a lesser extent, due to aerosol suspensions typically containing enough aerosol particles active as INP at temperatures above about $-25\,^{\circ}\mathrm{C}$. A separation of the frozen fraction spectra of the aerosol suspension and the Nanopure$^{\mathrm{TM}}$ water solution is needed to obtain a physical result. If the frozen fraction of the Nanopure$^{\mathrm{TM}}$ water solution is increasing more than the aerosol suspension at the same temperature range, the resulting INP freezing spectra will show a decrease with decreasing temperature. This issue is more typical for the aerosol suspension obtained from handling blank filters, since they are usually very clean and therefore very close to the Nanopure$^{\mathrm{TM}}$ water solution. INP freezing spectra from aerosol suspensions are flagged accordingly, if the corresponding handling blank shows a higher INP concentration. The following equation is used to normalize the INP concentration to the air volume that was sampled through the filter

$$c_{\mathrm{INP,\,air}} = \frac{V_{\mathrm{sus}}}{V_{\mathrm{air}}} \cdot c_{\mathrm{INP,\,sus}} \ , \tag{3.6}$$

where the volume of air V_{air} is calculated via

$$V_{\text{air}} = F_{\text{air}}^{\text{std}} \cdot t_{\text{filter}} \ , \tag{3.7}$$

where $F_{\text{air}}^{\text{std}}$ is the standrd flow over the filter and t_{filter} the duration of the active air flow over the filter. To compare measurements at different locations, the measured flow is normalized to standard conditions ($T_{\text{n}} = 273.15\,\text{K}$, $p_{\text{n}} = 101\,325\,\text{Pa}$)[4] according to

$$F_{\text{air}}^{\text{n}} = F_{\text{air}} \left(\frac{T_{\text{n}}}{T}\right) \left(\frac{p}{p_{\text{n}}}\right) \ . \tag{3.8}$$

The following describes the uncertainty budget refereing to INP concentration calculations of INSEKT. The immersion freezing inside each well is independent from the freezing in other wells. Therefore, each freezing event can be described as a Bernoulli trial, where the trial has two possible outcomes, a 'success' with probability p and a 'failure' with probability $q = 1 - p$. The binomial distribution describes the probability of exactly x successes in n trials for a specific sample and a given temperature

$$f(x) = \frac{n!}{x!(n-x)!} p^x q^{n-x} \ , \tag{3.9}$$

with $n! = \prod_{i=1}^{n} i$ denoting the factorial of n. For large[5] n the normal approximation can be used to approximate the binomial distribution by the normal distribution. This is especially useful since the binomial distribution is computationally expensive (Wallis 2013). Using Stirling's formula

$$n! = n^n \exp(-n)\sqrt{2\pi n} \left[1 + \mathcal{O}\left(\frac{1}{n}\right)\right] \tag{3.10}$$

one can derive the following equation

$$f(x) = \left(\frac{np}{x}\right)^x \left(\frac{nq}{n-x}\right)^{n-x} \sqrt{\frac{n}{2\pi x(n-x)}} \left[1 + \mathcal{O}\left(\frac{1}{n}\right)\right] \ . \tag{3.11}$$

Defining $\delta = x - np$, it follows that

$$\ln\left(\frac{np}{x}\right) = \ln\left(\frac{np}{np+\delta}\right) = -\ln\left(1 + \frac{\delta}{np}\right) \tag{3.12}$$

$$\ln\left(\frac{nq}{n-x}\right) = \ln\left(\frac{nq}{nq-\delta}\right) = -\ln\left(1 - \frac{\delta}{np}\right) \ . \tag{3.13}$$

The first part of equation (3.11) can therefore be written with the series $\ln(1+x) = x - 1/2x^2 +$

[4] In this work, standard conditions always take $T_{\text{n}} = 273.15\,\text{K}$, $p_{\text{n}} = 101\,325\,\text{Pa}$ as reference points. This is in accordance with International Union of Pure and Applied Chemistry (IUPAC) with a slight change due to the slightly different pressures used (Calvert 1990, p. 2216).

[5] Technically n, np and nq need to be large for the normal approximation to be valid, but if p and q are not close to 0 or 1, np and nq are both of order $\mathcal{O}(n)$ for large n.

$\mathcal{O}(x^3)$ as

$$\begin{aligned}\ln\left[\left(\frac{np}{x}\right)^x\left(\frac{nq}{n-x}\right)^{n-x}\right] &= x\ln\left(\frac{np}{x}\right)+(n-x)\ln\left(\frac{np}{n-x}\right)\\ &= -(\delta+np)\left[\frac{\delta}{np}-\frac{1}{2}\frac{\delta^2}{n^2p^2}+\mathcal{O}\left(\frac{\delta^3}{n^3}\right)\right]\\ &\quad-(nq-\delta)\left[-\frac{\delta}{nq}-\frac{1}{2}\frac{\delta^2}{n^2q^2}+\mathcal{O}\left(\frac{\delta^3}{n^3}\right)\right]\\ &= -\delta\left[1+\frac{1}{2}\frac{\delta}{np}-1+\frac{1}{2}\frac{\delta}{nq}+\mathcal{O}\left(\frac{\delta^2}{n^2}\right)\right]\\ &= -\frac{\delta^2}{2npq}+\mathcal{O}\left(\frac{\delta^3}{n^2}\right)\ .\end{aligned} \tag{3.14}$$

The second part of equation (3.11) can be approximated by

$$\sqrt{\frac{n}{2\pi x(n-x)}}=\sqrt{\frac{n}{2\pi(np+\delta)(nq-\delta)}}=\sqrt{\frac{1}{2\pi npq}}\left[1+\mathcal{O}\left(\frac{\delta}{n}\right)\right]\ , \tag{3.15}$$

which combines to the binomial probability function (by dropping the $\mathcal{O}\left(n^{-1}\right)$ term from equation (3.11) and exponentiating equation (3.14))

$$f(x)=\frac{1}{\sqrt{2\pi npq}}\exp\left(-\frac{(x-np)^2}{2npq}\right)\left[1+\mathcal{O}\left(\frac{1}{\sqrt{n}}\right)\right]\ . \tag{3.16}$$

Comparing this to the PDF of the normal distribution

$$\theta(x)=\frac{1}{\sqrt{2\pi}\sigma}\exp\left(-\frac{1}{2}\left(\frac{x-\mu}{\sigma}\right)\right)\ , \tag{3.17}$$

gives the mean $\mu=np$ and the standard deviation $\sigma=\sqrt{npq}$, the same as for the PDF of the binomial distribution.

Agresti and Coull (1998) argue that the approximation via the Wilson interval is better than the exact solution, because of the approximated confidence interval aligning closer to the nominal confidence level described by $(1-\alpha)$. The Wilson interval can be derived, starting with the normal approximation

$$z\approx\frac{p-\hat{p}}{\sigma_n}\ , \tag{3.18}$$

with the sample standard deviation

$$\frac{\sigma}{n}=\sigma_n=\sqrt{\frac{p(1-p)}{n}}\ , \tag{3.19}$$

where p denotes a binomial parameter, $\hat{p}$ the sample proportion and n the sample size. Combining equations (3.18) and (3.19), one finds a quadratic equation in p

$$(\hat{p}-p)^2=z^2\cdot\frac{p(1-p)}{n}\ , \tag{3.20}$$

with the suspension representing the Wilson confidence interval (Wilson 1927):

$$p \approx (\mathrm{CI}_{\mathrm{lower}}, \mathrm{CI}_{\mathrm{upper}}) = \frac{1}{1+\frac{z^2}{2n}} \left(\hat{p} + \frac{z^2}{2n} \pm z \sqrt{\frac{\hat{p}(1-\hat{p})}{n} + \frac{z^2}{4n^2}} \right) . \tag{3.21}$$

It can be used with small samples and skewed observations, because it does not overshoot for small sample sizes or probabilities close to 1 (i.e. the probability of success stays between 0 and 1, Wallis (2013)).

Using the variables used during INSEKT experiments, results in the following formula for the Wilson confidence interval (Hill et al. 2016; Kaufmann 2019; Schiebel 2017)

$$\mathrm{CI}_{\mathrm{upper,\ lower}} = \frac{1}{1+\frac{z^2_{\alpha/2}}{N_{\mathrm{all}}}} \left(p + \frac{z^2_{\alpha/2}}{2N_{\mathrm{all}}} \pm z_{\alpha/2} \sqrt{\frac{p(1-p)}{N_{\mathrm{all}}} + \frac{z^2_{\alpha/2}}{4N^2_{\mathrm{all}}}} \right) , \tag{3.22}$$

with $z_{\alpha/2} = 1.96$ for a 95 % confidence interval, according to the (1 - $\alpha/2$) quantile of the standard normal distribution, p the frozen fraction $(1 - f_{\mathrm{l}})$ and N_{all} the total number of wells filled by the given suspension.

The limits for the wells are given by

$$\mathrm{WL}_{\mathrm{upper,\ lower}} = \mathrm{CI}_{\mathrm{upper,\ lower}} \cdot N_{\mathrm{all}} \tag{3.23}$$

and the limits for the INP concentration is given by

$$\mathrm{IL}_{\mathrm{upper,\ lower}} = -\frac{d}{V_{\mathrm{well}}} \cdot \ln \left(\frac{N_{\mathrm{all}} - \mathrm{WL}_{\mathrm{upper,\ lower}}}{N_{\mathrm{all}}} \right) , \tag{3.24}$$

which results in the errorbars

$$\begin{aligned} \mathrm{UNC}_{-} &= c_{\mathrm{INP,\ air}} - \mathrm{IL}_{\mathrm{lower}} \cdot \frac{c_{\mathrm{INP,\ air}}}{c_{\mathrm{INP,\ sol}}} \\ \mathrm{UNC}_{+} &= \mathrm{IL}_{\mathrm{upper}} \cdot \frac{c_{\mathrm{INP,\ air}}}{c_{\mathrm{INP,\ sol}}} - c_{\mathrm{INP,\ air}} \ . \end{aligned} \tag{3.25}$$

The number of data points is further limited by a quality factor q established by Kaufmann (2019) to increase the overall statistical significance of the data set as a whole. It is defined as

$$\frac{\mathrm{CI}_{\mathrm{upper}}}{\mathrm{CI}_{\mathrm{lower}}} \leq q \ . \tag{3.26}$$

A 'good' value is given in Kaufmann (2019) as $q = 8$. By increasing this value, more data points are added to the whole data set, whereas a smaller value decreases the size of the data set. This value can also be understood as a limiting factor for when the approximation is valid (e.g., Schulz 2016).

These equations are implemented in a Python code developed during this work. It is publicly accessible on the Helmholtz gitlab instance[6]. Additional implemented features and quality control measures are explained in section 3.2.1.4.

[6] https://codebase.helmholtz.cloud/insekt/py_raw_insekt (last access: 22nd January 2025, see also Böhmländer 2021)

3.2.1.3. Typical experiment

In this work, two different types of experiments where performed with INSEKT. Bulk experiments denote the analysis of some aerosol suspended in water, i.e., aerosol particles suspended in ocean water or an aerosol sample introduced by mass into the water. For bulk experiments the INP concentration is calculated the same way as specified in the previous section, but the normalizing factor is the volume of the water analyszed or the mass of the aerosol sample. On the other hand, aerosol suspensions prepared from filters are normalized with the air volume sampled during the filter exposure to ambient air. For this the filters are placed via forceps inside a 50 ml sterilized polypropylene centrifuge tube filled with 8 ml of Nanopure^{TM} water that is filtered through a 0.1 µm pore-diameter filter. Afterwards, the tube is tumbled for 20 min at 60 rpm on a rotator to wash the aerosol off the filter. This aerosol suspension is subsequently pipetted into the PCR trays. The suspensions are chosen, in relation to the amount of INPs collected, using the assumption of approximately one aerosol particle active as an INP at a given temperature. One part of the PCR trays is filled with Nanopure^{TM} water for the water correction, while other parts of the trays are filled with the original aerosol suspension and/or dilutions of this original aerosol suspension. The filled trays are subsequently placed onto the aluminium blocks and cooled down by the cryostat at a freezing rate of $0.33\,\mathrm{K\,min^{-1}}$.

The aerosol suspension can also be subjected to different treatments before analysis to gain a deeper understanding of the nature of the potential INP population. One common treatment used during INSEKT experiments is a heat treatment, where the aerosol suspension is heated to 100 °C for 20 min. This removes heat-labile INPs from the INP population, which often indicates that a biogenic component contributes to the total INP population (Hara et al. 2016). However, this is not always clear, since also non-biogenic aerosol particles may be impacted by the heat treatment (Daily et al. 2022; O'Sullivan et al. 2014; Perkins et al. 2019). This treatment therefore can indicate a biogenic component, but does not need to be related to a biogenic component.

3.2.1.4. Data analysis

Figure 3.5 shows a typical INSEKT INP temperature spectra. The chosen filter was washed and subsequently suspensions with three different dilution scales ($d_1 = 1$, $d_2 = 15$, $d_3 = 225$) were prepared. In this way, INSEKT is sensitive to INP concentrations in the temperature range above −25 °C. Each well is filled with 50 µl of the suspension. The data is given in 0.5 K steps using a quality factor $q = 8$ and the different dilutions are homogenized to a single dataset. The overlapping data points of the different suspensions are merged using an approximated convolution described in Laursen et al. (2019). The data is also quality controlled using three simple quality checks. The data is flagged for two categories: warning and error. The data is afterwards visually inspected, when a warning flag occurs. An error flag is automatically removed from further analysis. For an experiment with three different suspensions (A, B, and C) with three dilution factors (i.e. $d_\mathrm{A} < d_\mathrm{B} < d_\mathrm{C}$) the three conditions are:

1. **quality of water:** error if the condition is true

$$\mathrm{abs}(T(f_\mathrm{f}^\mathrm{water} = 0.5) - T(f_\mathrm{f}^\mathrm{suspension} = 0.5)) < 1\,\mathrm{K}\ , \tag{3.27}$$

2. **quality of dilutions (separation):** warning if the condition is true

$$\mathrm{abs}(T(f_\mathrm{f}^\mathrm{suspensionA} = 0.5) - T(f_\mathrm{f}^\mathrm{suspensionB} = 0.5)) < 1\,\mathrm{K}\ , \tag{3.28}$$

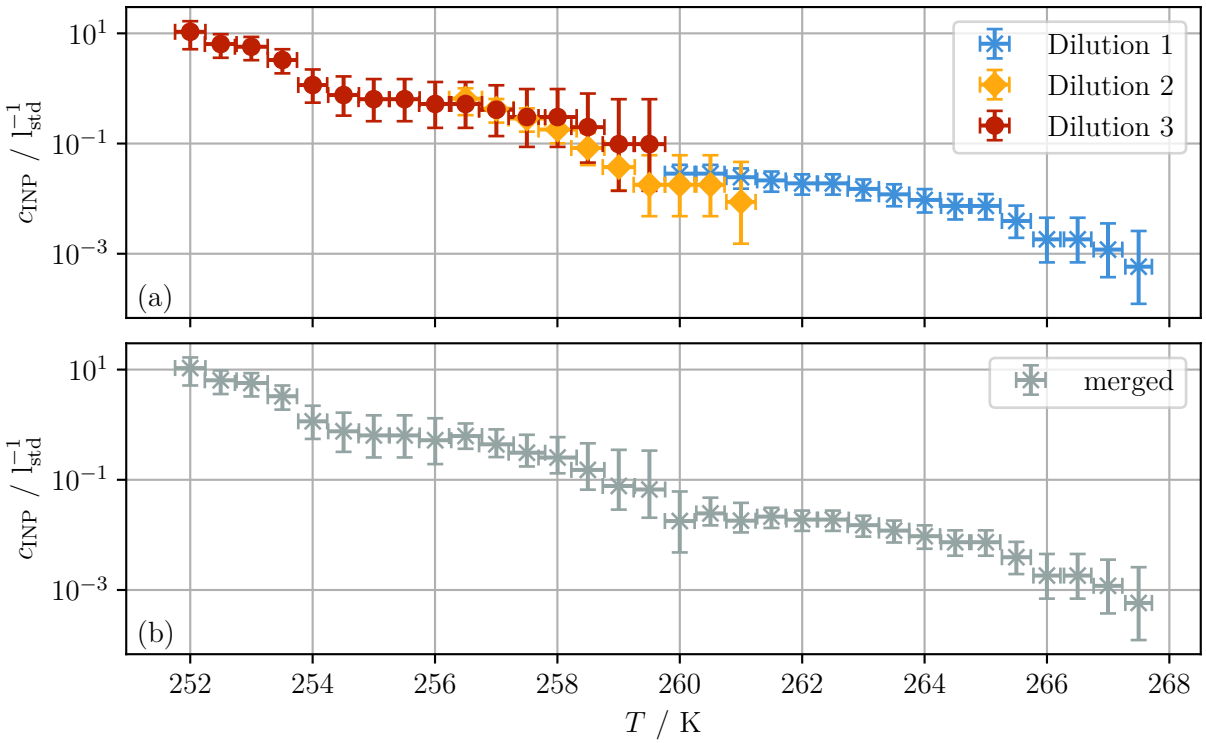

Figure 3.5.: **INP concentration c_{INP} as a function of the freezing temperature T for a typical INP experiment with two dilutions (panel (a)) and the merged distribution (panel (b)).** The INP concentration as a function of the freezing temperature shows roughly an exponential behaviour. By using two dilutions (dilutions 2-3) together with the undiluted aerosol suspension (dilution 1), the frozen fraction can be assessed down to 252 K (−21.15 °C). The merged INP temperature spectra in panel (b) combines the overlapping data points using an approximated convolution (Laursen et al. 2019). The temperature uncertainty is given by the standard deviation of the population of the eight temperature sensors with a coverage factor according to a 95 % confidence interval of a Student's t distribution.

3. **quality of dilutions (freezing order):** error if the condition is false

$$\text{abs}(T(f_{\text{f}}^{\text{suspensionA}} = 0.5) > T(f_{\text{f}}^{\text{suspensionB}} = 0.5)) > T(f_{\text{f}}^{\text{suspensionC}} = 0.5)) \ . \tag{3.29}$$

3.2.2. PINE

The PINE is an online instrument that measures the INP concentration in the immersion freezing and deposition nucleation modes (Möhler et al. 2021). It is an expansion-type cloud chamber with a volume of 10 l. In an expansion-type cloud chamber, the pressure is decreased rapidly, leading to a decrease in temperature due to expansion cooling, while the relative humidity increases (e.g., Wagner et al. 2006). Present aerosol particles in the chamber can act as CCN and/or as INP, leading to the formation of cloud droplets and/or ice crystals, respectively. The PINE can be operated above −60 °C to measure the mixed-phase regime (> −35 °C) and the cirrus regime (< −35 °C). The created cloud droplets and/or ice crystals are detected optically with an OPC and separated by their optical size using a dedicated algorithm (see section 3.2.2.3).

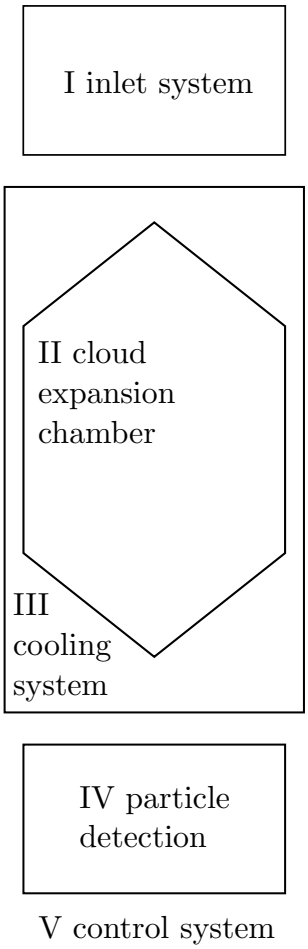

Figure 3.6.: **The five basic components of PINE.** Adapted from Möhler et al. (2021).

3.2.2.1. Main components

The PINE consists of five main components, visualized in figure 3.6. The inlet system (I) contains two Nafion membrane diffusion dryers (MD-700-24S-1, Perma Pure) in parallel. The cylindrical membranes are located inside a stainless steel tube with an additional connection to the outer cylinder. Ambient air flows through the outer cylinder in a counterflow arrangement, but with a reduced pressure ($> 50\,\mathrm{hPa}$). The difference in partial pressure leads to the diffusion of water through the membrane. The sample flow passes through the dryers and then via two 90° bends into the cloud expansion chamber. The transport efficiency is around 50 % at 4 µm (see also chapter A). The cloud expansion chamber (II) consists of an aluminium chamber with two cones at the top and the bottom, which is located inside a stainless steel isolation chamber. The aluminium chamber has a volume of 10 l and its temperature is controlled by the cooling system (III). Inside the chamber three temperature sensors (Pt100 RS 1/5 class B, Sensorshop 24) are located on the wall on the top (Tw1), the middle (Tw2) and the bottom (Tw3). In addition, five temperature sensors (Thermoelement Typ K IKT 10/070/D2.5x15/2KK06/09 IEC 583-3 class 1, unknown manufacturer) are located inside the chamber in equidistant positions from the top (Ti1-Ti5). The five gas temperature sensors are calibrated by the manufacturer at 293.15 K, 273.15 K, 253.15 K, 233.15 K and 213.15 K against a Pt100 1/3 class B sensor. The accuracy is given in table A.2.

The cooling system consists of a Stirling cooler (Thales, LPT9310, Johnson et al. 2014; McKinley et al. 2024), which is able to achieve a cooling rate of approximately $0.6\,\mathrm{K\,min^{-1}}$ (Möhler et al. 2021). This allows for rapid temperature scans to measure the INP concentration at different freezing temperatures. The particle detection (IV) of PINE is done optically utilizing a full flow OPC (fidas-PINE, Palas GmbH, see also section 3.1.3).

The control system (V) is a custom LabVIEW program[7] that controls the conditions of PINE. Utilizing all five components the INP concentrations can be measured with a high temporal resolution of minutes down to approximately $-60\,^{\circ}\mathrm{C}$.

3.2.2.2. Typical experiment

A typical experiment of PINE consists of three modes: flush, expansion and refill (see also figure 3.7). During the flush mode, the cloud expansion chamber is flushed with ambient air containing the aerosol particles under investigation at ambient pressure. The relative humidity of the sampled air is controlled via the dryers and the dew point temperature above the cloud expansion chamber is measured with a dew point sensor (DRYCAP® DMT143, Vaisala). The relative humidity needs to be high enough to allow liquid cloud formation, but it needs to be low enough to not lead to the fast build up of ice on the cloud expansion chamber walls. The volume flow during the flush mode is typically around 1 to $2\,\mathrm{l\,min^{-1}}$ in the experiments presented in this work and the flush mode lasts around 300 s. With a flow of $2\,\mathrm{l\,min^{-1}}$ this equals a net volume of 10 l, equal to the total volume of the cloud expansion chamber. A lower flow is beneficial to the dryer efficiency and thus used at higher ambient humidity conditions.

In the expansion mode, the valve on top of the cloud expansion chamber is closed and the chamber is evacuated with a constant volume flow of typically $3\,\mathrm{l\,min^{-1}}$. The flow is controlled with a mass flow controller (EL-FLOW Select F-201CV 10 l, Bronkhorst Instruments GmbH, reference conditions are $T_\mathrm{n} = 273.15\,\mathrm{K}$ and $p_\mathrm{n} = 101\,325\,\mathrm{Pa}$), the value set according to the current pressure inside the chamber. The expansion continues until a pressure is reached, that is typically defined to be around 80 % of the ambient pressure. This threshold is set to assure a near-adiabatic expansion. A system that does not transfer heat to or from itself is adiabatically isolated. No process is truly adiabatic since the entropy always increases according to the second law of thermodynamics (e.g., Philippi 2024, p. 72). Considering an adiabatic expansion of an ideal gas, leads to the following condition

$$p_\mathrm{start}^{1-\gamma} T_\mathrm{start}^{\gamma} = p_\mathrm{end}^{1-\gamma} T_\mathrm{end}^{\gamma}\ , \tag{3.30}$$

where: $p_\mathrm{start|end}$ – pressure at the start or end of expansion (Pa),
$T_\mathrm{start|end}$ – absolute temperature at the start or end of expansion (K),
γ – heat capacity ratio.

Accordingly, during the expansion, the temperature decreases, while the wall temperature remains relatively constant. The temperature difference between the chamber wall and the gas increases during the expansion, leading to an increased heat transfer from the chamber wall to the gas. This is one of the effects that restricts the duration of the expansion. During this expansion, the supercooled liquid droplets and the ice crystals - if INPs are present - are detected by the OPC. The photo multiplier amplification (PMA) voltage is adjusted to make sure that a liquid cloud is detected to assure a possible separation of liquid and solid phase. At the same time, the PMA voltage cannot be set too high, since an increasing number of particles would lead

[7] Designed and developed by Jens Nadolny (Karlsruhe Institute of Technology (KIT), IMKAAF).

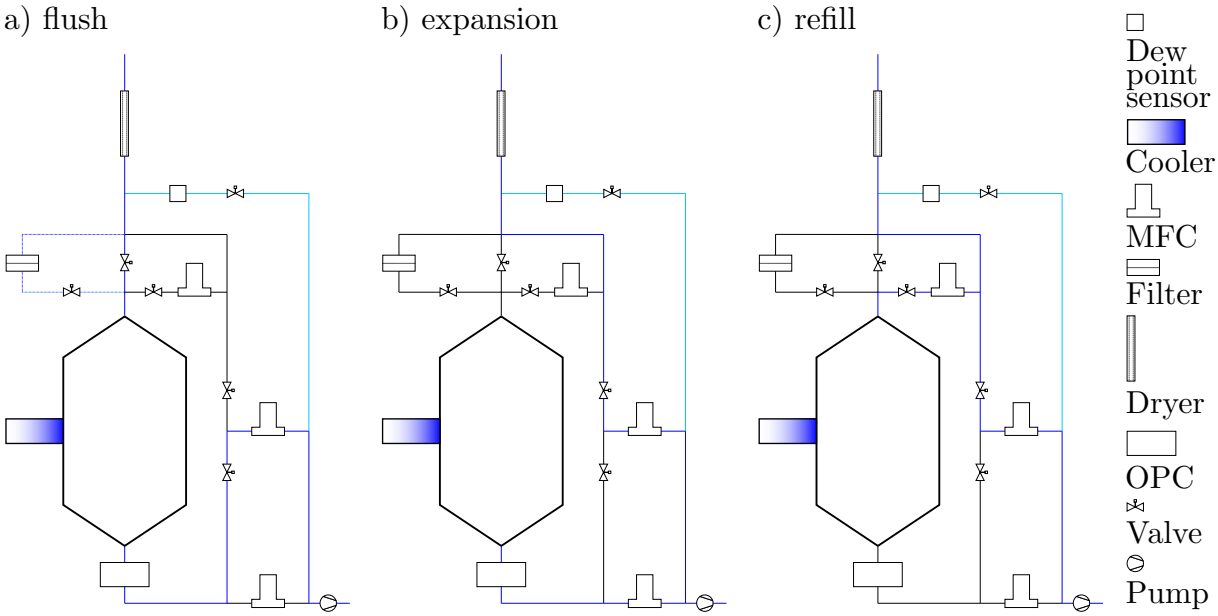

Figure 3.7.: **The three modes of PINE.** Panel (a) shows the flow path for the flush mode (dotted for the background mode), panel (b) shows the flow path for the expansion mode, and panel (c) shows the flow path for the refill mode. The flow over the dew point sensor is present during all modes.

to coincidence, where the total concentration is undercounted. Therefore, the smallest cloud droplets are normally not detected. The liquid cloud is typically detected around ten seconds after the start of the expansion, depending on temperature and humidity conditions.

The refill mode starts after the pressure threshold is reached. A valve on top of the cloud expansion chamber is opened and the volume flow is set to a value below or equal to the flush flow. The refill air passes a high efficiency particulate air (HEPA) filter (HEPA-CAP, Whatman^{TM}) to remove aerosol particles from the ambient air. The refill mode ends and continues again with the flush mode once the ambient pressure is reached. One cycle is called a run and lasts typically around six minutes.

3.2.2.3. Data analysis

The data provided by the LabVIEW software contains housekeeping data, i.e., valve states, as well as sensor data. The data is grouped into operations, which contain runs. An operation is defined by a certain operation procedure such as measurements at a constant temperature or during a temperature ramp. Another common operation type is the background measurement where the ambient air is filtered before entering the expansion chamber to ensure that the chamber is free of aerosol particles. One run contains one cycle of flush, expansion and refill (see section 3.2.2). The gas temperature sensor at the bottom of the cloud expansion chamber (Ti5) is used as the reference temperature for the INP concentration as it records the lowest temperature during the expansion. The lowest temperature is relevant due to the freezing spectrum being a cumulative spectrum. The single particle data from the OPC is used to determine an ice threshold, with optical particle diameters smaller than the threshold considered supercooled liquid droplets, and optical particle diameters larger than the threshold considered ice crystals formed via heterogeneous nucleation (see also section 3.1.3). Each ice crystal results from an aerosol

particle that was active as an INP at the lowest temperature measured during the expansion.

The ice threshold is determined automatically using the custom Python software Portable Ice Nucleation Experiment ice-nucleating particle AnalDraxler1998ysis (PIA)[8]. PIA implements an automatic ice threshold finder that determines the ice threshold individually for each run, utilizing the following algorithm:

1. normalize the number of particles per size bin to the total number of particles.
2. Calculate the cumulative distribution function (CDF) $F(x)$

$$F(x) = \sum_{t=0}^{x} f(t) \ . \tag{3.31}$$

3. Take the second derivative of the CDF $F''(x)$

$$F''(x) = \frac{\mathrm{d}^2 F(x)}{\mathrm{d}x^2} \ . \tag{3.32}$$

4. Select all bins larger than the first minimum of $F''(x)$.
5. Select the smallest bin where $F''(x) \geq 0$.

An example of three typical runs is shown in figure 3.8. PIA uses the housekeeping and sensor data to create a dataset containing the minimal temperature and the INP concentration for each run, therefore providing a temporal resolution of around six minutes. The INP concentration is calculated from the normal flow F, the expansion time t and the number of ice crystals N_{INP} detected

$$c_{\mathrm{INP}} = \frac{N_{\mathrm{INP}}}{F \times t} \ . \tag{3.33}$$

The PIA software also implements automatic data quality control on the basis of the System for automated Quality Control (SaQC) framework for the assignment of data quality flags (Schäfer et al. 2024; Schmidt et al. 2023). Quality flags are ordered into three classes: info, warning and error. The flags are used to assess the quality of the data 'in a [*sic*] accessible, consistent, objective and reproducible way'.[9] The data used in the present work is using this flagged data, removing invalid data, where the error flag is set. In addition, the data is inspected visually and manual flags are set utiziling the PINE ice-nucleating particle analysis for Manual and Automatic Versioning (PIMAV)[10] code, which was developed during this work to simplify the handling of larger datasets of PINE according to the FAIR[11] data principles. The uncertainty budget originating from the measurements are detailed in the following.

The standard deviation is related to the calculation of the INP concentration (see equation (3.33)). The mass flow controller sets the mass flow F during the expansion and the duration of the expansion t determines the total volume of air. The mass flow controller has an accuracy of

$$\sigma_F = 0.5\,\%\mathrm{RD} + 0.1\,\%\mathrm{FS} \ , \tag{3.34}$$

[8] https://codebase.helmholtz.cloud/pine/pia_software, last access: 28th January 2025.
[9] https://rdm-software.pages.ufz.de/saqc/, last access: 28th January 2025.
[10] https://codebase.helmholtz.cloud/pine/pimav, last access: 28th January 2025.
[11] FAIR data meets the FAIR principles of findability, accessibility, interoperability, reusability (Wilkinson et al. 2016).

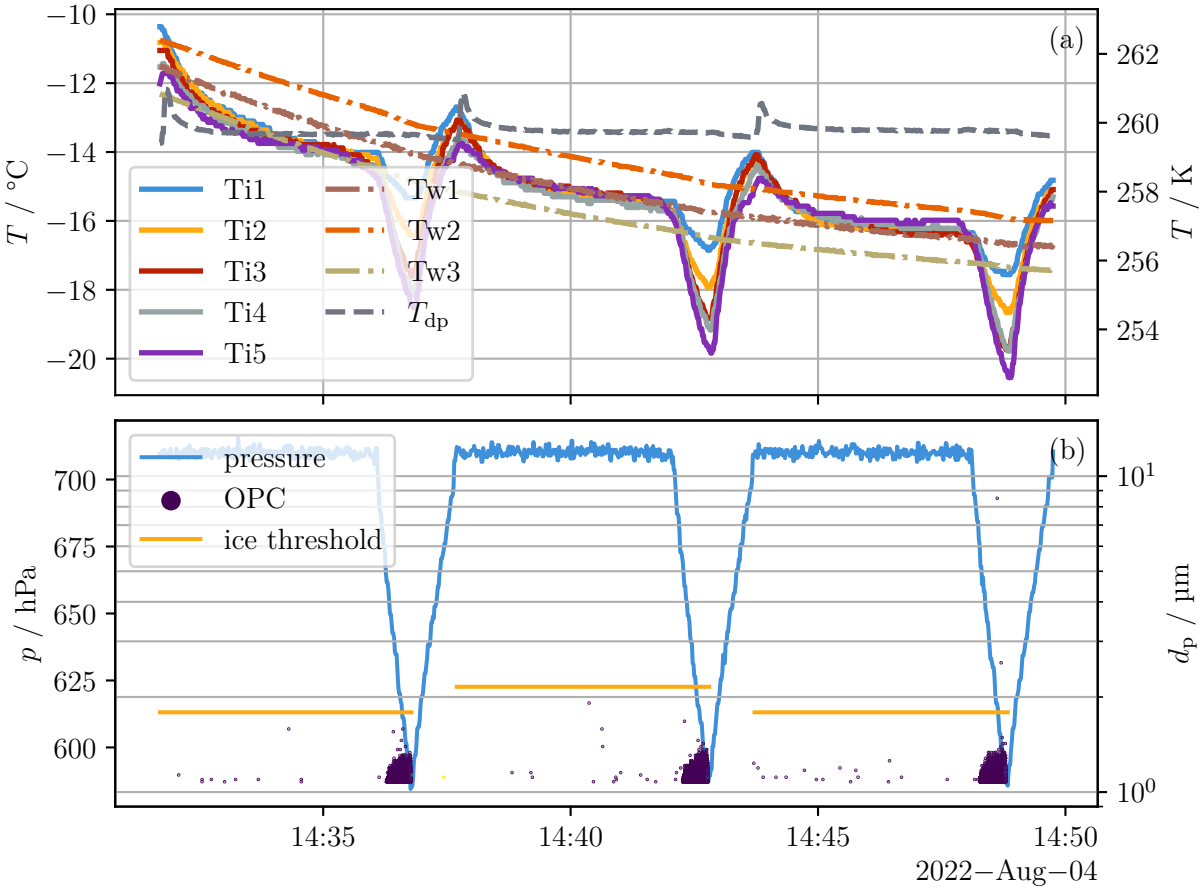

Figure 3.8.: **Example of three typical PINE runs.** Panel (a) contains the temperature sensor data for the gas and wall sensors as well as for the dew point temperature (T_{dp}). Panel (b) visualized the pressure inside the chamber and the single particle data measured by the OPC. The ice threshold are visualized as horizontal lines, which are individually determined for each run. The figure contains data from the runs, during which the temperature was decreased, leading to an increase in INP concentration in the last run.

where RD and FS denote the reading value and the full scale, respectively. The volume flow stays constant during the expansion, while the mass flow is adjusted according to the current pressure inside the chamber. The accuracy therefore changes between 0.025 $l_n\,min^{-1}$ and 0.0226 $l_n\,min^{-1}$ during the expansion, considering a pressure change from 1000 hPa to 840 hPa. The larger value is used to assess the maximum uncertainty.

The second source of uncertainty originates from the duration of the expansion. Considering only immersion freezing, the saturation ratio with respect to water needs to be above unity to achieve a liquid cloud and possibly also ice crystals via primary ice nucleation. Since the OPC might not detect the onset of the liquid cloud, the start of the expansion is considered as the point where supersaturation is reached. A typical expansion lasts around 40 s, where it can be estimated that supersaturation with respect to water is reached quickly in the first ten seconds of the expansion, which would lead to a negative bias of

$$b_t = 0 \text{ to } 10\,\text{s} \; . \tag{3.35}$$

This bias can be estimated to be uniform, since the relative humidity and temperature in the chamber can be different for each expansion as well as the concentration and size of the CCN,

which can impact the cloud droplet size. Considering uniformity between 30 to 40 s, the associated standard deviation is determined by

$$\sigma_t = \frac{(t_b - t_a)^2}{12} \approx 2.887\,\mathrm{s}\ . \tag{3.36}$$

where: t_b – maximum time where $s > 1$ (40 s),
t_a – minimal time where $s > 1$ (30 s).

This therefore leads to a potential bias in the INP concentration of

$$b_{c_{\mathrm{INP}}}[t] \approx +\frac{N_{\mathrm{INP}}}{F \times (40\,\mathrm{s} - 2.887\,\mathrm{s})}\ . \tag{3.37}$$

The uncertainty of the number of ice crystals is hard to estimate. The counting statistics of the fidas-PINE are relevant as well as the analysis step of setting the ice threshold. As described in section 3.1.3, the total number of particles might be underestimated due to the optical setup of the fidas-PINE with the widening aerosol stream, which would lead to a potential negative bias of up to 15.9 %

$$\sigma_{N_{\mathrm{INP}}} = \frac{(1-\eta)^2}{12} \approx 0.002\ , \tag{3.38}$$

$$b_{c_{\mathrm{INP}}}[N_{\mathrm{INP}}] \approx +\frac{0.002 \times N_{\mathrm{INP}}}{F \times t}\ . \tag{3.39}$$

This is likely to be less due to the aerosol distribution not being uniform along the radial axis, but for simplicity a uniform distribution of the bias is used. The uncertainty of the sensor itself can be related to a similar sensor used at the Aerosol Interaction and Dynamics in the Atmosphere (AIDA) facility since more than two decades, the white light aerosol spectrometer (WELAS) (Pallas GmbH, e.g., Vogel et al. 2022). The WELAS measures the scattering signal of aerosol particles passing through a white light beam at a 90° angle. It uses a T-shaped odv to measure single particle data and to classify border zone particles, finally multiplying the obtained value by a certain factor to estimate the total concentration of the measured particles in the aerosol stream. The number concentration is estimated to around 20 % of the reading value, mainly due to the uncertainty of the odv and the flow (e.g., Möhler et al. 2021). Since the fidas-PINE is a full-flow sensor, the uncertainty should be smaller due to the more accurate method of counting each particle instead of relying on estimates of a uniform distribution of particles. For this uncertainty budget, a value of $\sigma_{N_{\mathrm{INP}}} = 10\,\%$ on the number of aerosol particles and in turn ice crystals is estimated. The uncertainty related to the ice threshold finder is taken to be zero, since an accurate estimate would require single particle analysis of each particle and determining their phase, which is beyond the scope of the present work.

Combined, the variance of the INP concentration measured by PINE is

$$\mathrm{VAR}(c_{\mathrm{INP}}) = \left(\frac{1}{F \times t}\right)^2 \times \left[\sigma^2_{N_{\mathrm{INP}}} + \left(\frac{\sigma_F}{F}\right)^2\right]\ . \tag{3.40}$$

The relative uncertainty therefore converges for $N_{\mathrm{INP}} > 1$ quickly to

$$\frac{\sigma_{c_{\mathrm{INP}}}}{c_{\mathrm{INP}}} \approx 0.1\ , \tag{3.41}$$

which is the uncertainty assumed for the fidas-PINE.

The relative bias originating from the expansion time is

$$\frac{b_{c_{\mathrm{INP}}}[t]}{c_{\mathrm{INP}}} \approx 1.078\ . \tag{3.42}$$

And the relative bias originating from the uncertainty of the odv is

$$\frac{b_{c_{\mathrm{INP}}}[N_{\mathrm{INP}}]}{c_{\mathrm{INP}}} \approx 1.002 \ . \tag{3.43}$$

This bias is likely to be lower, but generally, the INP concentration might be slightly larger than recorded. The uncertainty is not taken into accound in the final analysis, where the data is generally grouped and a statistic is used to determine the median and the respective quantiles.

3.2.3. Infrared cold stage (IR-CS)

The IR-CS is used to assess the freezing temperature of small droplets with a volume of 20 nl or less. A silicon wafer (10 × 10 mm) is pre-cleaned with ethanol and subsequently cooled with liquid nitrogen at $10\,\mathrm{K\,min^{-1}}$ until its temperature reaches the dew point temperature. Afterwards, droplets are dispensed onto it. Any object with a temperature greater than absolute zero produces a thermal radiation spectra that is dependent on its temperature. The wavelength corresponding to the maxima of this spectra is described by Wien's displacement law[12]

$$\lambda_{\mathrm{max}} = \frac{b}{T} \approx \begin{cases} 10.6\,\mu\mathrm{m} & (T = 273.15\,\mathrm{K}), \\ 12.3\,\mu\mathrm{m} & (T = 235.15\,\mathrm{K}). \end{cases} \tag{3.44}$$

where: b – Wien's displacement constant ($2897.771\,955\,\mu\mathrm{m\,K^{-1}}$),
T – absolute temperature (K).

An infrared camera measures the thermal radiation wavelength of the droplets to measure the temperature of each individual droplet. When a droplet freezes, the latent heat released leads to a sudden increase in temperature to 0 °C. A custom-made LabVIEW program[13] controls the cooling and reads out the infrared camera data and finally saves the data into a database.

3.2.3.1. Main components

Figure 3.9 shows the setup of the IR-CS with the individual components marked with numbers from (1) to (7). The liquid nitrogen tank (1) is connected to the cold stage ((2), MDBCS196, Linkam Scientific Instruments Ltd.), which is able to cool the sample at rates between $0.01\,\mathrm{K\,min^{-1}}$ and $150\,\mathrm{K\,min^{-1}}$. The barium fluoride ($BaF_2$) window covers the sample during the cooling period. BaF_2 offers a high transmission range between 0.15 to 12 µm, ideal for the thermal radiation spectra observed for temperatures in the mixed-phase regime (235.15 to 273.15 K). The infrared camera ((3), PI640i LT, Optris IR Sensing, LLC) has a spectral range of 8 to 14 µm and is mounted on a vertical stage (4) for focus alignment. The small volume of the droplets leads to a very fast transition from liquid to solid, requiring a high temporal resolution of the infrared temperature measurement, which is provided by the infrared camera with a frame rate of 32 Hz at full resolution (640 × 120 pixels). The injector ((5), PipeJet®-nanoDispenser, Hamilton Freiburg GmbH) is able to produce droplets of small volumes between 2 to 70 nl. A small elastic pipe is mounted between clamps and a piston driven by a piezo stack actuator deforms the elastic pipe to facilitate fast volume displacement leading to the formation of a small droplet. An additional optical setup containing the optical camera (6) and a cold light source ((7), KL 2500 LED, Schott AG) is available to observe individual droplets, but was not used during this work.

[12] Exact value for Wien's displacement constant from '2022 CODATA recommended values'.
[13] Designed and programmed by Tilia Gädeke and Denis Duft (IMKAAF).

3.2.3.2. Typical experiment

The temperature of the silica wafer is measured via a Pt100 sensor (RS PRO Platinum Resistance Temperature Sensor, temperature accuracy: 0.5 K) placed on one of its corners and by the cold stage temperature control. Depending on the placement of the Pt100 sensor, the two temperatures can show a slight offset due to a not ideal heat transfer between the silica wafer and the Pt100 sensor, especially at higher cooling rates. The temperature measurement of the infrared camera is only used to detect the freezing of the droplets, since the accuracy is poor (±2 K or 2 % of the reading (in °C), whichever is greater). The Pt100 sensor is calibrated with the same sensor used during the calibration of the temperature sensors of INSEKT (see also section B.1). The frozen fraction obtained over a wide temperature range originates from a similar number of droplets as INSEKT, i.e. around 100 (see section 3.2.1). Therefore, the same uncertainty estimation is utilized: the approximated binomial distribution (see section 3.2.1.2 and Agresti and Coull 1998). The IR-CS is a useful addition to the analysis of aerosol samples with INSEKT and PINE, since it covers the temperature range down to the lower temperatures of PINE, while still being sensitive to higher INP concentrations at higher temperatures. For the present work, the IR-CS was used to analyze snow samples (see section 3.5.4).

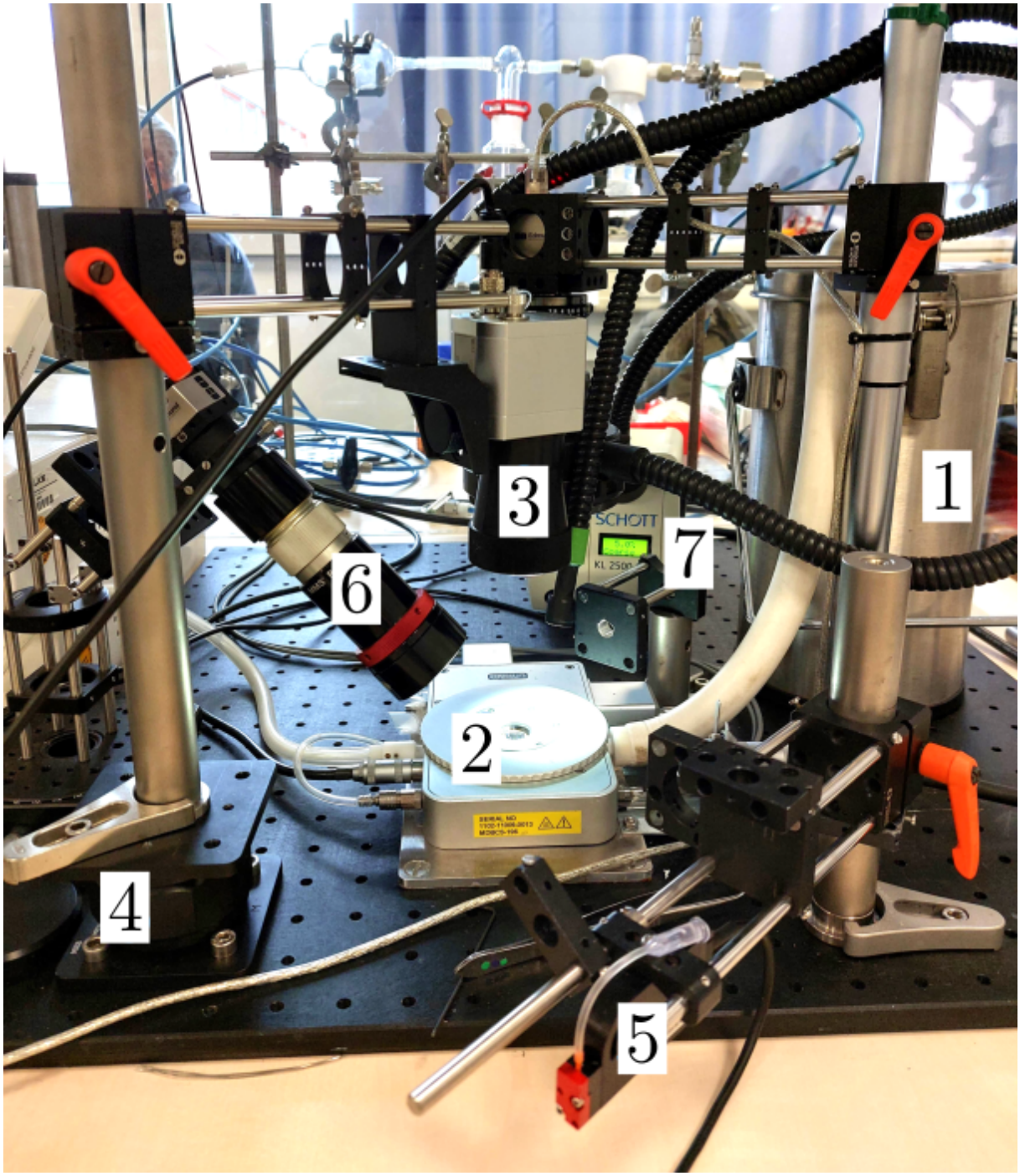

Figure 3.9.: **Picture of the IR-CS setup.** The different components are marked by numbers: (1) liquid nitrogen tank, (2) cooling stage covered with a barium fluoride (BaF_2) window, (3) infrared camera, (4) vertical stage for focus alignment of infrared camera, (5) droplet injector, (6) optical camera and (7) light source for optical camera.

3.3. UAV instrumentation

In the course of this work, a novel filter-based sampler was developed, refined and tested during multiple field campaigns. The mobile and lightweight sampler can be used onboard of a fixed-wing UAV and collect aerosol samples on different vertical levels. The sampler itself is described in detail in section 3.3.2 and the integration onboard of the fixed-wing UAV in section 3.3.1. The setup and first results are published in Böhmländer et al. (2024).

3.3.1. Platform

The sampler can be used on its own, but it has been integrated into a fixed-wing UAV. Therefore, the flight platform is described first to motivate some key development steps for the sampler. UAVs have become a recent focus in atmospheric measurements (e.g., Bärfuss et al. 2018; Böhmländer 2021; Böhmländer et al. 2024, 2025b; Brus et al. 2025; Girdwood et al. 2020, 2022; Kezoudi et al. 2021; Lampert et al. 2020; Marinou et al. 2019; Villa et al. 2016; Yu et al. 2017). They offer a flexible and cost efficient way to probe the lower atmosphere. Most setups are developed to measure atmospheric variables, such as temperature, pressure, and relative humidity. One aim is to measure the same variables as radio sondes and provide a potential setup with reuseability. In addition, more complex systems have been developed, that measure additional variables, such as the aerosol number size distribution (Bärfuss et al. 2018). INPs have been measured onboard of UAVs (e.g., Bieber et al. 2020; Böhmländer et al. 2025b; Schrod et al. 2017) and on balloon-based setups (e.g., Porter et al. 2020) before. Bieber et al. (2020) measured biogenic INPs up to 100 m above ground level (agl) with flight times around ten minutes using an impinger-type setup onboard a multicopter. Higher altitudes (< 2.5 km agl) and longer sampling times (< 90 minutes) were achieved by Schrod et al. (2017) using a two fixed-wing setup to measure dust events in the Eastern Mediterranean. A payload developed by Porter et al. (2020) has been tested during campaigns in Hyytiälä (southern Finland), Leeds (northern England), Longyearbyen (Svalbard, Norway), and Cardington (southern England). The balloon-borne setup is tethered at a fixed altitude (< 2.3 km) and can sample up to 11 hours. Creamean et al. (2018b) developed a similar setup but mounted onto a launched balloon. The system collects aerosol onto a filter, measures the total particle concentration and was tested up to an altitude of 1.1 km agl.

The sampling time and the flow determine the lower detection limit for the INP concentration. This is especially important for higher subzero temperatures and regions, where the INP concentration is especially low (e.g., DeMott et al. 2010; Kanji et al. 2017). Longer sampling times of course also lead to a reduction in temporal resolution, possibly not allowing to observe short-termed variabilities such as a diurnal cycle.

For this study, a payload was integrated into a fixed-wing UAV of the Skywalker 1830 model year 2015 (customised by Yugen Oy). The Skywalker has a wingspan of 1830 mm and a maximum takeoff mass of 3000 kg. Removing its own weight, this allows for a maximum payload weight of roughly 1200 g. The payload is located inside the fuselage, spanning 220 mm in length and at a width of 120 mm. Two openings below the wings are covered via two wooden plates (150 mm $\times$ 75 mm). The UAV is powered by two Lithium-Ion (LiIon) batteries (4S, 7000 mA h) connected in parallel, providing a maximum flight time of around 2 hours in ideal weather conditions. Low power consumption is ensure due to its efficient glider-type airframe. It can be operatored with two persons, one launching the UAV by hand, the other controlling the ascend and landing. The Skywalker can land on its belly on a flat surface (i.e., grass or snow, see also figure 3.10). In addition, a fixed-wing can glide at one constant altitude to ensure aerosol

Figure 3.10.: **The Skywalker shown with its final setup after a successful flight.** The filter holder is visible below the left wing, mounted via the 3D-printed parts shown in figure 3.11. The inlet is blocked until lunch. One of the two ambient sensors is visible on the front left (BME280, Bosch), and the airspeed sensor is visible on the right side (ASPD-7002, Matek Systems).

sampling only at the designated altitude. The UAV contains additional components to ensure safe operation, such as a flight controller using arduplane firmware 4.06 (F405-WING, Matek Systems), an analogue airspeed sensor (ASPD-7002, Matek Systems), and a compass module (M8Q-4883, Matek Systems). This data is also used to track the UAV flight path via global navigation satellite system (GNSS) data.

Figure 3.11.: **3D printed parts for mounting the filter holder to the Skywalker wing.** From left to right: mount base, mount backplate, filters mount, and final setup. The mount base and mount backplate are fixed to the wing of the airframe. The filder holder mount can be locked onto the filter holder and clipped into the mount base. This allows a quick replacement of the filter holder between flights.

3.3.2. Payload

The aerosol sampler contains a pump to generate a flow over a filter. The aerosol particles are collected onto the filter via impaction and diffusion (see also Böhmländer 2021). Afterwards the aerosol particles are washed off the filter and analysed with INSEKT and a freezing spectra is obtained (see also section 3.2.1). Following, the iterations of the setup development are detailed and the final version is described at the end (see also tables 3.2 and 3.3).

3.3.2.1. 1st version

The first version of the filter sampler featured a stainless steel tube as an inlet. The air was pulled from below the wing, entering the fuselage via a 90° bend and featuring a second 90° bend before entering the filter holder. This version was deployed during a first field campaign in Pallas, Finland (see also table 3.2). This setup showed the technical feasibility of measuring the INP concentration during a single flight lasting between 45 and 90 minutes in a region with typically low aerosol concentrations during spring and autumn, equating to a total volume of sampled air of 450 l and 900 l (see section 3.5.1). Figure 3.12 shows the frozen fraction of a suspension made from aerosol collected on a filter during autumn 2020 at Pallas and a corresponding ground-based filter. A clear separation between the frozen fraction of the aerosol suspension and the Nanopure water background is visible in panel (a) and (b). This shows that even though the volume of air analyzed is relatively small, it is large enough to obtain results for temperatures above around 248 K. Further, the setup should be improved in term of handling as well as in terms of the accurate representation of the local aerosol population.

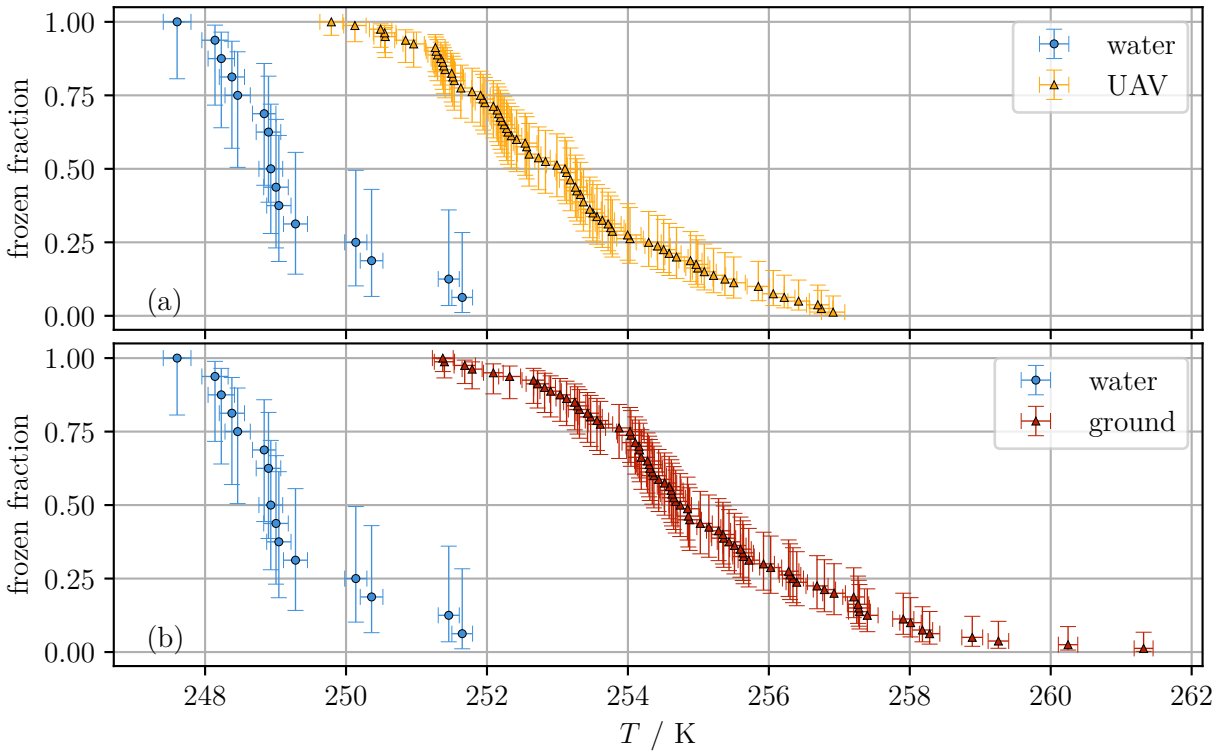

Figure 3.12.: **Frozen fraction as a function of the freezing temperature for two different aerosol suspensions.** Both panels show the frozen fraction of an aerosol suspension and its corresponding Nanopure water background. Panel (a) visualizes the frozen fraction of a suspension containing aerosol collected on-board of the UAV during Campaign 1 in autumn 2020, while panel (b) shows the same for the aerosol collected at the ground. The errorbars represent the 95 % confidence interval.

3.3.2.2. 2nd version

For the second version of the filter sampler, the filter was moved to the belly of the UAV, allowing for a straight horizontal sampling line with an inlet tube at the nose of the UAV. This increased the amount of larger particles collected due to the removal of the two 90° bends, which lead to inertial losses. The theoretical sampling efficiency of the three setups is shown in figure D.1 for a typical use case during flight. This does not take into account losses at the inlet or bias due to the body of the UAV. The scientific feasibility was demonstrated during campaign 2, where one handling blank filter was taken for the UAV and one for the ground. The handling blank provides an assessment of the aerosol contamination during handling, which is especially important during field campaigns, where clean conditions cannot always be guaranteed (see also section 3.2.1.2). Figure 3.13 shows the frozen fraction of aerosol suspensions collected during campaign 2 alongside two frozen fractions of aerosol collected from handling blanks. Panel (a) demonstrates the aerosol suspensions collected onboard of the UAV, while panel (b) shows the equivalent for the aerosol collected on the ground. The UAV aerosol samples were collected between 250 m and 1000 m agl. The frozen fraction of the aerosol filters show a clear separation to the Nanopure water background for both panels, with the individual droplets starting to freeze between 2 to 7 K higher for the UAV and between 2 to 5 K higher for the ground filter compared to the handling blank. The handling blank aligns with the Nanopure water background for the ground-based sampling, while the handling blanks of the UAV shows a deviation from the

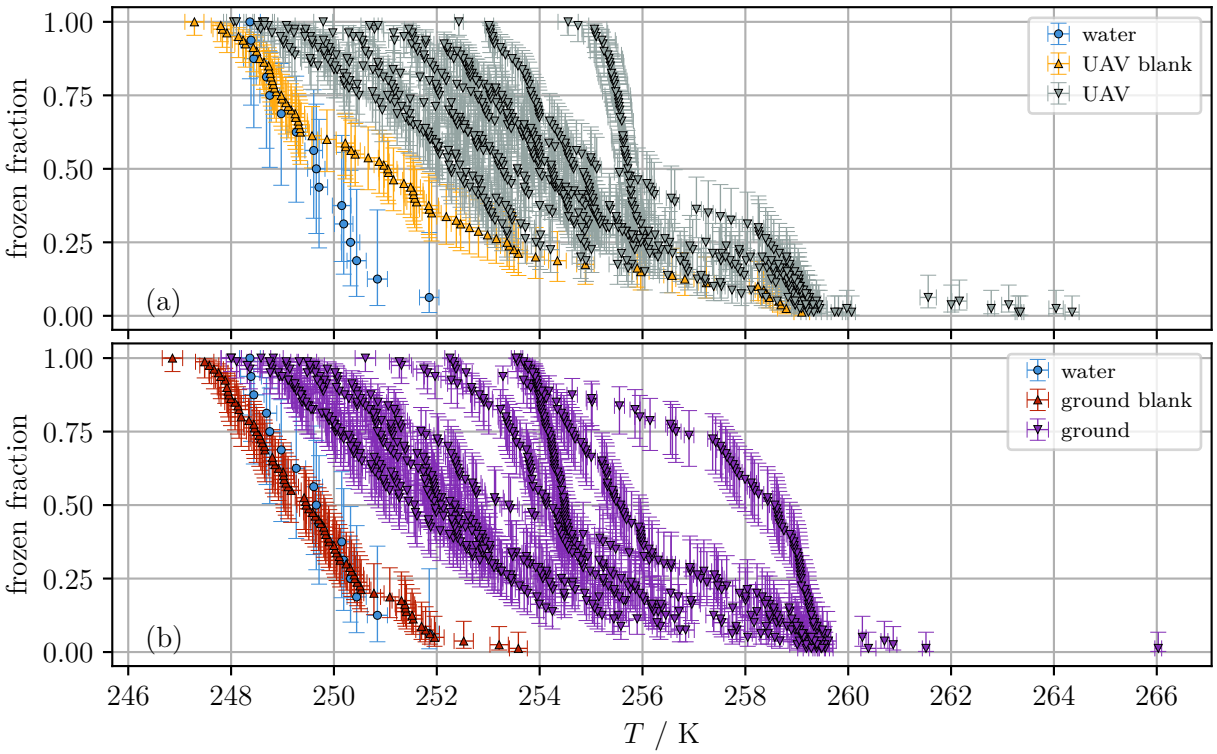

Figure 3.13.: **Frozen fraction as a function of the freezing temperature T for aerosol collected during Campaign 1.** The frozen fraction is shown for filters collected during campaign 2 during spring 2021 in Pallas, northern Finland. Panel (a) visualizes the aerosol suspensions obtained from filters onboard of the UAV and of the handling blank. The same is shown in panel (b) for the filter obtained with the same setup on the ground. Both panels contain the frozen fraction of the Nanopure water background used in INSEKT. Both panels show a clear separation to the Nanopure water background. The aerosol suspension obtained from the handling blank filters both are lower than the aerosol suspensions obtained from the UAV and ground filters. The errorbars represent the 95 % confidence interval.

Nanopure water background, especially for temperatures above 256 K. The frozen fraction of the handling blank of the UAV is still below all of the aerosol suspensions obtained on the UAV, demonstrating that the handling in the field does not significatnly contribute to a contamination with INPs.

In addition, some filters were flown for two consecutive flights to lower the detection limit further. The INP concentration as a function of the freezing temperature T is shown in figure 3.14 for a filter flown once at 400 m agl (panel (a)) and twice at 500 m agl (panel (b)). The minimal detection limit $c_{\mathrm{INP,\,low}}$ is shown as a horizontal red line, decreasing by around half for the filter flown twice due to the doubling of sampling time. Panel (a) shows that the INP concentration is very similar on the ground and at 400 m agl, with a maximum INP concentration of around $6 \times 10^{-1}\,\mathrm{l}_{\mathrm{std}}^{-1}$ at 248 K and a freezing onset at around 259 K. Panel (b) shows a slight separation between the UAV and ground filter suspension, with a freezing onset at around 259 K (258 K) for the UAV (ground) filter. All droplets are frozen within 5 K (5 K) for the UAV (ground) filters, showing that more aerosol was ice active during the observed temperature range. Additional dilutions would lead to an increased temperature range. These results demonstrate that the INP concentration can be determined with the described setup and comparisons can be made between the concentration on the ground and one designated altitude.

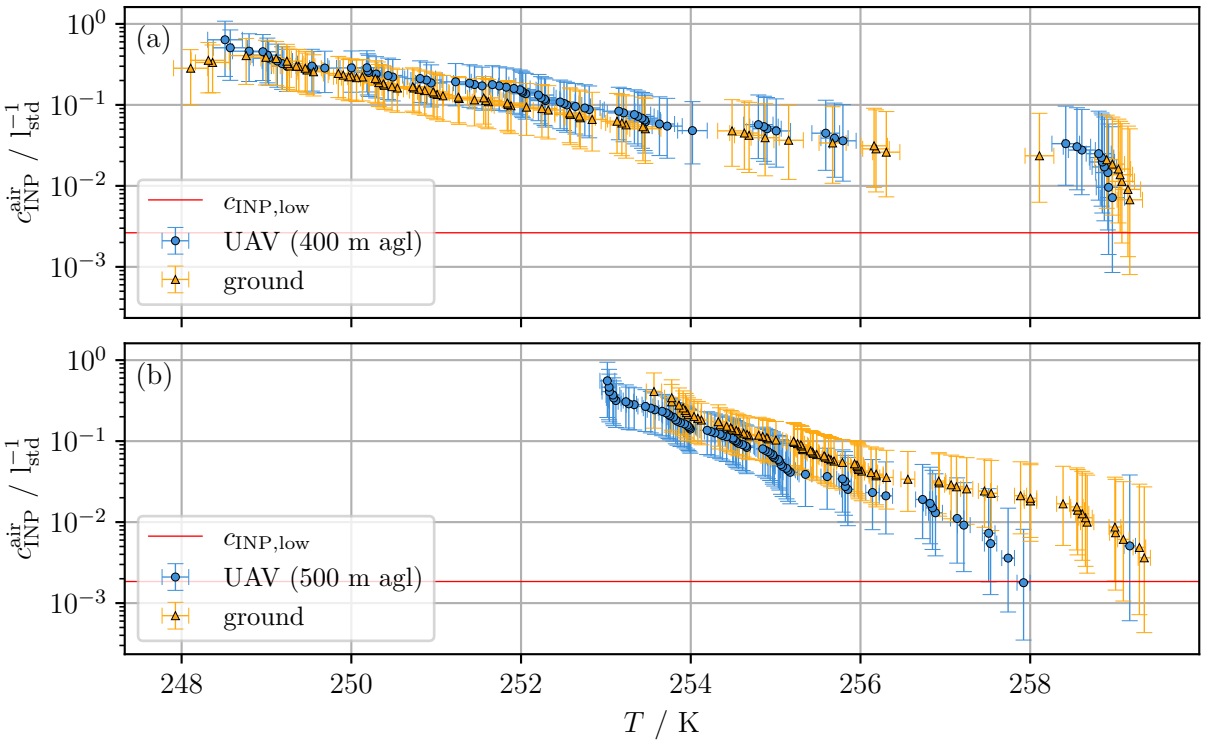

Figure 3.14.: **INP concentration as a function of the freezing temperature T for a single flight (panel (a)) and two consecutive flights (panel (b)).** Panel (a) shows the INP concentration in air $c_{\mathrm{INP}}^{\mathrm{air}}$ at 400 m agl and on the ground. Both samples show very similar behaviour over a temperature range of 10 K. Panel (b) shows the same for a filter flown on two consecutive flights at the same altitude of 500 m agl. The lower detection limit is shown as a horizontal red line, showing the decrease of the lower detection limit in panel (b). The errorbars represent the 95 % confidence interval.

Only the smaller filter holder was able to fit inside the body of the UAV, which meant a larger pressure drop across the filter and therefore a decrease flow. The handling was tedious due to the placement of the filter during campaign 2 (see table 3.2), and therefore, the next setup should be improved on these two aspects.

3.3.2.3. 3rd version

In the third and final version of the filter sampler, the larger filter holder was mounted via custom 3D-printed parts under the wing of the UAV, which removed most of the horizontal sampling tube and increased the ease of handling, since the filter holder could be mounted and unmounted without opening the fuselage of the UAV (see figures 3.10 and 3.11). Below the wing, a larger filter can be used to lower the pressure drop and therefore increase the flow over the filter. The increased weight lead to a lower flight time (from about 90 minutes down to 60 minutes), which was partly compensated by the increase in flow (from about 10.3 l min^{-1} to 11.1 l min^{-1} at 500 m above sea level (asl)) and the increase in transport efficiency (see figure D.1). The increase in transport efficiency allows for a more accurate representation of local aerosol population. The full list of components is given in table 3.3 for the three different versions. The final version was tested during campaign 3 and utilized to obtain scientific results during campaign 4, the Pallas Cloud Experiment (PaCE) 2022 (see also section 3.5.1.1).

Table 3.2.: **Campaign overview of UAV setup.**

Campaign	Number of flights	altitude / m agl min / max	Start	End	Description
1	13	100 / 800	2020-09-22	2020-09-30	proof of concept of the setup
2	12	250 / 1000	2021-04-19	2021-04-22	removal of bends in the sampling line leads to a decrease in sampling losses
3	3	150 / 300	2021-09-20	2021-09-23	shorter sampling line decreases diffusional losses, filter with a bigger diameter provides a lower pressure drop, leading to an increase in flow
4	29	100 / 1000	2022-09-15	2022-10-15	intensive measurement period (see also section 3.5.1.1)

Table 3.3.: **UAV-based aerosol sampler.** Description of the individual components inside the UAV-based aerosol sampler. The total weight of the sampling unit is about 870 g. Sensor specifications are taken from the respective data sheets (Bosch 2020; Sensirion 2013, 2021).

Name	Description	Details
Inlet[a]	Inner diameter: 6 mm	stainless steel, antistatic tubing
	Length: 172 mm (142 mm)[b]	
Filter holder	Diameter: 25 mm (47 mm)[c]	polypropylene, Whatman, 420200 (420400)[c]
	Weight: 10 g (62 g)[c]	
Filter	Diameter: 25 mm (47 mm)[c]	Nuclepore, Whatman, 110637 (111137)[c]
	Pore size: 0.4 µm	
Flow meter	Pressure drop: 25 hPa	Sensirion SFM4100 Air
	Flow range: 0 to 20 l_{std} min^{-1}	
	Accuracy: 0.15 % of full scale or 3 % of reading, whichever is bigger	
Pump	Weight: 380 g	KNF, NMP850.1.2KPDC-B HP
	Flow at 1013 hPa: 15 l min^{-1}	
	Maximum current: 2.4 A	
	Voltage: 12 V	
Single board computer	Weight: 9 g	Raspberry Pi Zero WH
LiIon battery	Weight: 280 g	4S
	Capacity: 3300 mA h	
Ambient sensor 1	Temperature range: −40 to 85 °C	Bosch Sensortec BME280
	Relative humidity range: 0 to 100 %	
	Pressure range: 300 to 1100 hPa	
Ambient sensor 2	Temperature range: −40 to 125 °C	Sensirion SHT40
	Relative humidity range: 0 to 100 %	

[a] The third version of the setup does not use an inlet.
[b] The second version has a decrease length of the inlet.
[c] The third version of the setup contains the larger filter holder.

3.4. Reanalysis and model data

This section provides a short introduction into the used data from reanalysis and model data.

3.4.1. European Centre for Medium-Range Weather Forecasts Reanalysis v5 (ERA5)

ERA5 provides global reanalysis data, where model data from the European Centre for Medium-Range Weather Forecasts (ECMWF) is assimilated with observations to obtain various atmospheric, land and oceanic climate variables from 1950 onwards (Hersbach et al. 2020). Data assimilation denotes the process of finding the best fit to both, the data as well as the model. The assimilated data is able to provide a global coverage. Atmospheric reanalysis data is provided on a spatial grid resolution of 31 km (Hersbach et al. 2020). Vertically, the atmospheric reanalysis data is available on different pressure (> 0.01 hPa), potential temperature and model levels (1 to 137). The data is available as a self-explanatory data file in the Network Common Data Format (netCDF) format.

Quality control is done on the observational data before data assimilation, which includes the blacklisting of data from certain satellites and/or over specific regions based on known issues or anomalies (e.g., Dee et al. 2011; Hersbach et al. 2020, 2018). Variational quality control is used to reduce the weight of data points if applicable (Hersbach et al. 2020; Tavolato and Isaksen 2014). ERA5 provides an uncertainty estimate, which is based on the spread of the data assimilations (Hersbach et al. 2020). This spread is smaller for recent data where more observations are provided.

The good performance of ERA5 has been evaluated against *in situ* measurements (e.g., radiosondes, Graham et al. 2019; or weather stations, Xu et al. 2019) by various studies (e.g., for the Arctic, Graham et al. 2019; for the Antarctic, Tetzner et al. 2019; for continental USA, Tarek et al. 2020; Xu et al. 2019; over the ocean, Belmonte Rivas and Stoffelen 2019; Kalverla et al. 2019; Olauson 2018).

3.4.2. FLEXible PARTicle dispersion model (FLEXPART) v10.4

The movement of gases and aerosol particles in the atmosphere can be modelled using multi-scale offline Lagrangian particle dispersion models (LPDMs). One LPDM used in the present work is FLEXPART (Pisso et al. 2019). Lagrangian and Eulerian specifications of the flow field, differ from their 'frame of reference'. Lagrangian specifications follows the motion of a parcel through space and time, whereas the Eulerian specifications describe the motion of a parcel at specific locations over time. Thomson (1987) showed that Lagrangian stochastic models produce consistent trajectories based on Eulerian PDFs.

FLEXPART uses meteorological fields as input to calculate the movement of gases and aerosol particles forward and backward in time. In this work, FLEXPART was run by Nikolaos Evangeliou (formerly Norwegian Institute for Air Research (NILU)[14]) to generate the movement of mineral dust aerosol particles generated by the FLEXDUST module (see also section 3.4.3). ECMWF

[14]FLEXPART model simulations are cross-atmospheric research infrastructure services provided by ATMO-ACCESS (EU grant agreement No 101008004). The simulations were performed on resources provided by Sigma2 - the National Infrastructure for High Performance Computing and Data Storage in Norway.

data is used as input data between 1st January 2023 and 31st December 2023. The resulting output is combined into four datasets:

- Footprint: the footprint emission sensitivity provides the probability of any release of mineral dust particles in any grid-cell to reach the receptor for the past 30 days.
- Continent Specification: timeseries of the mineral dust aerosol concentration at a three hour resolution categorized by their continental contribution (ocean, Greenland, South America, Central America, North America, Africa, Europe, Russia, Asia excluding Russia, Australia).
- Age Specification: timeseries of the mineral dust aerosol concentration at a three hour resolution categorized by the age of the air arriving at the receptor (up to 30 days).
- Total Dust: modelled contribution to the total mineral dust aerosol concentration (Groot Zwaaftink et al. 2016; Groot Zwaaftink et al. 2017; Wittmann et al. 2017).

The data is further categorized by the diameter of the mineral dust particles into ten different size species: 0.04 µm, 0.22 µm, 0.71 µm, 1.304 µm, 2.057 µm, 3.53 µm, 6.1 µm, 8.63 µm, 12.2 µm and 17.32 µm. The receptor is located at 78.907 15° N, 11.8866° E at four different altitudes: 0 m, 500 m, 1000 m and 1500 m asl. This matches the location of the Zeppelin Observatory (ZEP) (see section 3.5.3). In the following, an example of the different products is given and the plots are explained in greater detail.

An example for the footprint is shown in figure 3.15 with the normalized footprint $t_{\text{footprint}}^{\text{normalized}}$, defined by

$$t_{\text{footprint}}^{\text{normalized}} = \frac{t_{\text{footprint}}}{\max(t_{\text{footprint}})} \,. \tag{3.45}$$

The footprint shows the most likely contribution of mineral dust from northern Finland and Siberia, with an increased contribution for altitudes at and above 500 m asl. By further investigating the contributions from different sources, one can visualize the timeseries of the continental distribution at 500 m agl (see figure 3.16) Focusing just on 1st April 2023 in figure 3.16, one can see an increase in the dust emission from Russia. A small increase in emissions originates in Europe at the same time. Asia has the highest overall contribution during April 2023 for this species (0.71 µm). One can look the the age of the air parcel to understand if the mineral dust was 'fresh' or 'aged' (see figure 3.17). This might affect the mineral dust for example via chemical processes and coating during transport (Gaston 2020; Goel et al. 2020; Möhler et al. 2008). The largest peak around the 15th April 2023 shows the largest contribution from Asia with relatively old dust at around 15 days. Contrary, focusing on the 30th April 2023, the largest contribution is fresh dust, which fits the origin in Russia and Europe, with a small contribution from Asia that is likely linked to old dust. The total dust concentration is largest in Asia (22.98 ng m^{-3}), therefore it also contributes the most, even though Europe and Russia are much closer (2.56 ng m^{-3}). The combination of this data, allows an assessment of the mineral dust contribution and its origin. Together with the age of the mineral dust, an assessment of the efficiency of the mineral dust as an INP is possible (e.g., Baustian et al. 2012; Brooks et al. 2014; Jahl et al. 2021; Mahrt et al. 2020; Piedehierro et al. 2021).

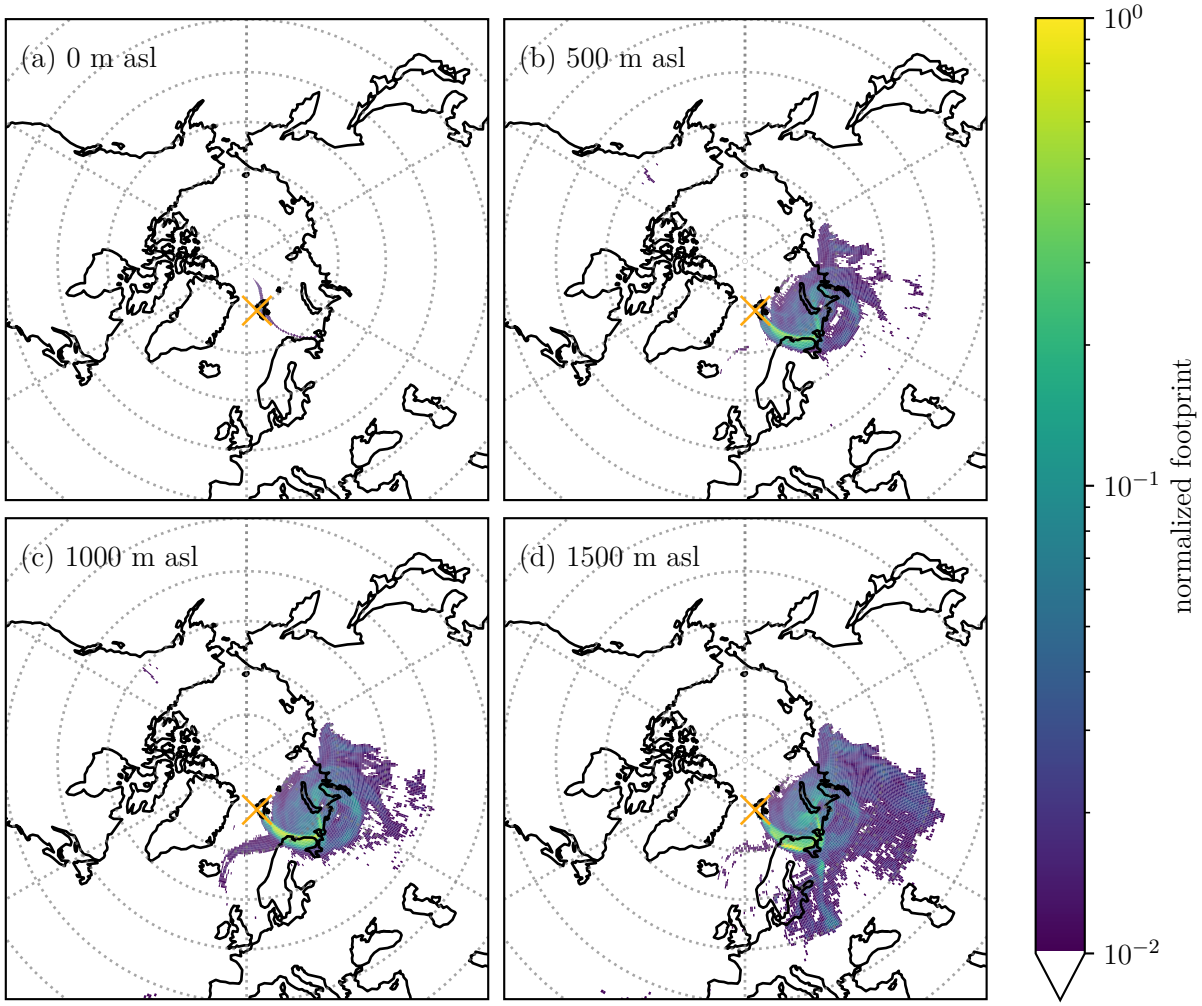

Figure 3.15.: **Example of footprint emission sensitivity simulated by FLEXPART.** The mineral dust of size 0.71 µm arriving at the receptor (marked by an orange x) at four different altitudes on 30$^{\text{th}}$ April 2023 midnight GMT. The data is color-coded with the normalized footprint (see also equation (3.45)).

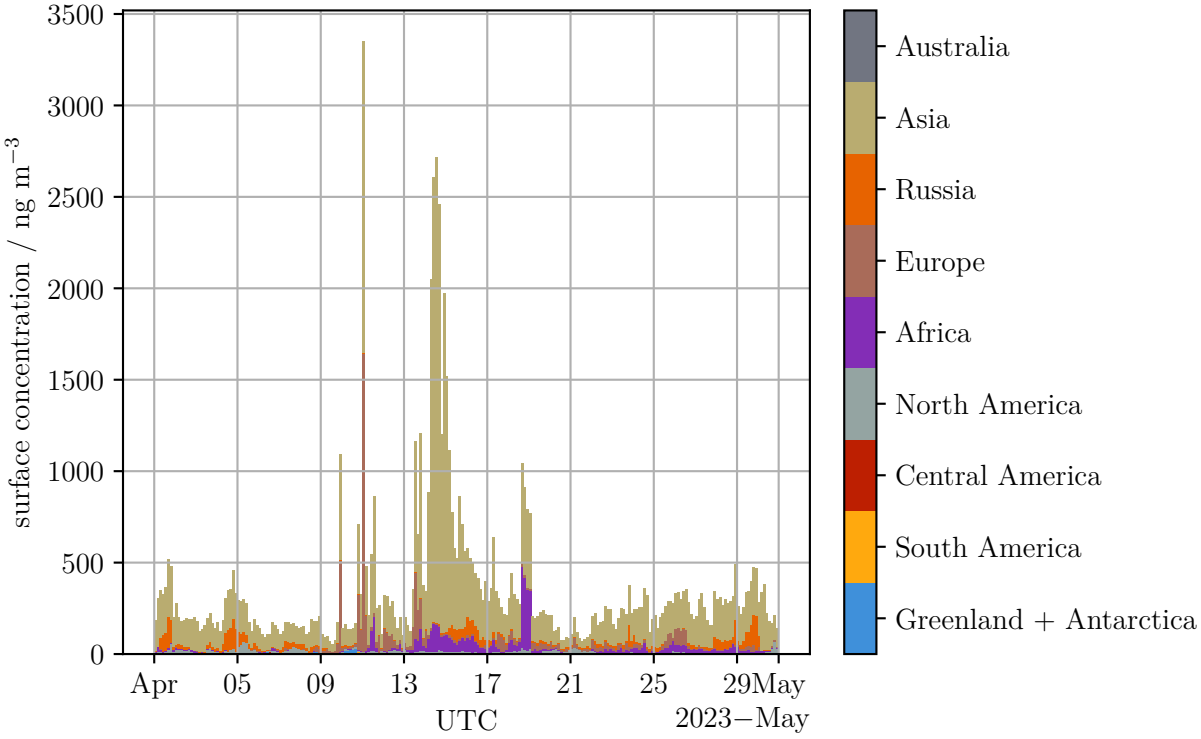

Figure 3.16.: **Example of continental contribution to the mass concentration at the surface simulated by FLEXPART.** The mineral dust of size 0.71 µm arriving at the receptor at an altitude of 500 m asl. The data is color-coded with the source of mineral dust as specified by FLEXDUST.

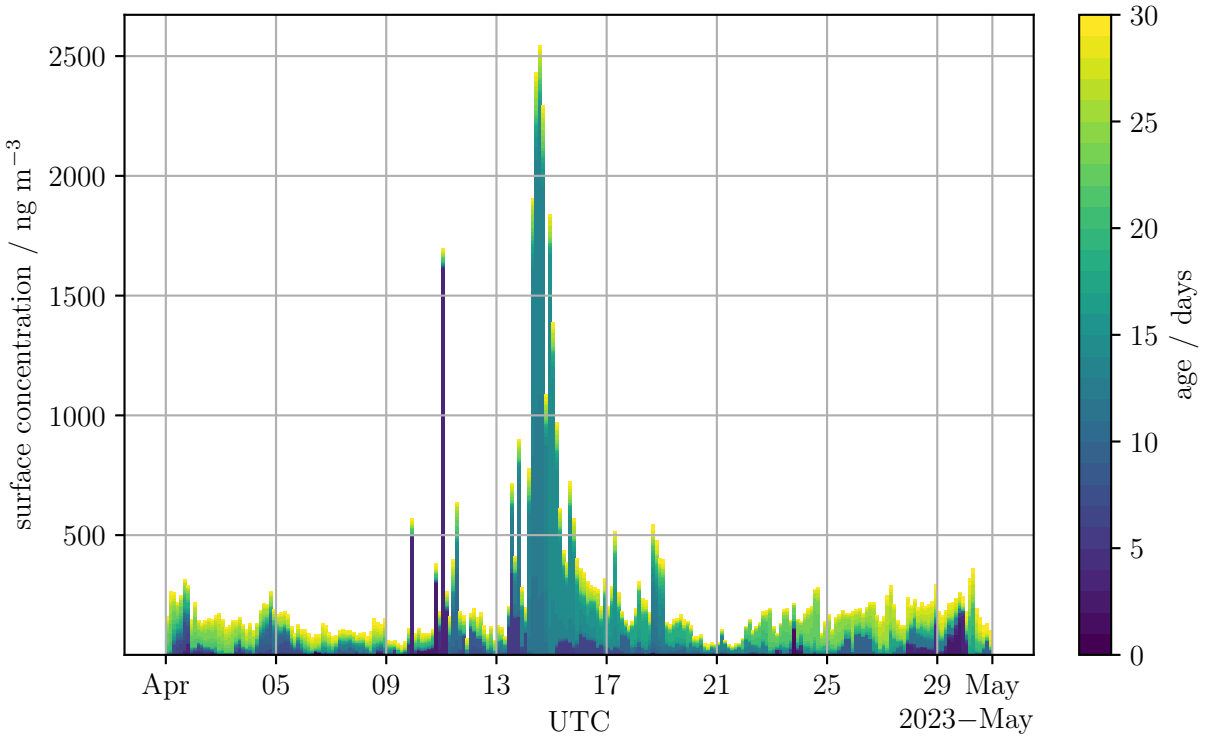

Figure 3.17.: **Example of contribution to the mass concentration at the surface of different dust ages simulated by FLEXPART.** The mineral dust of size 0.71 µm arriving at the receptor at an altitude of 500 m asl. The data is color-coded with the average age of the mineral dust.

3.4.3. FLEXDUST

FLEXPART simulates the movement of aerosol particles, but the emission of the aerosol particles needs to be modelled. FLEXDUST is a dust emission module, that was developed and tested for dust emission and transport in the western Sahara (Sodemann et al. 2015). It was further improved by Groot Zwaaftink et al. (2016) to improve the mineral dust mobilization scheme. A special focus was given to high-latitude dust sources, for example Iceland, where land cover data was used together with topographic effects (Arnalds 2010; Arnalds et al. 2016; Groot Zwaaftink et al. 2016; Groot Zwaaftink et al. 2017; Wittmann et al. 2017). Sediments are proportionally more likely to gather in depressions according to Ginoux et al. (2001) and Zender (2003), therefore they are considered more favourable to emit dust. To estimate the emission of mineral dust, the local elevation is taken into account by applying an erodibility scaling S (Ginoux et al. 2001; Groot Zwaaftink et al. 2016)

$$S = \left(\frac{z_{\max} - z_i}{z_{\max} - z_{\min}} \right)^5 \tag{3.46}$$

where: $z_{\max}$ – maximum elevation in a surrounding $10° \times 10°$ area (m),
$z_{\min}$ – minimum elevation in a surrounding $10° \times 10°$ area (m),
z_i – local elevation (m).

Due to this erodibility scaling some areas show up as stronger mineral dust sources (e.g., Arabian Peninsula and Greenland). The erodible soil fraction taken into account for FLEXDUST is visualized in figure 3.18 by Groot Zwaaftink et al. (2016). Emission of this dust may happen via aerodynamic entrainment and ejection via impacting particles (Groot Zwaaftink et al. 2016). The threshold friction velocity upon which wind erosion occurs is defined as

$$u_t = \sqrt{A_n \left(\sigma_p g d_\mathrm{p} + \frac{\gamma}{\rho d_\mathrm{p}} \right)} \tag{3.47}$$

where: u_t – threshold friction velocity ($\mathrm{m\,s^{-1}}$),
A_n – empirical factor (0.0123, Shao and Lu 2000),
σ_p – particle to air density ratio,
g – acceleration due to gravity ($\mathrm{m\,s^{-2}}$),
d_p – particle diameter (m),
γ – empirical factor ($3 \times 10^{-4}\,\mathrm{kg\,s^{-2}}$, Shao and Lu 2000)),
ρ – air density ($\mathrm{kg\,m^{-3}}$).

For soil containing sand, it is assumed that particles of size 75 µm determine the threshold friction velocity, whereas when clay or silt is present, a particle of size 10 µm is used. Soil moisture is taken into account, leading to a reduction in the threshold friction velocity for wet condtions. Taking the threshold friction velocity at different conditions into account, the dust emission amount is estimated:

$$\frac{\mathrm{d}V_d}{\mathrm{d}\ln d_\mathrm{p}} = \frac{d_\mathrm{p}}{c_\mathrm{V}} \left[1 + \mathrm{erf} \left(\frac{\ln d_\mathrm{p} - \ln \overline{d}_\mathrm{s}}{\sqrt{2} \ln \sigma_\mathrm{s}} \right) \right] \exp \left[- \left(\frac{d_\mathrm{p}}{\lambda} \right)^3 \right] \tag{3.48}$$

where: V_d – normalized volume of dust particels with size d_p (µm),
c_V – normalization constant (12.62 µm),
$\overline{d}_\mathrm{s}$ – median of volume size distribution (µm)
σ_s – geometric standard deviation (3.0),
λ – propagation distance (12 µm).

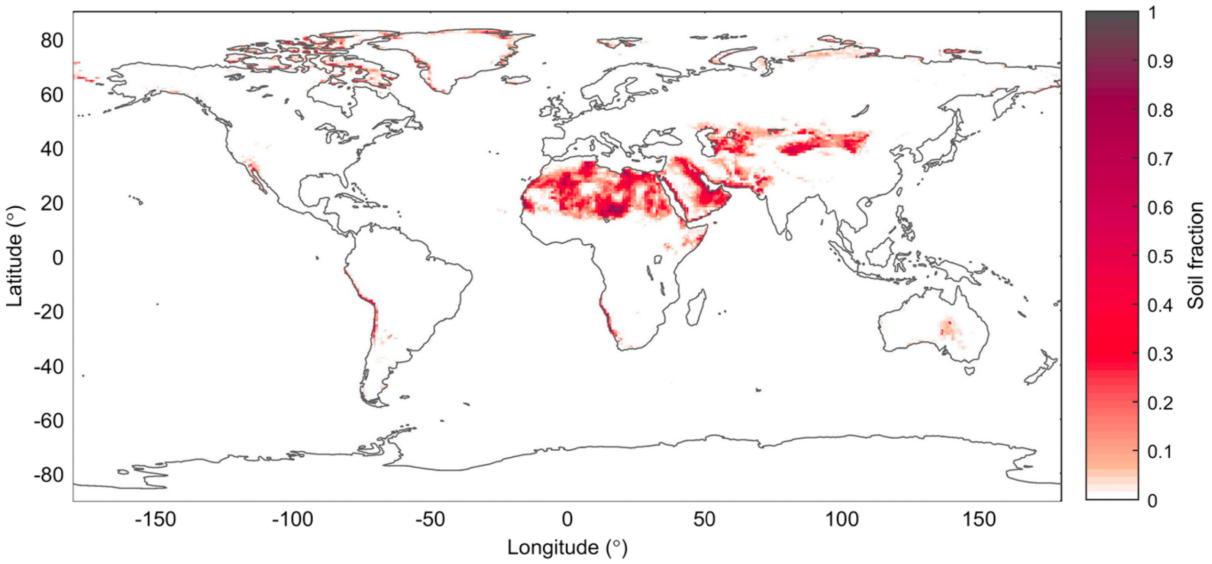

Figure 3.18.: **Erodible soil fraction used by FLEXDUST.** The fraction is scaled by the elevation according to (3.46). Figure taken from Groot Zwaaftink et al. (2016).

This assumes a volume size distribution between 0.2 µm and 18.2 µm (Groot Zwaaftink et al. 2016; Kok 2011). More detailed explanations on the mobilization and transport of mineral dust implemented in FLEXDUST is described in Groot Zwaaftink et al. (2016, section 2.1 therein).

3.5. Measurement sites and campaigns

This section describes the different measurement sites of the campaigns performed during this work. The locations are shown in figure 3.19. Both locations are in the Arctic, although Sammaltunturi station is located on the northern edge of the boreal forest.

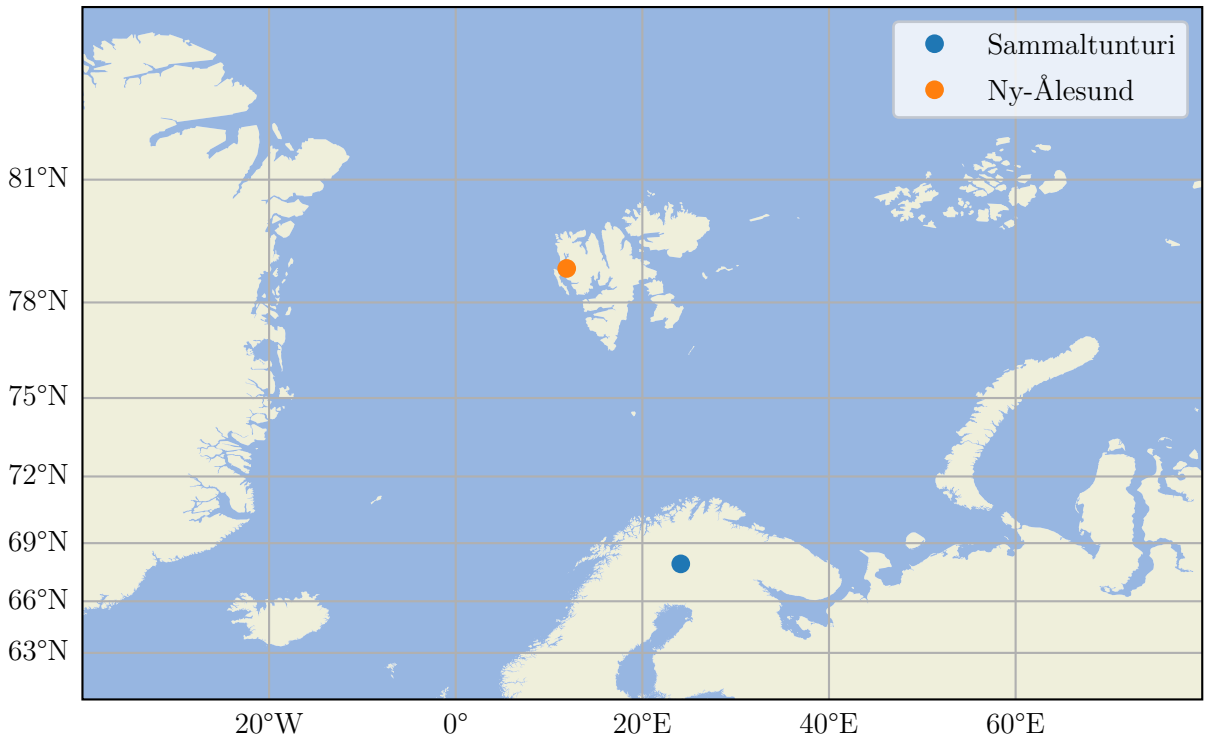

Figure 3.19.: **Map of the campaign locations.** Made with Natural Earth. Free vector and raster map data @ naturalearthdata.com.

3.5.1. Sammaltunturi station

Sammaltunturi is a measurement station at Pallas in northern Finland around 170 km north of the Arctic Circle inside the Pallas-Yllästunturi National Park (Lohila et al. 2015). Pallas is located in Lappland at the edge of the northern-boreal and subarctic climatic zones according to the Köppen climate classification (Hatakka et al. 2003; Köppen 2011; Lohila et al. 2015). Due its location north of the Arctic Circle, Pallas features around three and a half weeks of polar day in summer, and seven weeks of polar night in winter. Snow is present for more than 200 days per year, typically setting in during October and starting to melt in late May (Hatakka et al. 2003).

Since 1994, air quality measurements at Pallas have been part of the Global Atmosphere Watch (GAW) programme of the World Meteorological Organisation (WMO). The Sammaltunturi station is located at the top of a barren hill at 565 m asl (67°58′24″ N, 24°6′58″ E). Figure 3.20 shows the location of Pallas in northern Finland (lower right) as well as the location of Sammaltunturi in the surrounding region (left). The hill is extending 100 m past the tree line, continuing to rise due to climate change (Hatakka et al. 2003; Sutinen et al. 2012). Trees are mostly of the conifer species (Norway spruce, Scots pine, Lohila et al. 2015; Sutinen et al. 2010). The surrounding hill is mostly covered with low vascular plants, mosses and lichen (Lohila et al. 2015). Lichen are known to be effective INPs to high subzero temperature (e.g., Kieft 1988). The surrounding area is hilly between 250 to 400 m asl and covered in forest, swamps and lakes at around 250 m asl. The southern and western directions are open (180 to 330°) as well as the south eastern direction (100 to 130°). Anthropogenic influences are generally minimal, representing 'background conditions' in Europe (Lohila et al. 2015).

The Sammaltunturi station is sometimes within cloud cover, a maximum is reached during

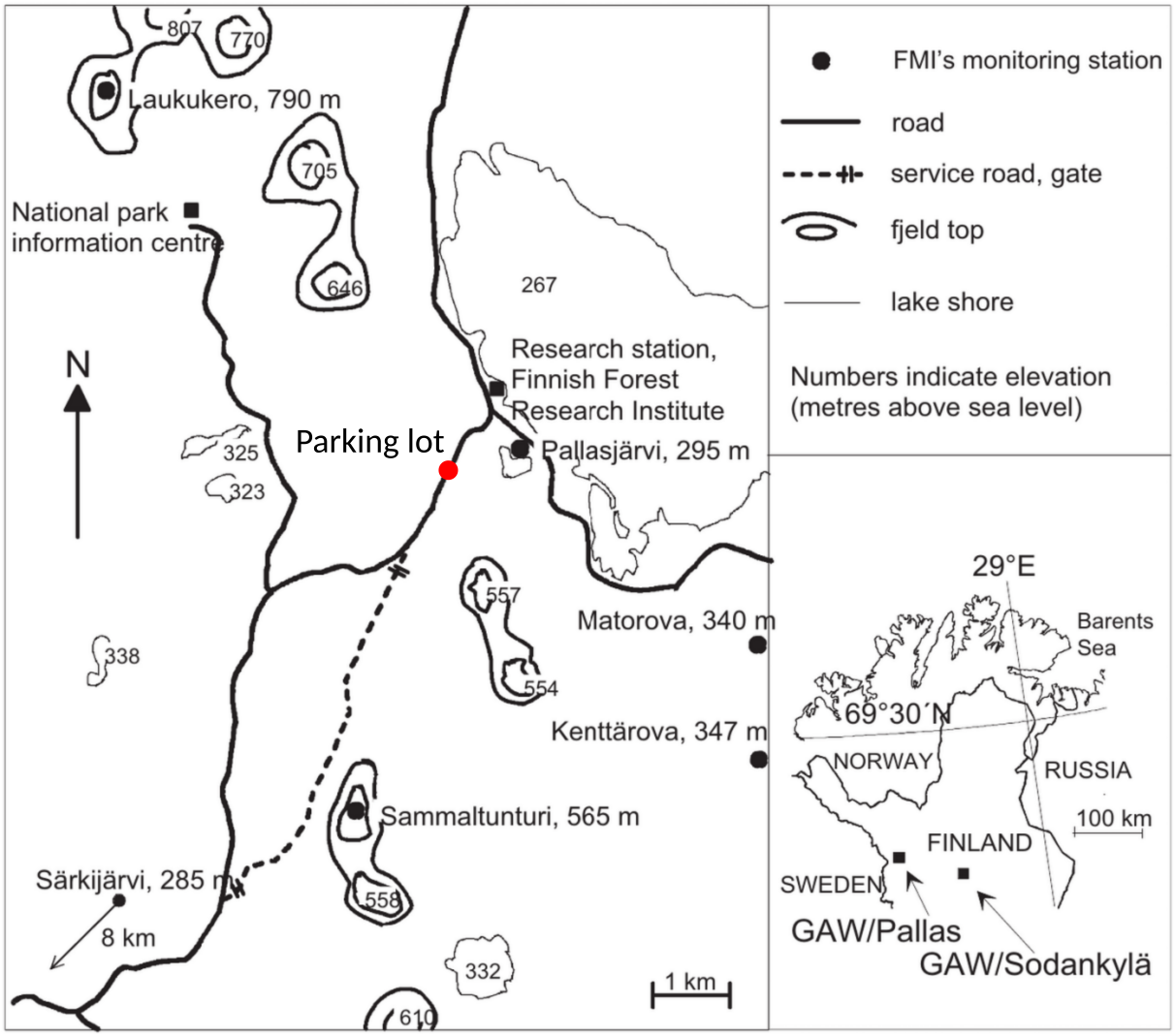

Figure 3.20.: **Location of Pallas (lower right) and Sammaltunturi (left).** The red dot marks the location of the parking lot used for some UAV operation during PaCE 2022 (see also section 3.5.1.1). Figure adapted from Hatakka et al. (2003).

autumn, where the visibility is less than 1 km at around 40 % of the time (Hatakka et al. 2003). This, together with a relative humidity around 100 % indicates that the station is inside a cloud (e.g., Doulgeris et al. 2020, 2022, 2023). Aerosol measurements of the total particle concentration started in 1996 at Sammaltunturi station. Additional continuous measurements of the particle number size distribution and other aerosol properties were added in the 2010s (Lohila et al. 2015). The predominant air mass arriving at Sammaltunturi is from the Arctic (Asmi et al. 2011). Since 2004, PaCE campaigns have been organized during autumn at Pallas to study aerosol-cloud-interactions (Anttila et al. 2012, 2009; Asmi et al. 2011; Doulgeris et al. 2020, 2023; Filioglou et al. 2017; Gérard et al. 2019; Kivekäs et al. 2009; Komppula et al. 2005; Lihavainen et al. 2008, 2010). The latest PaCE campaign happened during autumn 2022 and is described in the following section. A special issue at Earth System Science Data (ESSD) describes 'Data generated during the PaCE 2022 campaign'.

3.5.1.1. PaCE 2022 campaign

The PaCE 2022 campaign was conducted at Pallas between 15$^{\text{th}}$ September – 15$^{\text{th}}$ December 2022 with the first month featuring intensive observations of various research groups. The campaign was hosted by the Finnish Meteorological Institute (FMI) and utilized multiple different approaches to collect datasets on atmospheric properties. Aerosol instrumentation was mostly installed at the heated total inlet at Sammaltunturi. Cloud *in situ* instrumentation was placed on the roof of the Sammaltunturi station. Remote sensing instrumentation was deployed at Kenttärova station (67°59′13.92″ N, 24°14′35.13″ E, 347 m asl, see also figure 3.20). Surrounding the Sammaltunturi station, a temporary danger area (TEMPO D area Pallas), functioning as a reserved squared air space (14 km × 14 km) up to an altitude of 2 km agl allows the deployment of UAVs and balloon-borne systems with Sammaltunturi acting as a reference point for vertical measurements. A full list of deployed instrumentation is given in table 3.4

Table 3.4.: **List of instrumentation used during PaCE 2022.**

Institute	Platform/instrument	Location	Measured properties	Dates of operation
Finnish Meteorological Institute	TBS	Pallasjärvi	Aerosols, cloud droplets, meteorology	16^{th} September – 10^{th} October 2022
	UAV	Pallasjärvi, parking lot	PM and meteorology	20^{th} September – 12^{th} October 2022
	Surface-based *in situ* cloud measurements	Sammaltunturi	Cloud droplets	15^{th} September – 15^{th} December 2022
	Surface-based *in situ* aerosol measurements	Sammaltunturi	Aerosols	15^{th} September – 15^{th} December 2022
	Remote sensing	Kenttärova	Cloud boundaries and microphysics, wind, turbulence	15^{th} September – 15^{th} December 2022
Max Planck Institute for Dynamics and Self-Organization	Helikite/MPCK^{+}	Pallasjärvi	Cloud microphysics, meteorology, turbulence	12^{th} – 29^{th} September 2022
	Helikite/WinDarts	Pallasjärvi	Turbulence, meteorology	12^{th} – 29^{th} September 2022
École Polytechnique Fédérale de Lausanne	Helikite	Matorova	Aerosols, cloud droplets, meteorology	24^{th} September – 16^{th} October 2022
University of Hertfordshire	UAV	parking lot	Aerosols, cloud droplets, meteorology	20^{th} September – 12^{th} October 2022
Karlsruhe Institute of Technology	UAV	parking lot	INP, PM, meteorology	20^{th} September – 12^{th} October 2022
	PINE	Sammaltunturi	INP	15^{th} September – 15^{th} December 2022
Vienna University of Technology	WIBS	Sammaltunturi	Fluorescent aerosol particles	17^{th} September – 13^{th} December 2022

The focus of this work is on the INP concentration data collected by the UAV and PINE. The development of the UAV setup is detailed in section 3.2.1. The description of the PINE is given in section 3.2.2. The data obtained by the UAV setup and PINE is explained in detail in Böhmländer et al. (2025a,b). These and other datasets are available in a special issue titled 'Data generated during the Pallas Cloud Experiment 2022 campaign' at ESSD and at a dedicated community[15] via the Zenodo Open Science data archive 'Pallas Cloud Experiment - PaCE2022'.

3.5.1.1.1. UAV operation during PaCE 2022 The UAV setup was used in conjunction with a ground setup at the parking lot between 20th September – 12th October 2022 (see figure 3.20 and table 3.4). The dataset obtained with the UAV setup contains 14 freezing spectra that feature a temporal overlap between the ground and the UAV. One additional freezing spectra from the UAV and the ground setup are available, but without temporal overlap. The datasets are provided as netCDF files following the Climate and Forecast (CF)-1.11 metadata conventions.[16] Three types of datasets are provided, split into the respective sampling conditions: (1) aerosol washed of a filter loaded on board of the UAV, denoted as Skw, (2) identical data obtained via the ground setup, denoted as SkwGN, and (3) aerosol washed of a filter that was not subjected to an active air flow (handling blank), denoted as BLANK. The third dataset is special in that it only contains data on the frozen fraction as a function of the freezing temperature, since it cannot be normalized to an actual volume of air sampled. In total, two handling blanks were collected during the campaign, but the data of one of the experiments was corrupted and could not be repeated. For the specific data analysis and quality assessment for aerosol suspension analysed via INSEKT see section 3.2.1.4.

3.5.1.1.2. PINE operation during PaCE 2022 The PINE was operated during the full duration of PaCE 2022: 15th September – 15th December 2022 at the Sammaltunturi station (see figure 3.20 and table 3.4). The PINE was connected to the heated total inlet at Sammaltunturi (Asmi et al. 2021; Hatakka et al. 2003) and measured on the same sampling line as other instrumentation, such as the WIBS and the cloud condensation nuclei counter (CCNC). The PINE was operated on temperature ramps between 240 K and 252 K at a temporal resolution of approximately 6 min. Regular background checks are performed to ensure a high quality of the measurements during operation. The data is provided as daily netCDF files following the CF-1.11 metadata conventions.[17] For the specifc data analysis and quality assessment analysed via the PIA and the SaQC software see section 3.2.2.3.

3.5.1.1.3. Aerosol measurements during PaCE 2022 Two instrument were utilized during the PaCE 2022 to measure the aerosol size distribution *in situ*. The APS (APS 3321, TSI Inc.) was connected to the same total inlet as PINE and measured the size distribution between $d_{ad} = 487$ to 20 000 nm at a temporal resolution of one minute. The SMPS (self-made DMA with CPC 3010, TSI Inc.) was connected to the interstitial inlet and measured the size distribution between $d_{em} = 10$ to 800 nm at a temporal resolution of around six minutes. Additionally, a CPC (CPC 3772, TSI Inc.) measured the total particle concentration at the interstitial inlet at a temporal resolution of 1 Hz, the data is provided with a resolution of around five minutes. Next to the PINE, a CCNC (CCNC 100, Droplet Measurement Technologies LLC.) was connected to

[15] https://zenodo.org/communities/pace2022/, last access: 28th February 2025
[16] https://doi.org/10.5281/zenodo.13911633, last access: 11th October 2024
[17] https://doi.org/10.5281/zenodo.13889647, last access: 28th February 2025

the total inlet and measured the CCN concentration at a temporal resolution of one minute for six supersaturations: 0.1 %, 0.2 %, 0.3 %, 0.6 %, 0.9 % and 1.0 %.

3.5.2. GVB

GVB is located in the high Arctic on the Svalbard archipelago, approximately 1200 km south of the North Pole (78°55′3.65″ N, 11°53′39.44″ E, 67 m asl, Lupi et al. (2016)). The station is located on the south of a west-east oriented fjord (Kongsfjord), approximately 1 km south of Ny-Ålesund (Amore et al. 2022). Ny-Ålesund is an international centre for Arctic research activities with collaboration of more than 20 research institutions. Four different flagships organize the broad research objectives of Ny-Ålesund: Atmosphere, glaciology, Kongsfjorden system, and terrestrial ecosystems. The Kongsfjord is shown in figure 3.21 as an aerial image taken during summer, visualizing the multiple glaciers, which introduce sediment into the fjord. The northern location leads to polar night between 24$^{\text{th}}$ October – 18$^{\text{th}}$ February, and to polar day between 18$^{\text{th}}$ April – 24$^{\text{th}}$ August (Maturilli et al. 2013).

The ground is snow-covered between October and May, with melting season starting in May/June (Maturilli et al. 2013). While snow is possible during summer, and rain events have occurred in winter with a recent increase in frequency due to climate change, the mean temperature at 2 m agl is lowest in February (−11.7 °C) and highest in July (5.8 °C) between 1$^{\text{st}}$ August 1993 – 31$^{\text{st}}$ June 2011 (Maturilli et al. 2013). The Arctic air is characteristically dry with an average H_2O mixing ratio during the summer maximum (July and August) of $(4.6 \pm 0.3)\,\mathrm{g\,kg^{-1}}$ and $(1.4 \pm 0.4)\,\mathrm{g\,kg^{-1}}$ during the winter months (December, January, and February, Maturilli et al. 2013).

The local orography leads to a prominent feature in the wind measurements. The main wind direction from east/south-east (110°) is present throughout the year, albeit with an increase in wind speed during winter. Wind speeds larger than $10\,\mathrm{m\,s^{-1}}$ are almost exclusively from east/south-east (Maturilli et al. 2013), channeled through the fjord, but also affected by katabatic flow from the Kongsvegen glacier (see figure 3.21, Beine et al. (2001)). Wind from south-west (225°) occurs with the second highest frequency with typically lower wind speeds $< 5\,\mathrm{m\,s^{-1}}$ (Maturilli et al. 2013).

During the period 1$^{\text{st}}$ August 1993 – 31$^{\text{st}}$ June 2011, the surface air temperature and the H_2O mixing ratio have steadily increased with a rate of $(1.4 \pm 0.9)\,\mathrm{K}$ per decade and $(0.2 \pm 0.1)\,\mathrm{g\,kg^{-1}}$ per decade, respecti(Maturilli et al. 2013). This is inline with other observations in the Arctic, showing that the Arctic is warming up to 4 times as fast as the rest of the globe (Rantanen et al. 2022). The mild temperatures for the high latitude are due to the West Spitsbergen Current (WSC), branching off of the Norwegian Atlantic Current (NAC), and transporting warm and salty water into the Arctic Ocean ($20 \times 10^6\,\mathrm{m^3\,s^{-1}}$ during the maximum in February, $5 \times 10^6\,\mathrm{m^3\,s^{-1}}$ during the minimum in August, Fahrbach et al. (2001)). Due to this, the western part of Svalbard remains relatively sea ice free during the whole year. The different currents affecting Svalbard are visualized in figure 3.22. Sea-ice data inside the Kongsfjorden is available from the long-term monitoring of the NPI (Gerland et al. 2020). Kongsfjorden being one of Svalbards fjord is subject to increasingly fast changes, leading to changing dynamics of the marine ecosystem, including the protist and zooplankton communities (Bischof et al. 2019). Algae spring bloom occurs typically between mid of April until mid of May (Hodal et al. 2011), late summer phytoplankton blooms have been linked to the mobilization of sediment-rich glacial meltwaters (Caroppo et al. 2017). Phytoplankton blooms in the Arctic have been connected to increases in ice nucleation ability of coarse mode aerosol samples at high subzero temperatures (−5 °C Creamean et al. 2019) as well as an increase of the mean ice-nucleating temperature of primary aerosol from $(-28 \pm 2)\,^{\circ}\mathrm{C}$

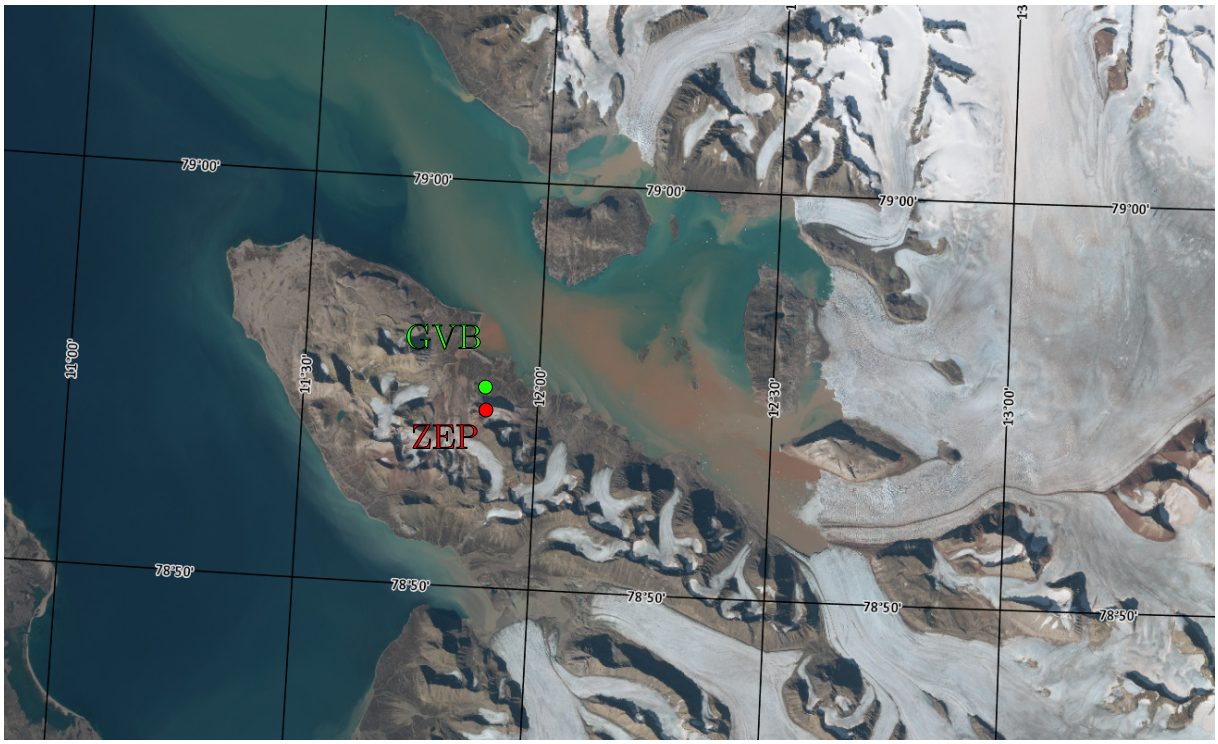

Figure 3.21.: **Location of Ny-Ålesund with the two measurement locations GVB and ZEP marked in red and green, respectively.** Map generated from TopoSvalbard (NPI).

to $(-24.5 \pm 0.9)\,°C$ (Wilbourn et al. 2020). It has been shown that algae are able to nucleate ice at relatively high subzero temperatures, with the snow algae *Chlamydomonas nivalis* being active as an INP at around $-6\,°C$, albeit with the important distinction, that the ice nucleation might be connected to ice nucleating bacteria and not to the algae itself (Kvíderová et al. 2013). Airborne and aquatic microalgae show ice nucleation at temperatures up to $-6\,°C$, albeit the majority are active at temperatures below $-12\,°C$ (Tesson and Šantl-Temkiv 2018).

Continuous permafrost exists at the unglaciated coastal aready down to about 100 m depth with an active layer extending to 1 to 2 m at the end of summer (Humlum 2005). The ground around the Bayelva site (see figure 3.21) consists of silty clay to sandy silt with a low stone content (Boike et al. 2008) and an average dry bulk density between 1.5 to $2.2\,g\,cm^{-3}$ (Boike et al. 2018). The vegetation cover is around 50 to 60 % (Boike et al. 2018) consisting of low vascular plants, moss and lichen (Lloyd et al. 2001; Ohtsuka et al. 2006; Uchida et al. 2006). The temperature of the active layer has been increasing at $(0.18 \pm 0.07)\,K\,yr^{-1}$ between 2009 and 2017, mimicking the increase in surface air temperature (Boike et al. 2018). Glacial outwash sediments in Svalbard show high ice nucleating efficiency below around $-15\,°C$, indicating that they might be important sources for high latitude dust (Tobo et al. 2019), with similar results observed at glaciers in Yukon, Canada (Xi et al. 2022) and southern Alaska (Barr et al. 2023). Further, Barr et al. (2023) showed that heat treatment on the samples lead to a general decrease in the freezing temperature between $-1.62\,°C$ and $-3.61\,°C$, indicating that there is a heat-sensitive biogenic component in the INP population present.

3.5.2.1. Examining ice-nucleating particles at Gruvebadet Atmosphere Laboratory (ExINP_GVB) 2023

In spring 2023, the ExINP_GVB 2023 campaign was conducted. The PINE was connected to the heated total inlet at GVB in collaboration with Dr. Naruki Hiranuma (West Texas A&M University (WTAMU)), whose team performed daily filter collection for subsequent analysis with West Texas Cryogenic Refrigerator Applied to Freezing Test system (WT-CRAFT), a cold stage type experiment to assess the ice nucleation ability of aerosol samples (Hiranuma et al. 2019; Vepuri et al. 2021). The suspensions originating from the filters were subjected to a heat treatment (95 °C for 20 min) to assess the contribution of heat-sensitive material to the total INP population (e.g., Barr et al. 2023; Christner et al. 2008; Daily et al. 2022; Hara et al. 2016). A total of 30 filters were collected between 13th March – 15th April 2023 (see also table C.1). PINE performed temperature scans between 240 K and 254 K between 15th March – 10th April 2023. Due to very low ambient relative humidity conditions with a dew point temperature of 250 K during the first half of the campaign, temperature scans only extended up to around 250 K.

At the same inlet, an APS (APS 3321, TSI Inc.) and SMPS (SMPS 3034, TSI Inc.) were operated with a 5 min resolution, the resulting data is given as 10 min means. After 29th March 2023 1.10 pm GMT, the SMPS did not collect data due to technical issues. The size distribution from APS and SMPS are merged using the algorithm described in section C.1.

3.5.2.2. ExINP_GVB 2024

During spring 2024, the PINE was connected again to the heated total inlet at GVB alongside the filter sampler in collaboration with Dr. Naruki Hiranuma (WTAMU). A total of 51 filters were taken between 3rd March – 15th June 2024. All filters were analysed with WT-CRAFT and subjected to heat treatment (see also table C.1 and Barr et al. 2023; Christner et al. 2008; Daily et al. 2022; Hara et al. 2016; Hiranuma et al. 2019; Vepuri et al. 2021). The PINE performed temperature scans between 238 K and 255 K between 2nd April – 5th June 2024. Due to technical issues with the OPC, some missing data is prevalent in the first part, which has been flagged accordingly (see also section 3.2.2.3).

The same aerosol measurements were conducted as described in section 3.5.2.1 and the data was merged according to the algorithm described in section C.1.

3.5.3. ZEP

ZEP is located on top of Zeppelin mountain to the south of Ny-Ålesund at an altitude of 472 m asl (e.g., Platt et al. 2022). Horizontal distance between GVB and ZEP is roughly 1.2 km. Atmospheric measurements started in 1989 with the Norwegian monitoring programme for GAW focusing on inorganic ions and CO_2 (Platt et al. 2022). Aerosol optical properties are continuously monitored within the ACTRIS framework since 2008 at ZEP. The station is owned by NPI, whereas all three partners (NPI, NILU, and Stockholm University (SU)) are responsible for the operation (Platt et al. 2022). While the general features are the same as for GVB, but differences due to the location and the altitude are detailed in the following. The wind field is similar to GVB and Ny-Ålesund and strongly influenced by the local orography and katabatic winds, due to frequent temperature inversions below 500 m agl, effectively shiedling ZEP from potential influence from Ny-Ålesund (Dekhtyareva et al. 2018). Some local anthropogenic

influence originated from cruise ship exhausts (Dekhtyareva et al. 2018; Eckhardt et al. 2013), but since a ban on heavy fuel oil use close to Svalbard, ship traffic emissions have been reduced considerably since 2015 (Platt et al. 2022). The location of the station makes long-range transport to ZEP more dominant in comparison to local-scale transport (Platt et al. 2022). Simulations via FLEXPART provide the footprint emission sensitivity for a BC tracer, indicating that during summer (June, July, and August) the emission sensitivity is largely restricted to ocean areas. This is in accordance with a polar dome, i.e. the transport happens mostly between regions with similar potential temperatures (Iversen and Joranger 1985; Stohl 2006). This changes during the winter and early spring (December, January, February, and March), where AH originating in northern Europe and Siberia increases anthropogenic pollution (Eleftheriadis et al. 2009; Platt et al. 2022). For a detailed assessment of the seasonal variation of source areas see also Tunved et al. (2013).

The general aerosol concentration at ZEP is very low between 50 to 200 cm^{-3} (Tunved et al. 2013). The bimodal size distribution has a peak in the Aitken mode ($d_\mathrm{p} < 60\,\mathrm{nm}$) and a second, more dominant accomodation mode peaking at around $d_\mathrm{p} = 150\,\mathrm{nm}$ (Tunved et al. 2013). A nucleation mode is visible during episodes of new particle formation, with a mode around 25 to 40 nm (Tunved et al. 2013). The increased presence of low-level clouds and accordingly a more effective wet removal during summer leads to a fast removal of AH particles (Garrett et al. 2011; Ström et al. 2003), resulting in shift of the aerosol size distribution from a dominant accumulation mode towards Aitken mode particles (<60 nm, Tunved et al. 2013). New particle formation increases to a peak in summer with an increase in photochemistry and biological activity (Engvall et al. 2008; Heintzenberg et al. 2015; Leaitch et al. 2013; Ström et al. 2009). The dominant accumulation mode is especially visible in the surface area concentration, which has a dominant peak during spring (March, and April) and minimum in autumn (August, September, and November, Tunved et al. 2013). This accumulation mode might act as a condensational sink to suppress new particle formation from precursor vapors (Lee et al. 2020).

Karlsson et al. (2021) studied cloud residuals using a ground-based counterflow virtual impactor (GCVI), which was switched on when the station was inside a cloud. This occured around 16 % between 2015–2018[18]. The station was considered to be inside a cloud when the visibility was below 1 km for at least 5 min (Karlsson et al. 2021). Cloud residuals are aerosol particles involved in cloud formation and cloud processes. They follow the general seasonal trend, with a peak in the number concentration during spring and summer and a decrease towards autumn and winter (Karlsson et al. 2021). Below updraught velocities of $1\,\mathrm{m\,s}^{-1}$ average activation diameters of 58 to 78 nm are observed decreasing with increasing updraught velocities (Karlsson et al. 2021). The median of the cloud residual number concentration is lower (26 cm^{-3}) compared to the median of the total particle concentration (55 cm^{-3}, Karlsson et al. 2021). Accumulation mode particles dominate the cloud residual size distribution between late spring and early autumn, with Aitken mode particles being able to activate as CCN and/or INP down to 20 to 30 nm during winter months (Karlsson et al. 2021).

3.5.3.1. Examining ice-nucleating particles at Zeppelin Observatory (ExINP_ZEP)

After its deployment at GVB during the ExINP_GVB 2023 campaign (see section 3.5.2.1), the PINE was transported to the nearby ZEP and connected to the SU part of the observatory. The

[18] Karlsson et al. (2021) mention that this does not align exactly with the annual cloud occurence due to an uneven amount of sampled months. In addition, due to just measuring at a single altitude, this value is much lower than the general occurence of clouds in the vertical column (61 % Shupe 2011; 81 % Nomokonova et al. 2019).

PINE is connected to the GCVI and a total suspended particulate (TSP) via a three-way valve (see also Karlsson et al. 2021, and section 3.5.3). The three-way valve is switched to the GCVI if the station is inside a cloud. The aerosol distribution measurements are connected to the same three-way valve, enabling the measurement of cloud residuals if a cloud is present at ZEP. The PINE was operated on temperature scans between 241 K and 250 K with regular background checks between 26$^{\text{th}}$ April 2023 – 21$^{\text{st}}$ April 2024.

At the same inlets, aerosol size distribution measurements were conducted by SU utilizing multiple SMPS and providing 30 min averages for a size distribution of aerosol particles of volume equivalent diameter 5 to 708 nm (see also Karlsson et al. 2021, and table 1 therein). The three SMPS consist of three different cylindrical DMAs to measure three different size ranges: 10 to 945 nm, 5 to 57 nm and 20 to 809 nm (Karlsson et al. 2021).

3.5.4. Ocean water and snow samples

Snow samples and ocean water samples were collected at Ny-Ålesund to assess the potential local influence to the atmospheric INP population. Surface snow samples were collected by AWIPEV[19], Consiglio Nazionale delle Ricerche (CNR), and NPI personell on 21$^{\text{st}}$ March 2023, 28$^{\text{th}}$ March 2023, 11$^{\text{th}}$ April 2023, and 2$^{\text{nd}}$ May 2023 at a snow pit close to GVB at the foot of the Zeppelin mountain. Ocean water samples were collected in the middle of the Kongsfjorden at Kingsbay 3 (Kb3) (see figure 3.22) by Dr. Clara Hoppe and her team three times per week between 29$^{\text{th}}$ March 2023 and 12$^{\text{th}}$ May 2023 from the surface and from 5 m depth. The collected ocean water and snow samples were stored and shipped at −20 °C until analysis with INSEKT and IR-CS (see section 3.2.1 and section 3.2.3). The ocean water samples were corrected according to the mean salinity of Kongsfjorden. Surface ocean water (0 to 2 m) has a mean salinity of 30.95 g kg^{-1} and for depths below 2 m the salinity increases to 33.97 g kg^{-1} (MacLachlan et al. 2007). Assuming an aqueous solution containing NaCl, this results in a molatility m of 0.53 mol kg^{-1} and 0.58 mol kg^{-1} for surface and deep water, respectively[20]. According to Lamas et al. (2022), the freezing point depression ΔT for NaCl can be calculated as a function of the molatility m

$$\Delta T = -v \cdot 1.998 \cdot m \left(\mathrm{K\,mol^{-1}\,kg}\right) - b \cdot m^{1.5} - c \cdot m^2 \ , \tag{3.49}$$

where: v – ions per mole of salt (2),
b – fitting parameter ($-1.639\,\mathrm{K(mol/kg)^{1.5}}$),
c – fitting parameter ($0.683\,\mathrm{K(mol/kg)^{2}}$).

This is true for homogeneous and heterogeneous nucleation (Zobrist et al. 2008). Potential INPs in the ocean water can enter the atmosphere via the production of SSA (e.g., DeMott et al. 2016; Russell et al. 2023).

Surface snow can enter the atmosphere during blowing snow episodes. Blowing snow is an important cause of snow cover redistribution and water loss via blowing snow sublimation (e.g., Li and Pomeroy 1997). In Antarctica, Gerber et al. (2023) modelled the influence of drifting and blowing snow and its sublimation to the surface mass balance and found an especially strong influence in regions of strong katabatic winds. Gong et al. (2023) observed the generation of fine-mode sea salt aerosol (< 300 nm) from the sublimation of blowing snow in the central Arctic. Model calculation shows a contribution from such particles of around 28 % to the total

[19] The joint research station of Alfred Wegener Institute Helmholtz Centre for Polar and Marine Research (AWI) and French Polar Institute Paul Emile Victor (IPEV) at Ny-Ålesund.
[20] Considerung a molar mass of 58.44 g mol^{-1} for NaCl.

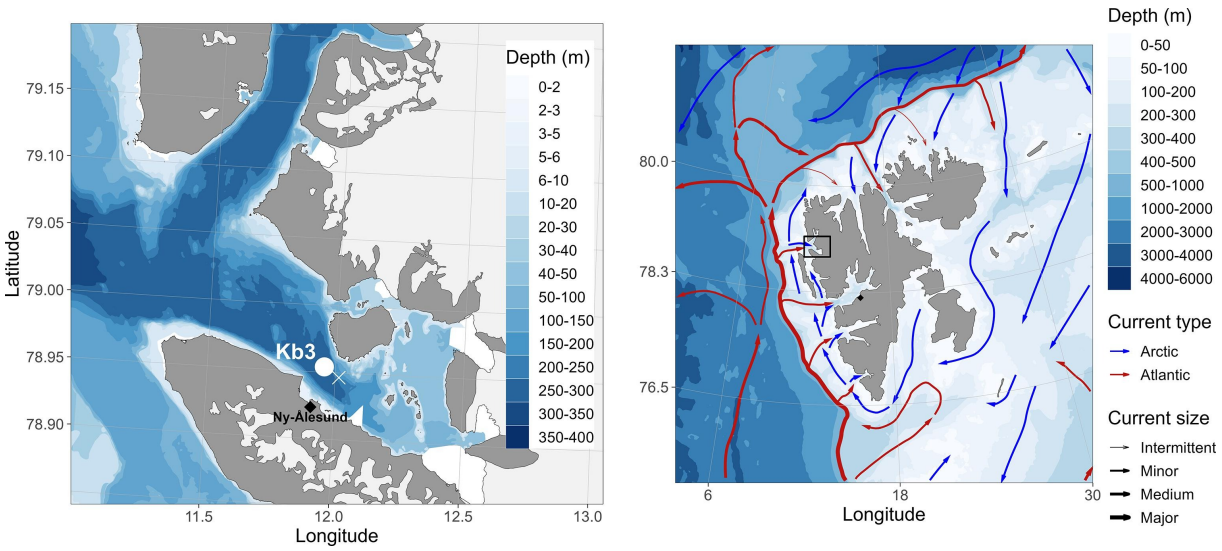

Figure 3.22.: **Water currents affecting the western part of Svalbard with the sampling location Kb3 marked on the left inside the Kongsfjord.** Figure taken from Assmy et al. (2023) with bathymetry data (Jakobsson et al. 2012) and land shapefiles (Vihtakari 2019) from the Norwegian Mapping Authority and Norwegian Polar Institute, respectively.

particle number, leading to an increased surface warming due to the contribution to CCN (Gong et al. 2023). Blowing snow events observed during spring at an Arctic coastal site showed an increase in the number concentration of smaller aerosol particles (factor of six for 10 to 60 nm) during blowing snow events, while the number concentration of larger particles decreased (82 % for 1 to 4 µm, Chen et al. 2022). To determine the occurence of blowing snow events, source functions using wind speed, snow age, and temperature are used (e.g., Li and Pomeroy 1997). The probability P_{bs} of the occurence of blowing snow with respect to wind speed follows a cumulative normal distribution (Li and Pomeroy 1997)

$$P_{\mathrm{bs}}(U) = \frac{1}{\sqrt{2\pi}\delta} \int_0^{U_{\max}} \exp\left(-\frac{(\overline{U}-U)^2}{2\delta^2}\right) \mathrm{d}U \ , \tag{3.50}$$

where: U – wind speed ($\mathrm{m\,s^{-1}}$),
$\overline{U}$ – mean wind speed ($\mathrm{m\,s^{-1}}$),
δ – standard deviation of the mean wind speed ($\mathrm{m\,s^{-1}}$),

A fit using experimental data of the Prairie Provinces of western Canada results in a function for the probability of blowing snow

$$P_{\mathrm{bs}} = -\frac{1}{2}\,\mathrm{erf}\left(\frac{\overline{U}-U}{\sqrt{2}\delta}\right) + \frac{1}{2} \ , \tag{3.51}$$

$$\overline{U} = (0.365T + 0.00706T^2 + 0.9\log_{10}(t_{\mathrm{snow}}) + 11.2)\,\mathrm{m\,s^{-1}} \ , \tag{3.52}$$

$$\delta = (0.145T + 0.00196T^2 + 4.3)\,\mathrm{m\,s^{-1}} \ , \tag{3.53}$$

where: erf – error function,
t_{snow} – snow age (h),
T – temperature (°C).

This is used to assess the likelihood of blowing snow conditions with corresponding changes in the INP population.

Chapter 4.

Results

This chapter described the results from the different campaign, focusing at first on correlation studies with the INP concentration in section 4.1. Afterwards, the INAS density is put into broader context utilizing existing INAS density parameterizations in section 4.2. Episodes, where the INAS density is lower or higher are identified and discussed in section 4.3. In section 4.4, the INAS density episodes are compared to FLEXPART simulations to identify a potential impact of the source and age of mineral dust. Finally, the contribution of local sources at Svalbard to the INP population and the UAV-based measurements during PaCE 2022 are discussed in section 4.5 and section 4.6, respectively.

4.1. INP concentration overview

4.1.1. PaCE 2022

For the PaCE 2022 campaign, one-hour averages of the INP concentration measured by PINE were calculated. The resulting dataset is correlated against atmospheric and aerosol parameters utilizing Spearman's rank correlation for the time period between 23$^{\text{rd}}$ September 2022 1 pm GMT and 13$^{\text{th}}$ December 2022 10 pm GMT. Figure 4.1 visualizes the timeseries of the INP concentration measured by PINE. The instrument mostly operated on a temperature between 245 K and 247 K, although during the first half of the campaign, a wider temperature range between 239 K and 251 K was investigated. To investigate possible connections between the measured INP concentration, Spearman's correlation coefficients between the INP concentrations and various other variables are visualized in figure 4.2 and further described below.

Ambient temperature T and relative humidity RH both show a positive correlation with the INP concentration, with the highest correlation ($r = 0.43$) seen for the INP concentration measured at 249 K and the ambient temperature T. A negative correlation is seen between the wind speed V and the INP concentration, which is only statistically significant ($p < 0.05$) at nucleation temperatures 241 K, 243 K and 247 K and decreasing in absolute value for higher nucleation temperatures.

These three atmospheric variables (T, RH, V) can indicate an influence of local aerosol sources, that contribute to the INP population at the measured nucleation temperatures. A positive correlation with the ambient temperature could be related to local emission of INP, that is dampened after snow fall. This was also seen in the boreal forest by Schneider et al. (2021). In addition, increased temperatures generally lead to an increased biogenic activity, which might

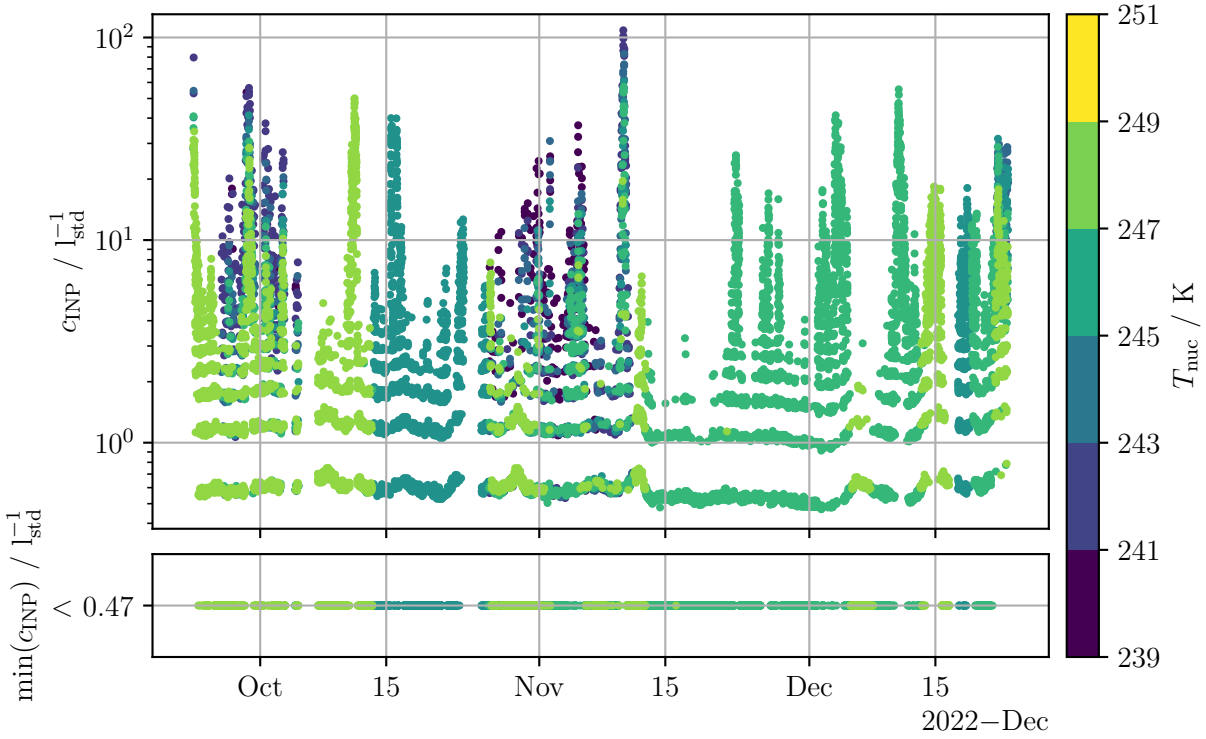

Figure 4.1.: **INP concentration measured by PINE during PaCE 2022.** The colorbar denotes the temperature at which the aerosol was activate as an INP. The lower panel visualizes all data where the INP concentration is below the threshold of PINE during PaCE 2022.

increase the emission of biogenic INPs. A negative correlation with wind speed could indicate, that the INP concentration, especially at 241 K with $r = -0.46$, is connected to a change in air mass. A local cyclone might bring an influx of relatively clean air from the Arctic and the Atlantic Ocean, therefore decreasing the INP concentration. Additional analysis and modelling is needed to gain a better insight.

The INP population is inherently linked to the aerosol population, since one is a subset of the other. According to the INAS density approach, larger aerosols of the same type are more effective INPs due to their increased surface area. To verify whether this can also be observed in INP population during PaCE 2022, the mean diameter of the number size distribution and the total number concentration are correlated with the INP concentration. The correlation coefficient is positive between the mean diameter of the number size distribution and the INP concentration, with a maximum correlation coefficient at 247 K with $r = 0.55$. This indicates that the INP concentration increases, when more larger aerosol particles are present. This effect becomes smaller for lower nucleation temperatures. The opposite behaviour can be seen for the correlation between the total number concentration and the INP concentration, where the correlation coefficient reaches a maximum at $r = 0.64$ for the measurements at 239 K. Together, this indicates that a larger fraction of aerosol particles may act as an INP at lower nucleation temperatures, and that larger particles contribute more to the INP concentration at higher nucleation temperatures. This is expected, when one uses the AS approach, where aerosol particles with a larger particle diameter provide a larger surface area. The pprobabiltiy of an AS that can faciliate primary ice nucleation at higher temperatures is increased. However, due to not all temperatures being equally measured during the whole campaign duration, this might be a seasonal change, which influence this correlation coefficient (see figure 4.1).

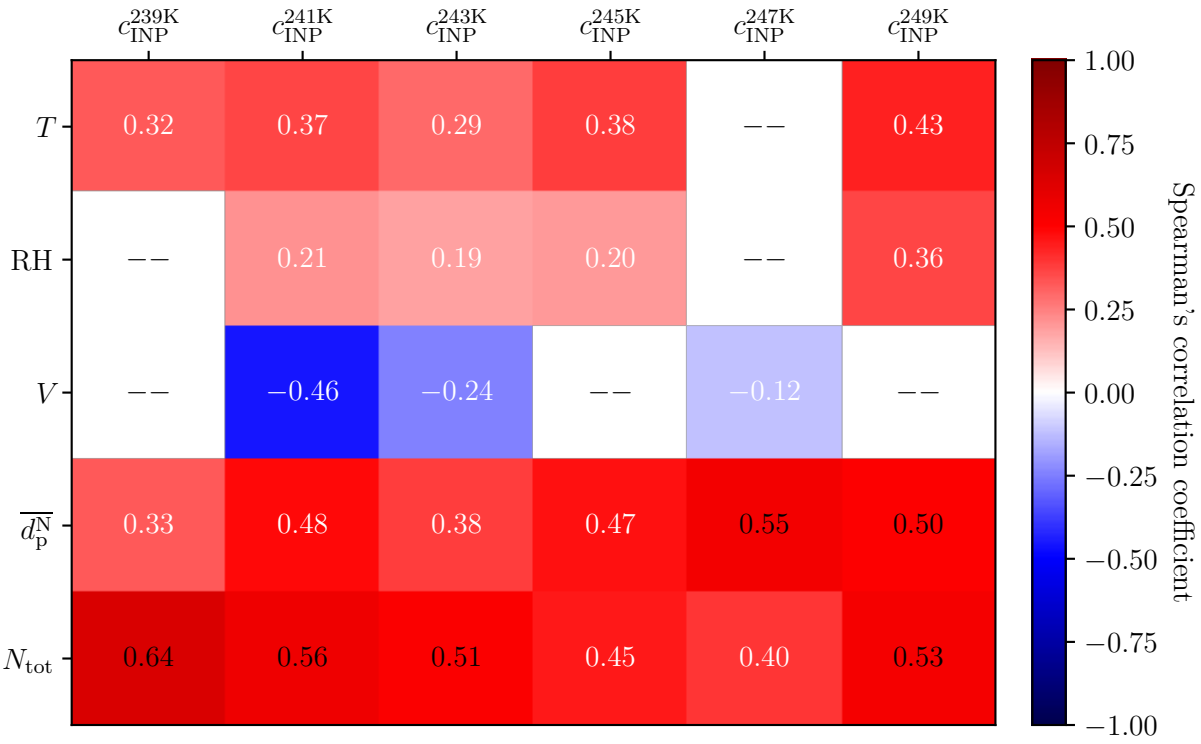

Figure 4.2.: **Correlation matrix between meteorological and aerosol data and the INP concentration measured during PaCE 2022.** The two-sided Spearman's rank correlation is calculated with data on a temporal resolution of 1 h. The correlation coefficient is not shown, when the p-value is above 0.05. The correlated variables are the ambient temperature T, relative humidity RH, wind speed V, mean diameter of the aerosol number size distribution $\overline{d_{\mathrm{p}}^{\mathrm{N}}}$ and the total number concentration N_{tot}.

4.1.2. ExINP_GVB 2023

The correlation coefficients between the INP concentration and other variables measured during the ExINP_GVB 2023 campaign between 15$^{\mathrm{th}}$ March 2023 11 am GMT and 10$^{\mathrm{th}}$ April 2023 7 am GMT are calculated in the same way as described in section 4.1.1. The INP concentration measured by PINE is visualized in figure 4.3 between nucleation temperatures between 239 K and 253 K. During the second half of the campaign, the ambient dew point temperature increased, allowing to measure at higher temperatures (>251 K). Spearman's correlation coefficients are visualized in figure 4.4.

The ambient temperature T and the relative humidity RH both show a negative correlation coefficient with the INP concentration. There is no significant difference between the correlation coefficients at different nucleation temperatures. The highest absolute value of the correlation coefficients between the INP concentration at a nucleation temperature of 247 K and the relative humidity is −0.4. This is opposite to the correlation coefficient seen during PaCE 2022, where the correlation was positive for both the ambient temperature and the relative humidity. This could indicate, that the local population of aerosol is not contributing largely to the INP population below 252 K. This can be expected due to the measurement time and location. During spring 2023, the area around GVB was covered in snow, with almost no biogenic activity.

The wind speed V correlates positively for lower nucleation temperatures, but has a negative

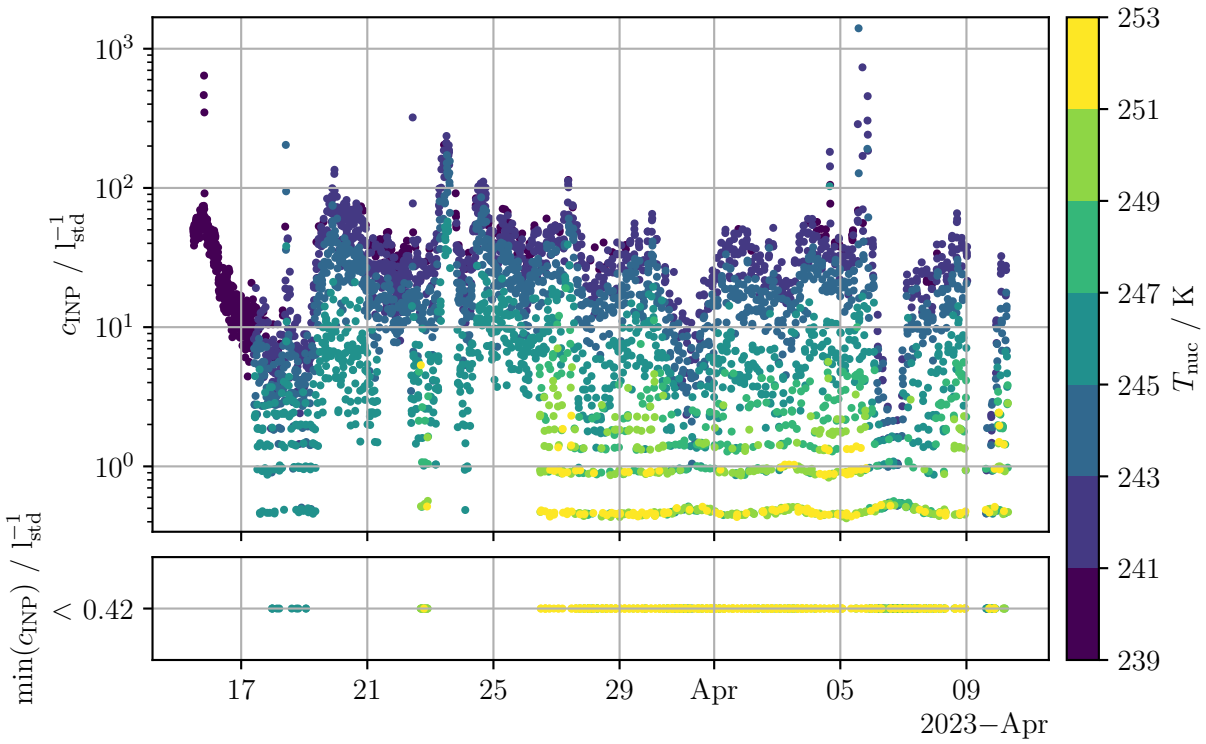

Figure 4.3.: **INP concentration measured by PINE during ExINP_GVB 2023.** The colorbar denotes the temperature at which the aerosol was activate as an INP. The lower panel visualizes all data where the INP concentration is below the threshold of PINE during ExINP_GVB 2023.

correlation of $r = -0.29$ at 249 K. This is the opposite observation as seen during PaCE 2022, where the correlation coefficient decreases for lower nucleation temperatures. This behaviour indicates, that the local influence is much less compared to PaCE 2022. A potential exchange of air masses, indicated by an increased wind speed, increases the INP concentration, especially at lower nucleation temperatures.

The total number of aerosol particles correlates positively with the INP concentration, showing an increasing trend towards lower nucleation temperatures up to a correlation coefficient of $r = 0.8$ at 241 K. This is a higher correlation coefficient compared to PaCE 2022, but follows the behaviour that a larger fraction of the total aerosol might be able to faciliate primary ice formation at lower temperatures. These could especially be smaller particle, which are larger in number and can be transported into the Arctic via long range transport. The correlation coefficient with a mean diameter of the number size distribution is not statistically significant, considering only p-values below 0.05. The lowest p-value larger than 0.05 is given with $p = 0.09$, where the correlation coefficient is $r = -0.12$, which is also opposite to PaCE 2022. This could indicate that smaller aerosol particles contribute more strongly to the INP population. However, this is not statistically significant, therefore a larger dataset is needed to provide a statistically robust conclusion.

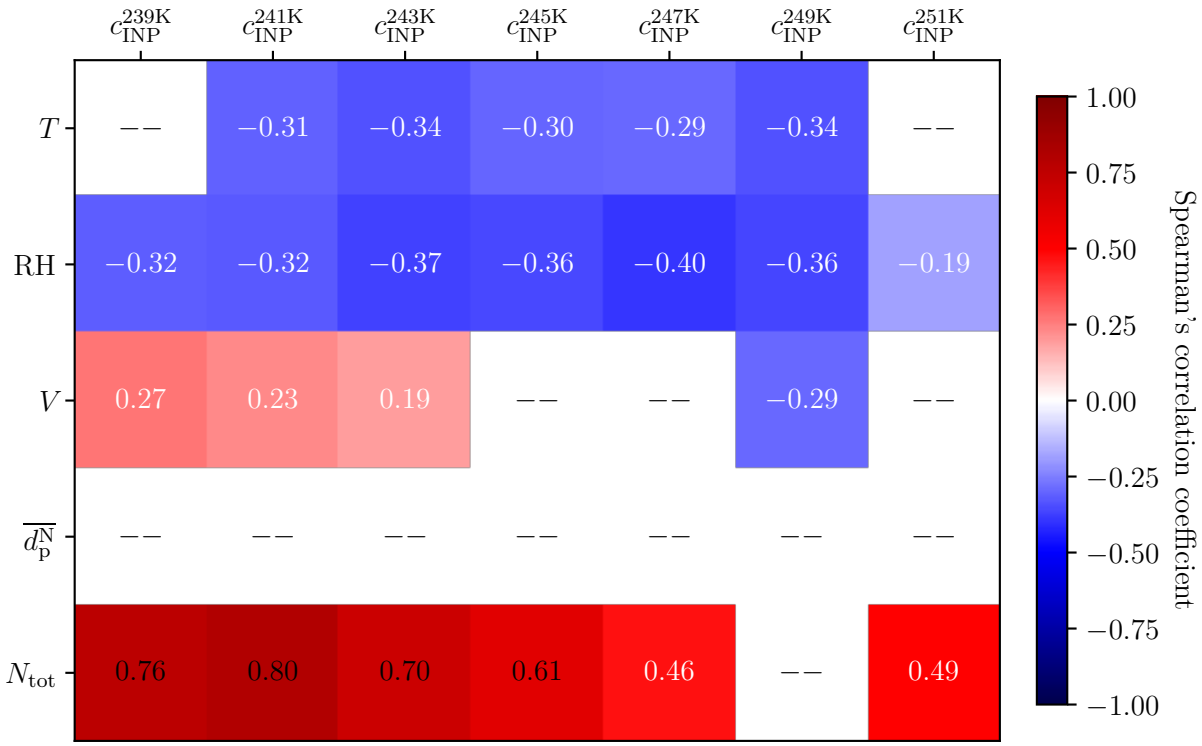

Figure 4.4.: **Correlation matrix between meteorological and aerosol data and the INP concentration measured during ExINP_GVB 2023.** The two-sided Spearman's rank correlation is calculated with data on a temporal resolution of 1 h. The correlation coefficient is not shown, when the p-value is above 0.05. The correlated variables are the ambient temperature T, relative humidity RH, wind speed V, mean diameter of the aerosol number size distribution $\overline{d_{\mathrm{p}}^{\mathrm{N}}}$ and the total number concentration N_{tot}.

4.1.3. ExINP_GVB 2024

The correlation coefficients between the INP concentration and other variables measured during the ExINP_GVB 2024 campaign between 2$^{\mathrm{nd}}$ April 2024 10 am GMT and 5$^{\mathrm{th}}$ June 2024 10 pm GMT are visualized in figure 4.5, with the nucleation temperature shown on the colorbar. This is the second campaign conducted at GVB after ExINP_GVB 2023 (see also section 4.1.2). During the first three weeks of the campaign, some technical difficulties lead to some data needing to be removed manually In the second half of the campaign, an increase in the ambient dew point temperature allowed measurements at higher temperatures (>254 K). This data was correlated as outlined in the preceding sections and Spearman's correlation coefficient is visualized in figure 4.4.

A similar behaviour as observed during the first ExINP_GVB in 2023 is seen for the ambient temperature T and relative humidity RH. The correlation coefficient increases towards higher nucleation temperatures up to $r = 0.55$ for the INP concentration measured at 254 K and the ambient temperature T. This positive correlation indicates that a higher ambient temperature influences the INP concentration especially at higher nucleation temperatures, since biogenic aerosol particles are more likely to nucleate ice. These biogenic aerosol particles can originate from local biogenic sources, which are more active at higher ambient temperatures. The later measurement period in the year, compared to ExINP_GVB 2023, leads to a generally higher mean temperature of −3.22 °C compared to −11.8 °C in 2023.

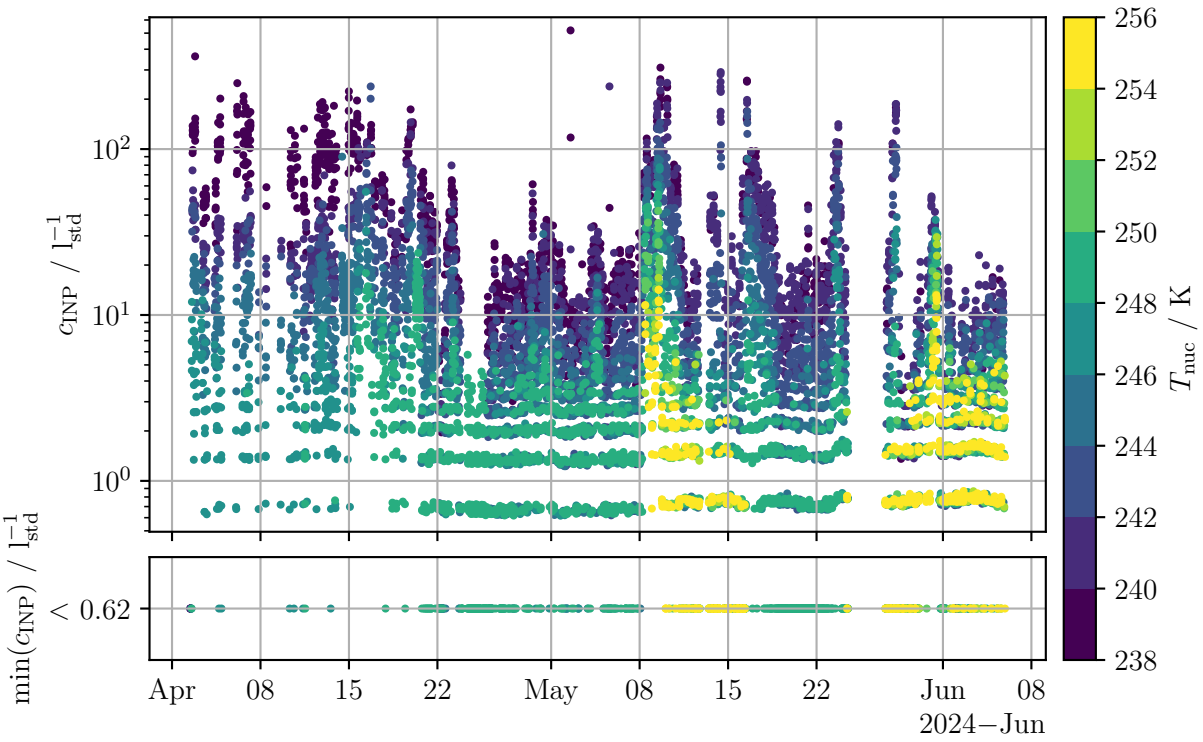

Figure 4.5.: **INP concentration measured by PINE during ExINP_GVB 2024.** The colorbar denotes the temperature at which the aerosol was activate as an INP. The lower panel visualizes all data where the INP concentration is below the threshold of PINE during ExINP_GVB 2024.

The wind speed V correlates positively as well, but does not show the same behaviour for different nucleation temperatures as during ExINP_GVB 2023. The INP population during ExINP_GVB 2024 might be more dominated by local sources compared to ExINP_GVB 2023. This can also be seen for the positive correlation for the mean diameter of the number size distribution and the total aerosol concentration. The correlation coefficient is $r = 0.44$ between the mean diameter and the INP concentration measured at 254 K. The positive correlation coefficient is smaller for the total number concentration. This could indicate that the INP population is dominated by local and larger aerosol particles, which are lower in number.

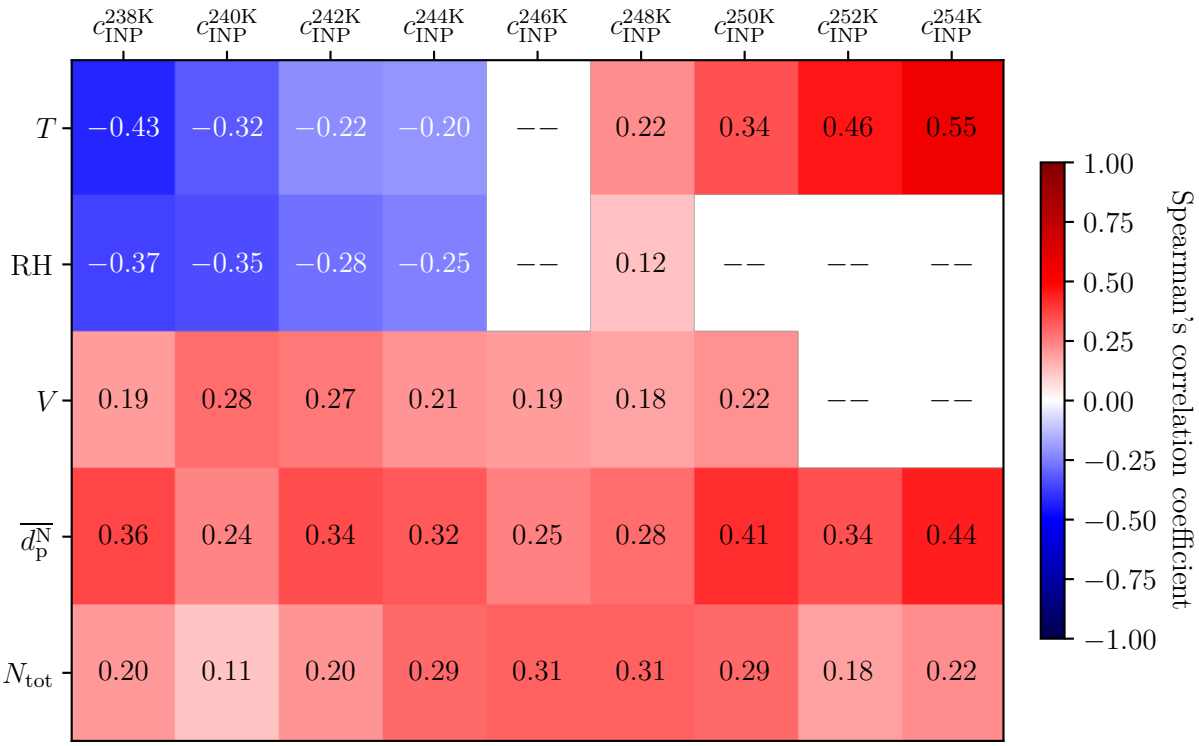

Figure 4.6.: **Correlation matrix between meteorological and aerosol data and the INP concentration measured during ExINP_GVB 2024.** The two-sided Spearman's rank correlation is calculated with data on a temporal resolution of 1 h. The correlation coefficient is not shown, when the p-value is above 0.05. The correlated variables are the ambient temperature T, relative humidity RH, wind speed V, mean diameter of the aerosol number size distribution $\overline{d_{\mathrm{p}}^{\mathrm{N}}}$ and the total number concentration N_{tot}.

4.1.4. ExINP_ZEP

An almost full-year dataset is measured during ExINP_ZEP between 25$^{\mathrm{th}}$ April 2023 midnight GMT and 8$^{\mathrm{th}}$ April 2024 9 am GMT. The measured INP concentration is visualized in figure 4.7. There is a short break during August 2023, which was related to a technical issue at the measurement site. The measurements mostly were done using temperature ramps between 239 K and 253 K. There is a slight seasonal change during autumn, which generally features the lowest INP concentrations. The highest are measured during Spring 2024. The Spearman's correlation coefficients between the INP concentration and other variables are calculated and visualized in figure 4.8.

The ambient temperature T and the relative humidity RH correlate negatively with INP concentrations measured below 248 K. This negative correlation follows the same behaviour as seen before for the campaigns at GVB and is opposite to the measurements during PaCE 2022. For higher nucleation temperatures, the correlation coefficient does not follow a clear trend with a maximum of $r = 0.54$ between the relative humidity and the INP concentration measured at 253 K.

The wind speed V shows a small negative correlation coefficient, but is not statistically significant for half of the nucleation temperatures. In general, this behaviour is similar to the one seen during the ExINP_GVB 2023 campaign, where the negative correlation coefficient with the ambient

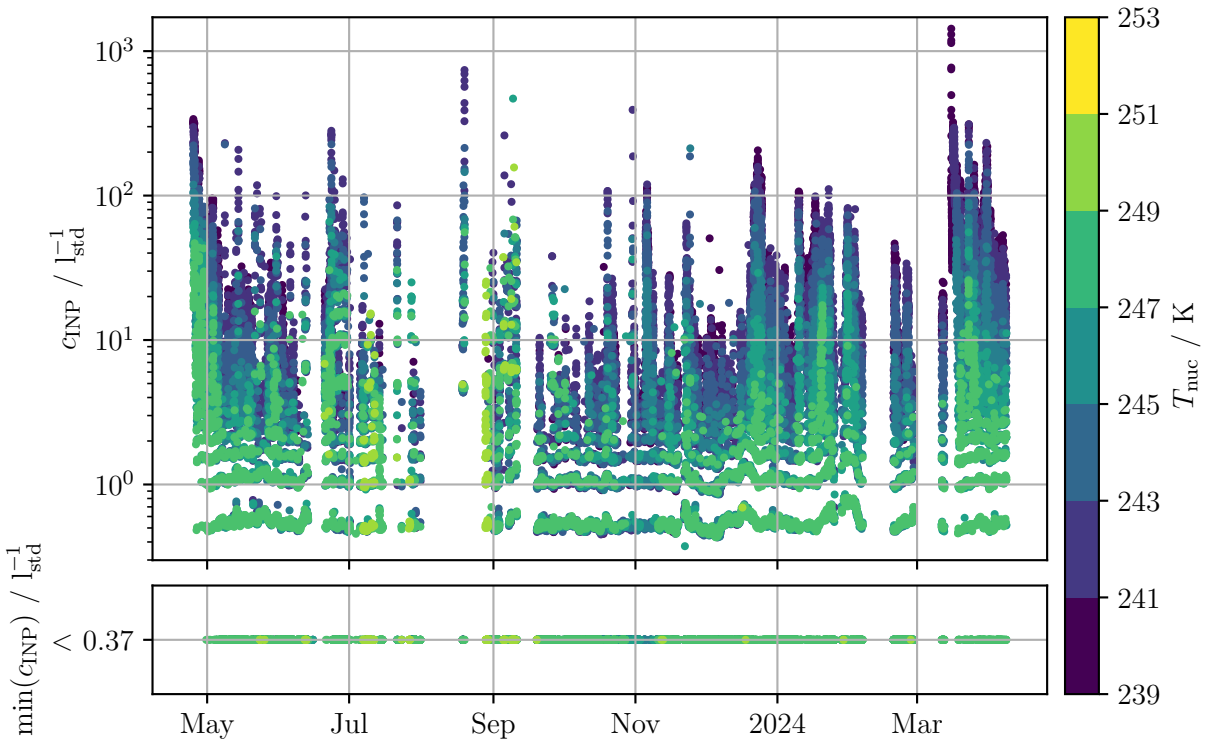

Figure 4.7.: **INP concentration measured by PINE during ExINP_ZEP.** The colorbar denotes the temperature at which the aerosol was activate as an INP. The lower panel visualizes all data where the INP concentration is below the threshold of PINE during ExINP_ZEP.

temperature and relative humidity indicates a stronger influence from long range transport. The small negative correlation coefficient for the wind speed is also seen during the PaCE 2022 campaign, which also lasted for a longer period compared to the two campaigns at GVB. Another similarity is the higher altitude: both measurement stations, ZEP and Sammaltunturi (PaCE 2022), are on top of a hill and therefore might be less influenced by local orography. The contribution of different aerosol sources to the local INP population is different, which is indicated by the correlation coefficients for the ambient temperature and the relative humidity.

The correlation coefficients with the aerosol parameters, namely the mean diameter of the number size distribution and the total number concentration, are positive. The correlation coefficient increases for lower nucleation temperatures up to $r = 0.36$ at 241 K for the mean diameter. There is an outlier seen at 253 K, where the correlation coefficient is increased again. While this is statistically significant, the number of data points is significantly less, with the rest of the data points having a mean of around 14 times as many data points as the data points at 253 K (see also figure 4.7). This is the same behaviour as seen for all campaigns, except ExINP_GVB 2023, where an increase in particle size also leads to an increase in INP concentration. An increase of the total aerosol concentration also increases the INP concentration, especially for lower nucleation temperatures, where a correlation coefficient of $r = 0.62$ is seen. This high correlation indicates, that ZEP is stronger influenced from long range transport compared to GVB, since smaller aerosol particles are larger in number and generally travel longer distances. Although, this might also be a seasonal effect, since the measurements at GVB were only conducted during Spring and early Summer.

During the whole duration of ExINP_ZEP, a CCNC measured at different supersaturations

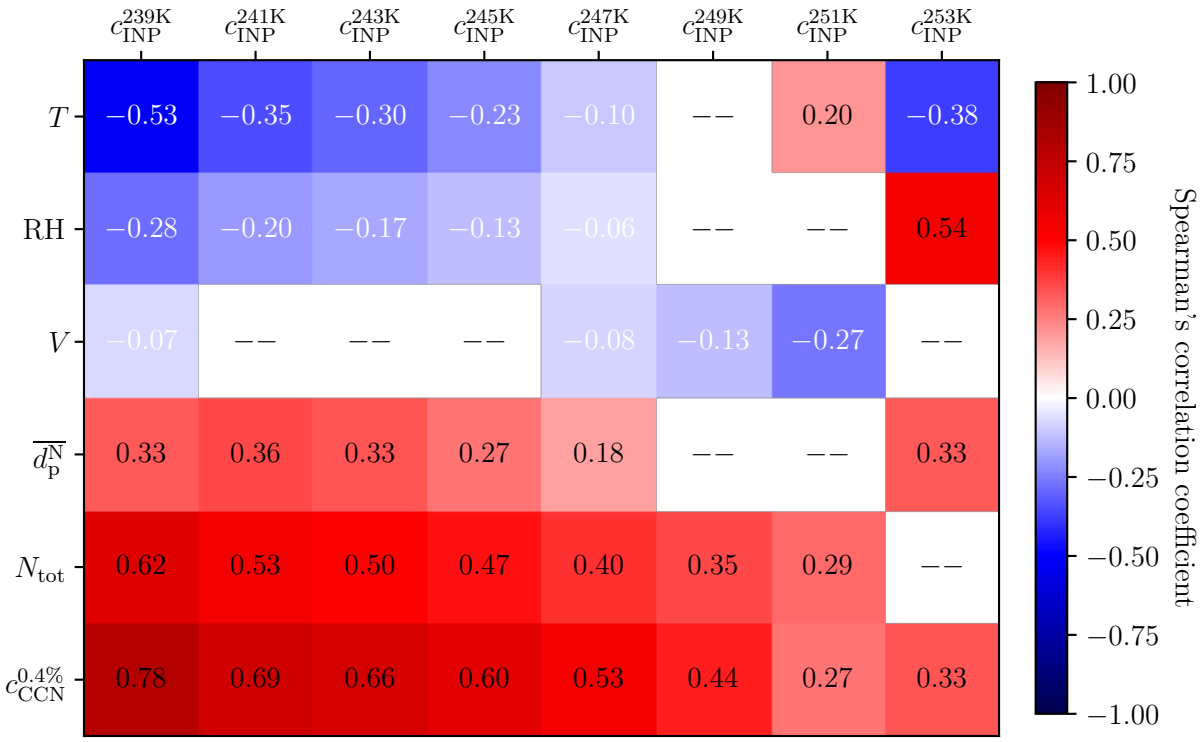

Figure 4.8.: **Correlation matrix between meteorological and aerosol data and the INP concentration measured during ExINP_ZEP.** The two-sided Spearman's rank correlation is calculated with data on a temporal resolution of 1 h. The correlation coefficient is not shown, when the p-value is above 0.05. The correlated variables are the ambient temperature T, relative humidity RH, wind speed V, mean diameter of the aerosol number size distribution $\overline{d_{\mathrm{p}}^{\mathrm{N}}}$,the total number concentration N_{tot} and the CCN concentration $c_{\mathrm{CCN}}^{0.4\,\%}$ at a supersaturation of 0.4 %.

on the same inlets as PINE. The concentration of CCN measured at a supersaturation of 0.4 % correlates positively with the INP concentration, reaching a maximum for lower nucleation temperatures. The PINE is sensitive to immersion freezing, which requires the INP to also be a CCN. The fraction of CCN that are also measured as an INP are shown in figure 4.9, with a continuous increase for lower nucleation temperatures up to a median value of 0.02 % at 239 K. This indicates that in general, more CCNs are also active as INPs at colder nucleation temperatures. This ratio is almost zero for nucleation temperatures above 248 K with a fraction of 0.0005 %. The CCN and the INP concentration might also show a positive correlation, since air masses, that contain an increased number concentration of aerosol particles, which might be active as CCN and INP, arrive at ZEP.

All four campaigns show a clear dependence on the size of the aerosol size distribution. Therefore, the INP concentration is normalized according to the INAS approach in the following sections to investigate the nature of the INP population in more detail (see also section 2.3.2).

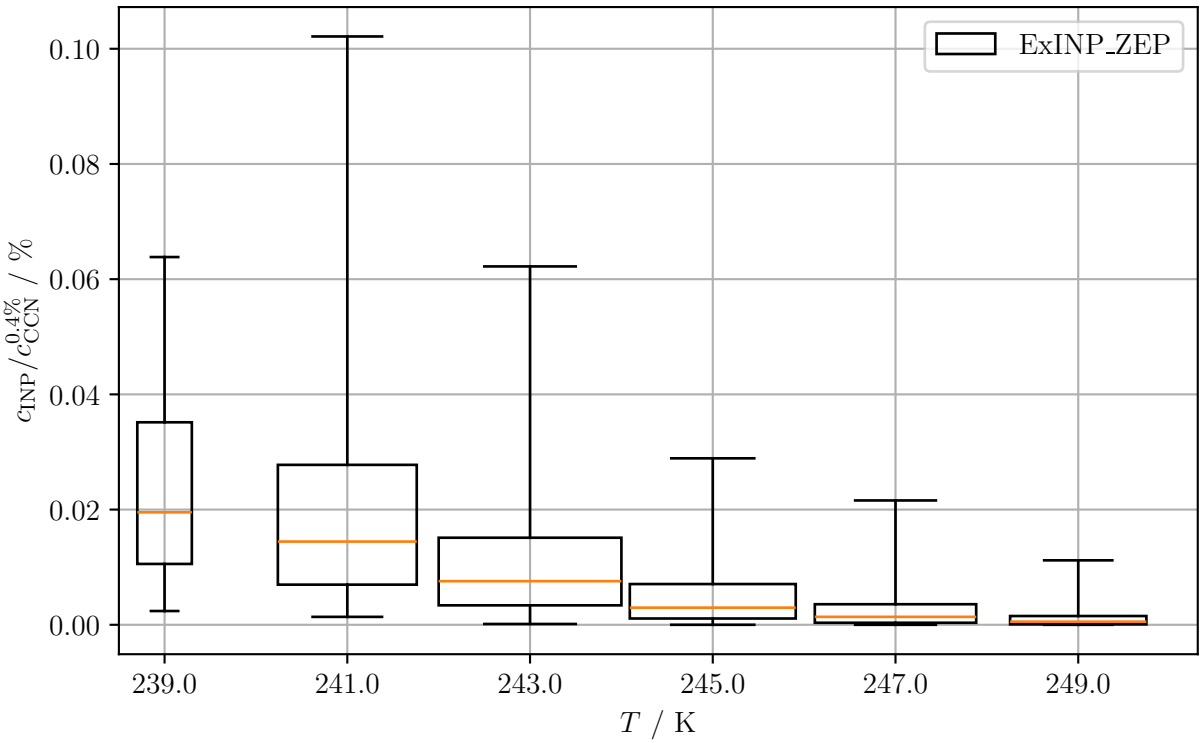

Figure 4.9.: **Fraction of INP concentration over CCN concentration as a function of the nucleation temperature T.** The interquartile range represents the first and third quartile, while the whiskers represents the (5, 95) percentiles. Fliers are not shown.

4.2. INAS density overview

The present section puts the measured INP concentration into context to existing parameterizations utilizing the INAS density.

4.2.1. PaCE 2022

The INP concentration was normalized with the surface area concentration determined by merging the APS and SMPS datasets measured at Sammaltunturi during PaCE 2022. The final dataset starts at 23rd September 2022 1.30 pm GMT until 23rd December 2022 1.30 am GMT on a 30 min temporal resolution. The same temporal resolution is chosen for the other campaign data. This is shorter compared to the correlation studies, since the CCNC data is only available on a one-hour temporal resolution. The boxplot repesentation is shown in figure 4.10 and is compared to a set of lab-based and field-based INAS parameterizations. The number of data points per temperature bin (spanning 2 K) are visualised on the secondary y-axis with a maximum of 1899 at 248 K.

The median INAS parameterization increases to lower temperatures, with an INAS density of 7833 cm^{-2} at 250 K to 99 072 cm^{-2} at 240 K. For all temperatures, the lowest 5 % contain values below the limit of detection. Outliers increase up to 13 858 913 cm^{-2} at 242 K. For the higher temperatures, the INAS density aligns well with the parameterization proposed by Schneider et al. (2021) for the boreal forest during summertime, although the overlap is minimal. For lower temperatures, the measured INAS density during PaCE 2022 drops below the parameterization

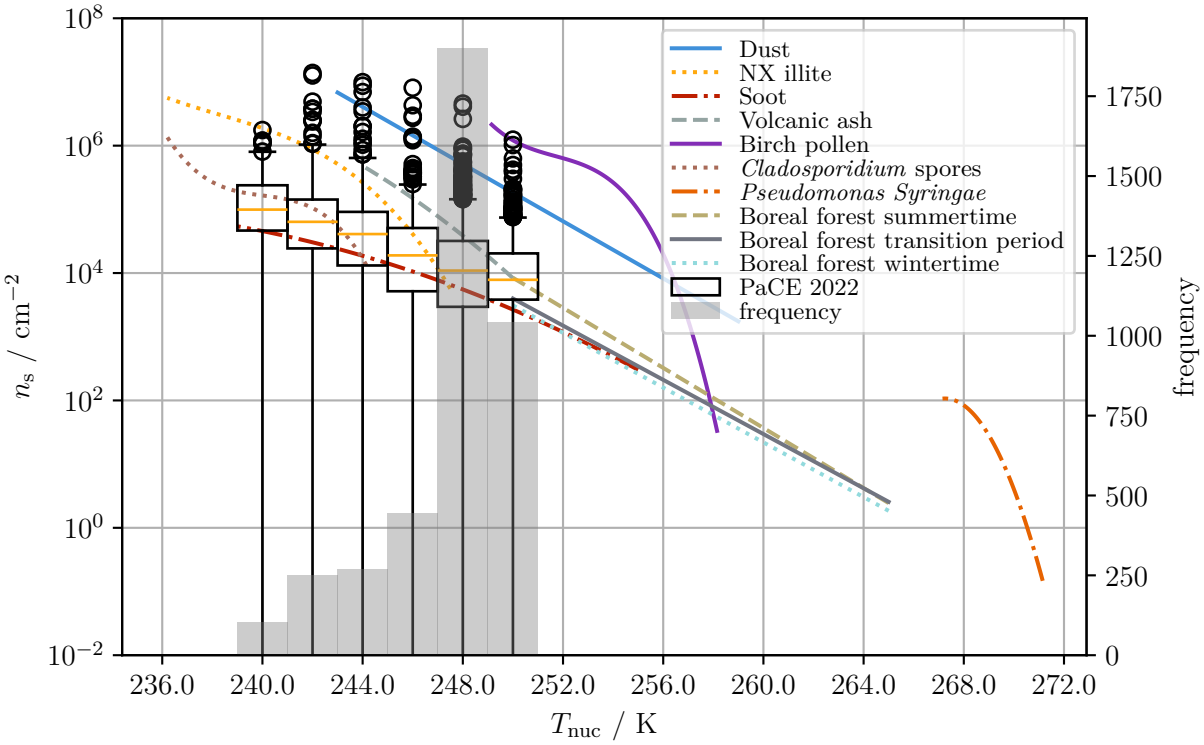

Figure 4.10.: **The INAS density n_s shown as a function of the nucleation temperature T_{nuc} for the INP concentration measured during PaCE 2022.** The boxplots represents the median and the first and third quartiles. The whiskers show the (5, 95)-quantiles, while fliers denote outliers.

representing *Cladosporidium* spores and stays slightly above the soot parameterization by Ullrich et al. (2017).

From the previous section, the INP concentration was positively correlated with the ambient temperature, indicating an influence from local biogenic sources. This is the same as was seen during the HyICE-2018 campaign, from which the parameterization was developed by Schneider et al. (2021) for the boreal forest. Snow cover lead to lower INP concentration during HyICE-2018, therefore three different parameterizations were developed, representing the different seasons, i.e. summertime and wintertime and the transition period in between (Schneider et al. 2021). PaCE 2022 was conducted during the transition period, spanning into wintertime. The increased INAS density compared to HyICE-2018 might be related to a positive bias from the PINE instrument (see also section 3.2.2.3). The parameterization was developed utilizing filter-based measurements, where the PINE usually shows a positive bias for higher temperatures, where the INP concentration is close to the limit of detection. There might also be a discrepancy due to interannual variability and of course the different locations (see also figure 3.19).

4.2.2. ExINP_GVB 2023

The INAS density is calculated for the filter samples analysed with WT-CRAFT. Boxplots of the INAS density are shown in figure 4.11 as a function of the nucleation temperature T_{nuc}. The number of data points for each boxplots is shown on the secondary y-axis. Panel (a) shows the INAS density for the non-heated aerosol sample, ranging between 56 cm^{-2} at 263.15 K to

14 676 cm^{-2} at 244.65 K. For temperature above 257 K, the number of data points is lower and the INAS density stagnates. This is likely due to the limit of detection defined by WT-CRAFT. This heat treatment can be used to assess a potential biogenic component in the total INP population (see also section 3.2.1.3).

Panel (b) shows the results of the same aerosol after heat treatment (see also section 3.2.1). The INAS density ranges between 46 cm^{-2} at 260.65 K to 14 676 cm^{-2} at 242.15 K, showing a clear decrease and shift along the whole freezing spectra. Panel (c) shows the relative and absolute difference between the median INAS densities of the non-heated and heated aerosol samples. The differences between the first and third quartiles are shown as dashed and dotted lines, respectively. The absolute and relative difference is calculated as

$$e_{\text{abs}} = n_{\text{s}}^{\text{non-heated}} - n_{\text{s}}^{\text{heated}} \,, \tag{4.1}$$

$$e_{\text{rel}} = \frac{n_{\text{s}}^{\text{non-heated}} - n_{\text{s}}^{\text{heated}}}{n_{\text{s}}^{\text{non-heated}}} \,, \tag{4.2}$$

where the non-heated value is taken as a reference value. The absolute difference increases with a decreasing nucleation temperature, with the largest spread between first and third quartiles for a nucleation temperature of 255.15 K. The absolute difference increases from around 9 cm^{-2} at 260.65 K to 9299 cm^{-2} at 244.65 K. The relative difference remains generally constant at 0.53 between 252.15 K and 258.15 K, but showing a maximum of 0.74 at 247.15 K. This indicates that the largest population of heat-sensitive INPs is active at 247.15 K. A local minima exists at 251.15 K, although the spread is relatively large with the first quartile showing a relative difference of 0.57. For periods where the INAS density is generally low, the heat-sensitive INP population is active especially at 251.15 K and at higher temperatures (> 257 K). The third quartile shows a maximum at around 254 to 255 K, which indicates that during periods, where the INAS density is high, the heat-sensitive INP population is especially active at those temperatures.

The final datasets contains the INAS density between 15$^{\text{th}}$ March 2023 11.30 am GMT and 10$^{\text{th}}$ April 2023 7.30 am GMT. The filter data has a temporal resolution of around 24 h (see also table C.1), the PINE chamber was connected to the same inlet and measured the INP concentration at a higher temporal resolution of around six minutes, but was ultimately averaged to a 30 min temporal resolution. Both datasets are visualized as boxplots in figure 4.12 and put into context with the INAS parameterizations of different aerosol species. The two datasets for the non-heated and heated aerosol samples are shifted for visualisation by 0.25 K, while the width of the PINE dataset boxes is 2 K. The INAS density measured by PINE is generally higher than WT-CRAFT, with some values below the detection limit above 247 K. This difference between PINE and offline measurements has been observed before, which might be explained due to a breakup of aggregates inside the water suspension (DeMott et al. 2017; Lacher et al. 2024). In addition, the filter used to collect the aerosol particles might collect a different aerosol size distribution compared to PINE due to different transport and collection efficiencies (Chen et al. 2016; Ling et al. 2011; Ogura et al. 2016; Xiang et al. 2020).

The median of the INAS density measured by PINE aligns well above 248 K with the parameterization of Schneider et al. (2021) measured at the boreal forest of southern Finland. The INAS parameterization for volcanic ash increases faster with a decreasing temperature compared to the INAS density measured by PINE (Murray et al. 2012), aligning more closely with the parameterization of *Cladosporidium* spores (Murray et al. 2012).

The median of the INAS density obtained from WT-CRAFT is relatively constant at higher temperatures, likely a bias due to the limit of detection. The untreated aerosol sample aligns well with the parameterization of soot (Ullrich et al. 2017) for lower temperatures (< 248 K), but

is slightly below the parameterization of Schneider et al. (2021) for higher temperatures. The heated aerosol sample is generally below the lowest INAS parameterization, which is related to the normalization with surface area concentration of the whole aerosol population, and therefore cannot directly be compared to present parameterizations.

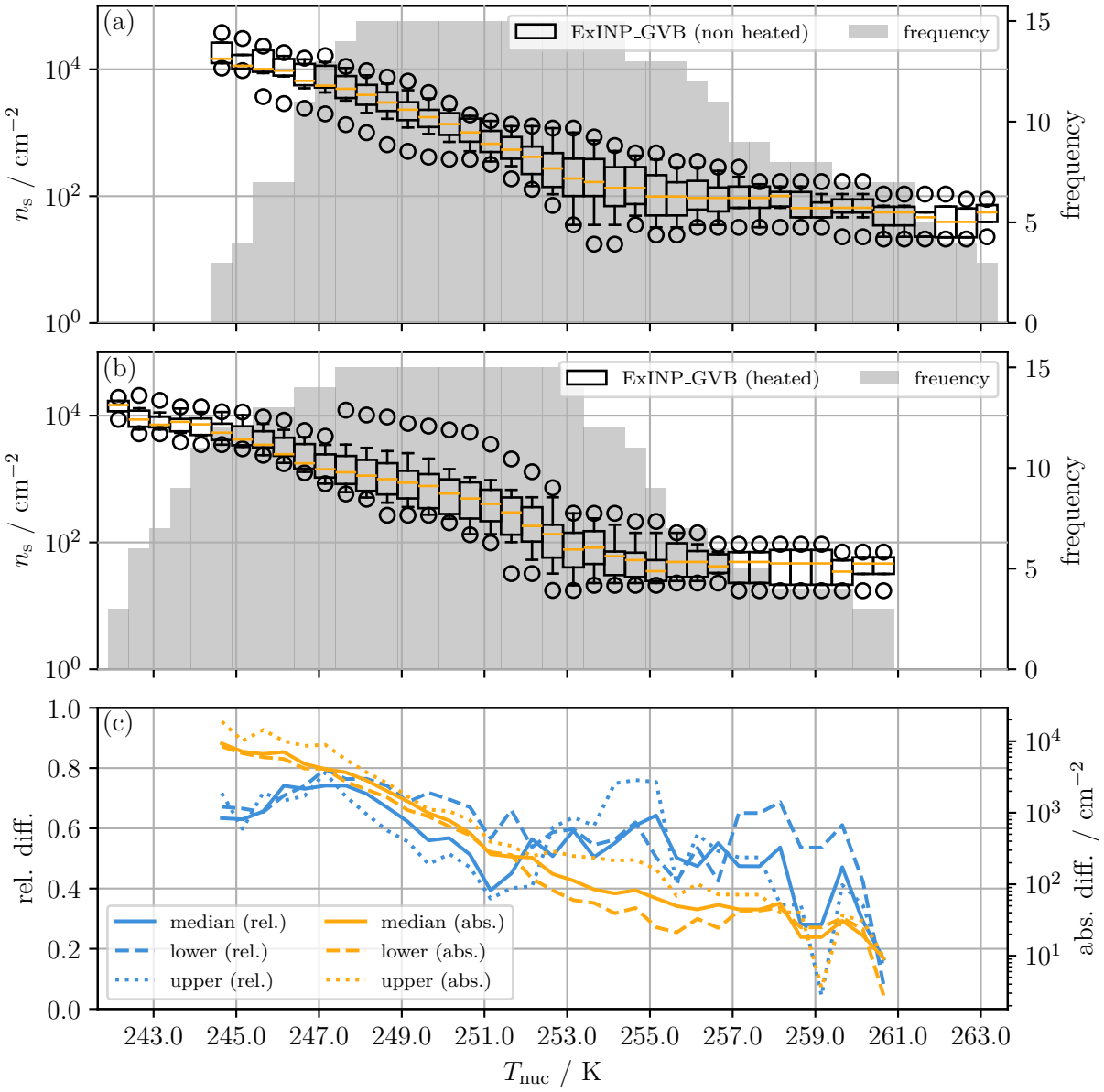

Figure 4.11.: **The INAS density n_s shown as a function of the nucleation temperature T_{nuc} for aerosol samples collected during ExINP_GVB 2023.** Panel (a) shows the non-heated aerosol suspensions, while panel (b) visualises the same after heat treatment. Panel (c) shows the absolute and relative differences between the medians and the first and third quartiles.

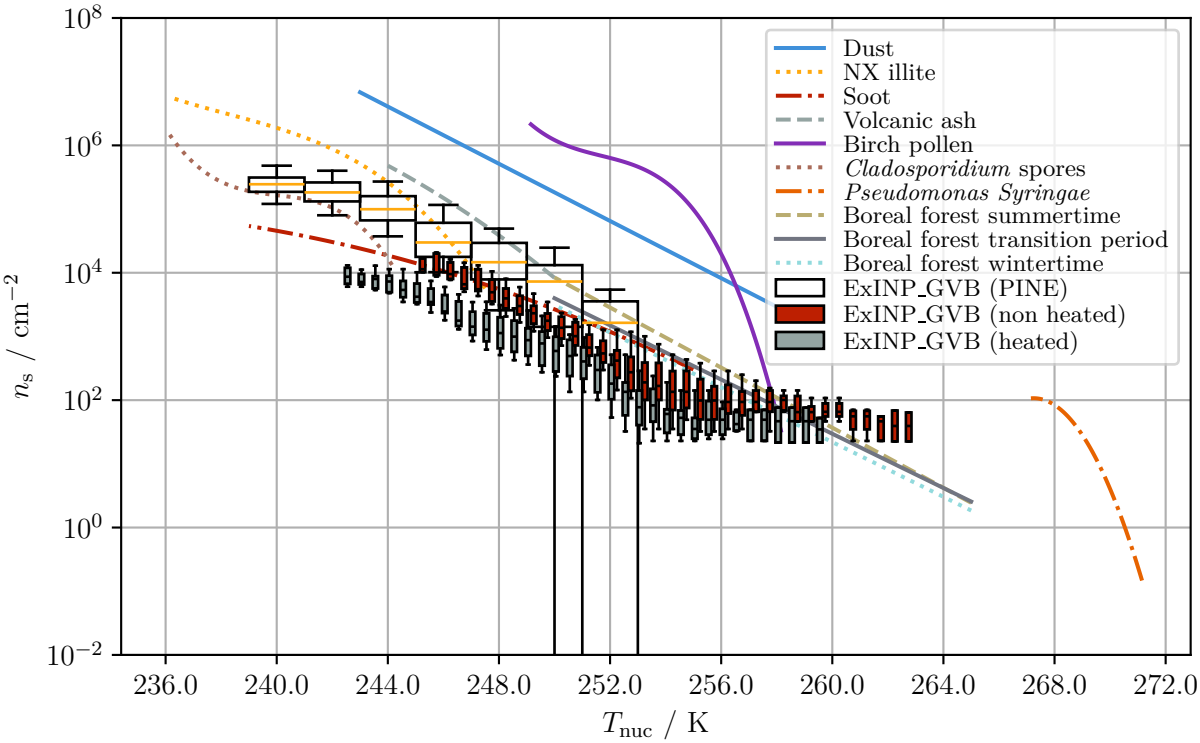

Figure 4.12.: **The INAS density n_s shown as a function of the nucleation temperature T_{nuc} for aerosol measured during ExINP_GVB 2023.** The boxplots represents the median and the first and third quartiles. The whiskers show the (5, 95)-quantiles, while fliers are not shown. The data collected via filters is shifted by 0.25 K for visualisation.

4.2.3. ExINP_GVB 2024

During ExINP_GVB 2024 a setup similar to the one of the first campaign was used. The two main differences were the PINE version and the timing of the filter sampling. The used PINE was the prototype version 'PINE-1A', which has two main differences to the commercial version: a slightly smaller chamber volume and a different cooling system. The data itself is not biased due to the use of the prototype version of PINE. The second difference to the prior campaign is that the filter-based measurements were not done at the exact same time as the PINE measurements. Due to some technical issues, the PINE started measuring on 2nd April 2024 10.30 am GMT until 5th June 2024 10 pm GMT, whereas daily filters were taken between 12th March 2024 and 4th April 2024. Afterwards, three-to-four-day filters were taken until 19th June 2024 (see also table C.1).

The results of the filters, calculated as INAS densities, are shown in figure 4.13. The panels follow the same visualisation as in the previous section. The INAS density of the non-heated aerosol samples ranges from 29 cm^{-2} to 18 858 cm^{-2} for nucleation temperatures 264.15 K and 242.65 K, respectively. The number of data points decreases for lower temperatures (< 248 K), which reduces their statistical significance. The heated aerosol samples have INAS densities below the limit of detection for temperatures above 259.65 K. For lower temperatures it increases exponentially up to 7001 cm^{-2} at 243.65 K. Afterwards, the median decreases, which is due to the lower amount of data points and not representative of the ambient aerosol population.

The lower panel of figure 4.13 shows the relative and absolute difference between the median and the first and third quartiles of the INAS density of the non-heated and the heated aerosol samples. The absolute difference increases from around 24 cm^{-2} at 259.15 K to around 17 755 cm^{-2} at 243.15 K. The spread behaves similarly, although there is a local minima at the absolute difference between the lower quartiles around 257 K, where the heated aerosol samples shows higher INAS densities during episodes, where the INAS density is generally low. This is likely related to the lower amount of data points, where some heated aerosol samples have INAS densities below the limit of detection.

The relative difference remains almost constant at 0.51 between 247.15 K and 255.65 K. The relative difference decreases for temperatures outside of this temperature range, but due to the lower amount of data points, this change might not be representative of the ambient aerosol population. A similar behaviour is seen for the relative differences between the first and third quartiles, although the relative difference between the third quartiles remains constant up to 259.15 K and shows a local minima at around 246.15 K, lowering to 0.22. The first quartile shows the same minima as for the absolute difference, but keeps increasing to around 0.93 for lower temperatures. The mean of the relative difference is lower (0.49) in 2024 compared to ExINP_GVB 2023 (0.54), indicating that more heat-sensitive aerosols contributed to the overall INAS density during ExINP_GVB 2023. Looking at the maximum relative differences, the contribution of heat-sensitive material is larger at certain temperatures during ExINP_GVB 2024 compared to ExINP_GVB 2023. This might be related to the additional measurements into early summertime. Heat-labile INPs are often of biogenic origin and might increase for higher ambient temperatures, where biogenic activity increases and the ocean becomes increasingly ice free.

Figure 4.14 shows the INAS density for the filter-based aerosol samples and the data obtained via PINE. Similar to ExINP_GVB 2023, the INAS density obtained via PINE is higher compared to aerosol samples analysed with WT-CRAFT. The difference is especially large for higher temperatures, where the PINE measures close to its limit of detection. The INAS density

is below the limit of detection in up to 5 % of the measurement time for temperature above 244 K. The difference decreases for lower temperatures, but still remains. The INAS density of aerosol samples analysed with WT-CRAFT aligns with the soot parameterization (Ullrich et al. 2017) for lower temperatures (< 249 K), but is typically below the parameterization for higher temperatures. The INAS density obtained via PINE aligns well with the parameterization for *Cladosporidium* spores (Murray et al. 2012) for lower temperatures (< 244 K). The stagnation of the INAS density measured with PINE does not align with any parameterization, which is expected, since it is related to the instrument. The parameterization for aerosol samples obtained in the boreal forest matches with the median for temperatures around 249 K (Schneider et al. 2021).

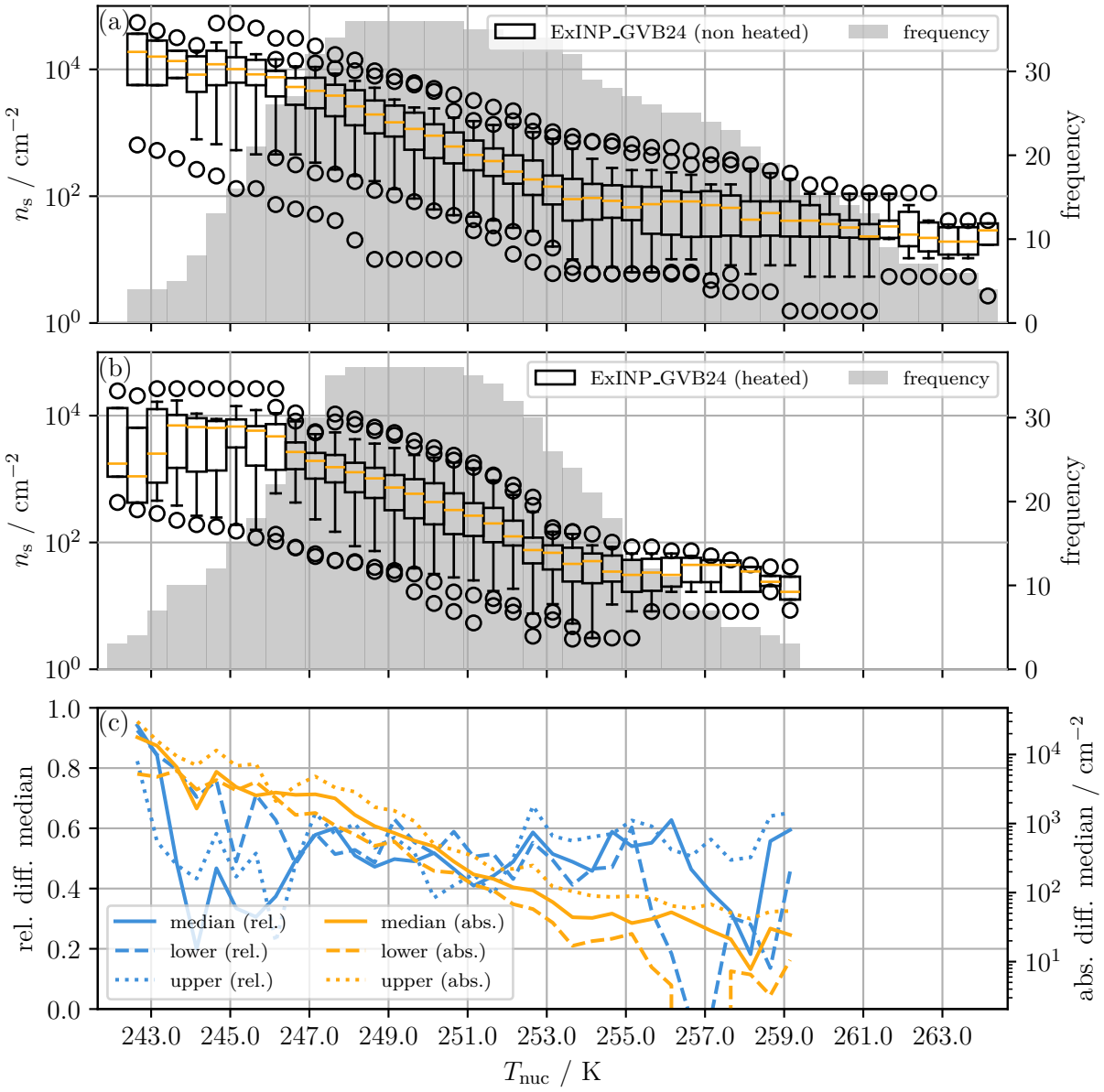

Figure 4.13.: **The INAS density n_s shown as a function of the nucleation temperature T_{nuc} for aerosol samples collected during ExINP_GVB 2024.** Panel (a) shows the non-heated aerosol suspensions, while panel (b) visualises the same after heat treatment. Panel (c) shows the absolute and relative differences between the medians and the first and third quartiles.

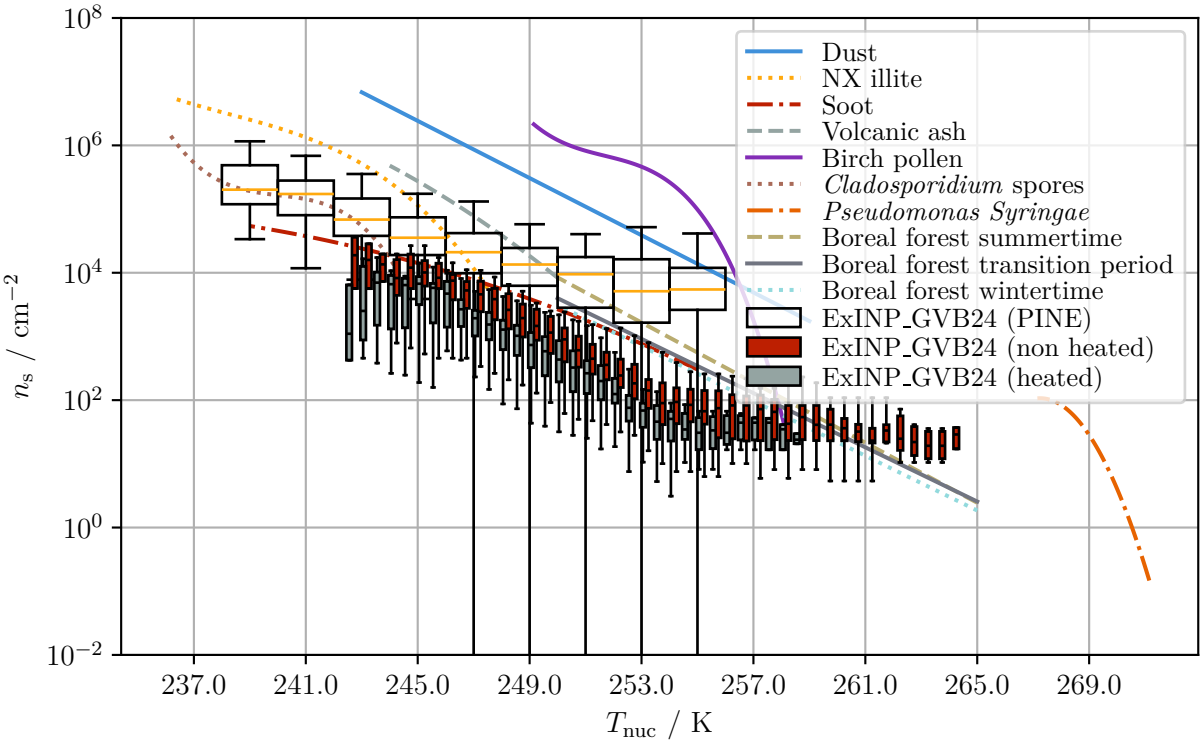

Figure 4.14.: **The INAS density n_s shown as a function of the nucleation temperature T_{nuc} for aerosol measured during ExINP_GVB 2024.** The boxplots represents the median and the first and third quartiles. The whiskers show the (5, 95)-quantiles, while fliers are not shown. The data collected via filters is shifted by 0.25 K for visualisation.

4.2.4. ExINP_ZEP

The INAS density calculated from SMPS and PINE is visualized as boxplots in figure 4.15. The PINE collects aerosol particles above a particle diameter of around 4 µm (see also figure A.1), while the aerosol size distribution is not available for particle diameters above 708 nm during ExINP_ZEP. This might lead to a positive bias, where a lower surface area per particle is used to calculate the INAS density (see equation (2.35)). The measured INP concentration was adjusted to account for the dilution of the aerosol concentration during times, where the GCVI was turned on (see section 3.5.3). The GCVI samples cloud residuals compared to the general aerosol population measured while the GCVI is turned off. The GCVI is only on, when the station is considered to be in a cloud (see section 3.5.3). During the measurement period of PINE, the GCVI was on 8 % of the time.

The INAS density is available between 25$^{\text{th}}$ April 2023 midnight GMT and 8$^{\text{th}}$ April 2024 9.30 am GMT on a 30 min temporal resolution. The median INAS density ranges between 158 731 cm^{-2} and 6787 cm^{-2} at 240 K and 254 K, respectively. A positive bias is shown close to the limit of detection at 254 K. The number of data points here is much lower (89) compared to the other temperatures with an average of 2216. The median INAS density aligns closely with the boreal forest transition period parameterization from Schneider et al. (2021) for the given temperature range. For lower temperatures, the median of the INAS density increases exponentially, although this increase is less pronounced at lower temperatures (< 241 K), fitting well to the *Cladosporidium* spore parameterization (Murray et al. 2012). The number of data points is less than half of the mean for those temperatures (1092). It is notable, that the whiskers representing the (5, 95)-quantiles reach below the limit of detection across the whole temperature range.

Separating the aerosol measurements (GCVI off) from the cloud residual measurements (GCVI on), leads to the boxplots in figure 4.16. Generally, the INAS density was larger, when cloud residuals were measured. There are only two exceptions: for temperatures below 241 K and for temperatures between 251 K and 253 K. For both of these temperature ranges, the number of data points is much lower compared to the other data points.

Over the whole temperature range, lots of outliers are visible, which indicate that the INAS density changes over several orders of magnitudes during the measurement period.

The median of the INAS density of cloud residuals is around 4 times as high as the median of the INAS density obtained from the aerosol population. The largest difference is seen at higher temperatures, increasing to 7 times at 250 K and 10 times at 254 K, although at the latter with a lower amount of data points. This could indicate that aerosol particles, that are activated as CCN, are more active as INP. But it could also indicate that during times with high INAS densities, the conditions for CCN activation and cloud droplet growth are favourable.

The INAS density associated with the cloud residuals aligns most closely with the parameterization for volcanic ash (Murray et al. 2012), although the increase towards lower temperatures is less pronounced. At 250 K the INAS density is higher compared to the parameterization for volcanic ash. The INAS density associated with the aerosol population is similar to the overall INAS density as described previously. Again, for higher temperatures, the limit of detection and the low amount of data points introduces a bias to the INAS density.

The following section investigates specific episodes, where the INAS density was exceptionally high or exceptionally low. From this determination, other data is used to understand the nature

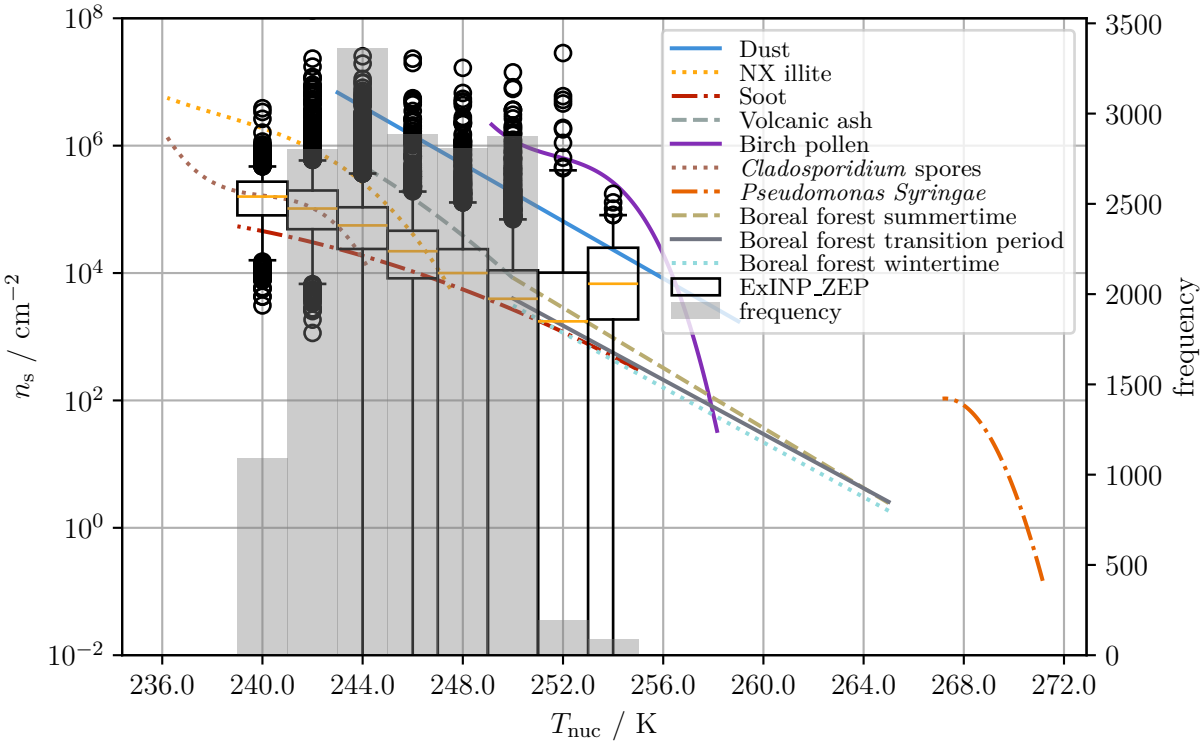

Figure 4.15.: **The INAS density n_s shown as a function of the nucleation temperature T_{nuc} for aerosol measured during ExINP_ZEP.** The boxplots represents the median and the first and second quartiles. The whiskers show the (5, 95)-quantiles, while fliers denote outliers.

and source of those INP better.

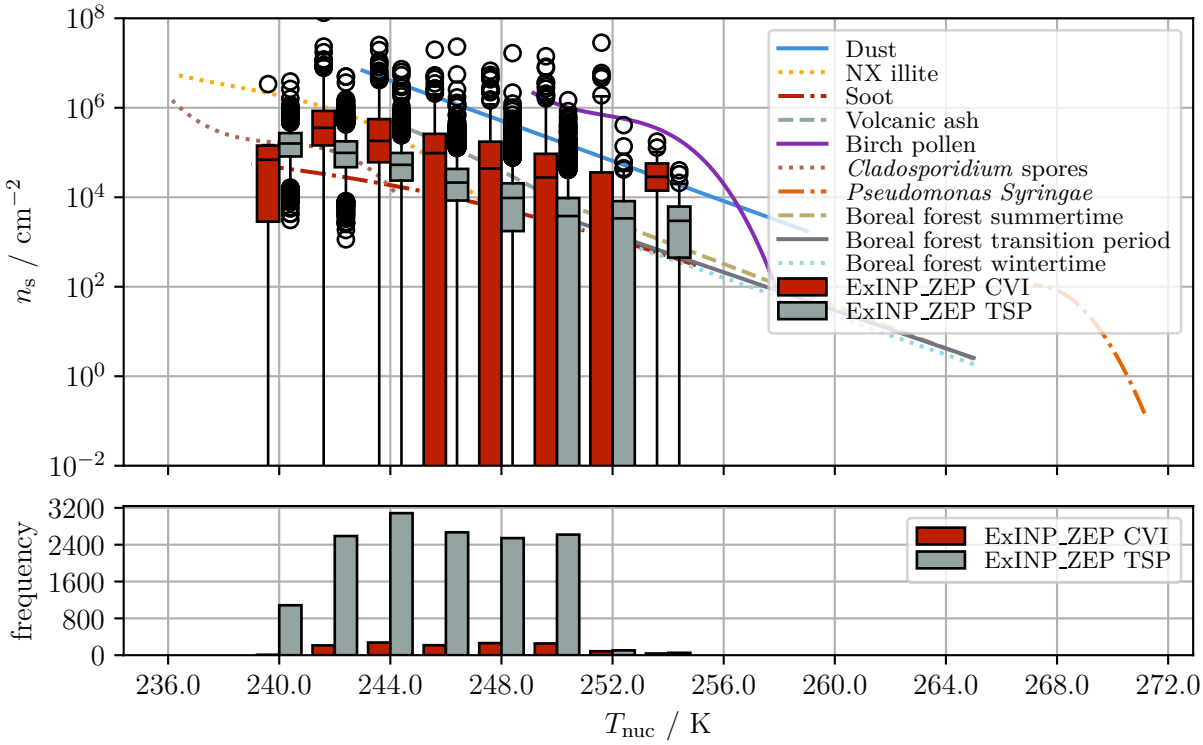

Figure 4.16.: **The INAS density n_s shown as a function of the nucleation temperature T_{nuc} for aerosol measured during ExINP_ZEP split into GCVI and TSP inlets.** The boxplots represents the median and the first and second quartiles. The whiskers show the (5, 95)-quantiles, while fliers denote outliers. The data is shifted by 0.5 K for visualisation.

4.3. Episodes of lower and higher INAS densities

4.3.1. PaCE 2022

Until now, the INAS density was always assessed based on statistics developed from data of the whole campaign duration. It is likely, that during different periods the INP population originated from different sources and is influenced by the local conditions. For PaCE 2022, the ambient temperature is positively correlated with the INP concentration, therefore it is likely that local meteorological conditions have an influence on the INP population. For this, temperature, relative humidity, wind speed and direction were assessed during the general campaign period and also during periods, where the INAS density is considered low or high. This was done by determining the first and third quartile of the INAS densities over the whole campaign duration, with lower INAS density episodes being less than the first quartile, and higher INAS density episodes being higher than the third quartile (see figure 4.17 and section C.4 for the classification of lower and higher INAS density episodes).

During the whole campaign duration, the ambient temperature at Sammaltunturi has a median of −2.2 °C with the first and third quartile being −5.5 °C and 1.1 °C, respectively. The relative humidity was generally close to saturation during the whole campaign with a median of 99 % and a first and third quartile of 97 % and 100 %, respectively. This is expected, since the station is often inside a cloud during autumn (see also section 3.5.1). The median of the wind speed is 6.5 m s^{-1} with a first and third quartile of 4.8 m s^{-1} and 8.3 m s^{-1}, respectively. The most

common wind direction was south-westerly wind with an occurence of 30 %, followed by southerly wind (21 %). Wind from the north was very rare with an occurence of 1 %.

A total of nine episodes where identified during which the INAS density was exceptionally low. For some INAS periods, no atmospheric data was available. There is a clear behaviour during the campaign period, where during the transition from autumn to winter, the ambient temperature and the relative humidity decreased. The wind speed did not change clearly during the same period. There is also no clear shift in wind direction during the transition into winter. For six lower episodes, atmospheric data is available. In general, the atmospheric conditions during all of the lower episodes is not different to the general atmospheric conditions, apart from the wind direction. For five of these lower episodes southerly and south-westerly wind direction was the most dominant (4, 5, 6, 7 and 9). Only during the first lower episode, the dominant wind direction was south-easterly. During lower episodes, westerly and north-westerly winds are more common, while all other winds are less common. Westerly and north-westerly winds indicate that aerosol from the Atlantic is transported to Sammaltunturi, which generally exhibits a lower INAS density compared to the general aerosol population present during the whole campaign.

A total of 12 episodes with exceptionally high INAS densities were identified (see figure 4.18). A similar behaviour as for the lower episodes can be seen with no clear relation to meteorological variables. There are no clear differences for the ambient temperature and the wind speed. The relative humidity is slightly lower compared to the general campaign period, with medians of 97 % and 99 %, respectively. The wind direction is similar to the lower episodes too, where all winds are enhanced in occurence, apart from the westerly and north-westerly winds. At the same time, while the occurence of southerly and southwesterly winds are reduced by 49 % and 31 % during lower episodes, respectively. This reduction is slightly less during the higher episodes with 37 % and 27 %, respectively. This still aligns well with previous results, where the correlation between INP concentration and ambient temperature and relative humidity is positive, indicating that local influence on the INP population is relevant. Long-range transport might be less relevant during the period, when PaCE 2022 was conducted.

During PaCE 2022, nine lower and 12 higher INAS density episodes were identified. All meteorological variables, but the wind direction, generally showed no difference between the episodes and the general measurements during the campaign. This indicates, that long-range transport plays a relevant role for the change in the INAS density at Sammaltunturi station.

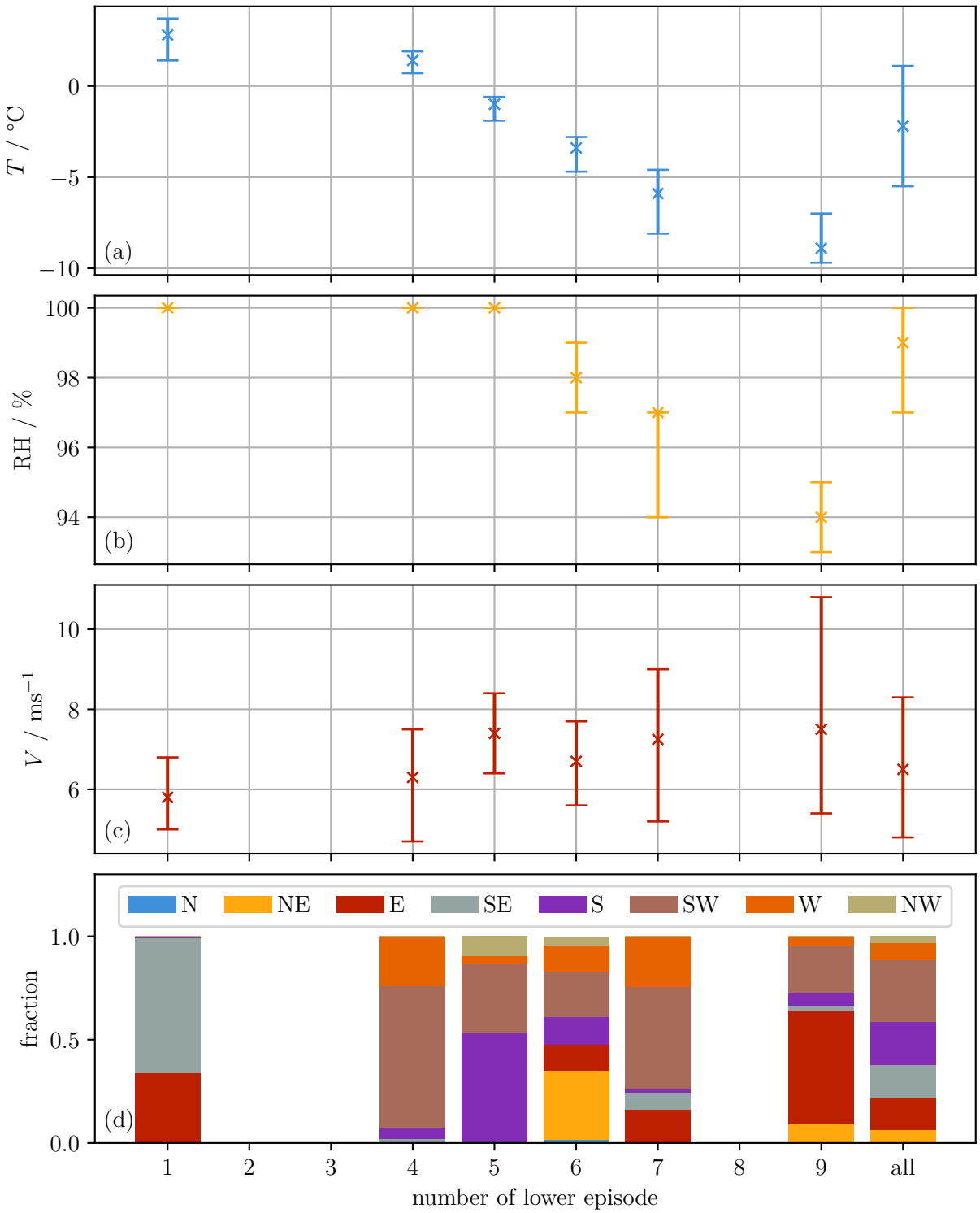

Figure 4.17.: **Atmospheric conditions during lower INAS density episodes during PaCE 2022.** Panel (a) shows the ambient temperature, with the median, the first and third quartile. Panel (b) and (c) represent the same for the relative humidity and the wind speed, respectively. Panel (d) visualizes the fraction of the eight wind vectors for the lower episodes. The atmospheric conditions during the whole campaign are shown on the far right.

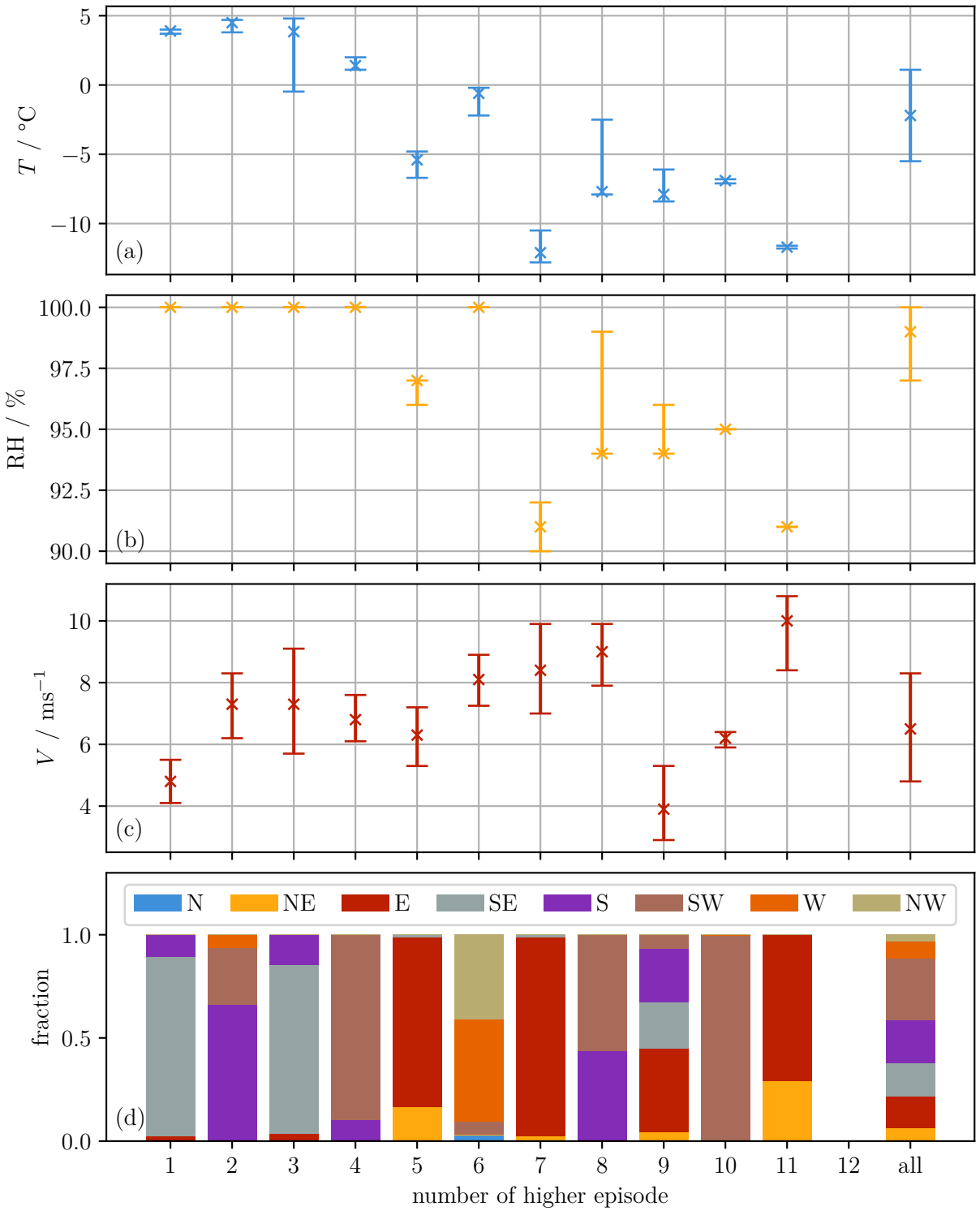

Figure 4.18.: **Atmospheric conditions during higher INAS density episodes during PaCE 2022.** Panel (a) shows the ambient temperature, with the median, the first and third quartile. Panel (b) and (c) represent the same for the relative humidity and the wind speed, respectively. Panel (d) visualizes the fraction of the eight wind vectors for the higher episodes. The atmospheric conditions during the whole campaign are shown on the far right.

4.3.2. ExINP_GVB 2023

The shorter measurement time during ExINP_GVB 2023 compared to PaCE 2022 and the issue, that the full size distribution is only available for half of the measurement campaign, leads to a much shorter period for the INAS density. Therefore, only one lower and higher episode were identified for the measurement period (see figure 4.19 and figure 4.20). The ambient temperature and the relative humidity are both lower compared to PaCE 2022 with medians of −12.4 °C and 67.7 %, respectively. The wind speed is also lower with a median of 3.3 m s^{-1} compared to 6.5 m s^{-1} at Sammaltunturi. All three of these difference are related to the different location and also the different altitude, with GVB being located close to sea level.

With just one episode, the statistics cannot be used to obtain a clear picture of typical lower and higher episodes. For the specific episodes, it is still interesting to investigate potential meteorological conditions, under which the INAS density changes. For the lower episode, the temperature and relative humidity are slightly lower, but this might just be related to the transition from winter into spring with constantly increasing temperatures and relative humidities. The wind speed does not vary significantly. There is a decrease in the occurence of easterly to southerly winds. South-easterly winds dominate the wind field at GVB due to the fjord channeling winds along its axis, but during the lower episode they decrease by 74 %, while winds from the north and west increase in occurence. This could indicate that aerosol from the partly open sea to the north and west of Svalbard have a lower INAS density compared to the typical aerosol arriving at GVB.

For the higher episode, the ambient temperature is slightly less and also the relative humidity is decreased compared to the general campaign period. The wind speed is slightly enhanced (21 % to 4 m s^{-1}), which could enhance the emission of larger aerosol particles from local sources or from SSA. Easterly and south-easterly winds are decreased by 17 % and 58 %, respectively. This is similar to the lower episode, where the northerly and westerly wind occurence was enhanced. For the higher episode, the northerly wind has the same occurence as the general campaign, but there is a stronger influence from southerly wind with an increase in occurence of 175 %. Northwesterly wind is almost non existent during the higher episode, which indicates that sources arriving from the south lead to an enhanced INAS density of the measured aerosol population.

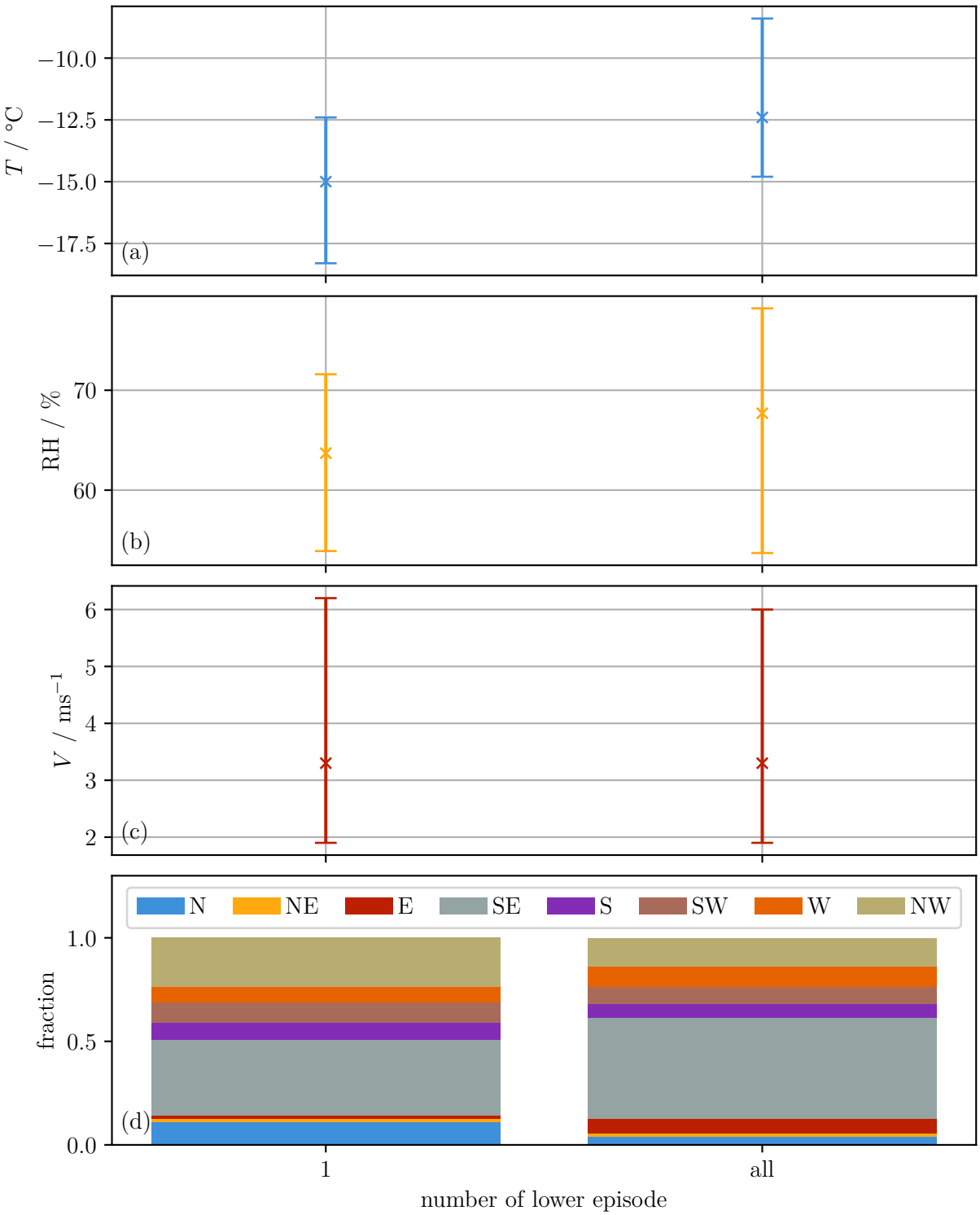

Figure 4.19.: **Atmospheric conditions during lower INAS density episodes during ExINP_GVB 2023.** Panel (a) shows the ambient temperature, with the median, the first and third quartile. Panel (b) and (c) represent the same for the relative humidity and the wind speed, respectively. Panel (d) visualizes the fraction of the eight wind vectors for the lower episodes. The atmospheric conditions during the whole campaign are shown on the far right.

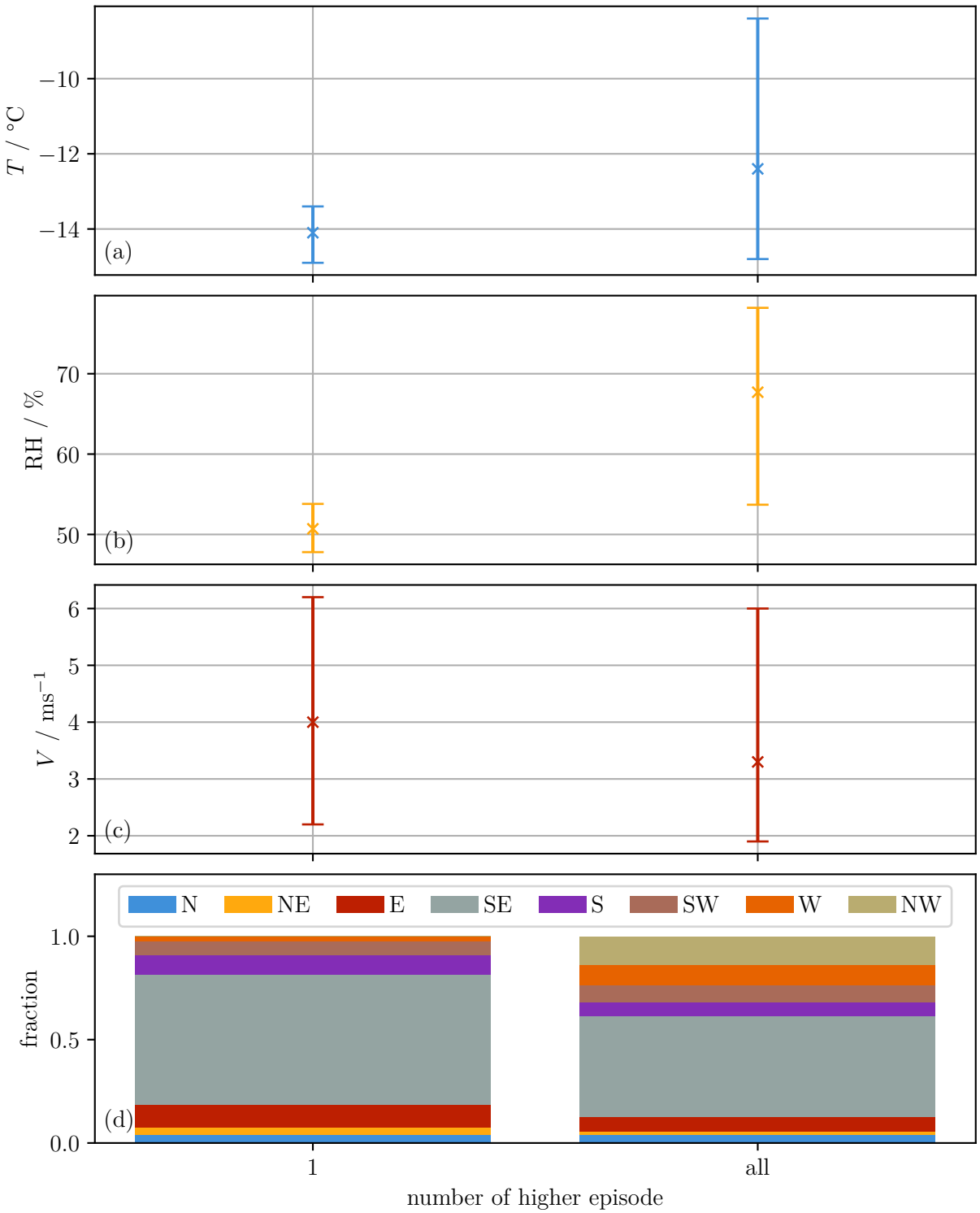

Figure 4.20.: **Atmospheric conditions during higher INAS density episodes during ExINP_GVB 2023.** Panel (a) shows the ambient temperature, with the median, the first and third quartile. Panel (b) and (c) represent the same for the relative humidity and the wind speed, respectively. Panel (d) visualizes the fraction of the eight wind vectors for the higher episodes. The atmospheric conditions during the whole campaign are shown on the far right.

4.3.3. ExINP_GVB 2024

The second campaign at GVB during April and May 2024 spanned two months, which is around eight times longer than the previous campaign in 2023. Therefore, the number of lower and higher INAS episodes are increased to three for each. In the previous correlation study, the INP concentration measured above a nucleation temperature of 247 K was positively correlated with the ambient temperature, indicating an increased biogenic activity that influences the INP population, especially at higher nucleation temperatures. During ExINP_GVB 2024, the median ambient temperature (−2.1 °C) was higher compared to ExINP_GVB 2023, which is mainly due to the measurement period. The relative humidity also increased, while the wind speed was similar. The wind field is again dominated by south-easterly wind, although the occurence is slighly less (18 %) compared to ExINP_GVB 2023.

The three lower INAS density episodes have similar temperature, relative humidty and wind speed, with a slight increase for the first two in the last episode (see figure 4.21). This is related to the increase of the temperature and relative humidty for the transition into summer. For the episodes 2 and 3, the wind direction is similar to the overall case, with a dominance of south easterly winds, but a contribution also from westerly and south-westerly winds. A clear difference is seen for the first episode, which features almost exclusively south-easterly winds. Overall, during lower episodes, the wind direction occurence reduces for easterly and south-easterly winds by 70 % and 65 %, respectively. A slight increase is seen for westerly winds, which is similar to the behaviour observed during ExINP_GVB 2023.

Looking at the three higher episodes, the second episode shows a strong difference to the general behaviour with a strong increase in temperature and wind speed (see figure 4.22). The temperature increased to a median of 0.9 °C compared to the median temperature of −2.1 °C during the whole campaing period. The median wind speed increased to 9.7 $\mathrm{m\,s^{-1}}$, which is an increase of 273 %. This indicates a rapid shift in air mass leading to influx of relatively warm air. For this single episode the wind direction was almost exclusively south and south-east. Looking at all higher episodes, there is a slight increase of the wind speed, mostly due to higher episode 2. The wind direction changes as observed before with a decrease in the occurence of south-easterly wind (54 %). North-easterly, southerly and westerly winds increase in occurence during episodes where the INAS density is increased.

For both occurences, where the INAS density is lower or higher, the most prominent difference to the general atmospheric condition is the change in the wind field, especially the decrease of south-easterly winds during most lower and higher episodes. This does indicate that, while the INP concentration is affected by local aerosol, a change in INAS density is typically observed when the air mass changes.

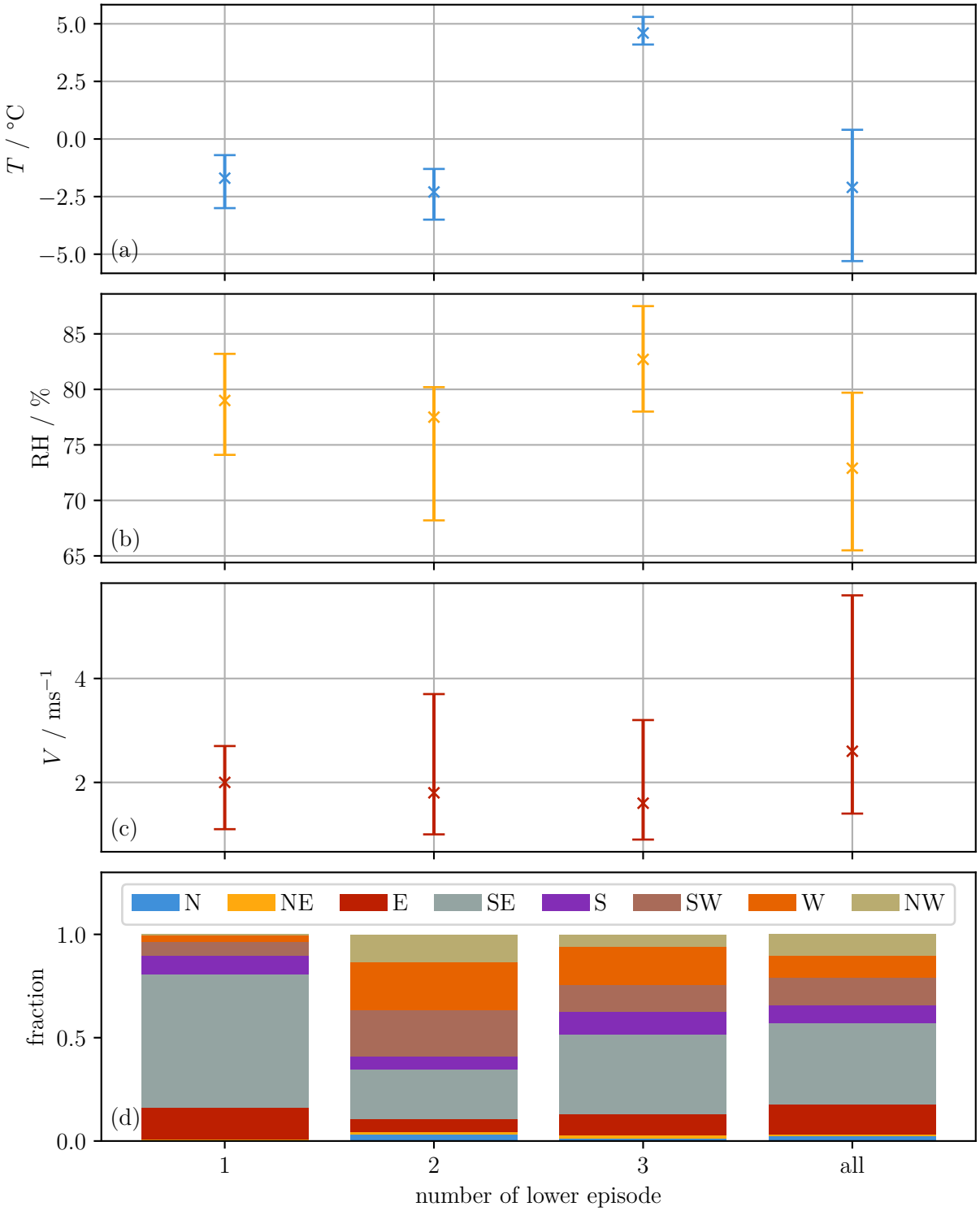

Figure 4.21.: **Atmospheric conditions during lower INAS density episodes during ExINP_GVB 2024.** Panel (a) shows the ambient temperature, with the median, the first and third quartile. Panel (b) and (c) represent the same for the relative humidity and the wind speed, respectively. Panel (d) visualizes the fraction of the eight wind vectors for the lower episodes. The atmospheric conditions during the whole campaign are shown on the far right.

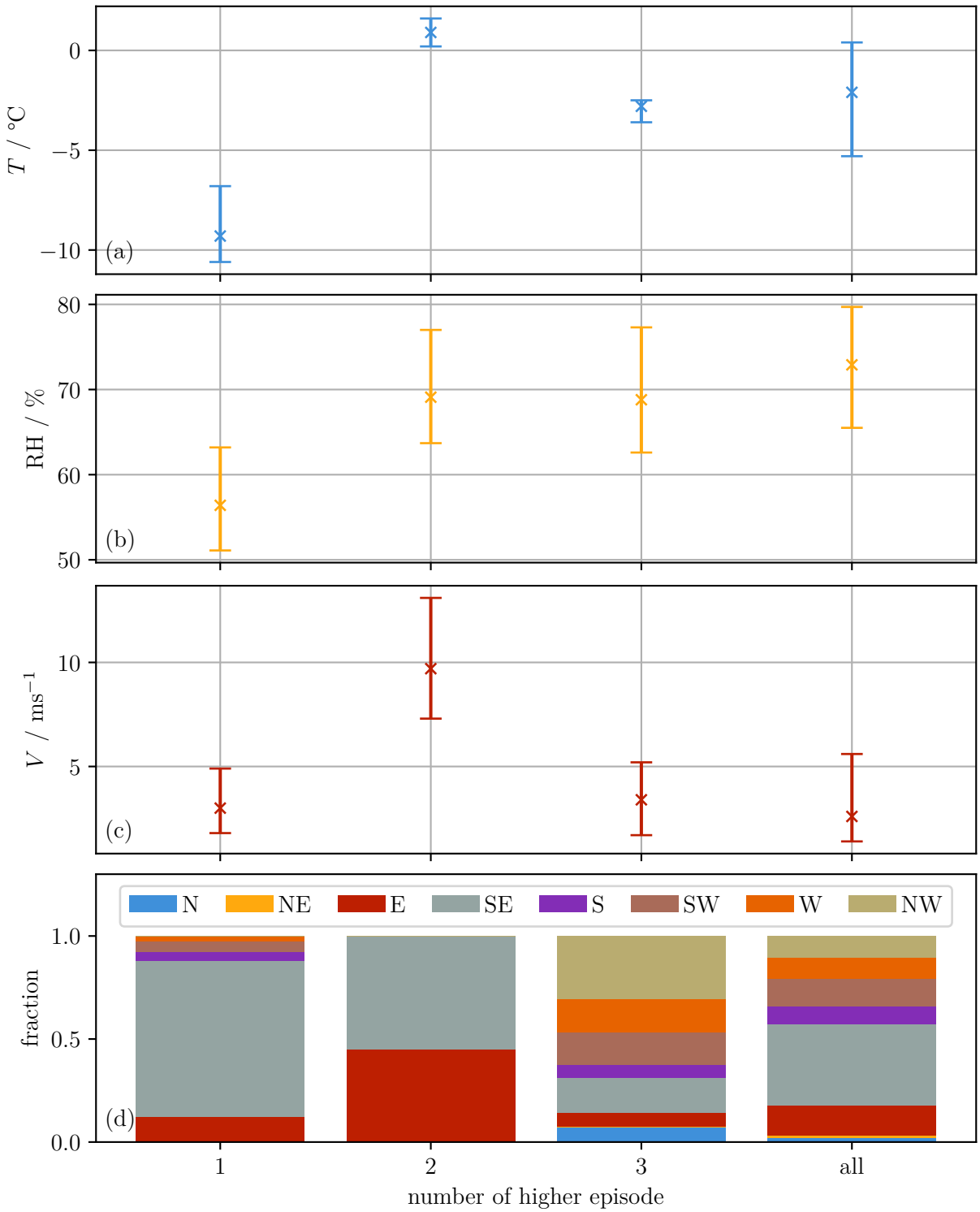

Figure 4.22.: **Atmospheric conditions during higher INAS density episodes during ExINP_GVB 2024.** Panel (a) shows the ambient temperature, with the median, the first and third quartile. Panel (b) and (c) represent the same for the relative humidity and the wind speed, respectively. Panel (d) visualizes the fraction of the eight wind vectors for the higher episodes. The atmospheric conditions during the whole campaign are shown on the far right.

4.3.4. ExINP_ZEP

Almost a full year of measurements during ExINP_ZEP leads to an increase in the number of lower and higher episodes compared to the three other campaigns. 19 lower episodes where identified alongside 23 higher episodes between April 2023 and April 2024. The meteorological data is taken from the AWI meteorological tower in Ny-Ålesund (Maturilli et al. 2013), therefore the actual meteorological data on ZEP might be slightly different, especially regarding the wind fields. The meteorological data as well as the INAS density for three selected temperatures is visualized in figure 4.23.

Over the whole year, the median of the ambient temperature is at −2.3 °C with a first and third quartile of −7.8 °C and 3.3 °C, respectively. This is higher compared to ExINP_GVB 2023 due to the different periods of the year and similar to ExINP_GVB 2024 which featured two months of the transition from springtime to summertime. The temperature is generally lower compared to PaCE 2022. The relative humidity and wind speed is similar to both ExINP_GVB campaigns. The relative humidity is much less compared to PaCE 2022, while the wind speed is also slightly lower. As expected, the local orography shapes the wind field, featuring south-easterly winds as most common (36 %), followed by easterly (18 %) and north-westerly (13 %) winds.

The lower episodes observed during ExINP_ZEP are visualized in figure 4.24. The median of ambient temperatures during lower episodes was −1.6 °C, 0.7 °C higher than during the whole campaign duration. The relative humidity did not change during lower episodes, whereas the wind speed was slightly higher with a median of 3.2 $\mathrm{m\,s^{-1}}$ compared to 2.5 $\mathrm{m\,s^{-1}}$ during the whole campaign period. The change in the wind direction occurence is similar as observed during the two ExINP_GVB campaigns, where the south-easterly and easterly wind occurence decreases by 64 % and 65 %, respectively. The INAS density generally decreases during periods, where southerly and northerly wind occurence increases.

For the higher episodes (see figure 4.25), the median ambient temperatures is lower −4.7 °C compared to the whole campaign period, with first and third quantile being −5.6 °C and −3.6 °C, respectively. The relative humidity remains unchanged and exhibits the same behaviour as for the lower episodes and for the general campaign period. The wind speed is higher with a median of 4.4 $\mathrm{m\,s^{-1}}$ and a first and third quartile of 3.2 $\mathrm{m\,s^{-1}}$ and 5.7 $\mathrm{m\,s^{-1}}$, respectively. Again, the strongest decrease in occurence is seen for south-easterly winds with a relative change of 60 %. In contrast to the ExINP_GVB campaigns, there is an increased occurence of southerly winds (90 %) with a total occurence of 13 %. There might be a bias, since the wind measurements are taken from the foot of the Zeppelin mountain, therefore not representating the exact wind fields at the top of the mountain.

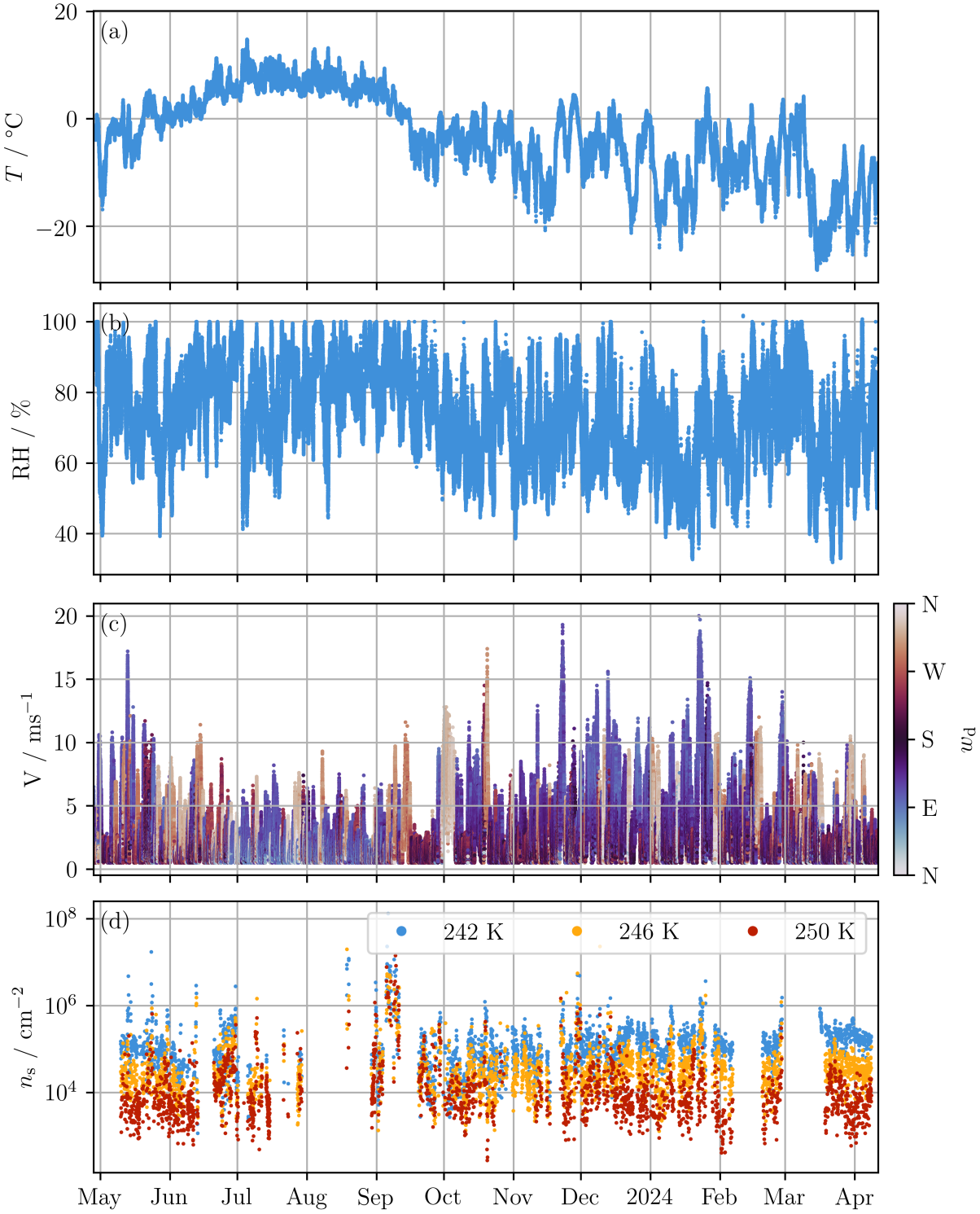

Figure 4.23.: **Atmospheric conditions during ExINP_ZEP.** Panel (a) shows the ambient temperature with the relative humidity visualized in panel (b). In panel (c) the wind speed is visualized with the corresponding wind direction denoted on the colorbar. Panel (d) visualizes the INAS density for three temperatures. All meteorological data is measured at 2 m agl.

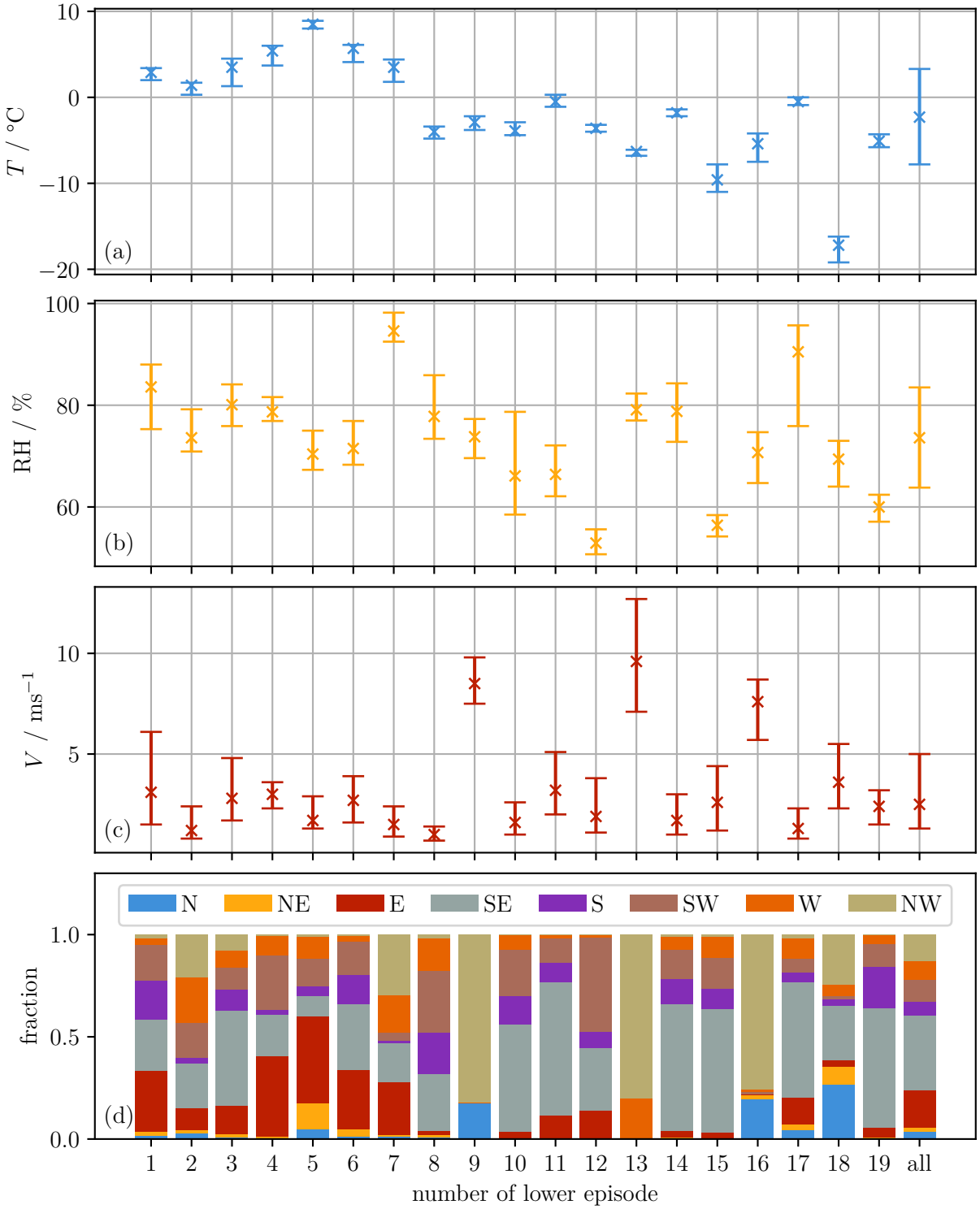

Figure 4.24.: **Atmospheric conditions during lower INAS density episodes during ExINP_ZEP.** Panel (a) shows the ambient temperature, with the median, the first and third quartile. Panel (b) and (c) represent the same for the relative humidity and the wind speed, respectively. Panel (d) visualizes the fraction of the eight wind vectors for the lower episodes. The atmospheric conditions during the whole campaign are shown on the far right.

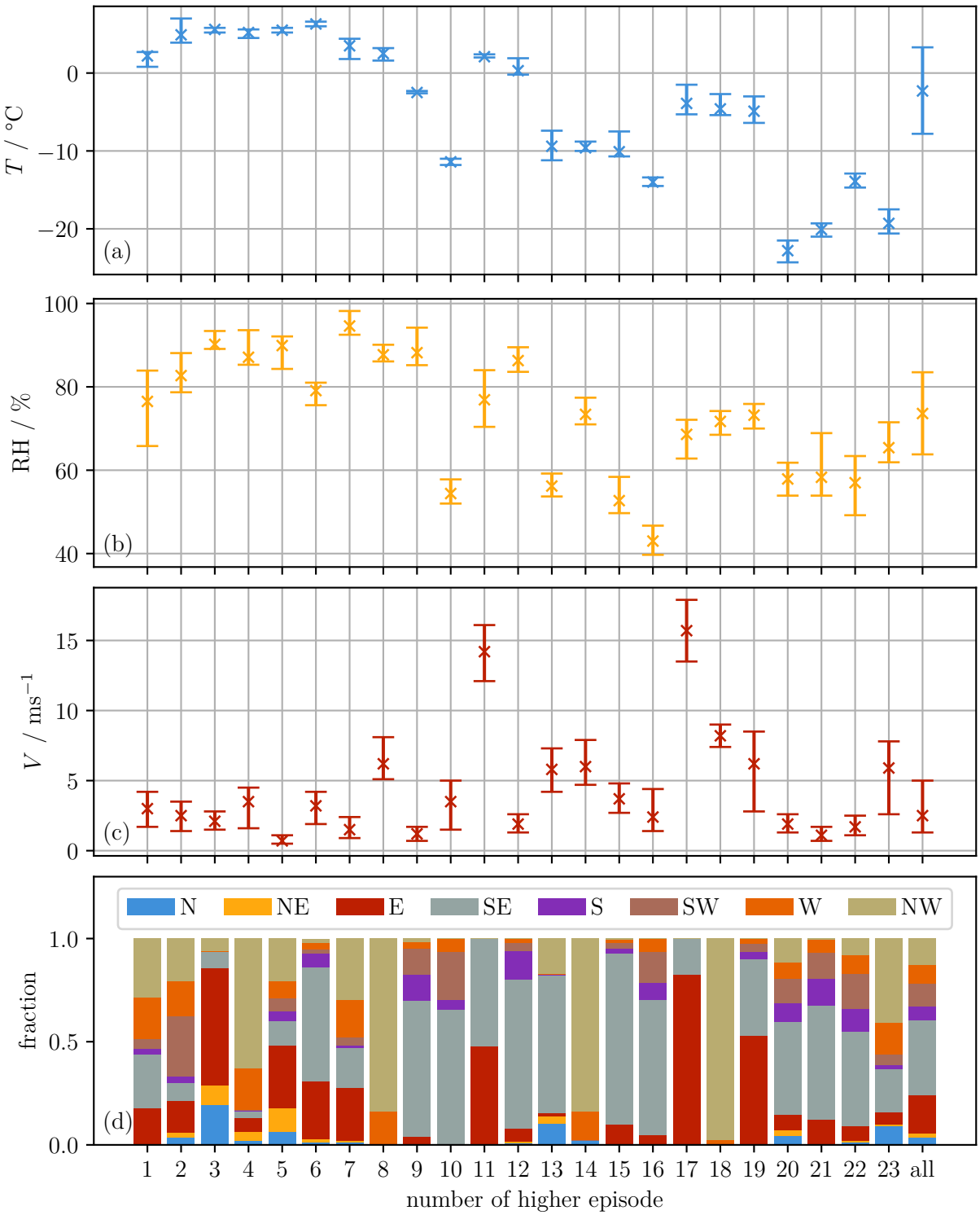

Figure 4.25.: **Atmospheric conditions during higher INAS density episodes during ExINP_ZEP.** Panel (a) shows the ambient temperature, with the median, the first and third quartile. Panel (b) and (c) represent the same for the relative humidity and the wind speed, respectively. Panel (d) visualizes the fraction of the eight wind vectors for the higher episodes. The atmospheric conditions during the whole campaign are shown on the far right.

4.4. Mineral dust age and source for INAS density measured during ExINP_ZEP

FLEXPART was used to calculate the arriving dust aerosol at ZEP in 2023. The sources are defined by the FLEXDUST module as described in section 3.4.2. The present section provides a concise overview of the typical dust age for the location and provides a detailed and summarized look at the conditions that are typical for lower and higher INAS densities to assess whether the different episodes are influenced by different dust sources.

4.4.1. General overview of dust age

The age of dust particles is calculated from the start of its emission up to a maximum age of 30 days. In the following, the dust aerosol arriving at an altitude of 500 m asl, which corresponds to the height of ZEP, is discussed. Figure 4.26 visualizes the mean dust age for each month for the seven smaller particle diameters DU01 to DU07 ($d_p = 0.04,\ 0.22,\ 0.71,\ 1.304,\ 2.057,\ 3.53$ and $6.1\,\mu m$). This roughly corresponds to the particle size that is able to enter the PINE chamber (see also section A.1 for the transport efficiency of the PINE inlet). There is a general seasonal behaviour with older dust arriving during summer months, with a maximum age around June. The age of dust is smallest during the winter months, especiailly during January and February. This is likely related to the build-up of AH during the transition from autumn into winter (see also section 2.4.1). While the polar dome restricts the long-range transport of aerosol from southern latitudes, the arriving dust might be from within the polar dome and is therefore travelling for a shorter duration to the recipient. This is even more pronounced when looking at dust arriving at 1500 m asl, visualized in figure 4.27. A difference in the vertical layers has been seen before during AH periods before (e.g., Bozem et al. 2019; Jurányi et al. 2023, see also section 2.4.1).

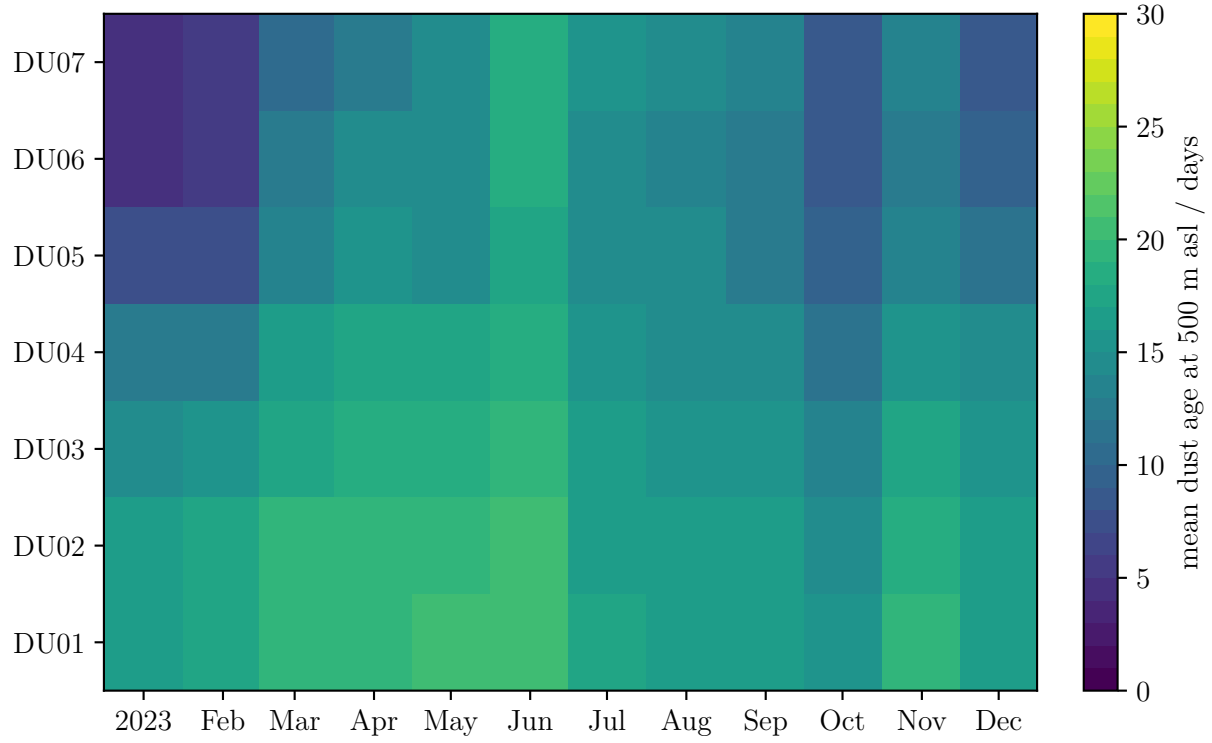

Figure 4.26.: **Mean age of dust arriving at ZEP at** 500 m **asl calculated for each month and each diameter bin.** The dust bins DU01, DU02, DU03, DU04, DU05, DU06 and DU07 correspond to the particle diameters 0.04, 0.22, 0.71, 1.304, 2.057, 3.53 and 6.1 µm.

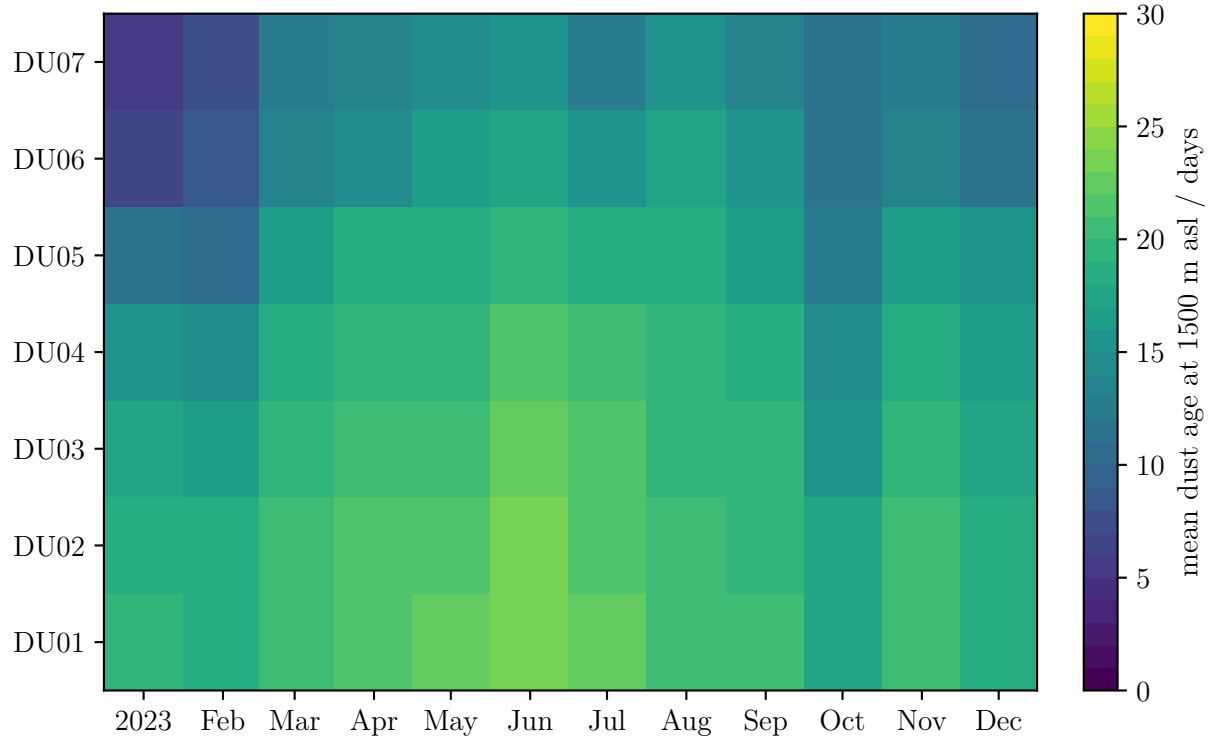

Figure 4.27.: **Mean age of dust arriving at ZEP at** 1500 m **asl calculated for each month and each diameter bin.** The dust bins DU01, DU02, DU03, DU04, DU05, DU06 and DU07 correspond to the particle diameters 0.04, 0.22, 0.71, 1.304, 2.057, 3.53 and 6.1 µm.

4.4.2. Dust age during lower and higher INAS density episodes

The dust age is calculated for the lower and higher INAS density episodes. The median dust age is shown in figure 4.28 for the general case and the lower and higher episodes. The smaller dust particles are generally older, reaching a median age of 17.1 d, while larger dust particles are typically younger with a median age of 13.7 d for the particle bin of size 3.53 µm (DU06). This median age decreases during lower episodes to 16.1 d and 10.9 d for the particle size bins DU01 and DU06, respectively. Lower ages indicate that the source is closer to the recipient, which would mean that sources closer to the recipient exhibit a lower INAS density, when considering only the dust contribution. It could also indicate that the dust has travelled faster to the receptor. Please note that other sources, i.e. biogenic sources, are not included in this analysis. For the higher episodes, the behaviour is typically the opposite with the median age increasing compared to the general median age to 18.2 d for the smallest particle size bin DU01.

For larger particle size bins, the age generally varies for lower and higher episodes to a higher degree. The first and third quartile of the particle size bin DU06 during higher episodes are 10 d and 18.2 d, respectively. This is likely due to the decreased statistic, where many more particles are emitted for smaller size bins. In summary, higher INAS density episodes happen during periods, where the median age of dust particles is higher compared to the general case, especially for smaller size bins (<1.304 µm, DU04). The opposite is true for periods, where the INAS density is considered to be low, with the median dust age lower for all size bins.

The INAS density of the dust particles does not only depend on their source, but might also be affected by aging effects that enhance or suppress the ice nucleation ability of dust particles during transport (e.g., Boose et al. 2016). To understand, if there is a clear dependence on the source of the dust particles, the source of the dust particles is grouped for all lower and higher INAS episodes and the general case in the next section.

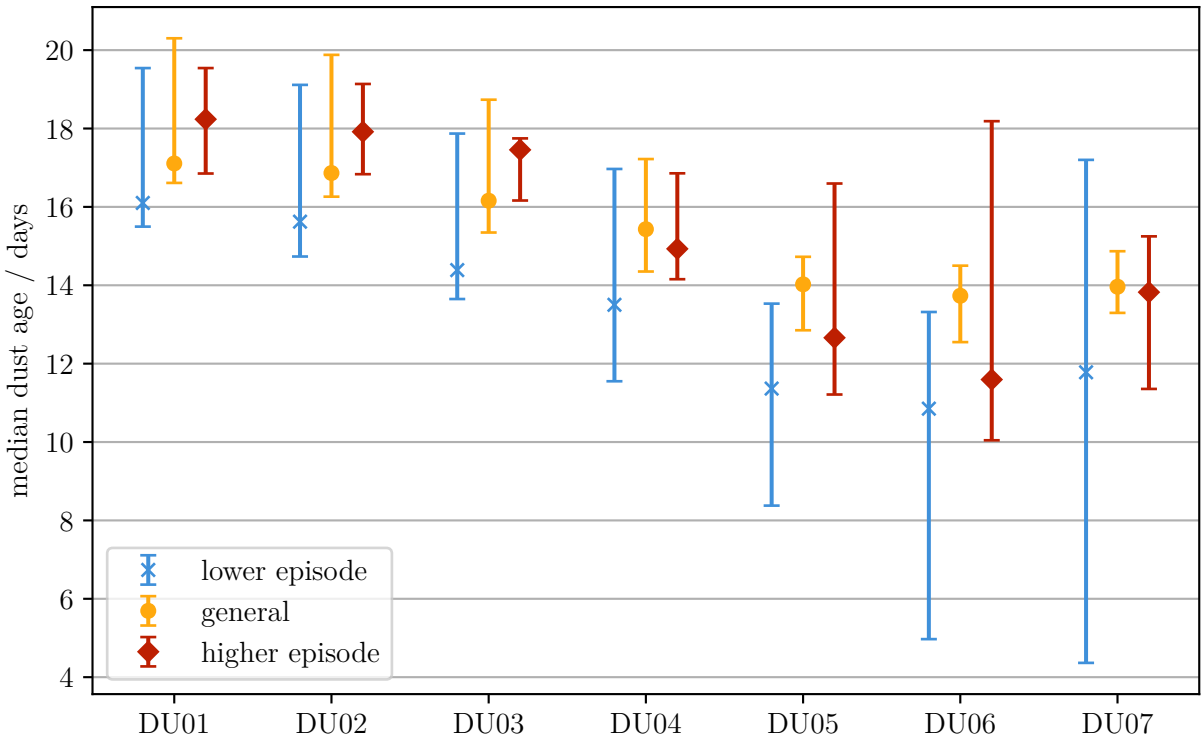

Figure 4.28.: **Mean age of dust arriving at ZEP at** 500 m **asl calculated for lower, general and higher INAS density episodes and each diameter bin.** The dust bins DU01, DU02, DU03, DU04, DU05, DU06 and DU07 correspond to the particle diameters 0.04, 0.22, 0.71, 1.304, 2.057, 3.53 and 6.1 µm. The median is shown and the errorbars denote the first and third quartile.

4.4.3. Dust source during lower and higher INAS density episodes

Ten different sources are defined for FLEXPART. The source 'ocean' is set to zero emission for the dust emission simulated by FLEXDUST. Some sources do contribute a negligible amount to the total mass of dust aerosols arriving at ZEP and are therefore removed from the following discussion, these are namely: South America, Central America and Australia. The other sources do contribute to the dust population at ZEP and are denoted as: GRE - Greenland, NA - North America, AF - Africa, EU - Europe, RU - Russia and AS - Asia (see also figure 3.18 and section 3.4.2). The contribution to the overall dust mass concentration is visualized in figure 4.29 as a fraction for the seven particle size bins DU01 to DU07. Each panel provides the contribution from one source region and the median and the first and third quartiles are plotted.

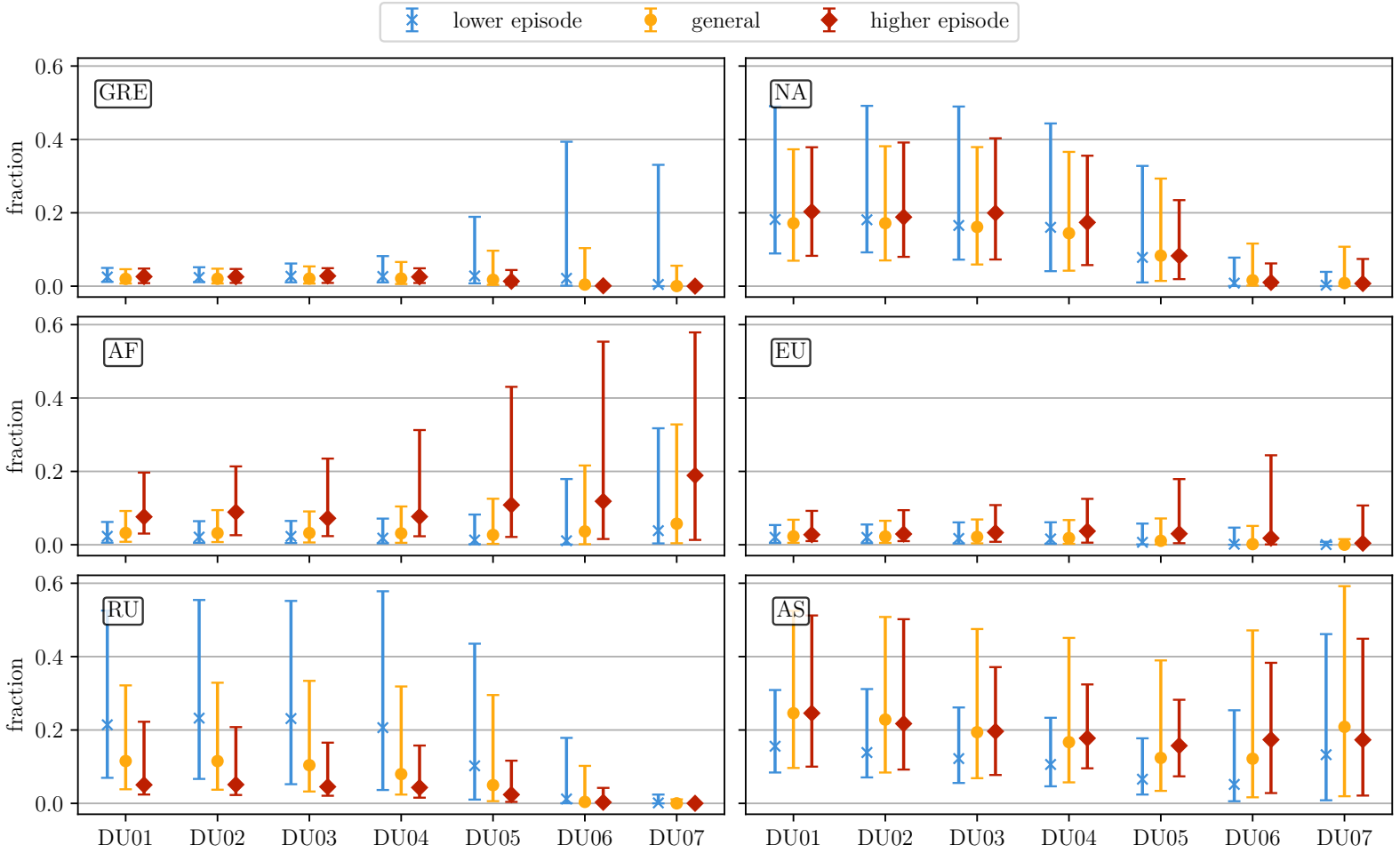

Figure 4.29.: **Mean age of dust arriving at ZEP at** 500 m **asl calculated for lower, general and higher INAS density episodes and each diameter bin.** The dust bins DU01, DU02, DU03, DU04, DU05, DU06 and DU07 correspond to the particle diameters 0.04, 0.22, 0.71, 1.304, 2.057, 3.53 and 6.1 µm. The median is shown and the errorbars denote the first and third quartile.

The general overview looks at the contribution during the whole period, where FLEXPART data and INAS densities are available, which is between April 2023 until the end of 2023. There is very little contribution from sources located in Greenland for all size bins, but the third quartiles generally increases for larger particle size bins. This is likely due to the distance between the recipient and Greenland: larger aerosol particles typically do not travel longer distances, therefore closer sources will contribute proportionally more towards the larger size bins. Approximately one fifth of the dust originates in North America for smaller particles sizes (<1.304 µm, DU04), decreasing for larger particle sizes. The contribution from sources located in Africa stays relatively constant for the different sizes with a median fraction of 3 % for the particle size 0.22 µm (DU02). There is a slight increase for larger particle sizes to 6 % for the particle size 6.1 µm (DU07). The contribution of sources in Europe are slightly smaller than the contribution from sources located in Africa and decrease for larger particle sizes with the median fraction of 2 % for the particle size 0.22 µm (DU02). Dust originating in Russia behaves similar to dust from sources in North America with a decrease in contribution for larger particles sizes with an overall fraction of 12 % for the particle size 0.22 µm (DU02). Sources located in Asia contribute the largest fraction of dust to the dust population at ZEP at an altitude of 500 m asl. For the smaller size bin DU02 the median fraction is 23 %, a relative increase of 33 % compared to the second most often occuring source region North America. This generally decreases for larger particles sizes, although there is a slight increase for the larger particle size bin DU07 (6.1 µm), although the first and third quartiles are 8 % and 51 %, respectively. The spread is generally higher for larger particle sizes.

Looking at the source contribution during lower and higher INAS density episodes, the behaviour is opposed for the dust originating in Greenland. The contribution during lower episodes is small, but larger than the general case with a median fraction of 2 % at the particle size 0.22 µm (DU02). There is a large spread towards larger particle sizes. For the higher episodes, the contribution is similar, but negligible for particle sizes above 2.057 µm (DU05). The behaviour for North America is very similar between the general period and lower and higher episodes, indicating that the dust contribution from North America is generally not leading to a decrease or increase of the INAS density of the dust population at ZEP. This is different for the contribution from sources located in Africa. During lower episodes, the fraction is lower compared to the general case. There is a clear increase of the source contribution during higher episodes, especially at larger particle sizes. At the smaller particle size bin of 0.22 µm (DU02) the median fraction is 9 %, which increases to 19 % for the size bin DU07 (6.1 µm). Larger dust particles originating from Africa contribute the largest fraction during higher INAS density episodes. The European contribution is largely similar, although there are some increases during higher episodes with a fraction of 3 % for the particle size 0.22 µm (DU02) compared to 2 % in the general case. This behaviour is contrary to the dust originating in Greenland, therefore indicating that an increased influence of European sources increases the INAS density, while an increased influence from sources located in Greenland decrease the INAS density. A strong difference is seen for sources located in Russia. During lower episodes, the strongest contribution to the dust population at ZEP are sources located in Russia. The median increase to a maximum of 23 % for the particle size 0.22 µm (DU02) and dropping for particle sizes larger than 1.304 µm (DU04). During higher episodes, the contribution is decreasing to 78 % for the particle size 0.22 µm (DU02) compared to the contribution during lower episodes. The contribution of dust originating in Asia is similar during the general period and higher periods, although there is a slight decrease for larger particle sizes. For lower episodes, the contribution of sources from Asia to the dust population is lower with a median fraction of 14 % for the particle size 0.22 µm (DU02). There is a general increase in the largest particle size bin (DU07), but the spread is generally very high.

To summarize, sources from North America and Asia generally contribute during the whole

campaign period, also during lower and higher INAS density episodes. They might be contributing to the overall background of the dust population and therefore not show a clear difference during differen episodes. The largest contribution of dust which exhibits a higher INAS density is from Africa, especially for larger particle sizes. The opposite is true for sources originating in Russia. Dust from sources located in Russia contribute largely during lower episodes.

4.5. Local source investigation during ExINP_GVB 2023

Previous discussions have focused on the investigation of the INP concentration and its connection to local atmospheric and aerosol parameters. INAS densities were calculated to normalize the INP concentration on the number of AS. To investigate a local influence of sources that are not attributed for when considering FLEXPART simulations, snow and ocean water samples were collected around Ny-Ålesund.

4.5.1. Snow samples

The frozen fraction of the four surface snow samples are visualized in figure 4.30. Each panel visualizes the water background used in INSEKT. For panel (a) all undiluted snow samples show freezing spectra differing from the water background. There is a clear difference between the four samples collected on 21st March 2023, 28th March 2023, 11th April 2023 and 2nd May 2023. To investigate differences in the measured INPs, the temperature at which half of the droplets is frozen

$$T_{0.5} \coloneqq T(f_f = 0.5) \tag{4.3}$$

is used. The highest freezing temperature is seen for the sample collected on 2nd May 2023 with $T_{0.5} = 265.5\,\mathrm{K}$. The second and third highest freezing temperatures were seen in the samples collected during the second half of March 2023 with $T_{0.5} = 263.0\,\mathrm{K}$ and $T_{0.5} = 260.5\,\mathrm{K}$, respectively. The lowest freezing temperature is seen in the sample collected in between those in April 2023 with $T_{0.5} = 253.5\,\mathrm{K}$. Panel (b) shows the same for the snow sample diluted with a dilution factor $d = 15$. The order in which the diluted samples freeze is the same as for the undiluted samples. The snow sample collected on 2nd May 2023 freezes at $T_{0.5} = 263.5\,\mathrm{K}$, which is around 9 to 11.5 K higher compared to the other diluted samples. The freezing spectra of the most diluted samples ($d = 225$) are visualized in panel (c). There is only very little difference between the water background and all diluted snow samples. The only significant difference is again shown for the sample collected in early May 2023, wich freezes at $T_{0.5} = 257.5\,\mathrm{K}$.

The four snow samples were also analyzed utilizing the IR-CS with the aim of expanding the temperature range towards lower temperatures. During the experiments, the water background froze at around $T_{0.5} = (243.15 \pm 0.35)\,\mathrm{K}$. The undiluted snow sample collected on 21st March 2023 had a freezing temperature of $T_{0.5} = (244.57 \pm 0.28)\,\mathrm{K}$. One week later, the freezing temperature is slightly higher with $T_{0.5} = (245.51 \pm 0.25)\,\mathrm{K}$. In early April 2023, the freezing temperature decreased slightly to $T_{0.5} = (243.92 \pm 0.25)\,\mathrm{K}$. Overall, these three samples do not show a clear difference in their INP concentration. In early May 2023, the freezing temperature increases to $T_{0.5} = (254.10 \pm 0.29)\,\mathrm{K}$, showing a clear change in the INP population contained in the snow sample. The frozen fraction is visualized in figure 4.31 with the differential spectrum calculated in bins of 0.5 K. The differential spectrum shows a maximum at around 252 K, indicating that the largest contribution to the INP population is active at 252 K considering only the temperature range between 250 K and 261 K.

The increase in ice nucleation ability at a relatively high temperature of $T_{0.5} = 265.5\,\mathrm{K}$ (INSEKT) and $T_{0.5} = (254.10 \pm 0.29)\,\mathrm{K}$ (IR-CS) indicates a biogenic component in the INP population measured in the surface snow. This could be from deposited material on the surface, for example from the local fjord. The following section investigates the INP concentration in the fjord from collected ocean water samples.

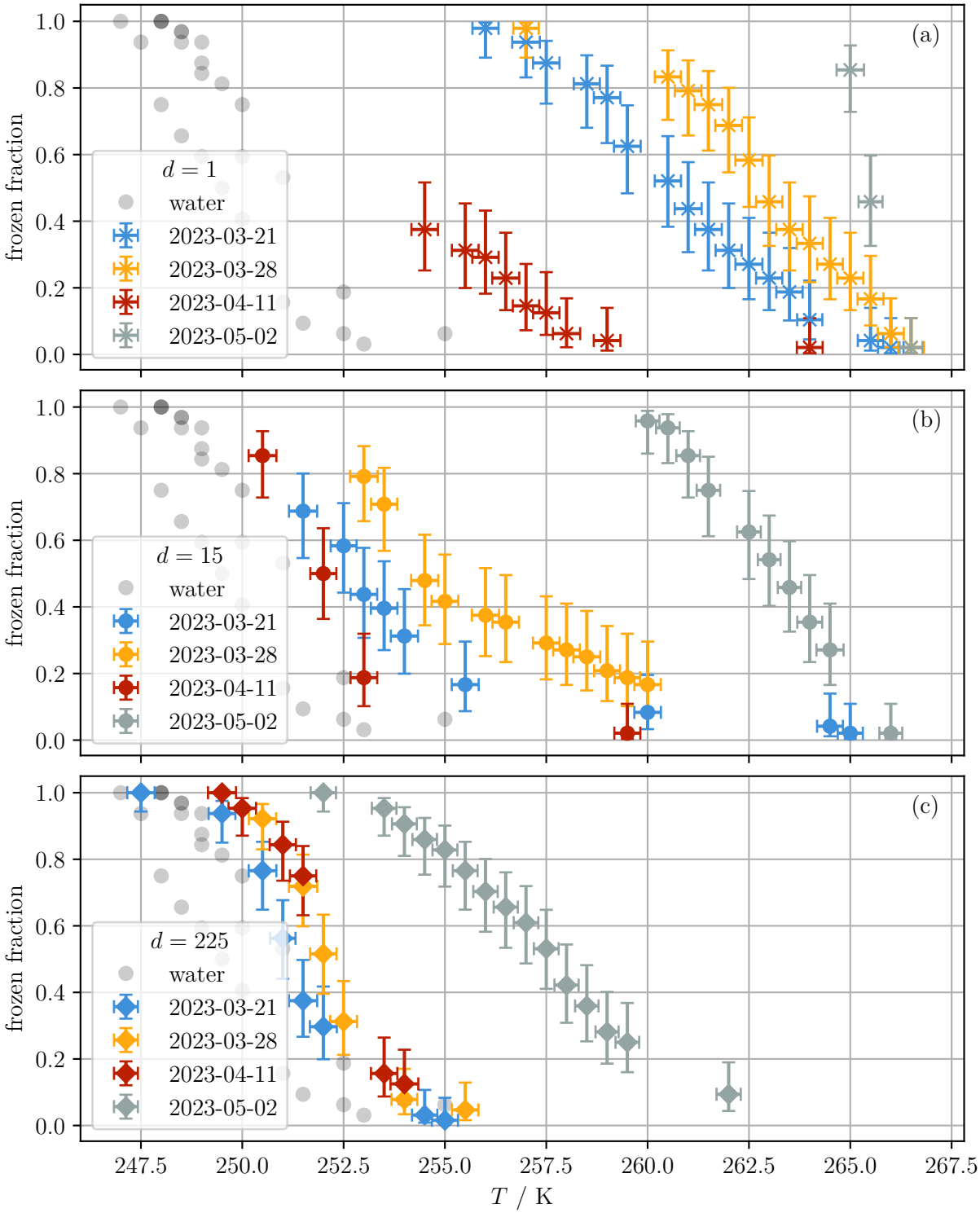

Figure 4.30.: **Frozen fraction of snow samples as a function of the nucleation temperature.** Panel (a) shows the frozen fraction of the undiluted samples. Panel (b) and (c) visualize the frozen fraction of diluted samples with dilution factors $d = 15$ and $d = 225$, respectively. In all panels the corresponding background water is plotted as grey circles.

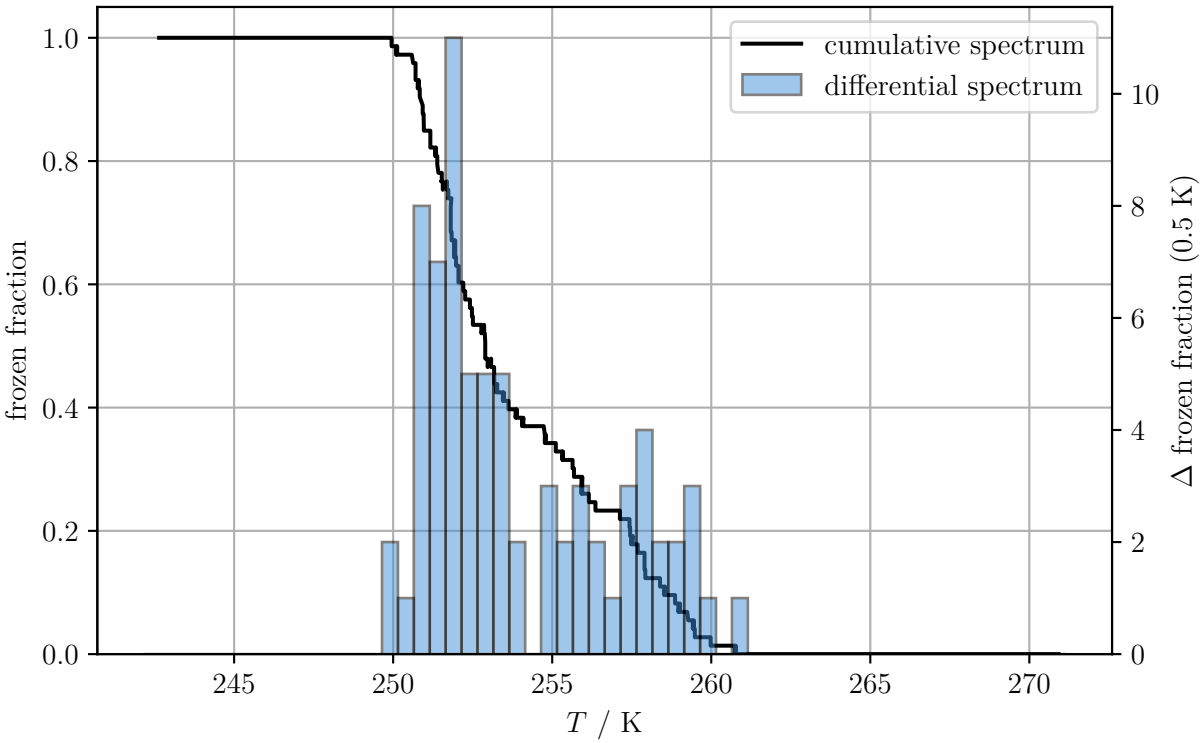

Figure 4.31.: **Frozen fraction of the snow sample collected on 2nd May 2023.**

4.5.2. Ocean samples

The ocean samples were analyzed using INSEKT and their freezing temperature corrected corresponding to its salinity. INPs originating from the ocean might be related to biogenic activity. The CHL mass concentration is used as a proxy for biogenic activity in the Kongsfjord. The Spearman rank correlation coefficients was calculated between the INP concentration and the CHL mass concentration. None of the correlation coefficients were statistically significant considering a p-value of 0.05. The frozen fraction of selected freezing temperatures are visualized in figure 4.32 over the time period investigated. The CHL mass concentration is visualized on the second y-axis, showing a clear increase between end of April and during the first half of May. This is coinciding with the algae bloom inside the Kongsfjord as can be seen in figure 4.32. This biogenic activity may lead to the emission of biogenic aerosol into the atmosphere. This can be seen by looking at the higher temperatures: at 262 K, most of the samples collected during May 2023 show an earlier freezing, although the statistic is not large enough to provide a statistically significant result.

After heating the samples at 100 °C for 20 min, the reduction in the ice nucleation ability of the INP population is investigated and visualized in figure 4.33 together with the CHL mass concentration. The same freezing temperatures as before are shown, and a clear difference can be seen to the original samples. The removal of heat-labile INPs leads to a strong decrease in the ice nucleation ability of the ocean water samples on the considered freezing temperatures, even below the limit of detection for freezing temperatures above 258 K. This could indicate that a biogenic component contributes to the total INP population. However, also other non-biogenic material may not be active as an INP after heat treatment.

The ocean samples were collected from the surface, but not from the SML. This might lead to a difference between the INP population in the bulk surface water and the fraction of the INP population that is actually emitted into the atmosphere. In addition, the data was corrected assuming a constant salinity, unaffected for example by the local melting of sea ice. This might lead to a bias, seen before by Irish et al. (2017), who associated INP found in bulk ocean water to melting sea ice. During this work, individual measurements of the salinity were not performed.

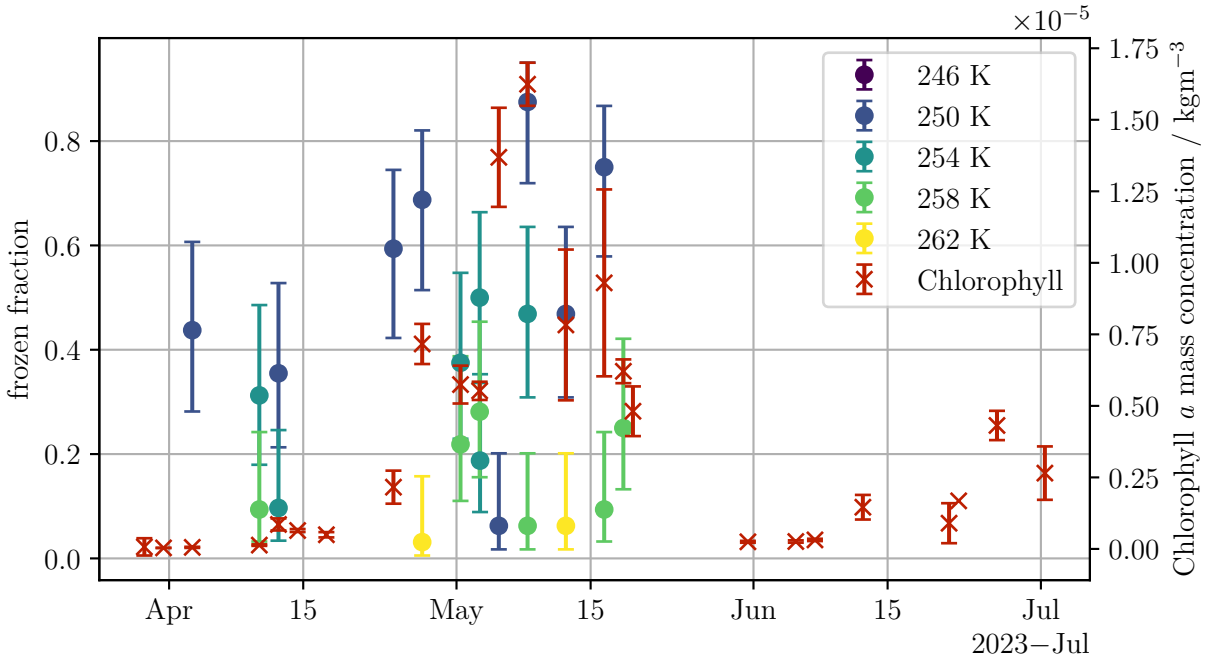

Figure 4.32.: **Frozen fraction of ocean samples collected from the surface as a timeseries during the ExINP_GVB 2023 campaign.** Five selected temperatures are used to assess the frozen fraction of the undiluted ocean water samples. The CHL mass concentration measured at a depth of 5 m is visualized on the secondary y-axis.

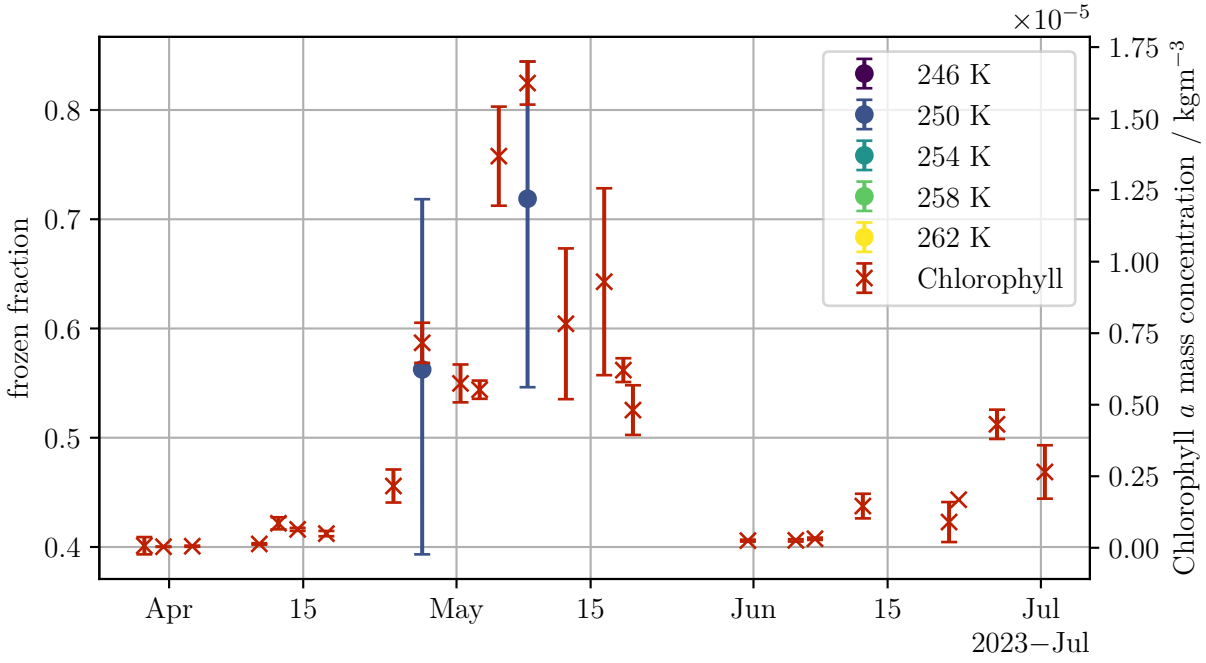

Figure 4.33.: **Frozen fraction of heated ocean samples collected from the surface as a timeseries during the ExINP_GVB 2023 campaign.** Five selected temperatures are used to assess the frozen fraction of the undiluted and heated ocean water samples. The CHL mass concentration measured at a depth of 5 m is visualized on the secondary y-axis.

4.5.3. Comparison between samples collected from surface snow, ocean samples and atmosphere

Aerosol can be emitted from snow surfaces as well as from the ocean. The probability of blowing snow can be estimated by using source functions that take the wind speed, the age of snow and the ambient temperature into account (Li and Pomeroy 1997). The probability of blowing snow is calculated utilizing the wind speed and ambient temperature measured at 2 m agl on the AWI meteorological tower (Maturilli et al. 2013). The snow age was determined using data provided by University of Cologne, utilizing a Pluvio (Pluvio^2 L 400 RH, OTT HydroMet GmbH Saha et al. 2021) and Parsivel (2.11.6, OTT HydroMet GmbH Park et al. 2017) system, and calculating the time since the last snow fall. The probability of blowing snow is visualized on a one hour resampled interval in figure 4.34 (see also section 3.5.4). There are six cases, where the probability is larger than 10 %, while a probability of 50 % is only reached twice. Focusing on the second event on 5th April 2023 (highest probability of blowing snow), the probability of blowing snow is visualized in panel (a) of figure 4.35. After noon on 5th April 2023, the probability of snow increases alongside the INP concentration measured below 243 K (see figure 4.35, panel (c)). No aerosol data is available during this period since the SMPS malfunctioned. After the maximum of the INP concentration, the precipitation sets in, mostly consisting of snow at higher intensity. The INP concentration decreases after 6th April 2023 midnight GMT. During this decrease snow turns into graupel and and rain, leading to the decrease of the INP concentration by more than two orders of magnitude in less than 24 h due to wet removal.

This is just one example so there can be no definite answer, whether blowing snow leads to an increase in local INP concentration. There is, however, some indication that surface snow can contain aerosol particles that are active as INPs at relatively high subzero temperatures (e.g., Macdonald et al. 2017). Together this could mean that locally deposited aerosol onto the surface snow layer might get introduced into the atmosphere, especially during higher wind speeds. More detailed measurements are needed to draw a conclusion, especially regarding the determination of blowing snow. For this case, the blowing snow was also observed in person, but the used source function does rely on measurements taken in Canada. The conditions for blowing snow might be different on Svalbard, where the local orography plays a large role in the distribution of snow and its density (e.g., Gallet et al. 2019).

The meteorological conditons can also be investigated utilizing the footprint of mineral dust simulated via FLEXPART. During noon of 5th April 2023, the footprint for mineral dust of size 0.71 µm is centered around Svalbard for the receptor at ground level (panel (a) in figure 4.36). There is some influence from nothern Europe for higher altitudes, but mainly from the eastern coast of Greenland and the Atlantic. Looking at the same visualization one day later (see figure 4.37), the influx of relatively warm and humid air can be clearly seen across all four selected altitudes (0, 500, 1000 and 1500 m agl). This air lead to an increase in temperature and subsequent wet precipitation that likely removed a large fraction of the INP population from the atmosphere.

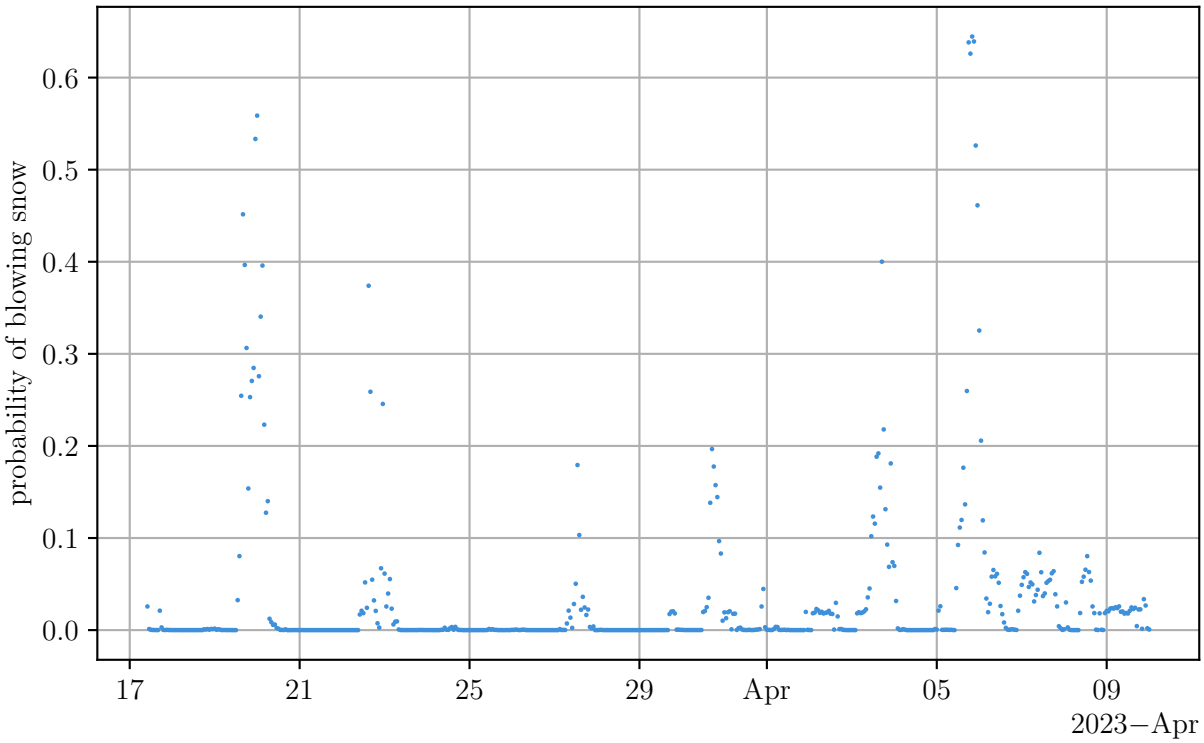

Figure 4.34.: **Probability of blowing snow during ExINP_GVB 2023.** The probability was calculated using measurements taken at 2 m agl after Li and Pomeroy (1997). The 1 h mean of the probability is visualized.

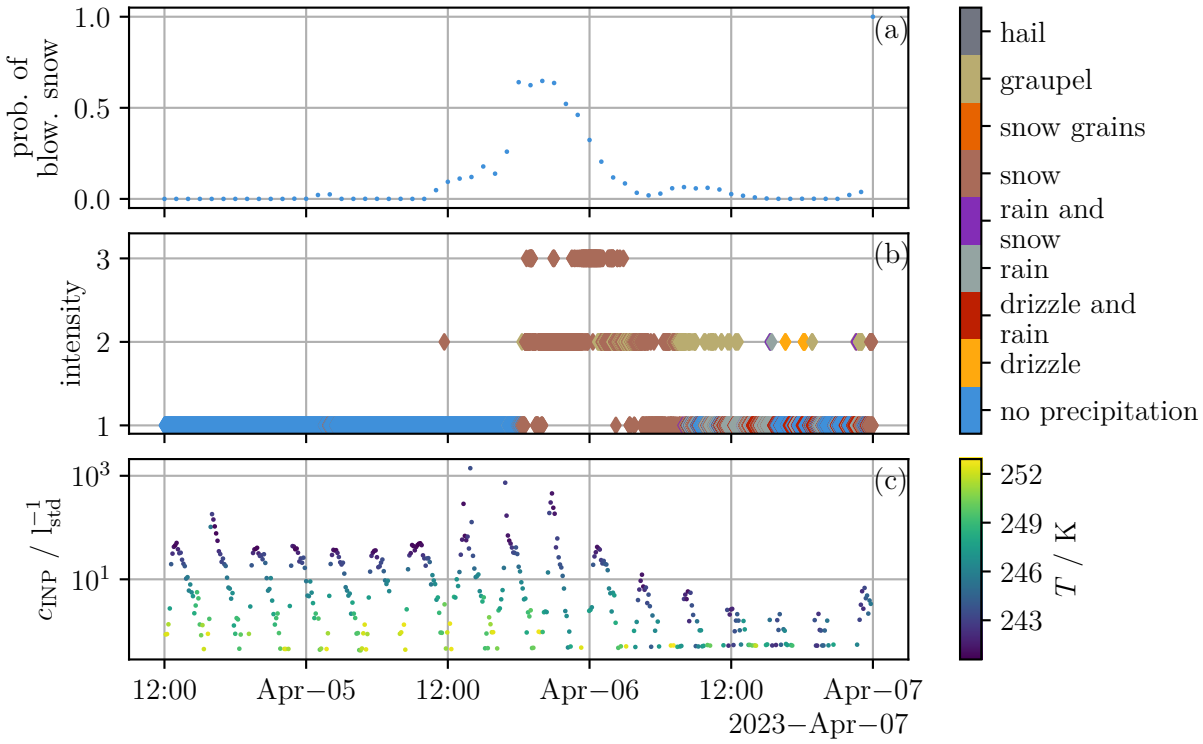

Figure 4.35.: **Blowing snow probability, precipitation properties and INP concentration measured during ExINP_GVB 2023.** Panel (a) shows the calculated probability of blowing snow. In panel (b) the intensity and type of precipitation are visualized. The INP concentration measured by PINE is shown in panel (c) with the freezing temperature shown on the corresponding colorbar.

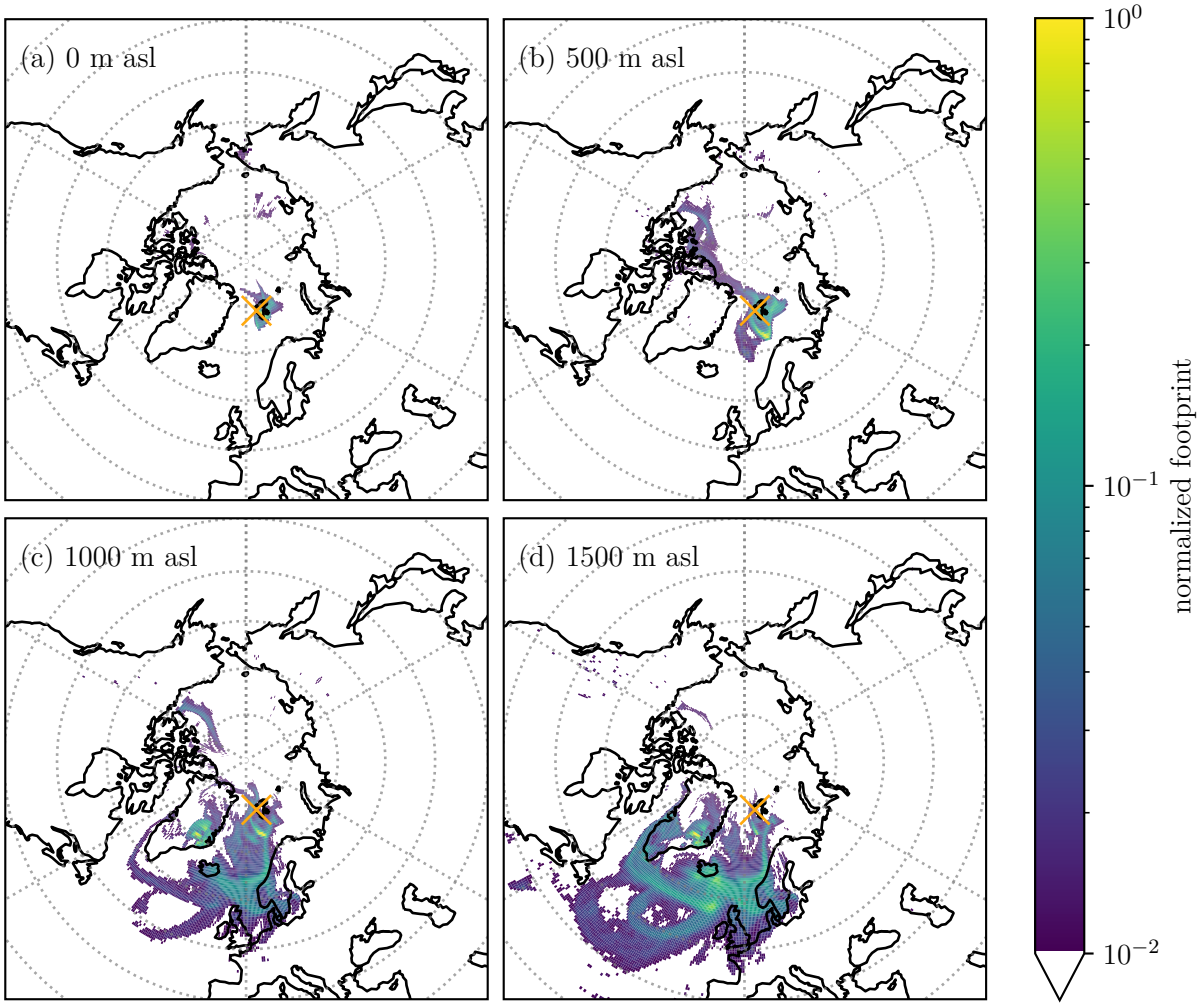

Figure 4.36.: **Footprint emission sensitivity simulated by FLEXPART during ExINP_GVB 2023 on 5th April 2023 noon GMT.** The normalized footprint is defined by equation (3.45). The orange cross marks the receptor location.

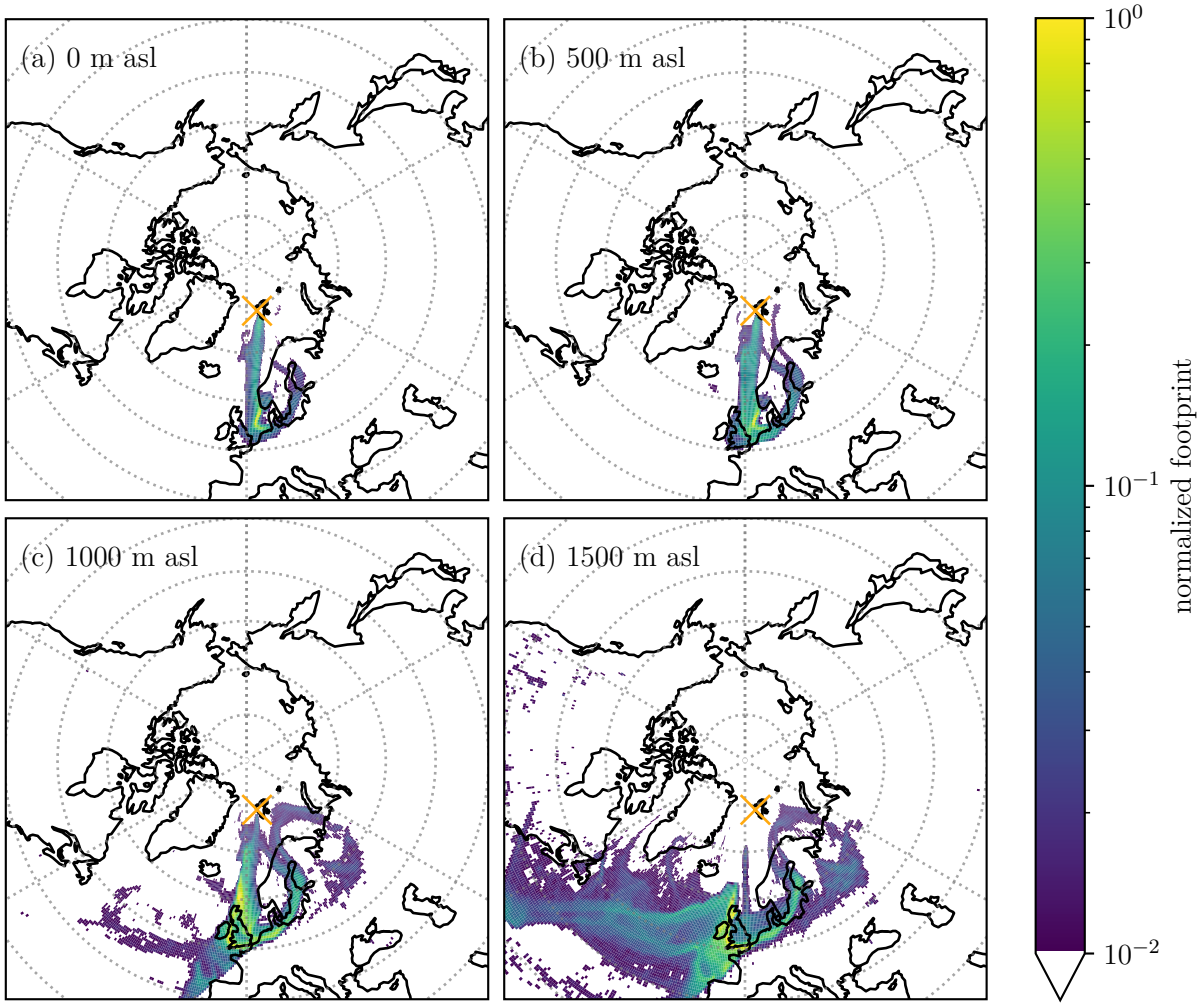

Figure 4.37.: **Footprint emission sensitivity simulated by FLEXPART during Ex-INP_GVB 2023 on 6th April 2023 noon GMT.** The normalized footprint is defined by equation (3.45). The orange cross marks the receptor location.

4.6. UAV-based measurements during PaCE 2022

During an intensive operation period during the PaCE 2022 campaign, the vertical distribution of the INP concentration was investigated. For this, a novel setup of a UAV-based aerosol filter sampler was applied and results were compared to ground-based filter measurements (see section 3.3). The technical description of the setup is published in its technical paper (Böhmländer et al. 2024).

4.6.1. Comparison between ground- and UAV-based measurements of the INP concentration

Figure 4.38 visualizes the INP concentration measured on the ground (GND) and on board the UAV (UAV) for eight selected temperatures: 248 K, 250 K, 252 K, 254 K, 256 K, 258 K, 260 K and 262 K. The errorbars represent the 95 % confidence intervall and are only plotted if both filters have a similar[1] start time.

Two experiments at the start of the campaign on 30th September 2022 9.43 am GMT (300 m agl) and 1st October 2022 10.55 am GMT (600 m agl) show a slight difference between the two altitudes. The INP concentration is generally higher for the higher altitude or within uncertainties at 256 K. For the second filter on 1st October 2022, where the altitude is double that of the first filter, the difference is increased. Looking at the individual freezing spectra (figures C.2 and C.3), the UAV filter shows high activity around 257.5 K, which is not seen on the ground. This might indicate different air masses that arrived at different altitudes, although more detailed analysis is needed.

Looking at the next two experiments on 5th October 2022 10.41 am GMT (300 m agl) and 6th October 2022 2.31 pm GMT (300 m agl), the INP concentration measured on the UAV is again higher for both experiments and across all temperatures (see also figure C.4). However, an issue during handling and a potential contamination cannot be ruled out for the second filter (see figure C.5).

On 8th October 2022 two experiments were conducted with the first filter being flown at 200 m agl and the second filter being flown at 300 m agl. The filter flown in the first half of the day shows the opposite behaviour as seen before with a higher INP concentration measured on the ground (see also figure C.6). The measured INP concentration is similar down to around 258 K and then the difference increases for lower temperatures. In the afternoon, the INP concentration measured at 300 m agl is higher across all temperatures compared to the ground-based filter (see also figure C.7). This indicates that a change during the day lead to an inversion of the INP concentration with altitude, although more data is needed to provide a more conclusive explanation.

Two days later, two experiments were conducted again, although for the second experiment in the afternoon on 10th October 2022 there is no corresponding data for the ground-based filter available. The INP concentration measured at 300 m agl is higher across the whole temperature range compared to the ground-based measurement in the morning (see also figure C.8). The INP concentration is similar around 256 K, but they are still clearly different, showing a clear dependence on the altitude for the selected case.

[1] The maximal difference is set to 300 s, since there are sometimes slight differences due to organization. Considering a typical sampling time of 2 h, this corresponds to 4 % of the typical sampling time.

In contrast, the two experiments on 11th October 2022 generally do not show a difference between the different altitudes as measurements are within uncertainties. For the sample collected in the morning at 200 m agl there is a slightly steeper increase in the INP concentration at 261 K for the ground-based filter, but the shift is still within uncertainties (see also figure C.9). It looks similar in the afternoon, where there is a strong increase around 258 K, seen in both filters, although there is a slightly steeper increase for the freezing spectra obtained from the aerosol collected at 350 m agl (see also figure C.10). Both of this indicate that the lower atmosphere is well-mixed, on the afternoon even showing a strong influence of a certain aerosol that is active around 258 K.

During all these measurements, the PINE was measuring on Sammaltunturi at 565 m asl, which is around 257 m higher compared to the ground-based filter and therefore can represent the INP concentration measured utilizing the filter on board the UAV at an altitude of around 257 m agl. The PINE measurements of the INP concentration typically do not overlap with the temperature range observed with INSEKT, therefore a direct comparison is not possible. However, generally the measurements align well and continue the freezing spectra for lower temperatures. This can be seen in the figures shown in section C.2.

The following two sections provide two cases and investigate the difference of air masses utilizing Hybrid Single-Particle Lagrangian Integrated Trajectory model (HYSPLIT) backward trajectories.

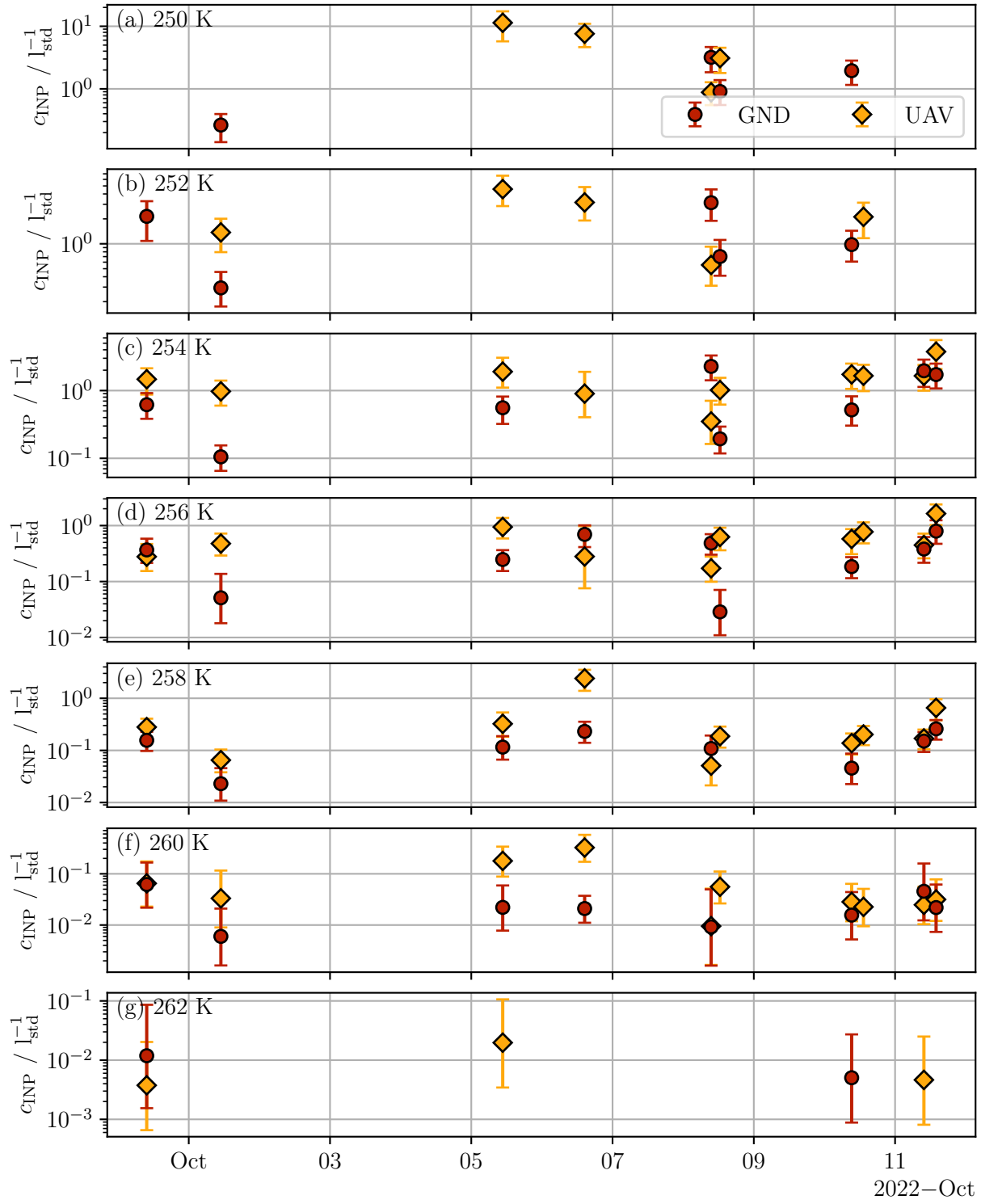

Figure 4.38.: **Ice-nucleating particle concentration for uncrewed aerial vehicle- and ground-based filters for selected freezing temperatures.** Pairs are defined for a start time of the filter sampling deviating less than 300 s.

4.6.2. Event: 11th October 2022 - same INP concentration at 200 m agl

To investigate the air masses during the vertical measurements, HYSPLIT was used to calculate hourly back trajectories over ten days on four different altitudes: 250, 500, 750 and 1000 m agl (see also section C.3.2).

The INP concentration is the same at the ground and at 200 m agl during the experiment on 11th October 2022 9.48 am GMT, visualized in figure 4.39. The measurements by the PINE instrument, corresponding to an altitude of 257 m agl, also continue the exponential increase of the INP concentration with lower temperatures, although there is no overlap between the instrument measurements.

Figure 4.40 visualizes the back trajectories before, during and after the measurements. Each panel corresponds to a different altitude of arrival for the given backward trajectory. At 250 m agl the air mass generally arrives from the Atlantic Ocean and travels along Sweden closer to the receptor. There is little difference between the different periods, although there is a slight contribution from the Arctic Ocean and northern Canada for the ten hours after the measurements. The air mass movement looks similar at 500 m agl, although the contribution after the event is shifted even more clearly to arctic air, originating on the coast of northern Greenland. Above 500 m agl, there is a clearer difference visible between the three periods. Air masses moving over Sweden and northern Germany are less pronounced for the measurement period and the ten hours after, with a clearly visible trend towards air masses originating in the Arctic Ocean at 750 m agl and 1000 m agl (see panel (c) and (d) in figure 4.40).

Additional data and modelling is needed to gain a deeper understanding of this case. It appears that there is a slight change in the air masses below and above 500 m agl, and a mixing of aerosol below 500 m agl might lead to the observed case of a constant INP concentration up to 257 m agl as measured by PINE.

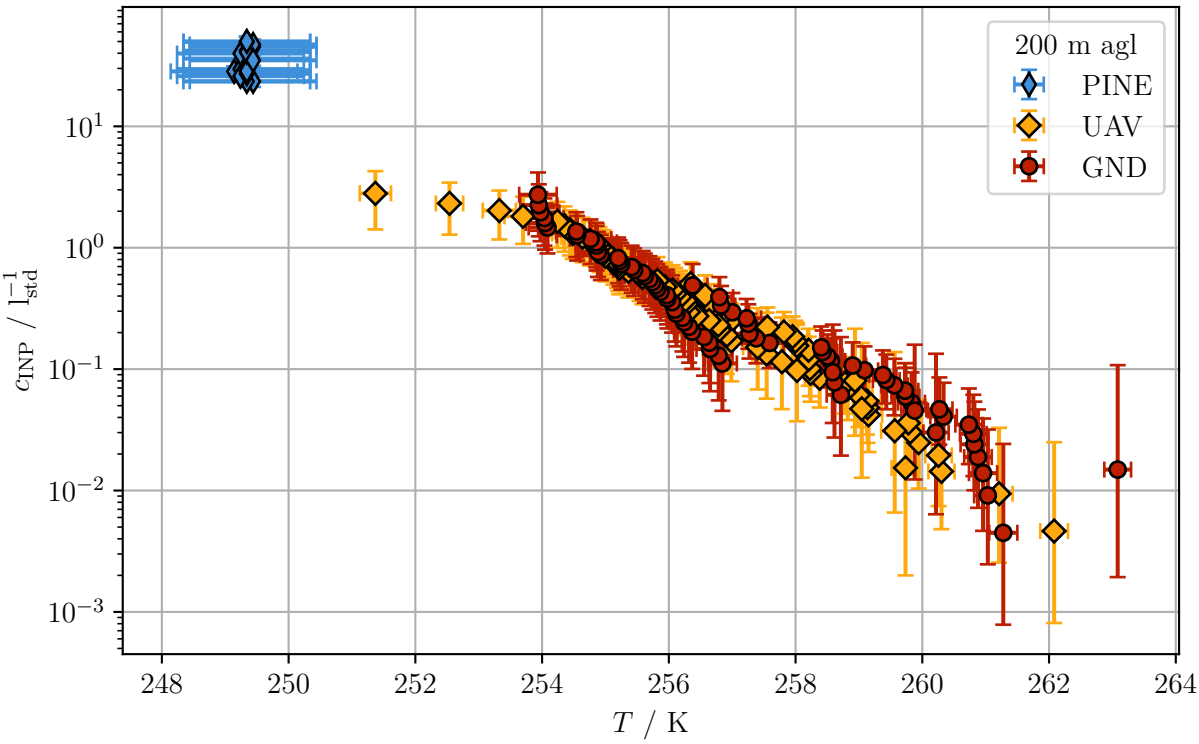

Figure 4.39.: **Freezing spectra measured on the ground and at an altitude of** 200 m **agl at 11$^{\mathrm{th}}$ October 2022 9.48 am GMT during PaCE 2022.**

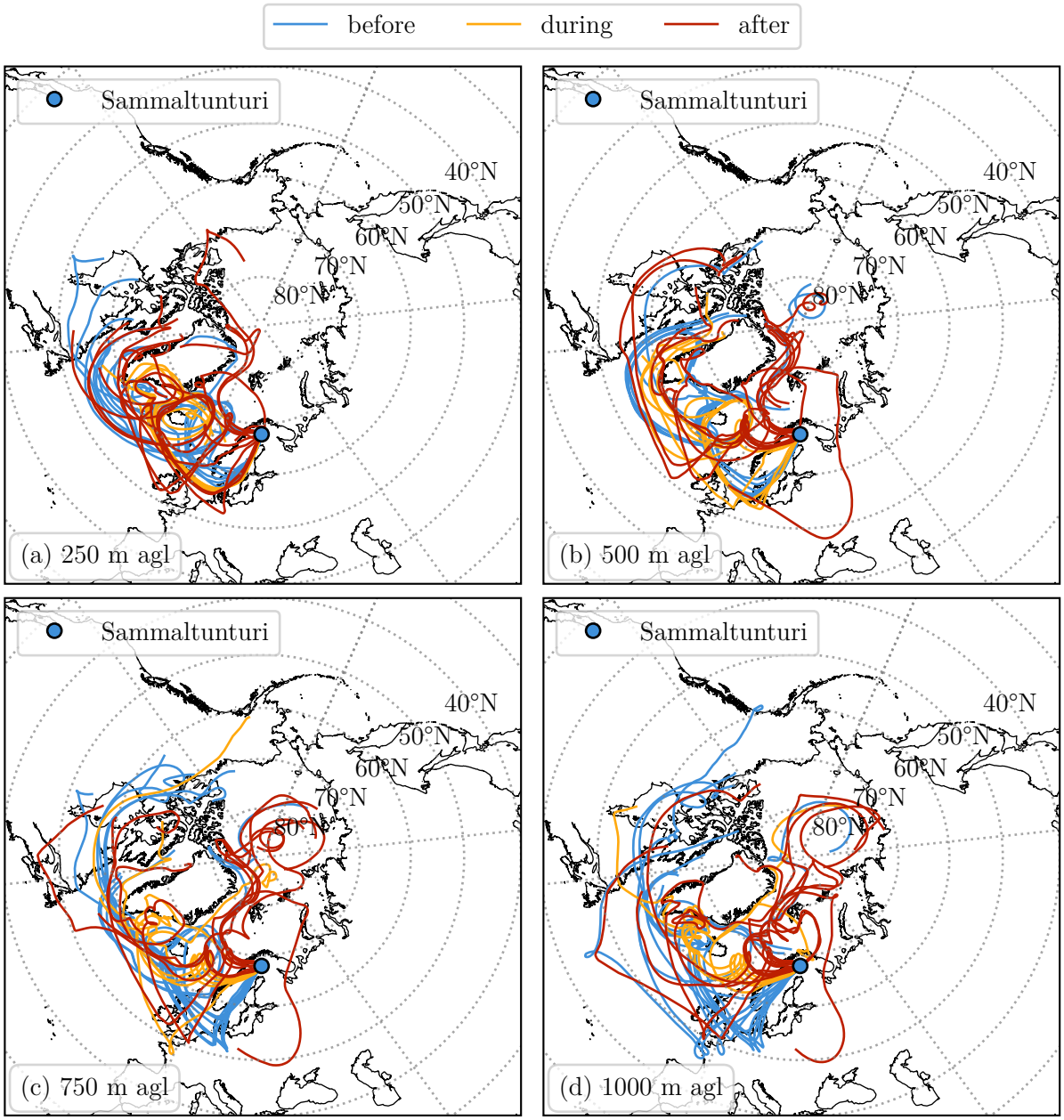

Figure 4.40.: **Backward trajectories calculated by HYSPLIT before, during and after the event on 11th October 2022.** Panel (a) to (d) visualize the trajectories at the four different altitudes 250, 500, 750 and 1000 m agl, respectively. Each trajectory has a length of ten days. Before and after correspond to the ten hours before and after the measurements, respectively.

4.6.3. Event: 5th October 2022 - higher INP concentration at 300 m agl

Figure 4.41 visualizes a different case, where the INP concentration measured at 300 m agl is higher compared to the one measured on the ground. This could indicate, that there are different air masses contributing to the total INP population at the different altitudes. No measurements of PINE are available during this period. Backward trajectories are calculated before, during and after the event (see figure 4.42), with the four different altitudes provided in panel (a) to (d). An altitude of 250 m agl corresponds roughly to the measurement altitude of the UAV, with backward trajectories arriving at 500 m agl corresponding to a potentially different air mass. Therefore, the expectation would be that there is a clear difference between 250 m agl and the other altitudes, although the situation on the ground might not be captured accurately by HYSPLIT.

Panel (a) of figure 4.42 visualizes the backward trajectories originating mostly in western Russia and travelling over land to Sammaltunturi station. There is a slight shift between the different periods, with relatively similar trajectories before and during the experiment. After the experiment, there is a shift with the air masses travelling closer to Eastern Europe, shifted clockwise with some influence from Central Europe and the Atlantic Ocean. Important to note is, that there are also some trajectories originating from the Atlantic Ocean before the event. This might indicate that there is a general shift in air mass, which could also introduce higher wind speeds, which might pick up local aerosol and therefore enhance the INP concentration. The ground-based measurements are located below the canopy, therefore they might be less affected by higher wind speeds and therefore a suppressed increase of the INP concentration.

The air masses arriving at 500 m agl show a shift closer to the receptor with all three periods having travelled similar paths. The air masses mostly travel over western Russia and the Baltic Sea with some influence from the Atlantic Ocean. Above 500 m agl, the air masses are shift clockwise, travelling mostly over the North and Baltic Seas, as well as an enhanced contribution from the Atlantic Ocean. This shift is observed for all three periods at 750 m agl and 1000 m agl.

Additional analysis and modelling is needed to understand how this shift in INP concentration along different altitudes can be explained. Especially remote sensing instrumentation would offer a great benefit to study different altitudes in the lower atmosphere in the region. Measurements below and above the canopy might lead to an inherent bias, which needs to be controlled by similar studies at different locations. Detailed simulations or measurements of the local wind fields could also provide more knowlegde on the impact of the canopy.

There is a need to measure the INP concentration at different vertical levels in the atmosphere to bridge the gap between ground-based measurements and models simulating the microphysics, especially of MPCs. Measuring the INP concentration is a first step towards this goal, but the measurements need to be connected to additional measurements to draw a more concise and clear conclusion.

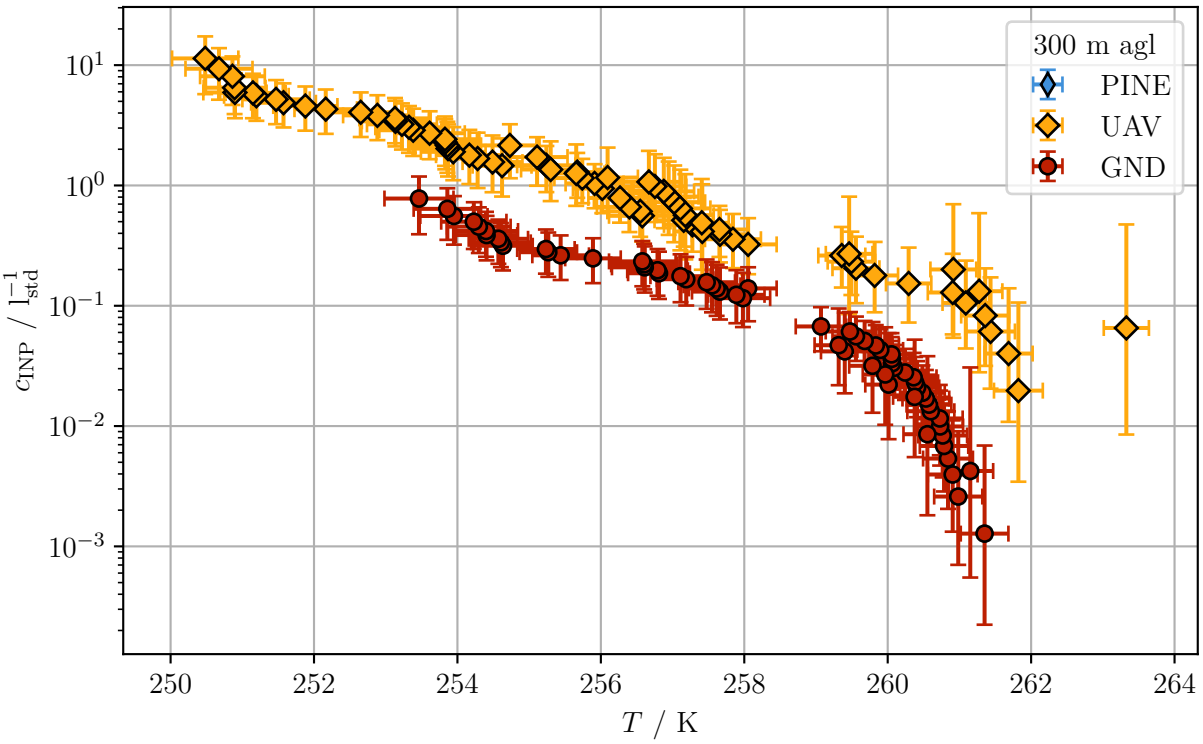

Figure 4.41.: **Freezing spectra measured on the ground and at an altitude of** 300 m **agl at 5$^{\mathrm{th}}$ October 2022 10.41 am GMT during PaCE 2022.**

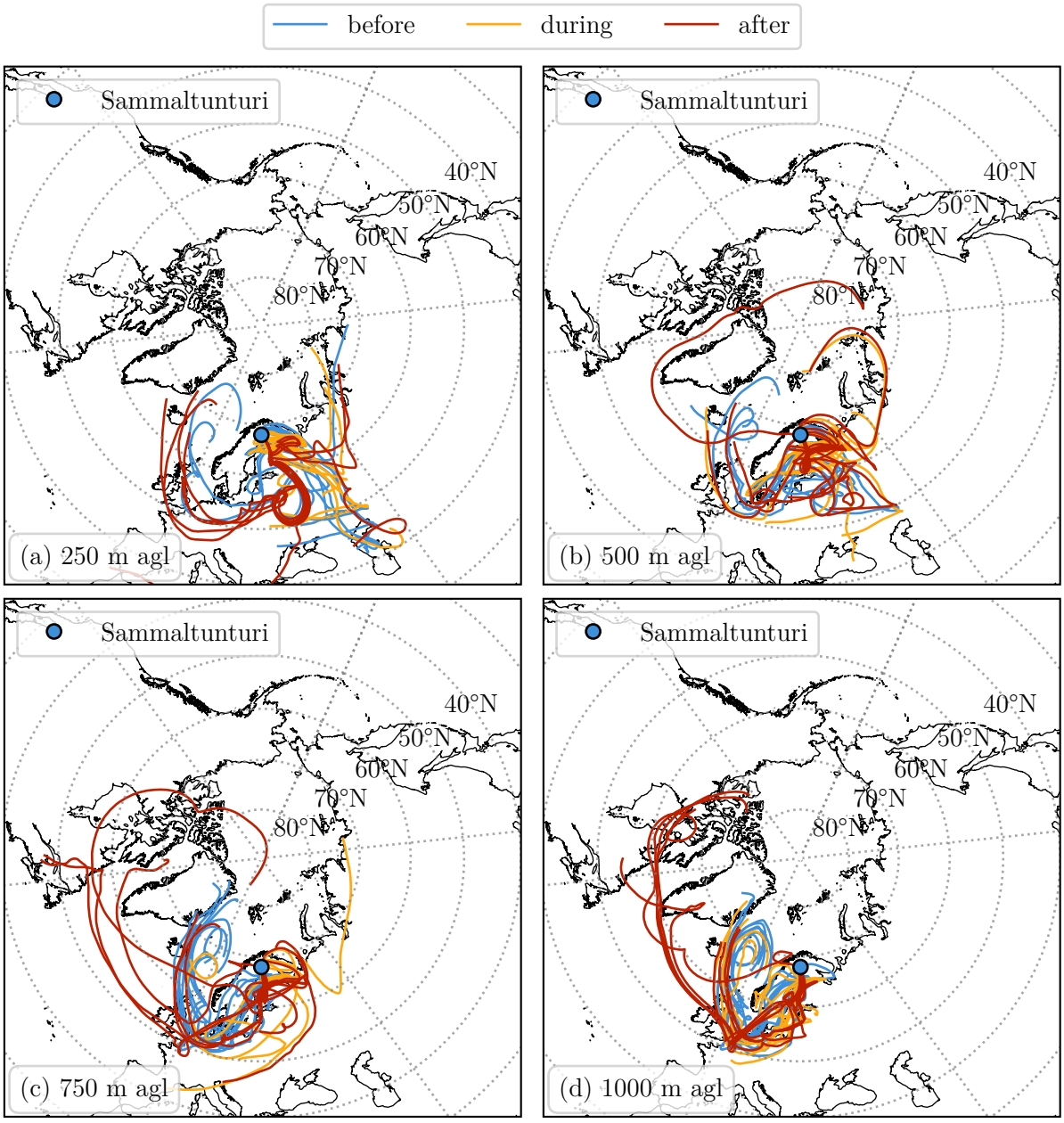

Figure 4.42.: **Backward trajectories calculated by HYSPLIT before, during and after the event on 5th October 2022.** Panel (a) to (d) visualize the trajectories at the four different altitudes 250, 500, 750 and 1000 m agl, respectively. Each trajectory has a length of ten days. Before and after correspond to the ten hours before and after the measurements, respectively.

Chapter 5.

Conclusion and outlook

This work investigates the influence of high-latitude dust and other aerosol sources on the INP population in the Arctic and sub-Arctic as well as the vertical distribution of the INP concentration in the lower atmosphere. The PINE chamber was used to assess the INP concentration at a high temporal resolution. In addition, a novel lightweight filter-based setup was developed during this work and used to collect aerosol onto filters for subsequent analysis with INSEKT to deterime the INP concentration at different altitudes.

The PINE chamber is able to measure the INP concentration over a wide range of nucleation temperatures and can be deployed autonomously over longer time periods (Möhler et al. 2021). Within this work the uncertainty of PINE was for the first time assessed in more detail, finding a relative uncertainty of 10 % of the INP concentration (see section 3.2.2) and there might be a potential positive bias of up to 8 %. For the analysis of the INSEKT freezing spectra a new Python-based software was developed, which provides additional quality control and quality assessment.

The novel lightweight filter-based setup was applied onboard of an UAV during three field campaigns. During these campaigns in Northern Finland, the setup has been tested and further improved. The INP concentration at different vertical levels in the lower atmosphere (600 m agl) was assessed during the PaCE 2022 campaign in Northern Finland. A technical description of the setup is given by Böhmländer et al. (2024), describing the development and the conducted feasibility studies in detail. Such a setup can be used in future studies to bridge the gap between measurements on the ground and at higher levels of the atmosphere, to better understand the INP concentration directly relevant for cloud formation.

In this work, I conducted a total of four intensive month-long field campaigns. In total, I analysed measurements of the INP concentration over 18 months with intensive field measurements of around 15 weeks. One campaign in Autumn 2022 at Sammaltunturi featured the PINE and the UAV setup (PaCE 2022). The other three campaigns featured PINE in the high Arctic on the Svalbard archipelago in Spring 2023 (ExINP_GVB 2023), Spring 2024 (ExINP_GVB 2024) and for a full year between Spring 2023 and Spring 2024 (ExINP_ZEP).

An analysis using correlation coefficients indicates that there is a clear difference in the connection of the INP concentration and meteorological variables between Northern Finland and the high Arctic during the respective measurement periods. While the correlation between the INP concentration and the ambient temperature and relative humidity is positive at Sammaltunturi station, the opposite is generally true for the high Arctic sites. This might be related to local emission of aerosols in Northern Finland that are able to act as INPs at the nucleation temperatures studied. A clear behaviour is seen, however, for both locations: a positive correlation

coefficient between the INP concentration and the mean diameter of the aerosol number size distribution is seen, especially at lower nucleation temperatures. Many studies (e.g., DeMott et al. 2010; Ullrich et al. 2017) found that the size of aerosols and their surface area are key components to described their ice nucleation ability. This is also seen in this study, underlying that a normalization based on the size and the number concentration of aerosol particles is useful to study the INP population.

The derived INAS densities from the measurements during these campaigns is compared to existing parameterizations and generally show a lower median INAS density compared to the dust parameterization developed by Ullrich et al. (2017). This might indicate that the INPs are not only dust particles, or that atmospheric aging impacts the ice nucleation ability of dust. The soot parameterization developed by Ullrich et al. (2017) is slightly below the measurements of PINE during the four campaigns. This is not necessarily related to soot particles contributing largely to the INP population, but highlights the low ice nucleation ability of the present aerosol particle population. For the small temperature overlap that exists with the parameterization developed by Schneider et al. (2021) for the southern boreal forest, the parameterization generally fits well. This could indicate that similar aerosols contribute to the various measurement sites and the southern boreal forest.

At ExINP_GVB 2023 and 2024 the INP concentration was also measured utilizing a filter-based method (WT-CRAFT). The collected aerosol on the filters was suspended in water and further subjected to a heat treatment to identify the contribution of heat-labile INPs to the total INP concentration. There was a clear decreased ice nucleation ability for the aerosol collected during both campaigns upon heat treatment, with a relative difference of around 0.53 in 2023 and 0.51 in 2024. This relative difference stays mostly constant with the nucleation temperature, and does not show a clear increase for higher nucleation temperatures. In 2023, the relative difference rather increase for lower temperatures (<249 K), which would show a strong contribution of heat-labile INPs to the INP population active at these temperatures. This behaviour has been seen before, with non-biogenic aerosol being deactivated as INP during heat treatment (Daily et al. 2022; O'Sullivan et al. 2014; Perkins et al. 2019).

During these campaigns, the offline-based INP concentrations are generally lower to the measurements of PINE, which could be explained by the breakup of aggregates inside the water suspension (DeMott et al. 2017; Lacher et al. 2024). Another hypothesis are the different collection and transport efficiencies of both methods (Chen et al. 2016; Ling et al. 2011; Ogura et al. 2016; Xiang et al. 2020). Further studies and intercomparisons between offline and online methods are needed to understand this effect fully.

At ZEP, the INAS density was calculated considering only the aerosol size distribution data from an SMPS, which might lead to a potential positive bias. The PINE was also connected to a GCVI, which only sampled cloud residuals during times when the station was inside a cloud. There is a clear difference between the cloud residuals and the general aerosol measurements, with the cloud residuals exhibiting a higher INAS density across most accounted nucleation temperatures. This could indicate, that during episodes of high INAS densities, the conditions for CCN activation and cloud droplet growth are favourable.

To identify different INP populations, that exhibit different INAS densities, the datasets were grouped with respect to the first and third quartiles into lower and higher INAS density episodes. During PaCE 2022, a total of nine lower and 12 higher INAS density episodes were identified. Comparing the meteorological conditions during those episodes and the general INAS density measured, showed only a clear difference for the wind direction. This dependency indicates a

potential influence of long-range transport on the local INAS density.

During ExINP_GVB 2023, only one lower and one higher INAS density episode were identified due to the short campaign duration. Generally, south-easterly winds dominate due to the local orography. During the higher INAS density episode, the occurence of these winds decreased by more than half, with an increased contribution from southerly winds. A similar behaviour is seen for the lower INAS density episode, which features a decrease in south-easterly winds as well. Contrary to the high INAS density episodes, the northern and western winds increase, which could indicate that sources originating from the partly open sea to the northern and western coast of Svalbard emit aerosol with a generally lower INAS density.

The number of lower and higher INAS episodes increased to three each for ExINP_GVB 2024 due to the longer measurement time. Similarly, during both episodes the generally dominant south-easterly wind occurence decreased. A less pronounced increase in the occurence from western winds is seen compared to 2023. In addition, during higher INAS density episodes the wind speed is also enhanced, which could introduce local particles deposited on the surface into the atmosphere. Together this indicates, that during dominant south-easterly winds, the INAS density generally stays constants, while lower and higher INAS density episodes occur when other wind directions dominate.

At ZEP, almost a full year of measurements showed that the INAS density decreases during periods, where southerly and northerly winds increase in occurence. Typically, the wind speed is also lower during these periods. Contrary to that, the wind speed is increases during higher INAS density episodes with a strong increase of southerly winds. This could indicate that air masses arriving from the south also bring aerosol, that has a higher INAS density compared to the general case. To investigate this further, FLEXPART was used to calculate the mineral dust age and its source region for ZEP during 2023.

Lower INAS density episodes featured dust that travelled for less time in the atmosphere compared to the general case and the higher INAS density episodes generally featured older dust. This might be related to aging processes, that enhance the ice nucleation ability (Boose et al. 2016). At the same time it could also be related to the dust source. Dust originating from sources in North America and Asia contribute always equally to the total dust aerosol population. This might be dust that can be understood as a background contribution to the total aerosol distribution. Higher contributions from Africa were seen during higher INAS density episodes, while dust originating in Russia typically had lower INAS densities.

During ExINP_GVB 2023, in addition to atmospheric measurements, also bulk samples from the surface snow and the ocean were collected and analyzed in regard to their ice nucleation ability. These are potential local sources of aerosol particles, that might get emitted into the atmosphere and consequently contribute to the INP concentration measured in the atmosphere. For the snow samples, the highest freezing temperature observed was from a snow samples collected in early May 2023, during 24-hour sun and during an algae bloom in the fjord. The water samples did not show a clear dependence on the time, but the collected water originated from the surface and not the SML, which might influence the measured INP concentration. This biogenic activity in the local fjord could not clearly be linked to the atmospheric measurements, but further studies, especially considering the SML, might improve the possible local source of INPs in the Arctic.

One episode of a blowing snow event was investigated, during which the highest INP concentration during ExINP_GVB 2023 was measured, with a subsequent suppression of the INP concentration, likely due to beginning wet precipitation. Although this is just one case, this could be a potential source of local aerosol, that get deposited on the ice- and snow-covered surfaces and get re-

suspended into the atmosphere during favourable wind conditions, and as such can act as a reservoir of INPs that is currently not considered in modelling studies. More specific measurements would be required to better assess the impact of blowing snow to the INP population snow-covered regions.

The newly developed setup for UAV-based measurements of the INP concentration was used to infer the difference between the ground and different vertical levels at altitudes up to 600 m agl. Vertical measurements of the INP concentration during PaCE 2022 sometimes showed a discrepancy between the ground- and UAV-based measurements, with the latter showing higher INP. There was no clear dependency on the altitude during these measurements. This could be due to the measurement location, since the ground-based measurements were done below the canopy, but also due to different meteorological conditions between the different measurements. To investigate different cases, HYSPLIT backward trajectories were calculated and two cases were selected, where the measurements align (case 1) and one where the INP concentration at 300 m agl was higher compared to the ground-based measurement (case 2). Cases such as the latter were the most common.

During case 1, the air masses were generally similar below and at 500 m agl. A clear trend is visible for higher altitudes towards air masses originating over the Arctic Ocean. This could indicate, that the lower atmosphere up to 500 m agl is well-mixed and therefore there is no observable difference visible. For case 2, there is an exchange of air masses observable in the backward trajectories. Different air masses might lead to a difference of the INP concentration at different altitudes. Due to the ground-based measurements being below the canopy, these effects might be suppressed closer to the ground. Additional analysis and measurements are needed to understand these results. Especially remote sensing data would provide an additional vertically resolved measurement of the local atmosphere regarding aerosol concentrations and wind fields..

More intensive measurements of the INP concentration with a high temporal resolution are still needed in the Arctic. Here, a key aspect is the additional measurement of the aerosol size distribution, which allows a better assessment of the underlying INP population. Models, such as FLEXPART, offer a key tool in understanding the transport processes for different aerosol types. With new research on other potential high-latitude dust sources, these dispersion models may play an even greater role in understanding these processes. To connect the source to the receptor, additional studies are needed also on the ice nucleation ability of aerosol at the source. Ground-based measurements are able to provide a great insight into the local INP population, but they are unable to conduct direct measurements at altitudes, where clouds typically form. Setups, like the one deployed at ZEP, which is able to sample only cloud residuals, offer an insight into the difference between aerosol, that impact clouds, and aerosol that might impact clouds. UAV-based approaches, like the one discussed in this work, offer a flexible and cost-efficient way to measure the INP concentration at or above cloud level. Future setups should also implement measurements of the aerosol particle size distribution to provide a reliable way to calculate the INAS density and compare to ground-based measurements.

Appendix A.

Additional information on PINE

A.1. PINE transport efficiency

The PINE contains an inlet system, which is defined by two 90° bends that introduces losses of aerosol particles inside the tubing. To measure the transport efficiency of PINE, an APS (model 3321, TSI Inc.) was used to measure before the inlet and at the entrance to the chamber. Further analysis is needed for a more accurate assessment on the transport efficiency, especially for smaller particles, which might be lost due to diffusional losses for lower flow velocities. The measurements are shown in figure A.1 for the raw size distribution measured by the APS (APS), the size distribution measured by the APS after the two bends (PINE_APS) and also with the dryers attached (PINE_dryer_APS). The aerodynamic particle diameter at which 50 % of particles are transported through the inlet are

$$d_{50}^{\text{PINE\_APS}} = (3.8 \pm 0.2)\,\mu\text{m}\ , \tag{A.1}$$

$$d_{50}^{\text{PINE\_dryer\_APS}} = (3.7 \pm 0.1)\,\mu\text{m}\ . \tag{A.2}$$

with the uncertainty representing a single standard deviation. Particles with an aerodynamic particle diameter smaller than d_{50} are transported with a higher efficiency into the PINE chamber, therefore the limit on the size distribution considered for calculated any normalization such as the INAS density calculation, uses aerosol particle with a diameter smaller thant 4 µm.

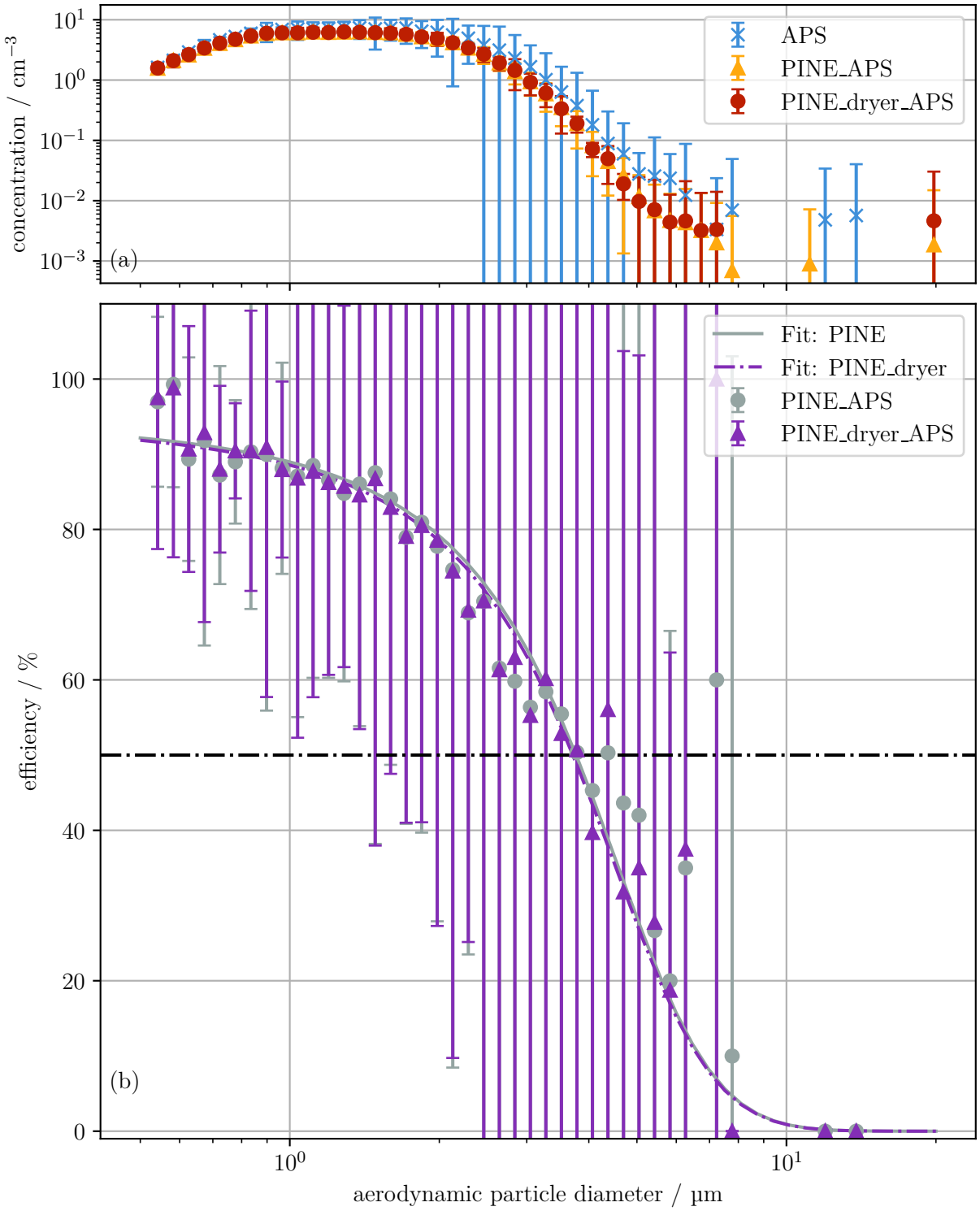

Figure A.1.: **Measurement of the PINE transport efficiency using an APS.**

A.2. PIA flags

The different flags that are used in PIA are provided in table A.1 alongside their use in which level of the data.

Table A.1.: **PIA flags.**

Condition	Flag	Data level
Times of the cycle need to increase in order	670	0
Expansion duration is limited to a valid range	699	0
Calculated duration of expansion is shorter than actual duration	677	0
Gaps in instrument data	999	0
Temperature is limited to a valid range	684	0
Temperature is constant over a span of time	699	0
End temperature during expansion is ordered	635	0
Pressure is limited to a valid range	684	0
Pressure is constant over a span of time	699	0
End pressure during expansion is limited to a valid range	699	0
Expansion flow is limited to a valid range during expansion	684	0
Expansion flow is limited to a valid range during flush and expansion	684	0
Main flow is limited to a valid range during flush and expansion	684	0
Outliers in the flow during flush and expansion	459	0
Mean flow during flush is limited to a valid range during flush	664	0
Mean flow during expansion is limited to a valid range during expansion	664	0
Dew point temperature is limited to a valid range	684	0
Dew point temperature is constant over a span of time	699	0
Dew point temperature at beginning of expansion has to be lower than Ti5		0
Gaps in OPC data during expansion	999	0
Detection of particles during refill	699	0
Ice threshold is limited to the OPC range	459	1
INP concentration is limited to a valid range	459	1

A.3. Accuracy of temperature sensors used in PINE

Two types of temperature sensors are used to measure the temperature inside the PINE chamber. The gas temperature sensors are used to measured the lowest temperature reached during the expansion, while the wall temperature sensors provide information on the wall temperature of the chamber. Their accurcay and range are provided in table A.2.

Table A.2.: **Accuracy of temperature sensors used in PINE.** Gas sensors are denoted with 'Ti' and wall sensors with 'Tw'.

Sensor	Accuracy	Range	Source
TiX	$\max(1.5\,°C,\ 0.4\,\%\lvert RD\rvert^{\dagger})$	−40 to 1000 °C	IEC 584-3
TwX	$0.3\,°C + 0.5\,\%\lvert RD\rvert^{\dagger}$	−196 to 600 °C	IEC 60751:2008

† |RD| denotes the absolute value in °C.

Appendix B.

Additional information on INSEKT

B.1. Temperature distribution for INSEKT 1 and 2

Both INSEKT contain eight temperature sensors (Pt100), that record the temperature inside the aluminium block during experiments. INSEKT has been used to determine the INP concentration in bulk and filter samples since 2017. The original calibration of the temperature sensors was performed at 27$^{\text{th}}$ July 2017, with a second calibration performed at 21$^{\text{st}}$ June 2023 for INSEKT 1. The same was done for INSEKT 2 at 20$^{\text{th}}$ June 2018 and 22$^{\text{nd}}$ June 2023. The reference temperature sensor was calibrated by Lake Shore Cryotronics, Inc. and has a total uncertainty of 24 mK at 300 K based on an approximate 95 % confidence interval with a coverage factor $k = 2$. An additional source of uncertainty is given from the fit of the measured sensor resistance to a temperature. Based on a Chebyshev polynomial fit of order 11, the mean uncertainty is 0.82 K for the temperature range 14 to 325 K. Figures B.1 and B.2 visualize the temperature deviation of the mean for the eight temperature sensors for INSEKT1; the same is shown in figures B.3 and B.4 for INSEKT2.

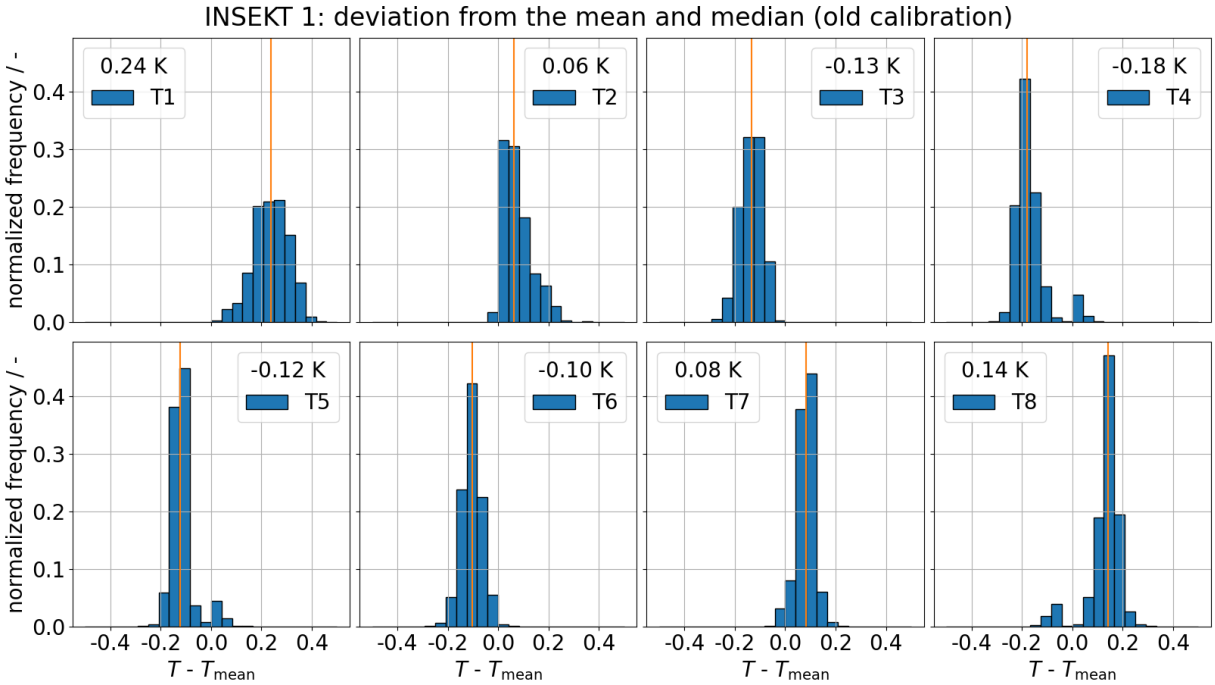

Figure B.1.: Temperature deviation of the eight temperature sensors of INSEKT1 for the old calibration.

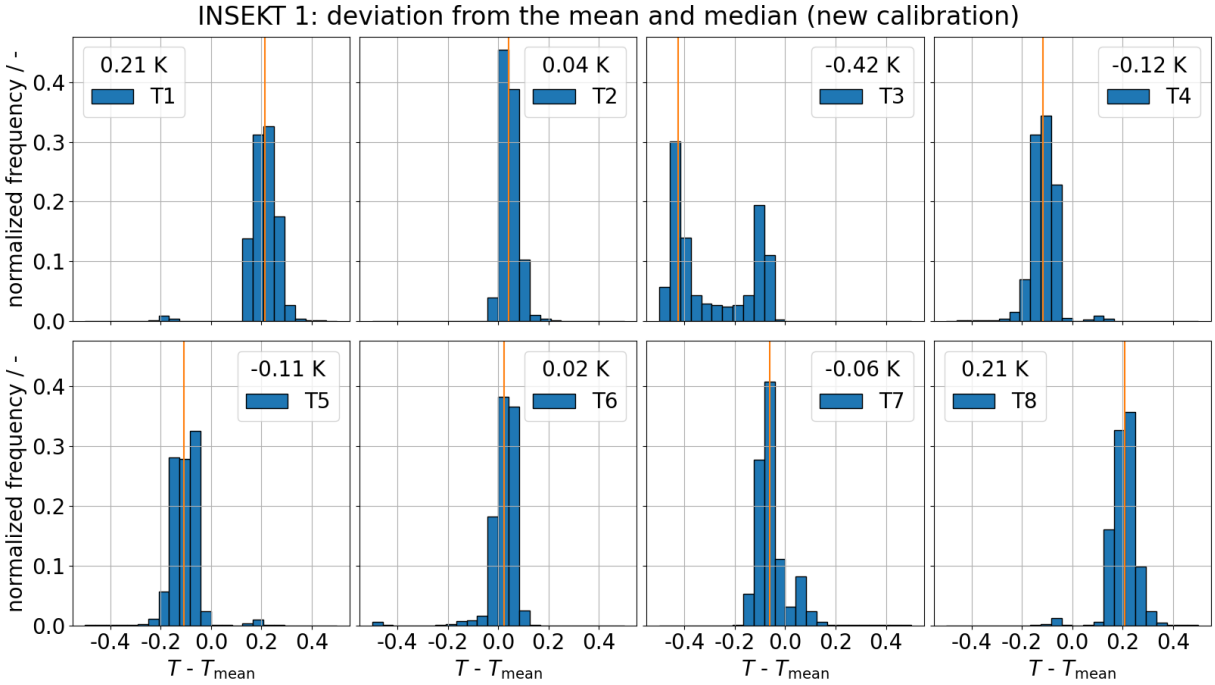

Figure B.2.: Temperature deviation of the eight temperature sensors of INSEKT1 for the new calibration.

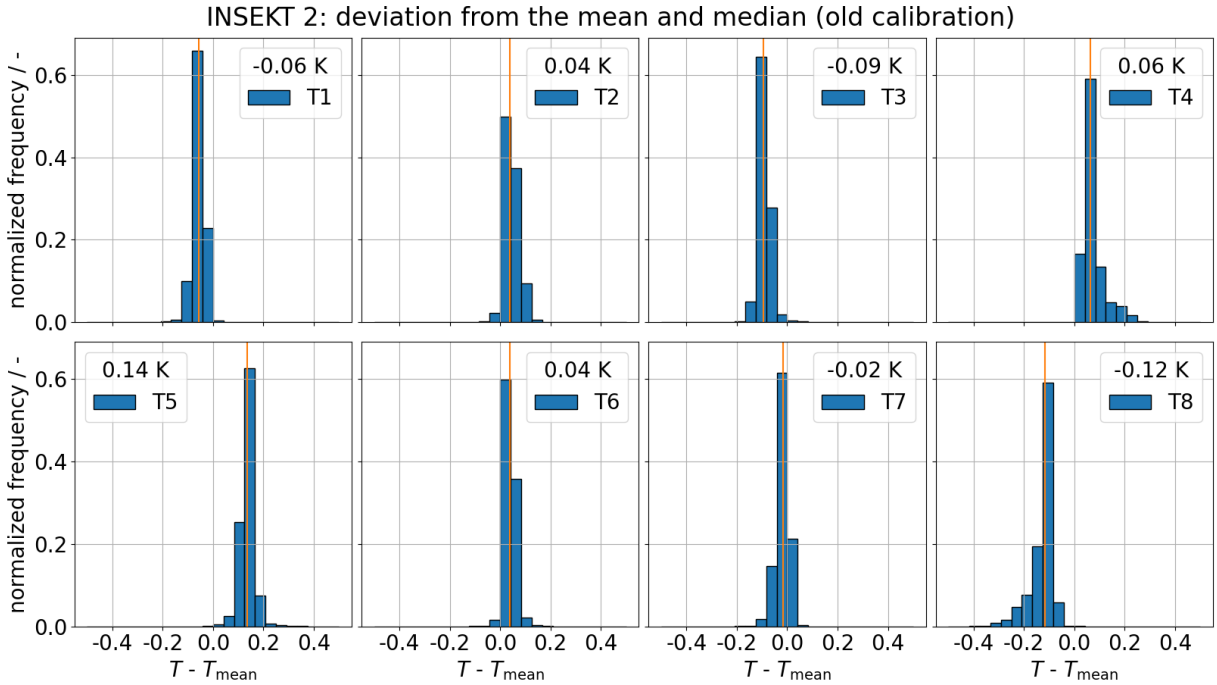

Figure B.3.: Temperature deviation of the eight temperature sensors of INSEKT2 for the old calibration.

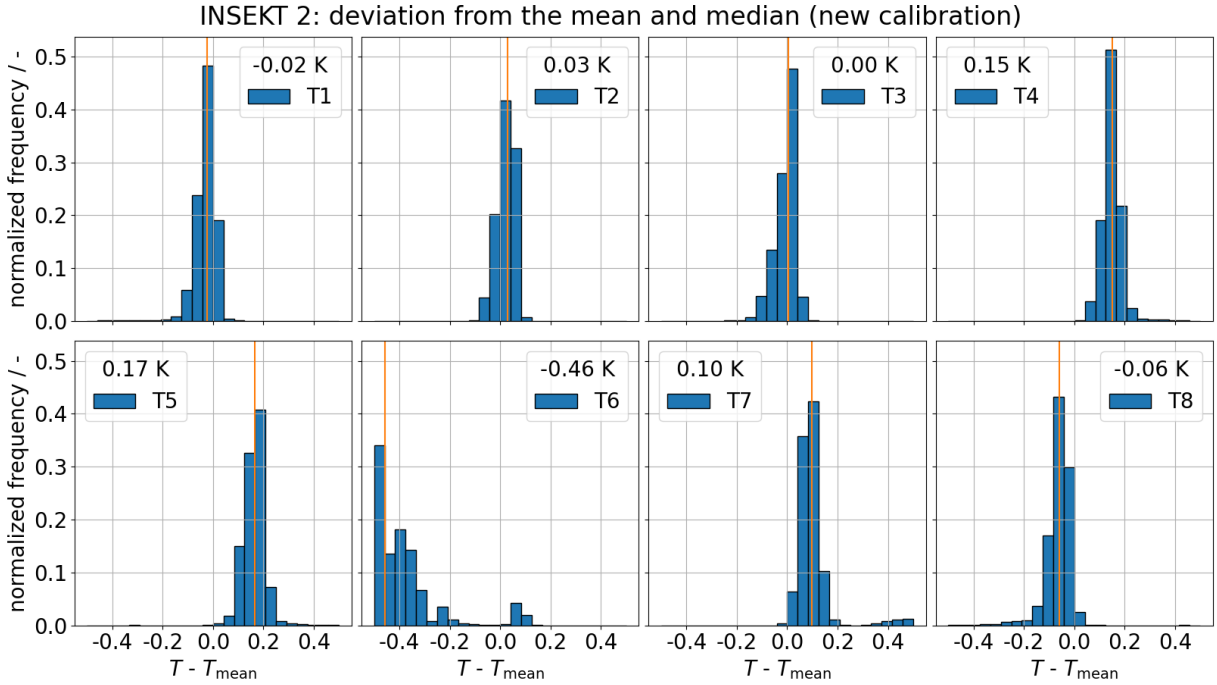

Figure B.4.: Temperature deviation of the eight temperature sensors of INSEKT2 for the new calibration.

Appendix C.

Additional information on campaigns

C.1. Merging of SMPS and APS at GVB

Data obtained from the SMPS and APS was first transformed to a volume-equivalent diameter considering a particle density of $1.95\,\mathrm{kg\,m^{-3}}$ and a shape factor of 1. Standard conditions were used with $p = 101\,325\,\mathrm{Pa}$ and $T = 293.15\,\mathrm{K}$. Afterwards, the overlapping diameter bins were identified and a new diameter was calculated. This new diameter is distributed equally on the log-scale between the respective lower and upper diameter. The bins are finally merged by calculated the weighted mean. The weight is defined by a logistic function f

$$f(x) = \frac{1}{1 + \exp(-k(x - x_0))} \tag{C.1}$$

where: x – particle diameter (µm),
k – slope parameter ($1\,\mathrm{\mu m^{-1}}$),
x_0 – mean of the particle diameters, where weight function is applied (µm).

An example for a merged size distribution is visualized in figure C.1 with an inset axes that visualizes the overlapping diameter range.

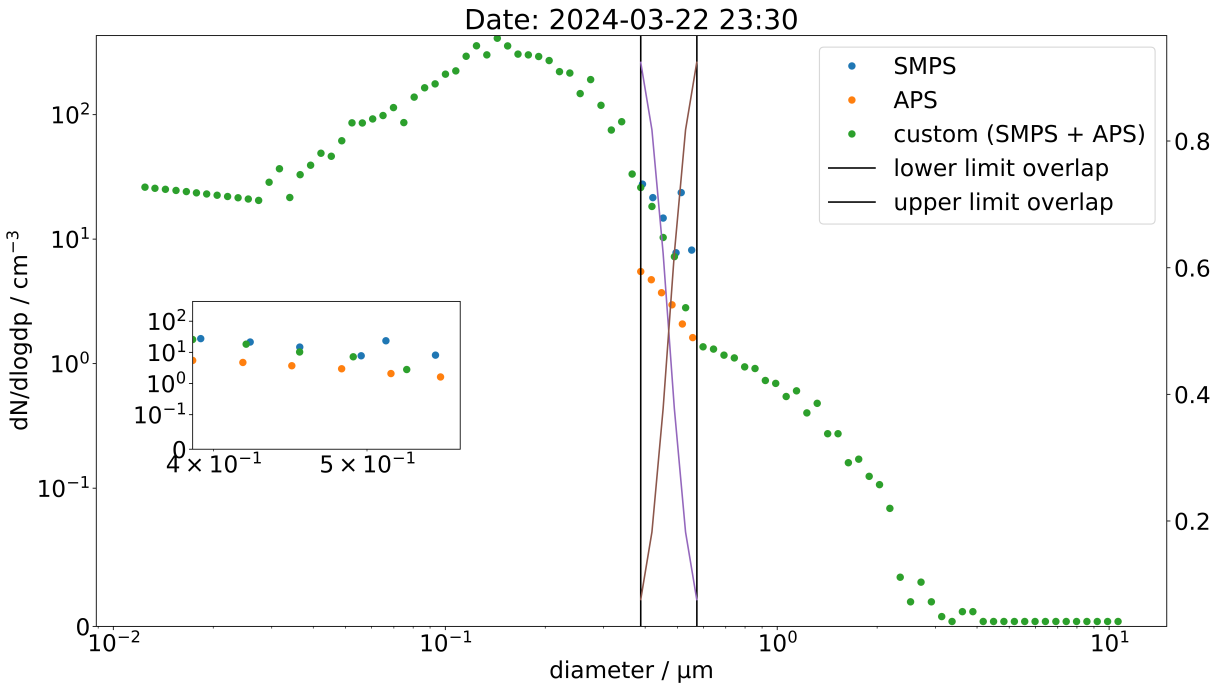

Figure C.1.: **Example for a merge size distribution measured by SMPS and APS at GVB.**

C.2. Individual freezing spectra measured during PaCE 2022

Individual freezing spectra are visualized in figures C.2 to C.10. The uncertainties of the INP concentration correspond to the 95 % confidence interval, calculated from the normal approximation of the binomial distribution (Agresti and Coull 1998). The confidence interval for the temperature is calculated using a Student's t distribution considering the number of temperature sensors used during the calculation of the mean.

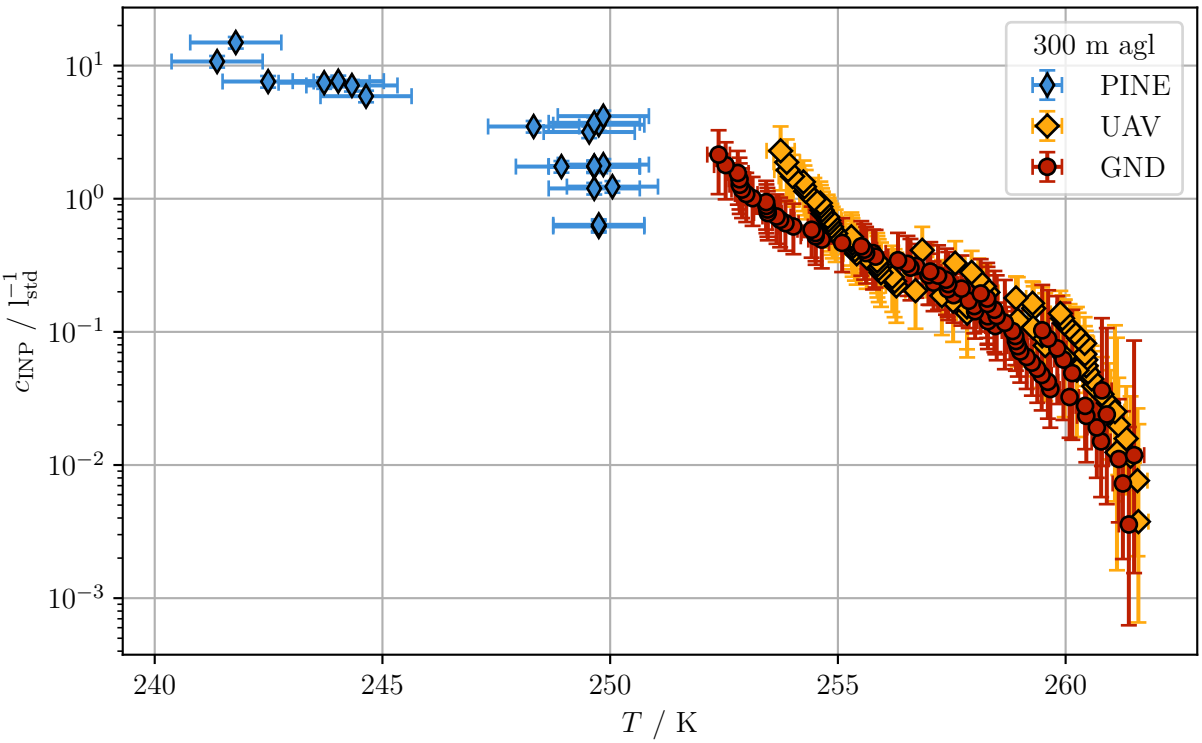

Figure C.2.: **Freezing spectra measured on the ground and at an altitude of** 300 m **agl at 30th September 2022 9.43 am GMT during PaCE 2022.**

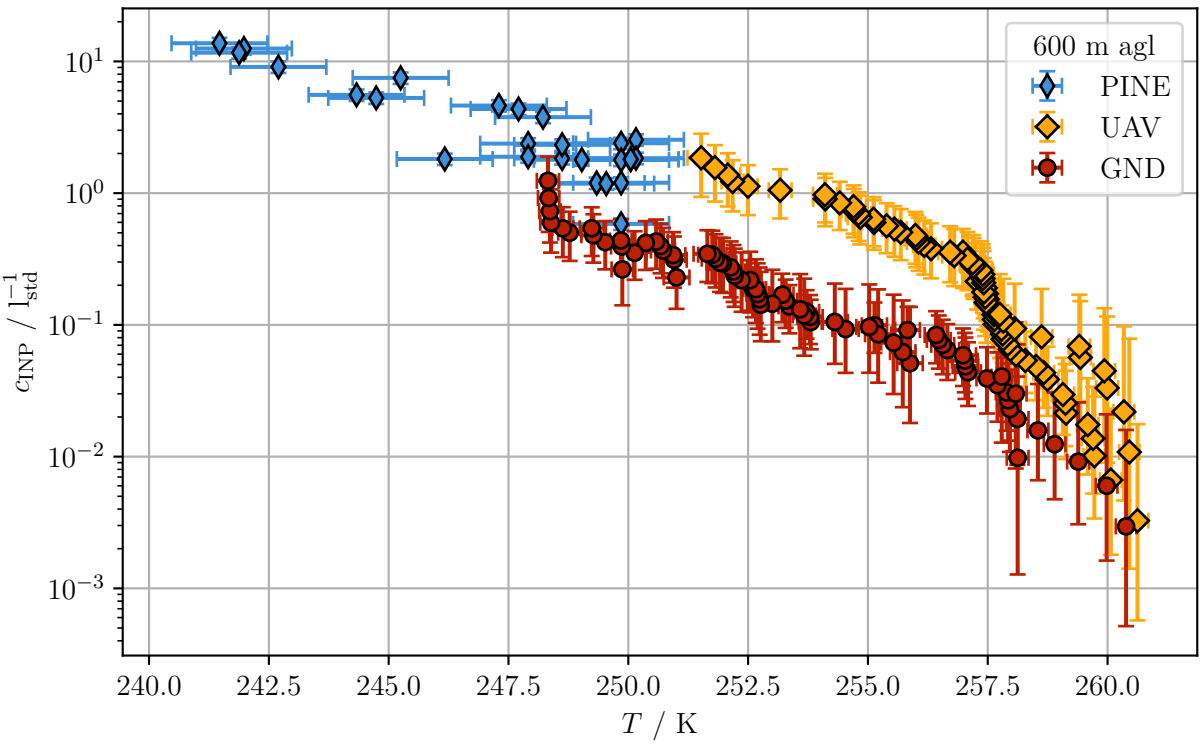

Figure C.3.: **Freezing spectra measured on the ground and at an altitude of** 600 m **agl at 1st October 2022 10.55 am GMT during PaCE 2022.**

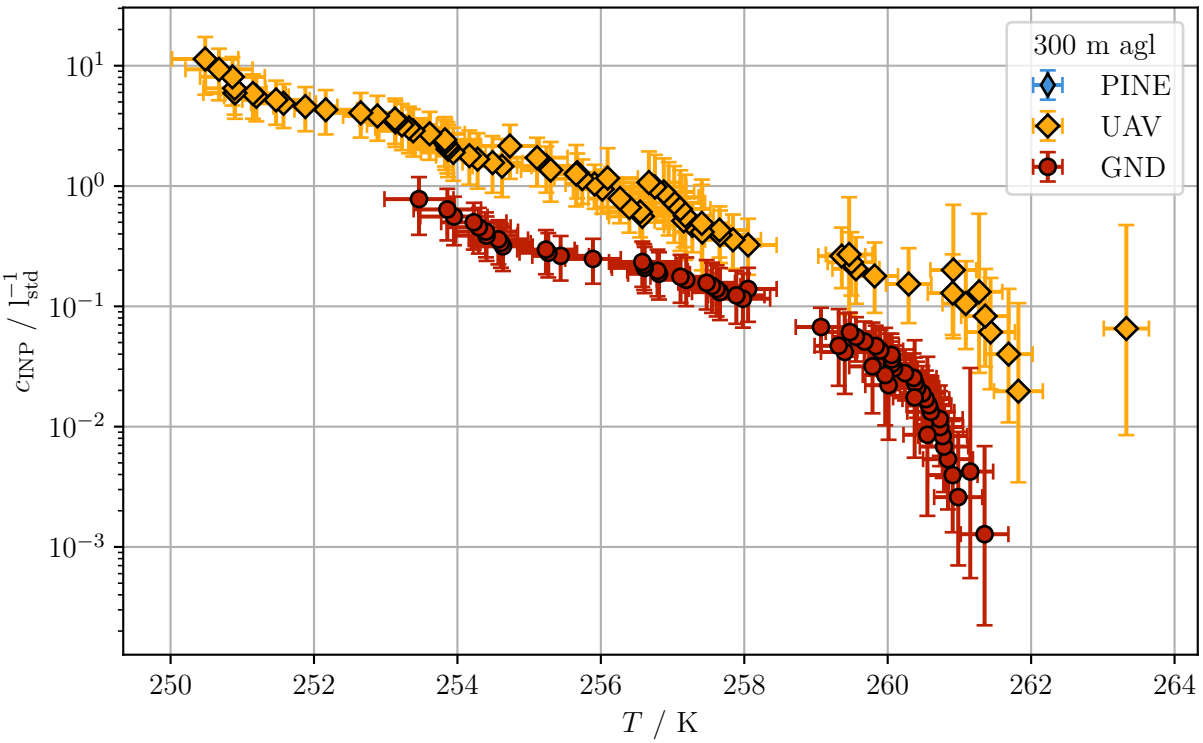

Figure C.4.: **Freezing spectra measured on the ground and at an altitude of** 300 m **agl at 5th October 2022 10.41 am GMT during PaCE 2022.**

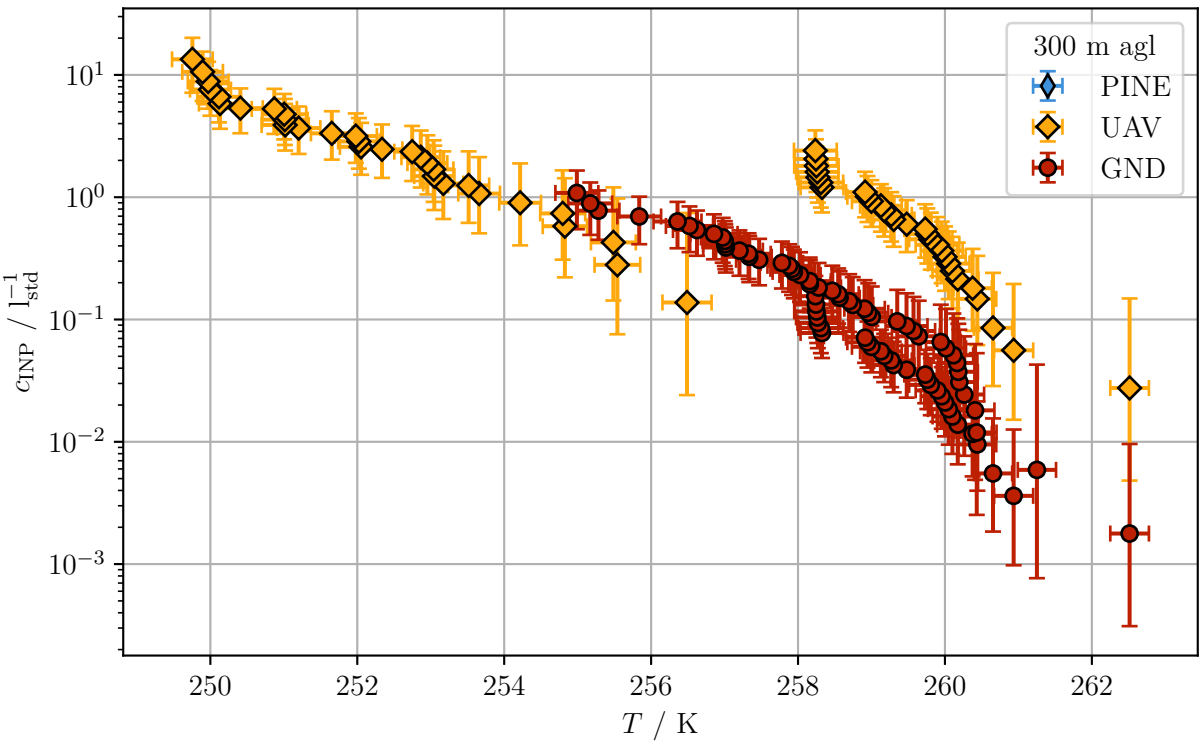

Figure C.5.: **Freezing spectra measured on the ground and at an altitude of** 300 m **agl at 6th October 2022 2.31 pm GMT during PaCE 2022.**

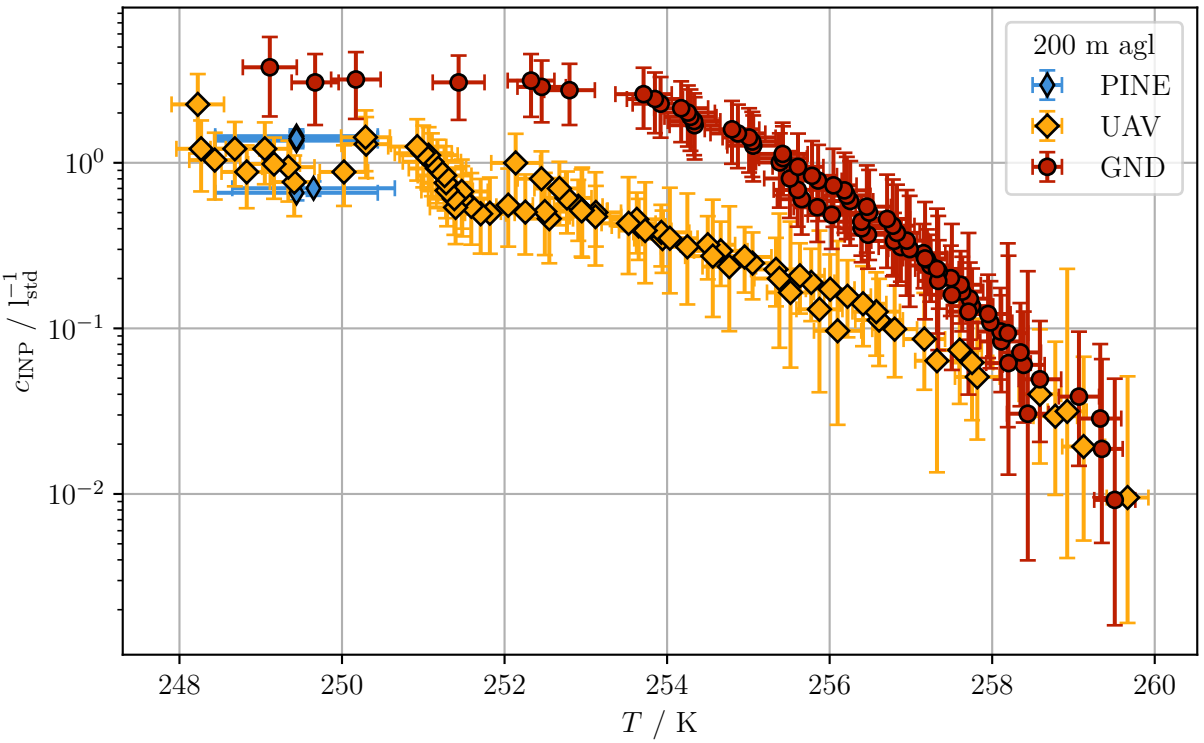

Figure C.6.: **Freezing spectra measured on the ground and at an altitude of** 200 m **agl at 8th October 2022 9.30 am GMT during PaCE 2022.**

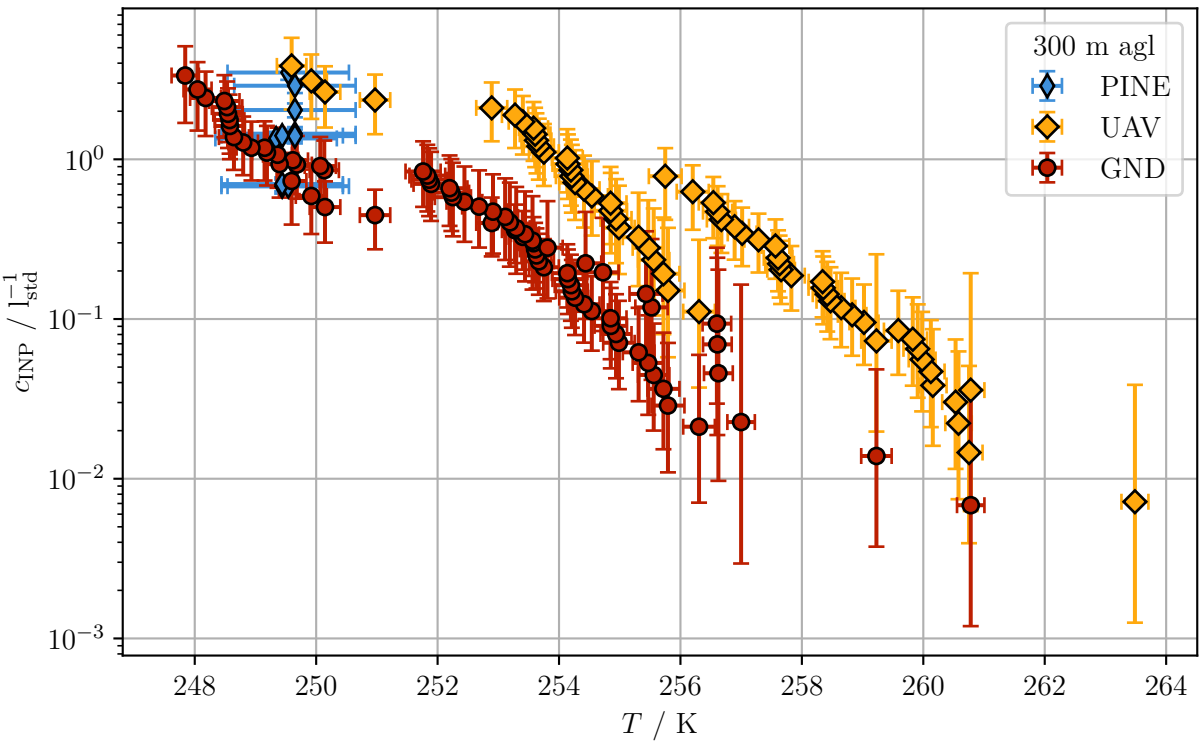

Figure C.7.: **Freezing spectra measured on the ground and at an altitude of** 300 m **agl at 8th October 2022 12.31 pm GMT during PaCE 2022.**

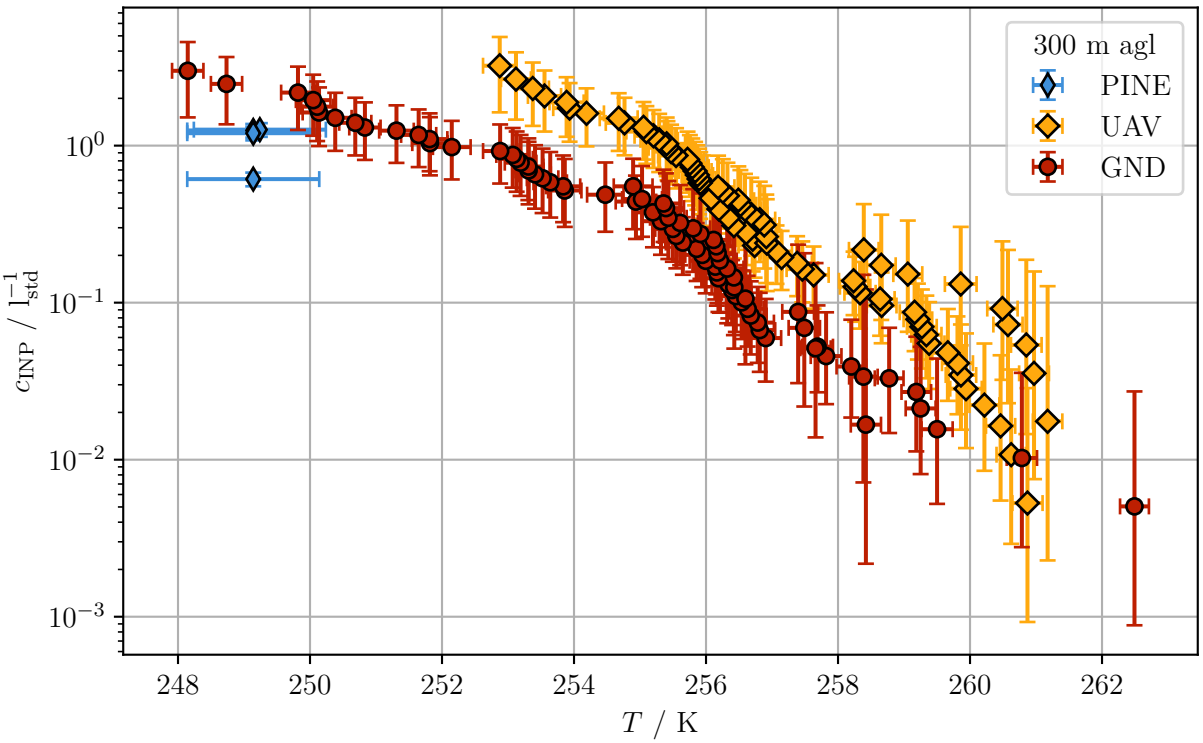

Figure C.8.: **Freezing spectra measured on the ground and at an altitude of** 300 m **agl at 10th October 2022 9.15 am GMT during PaCE 2022.**

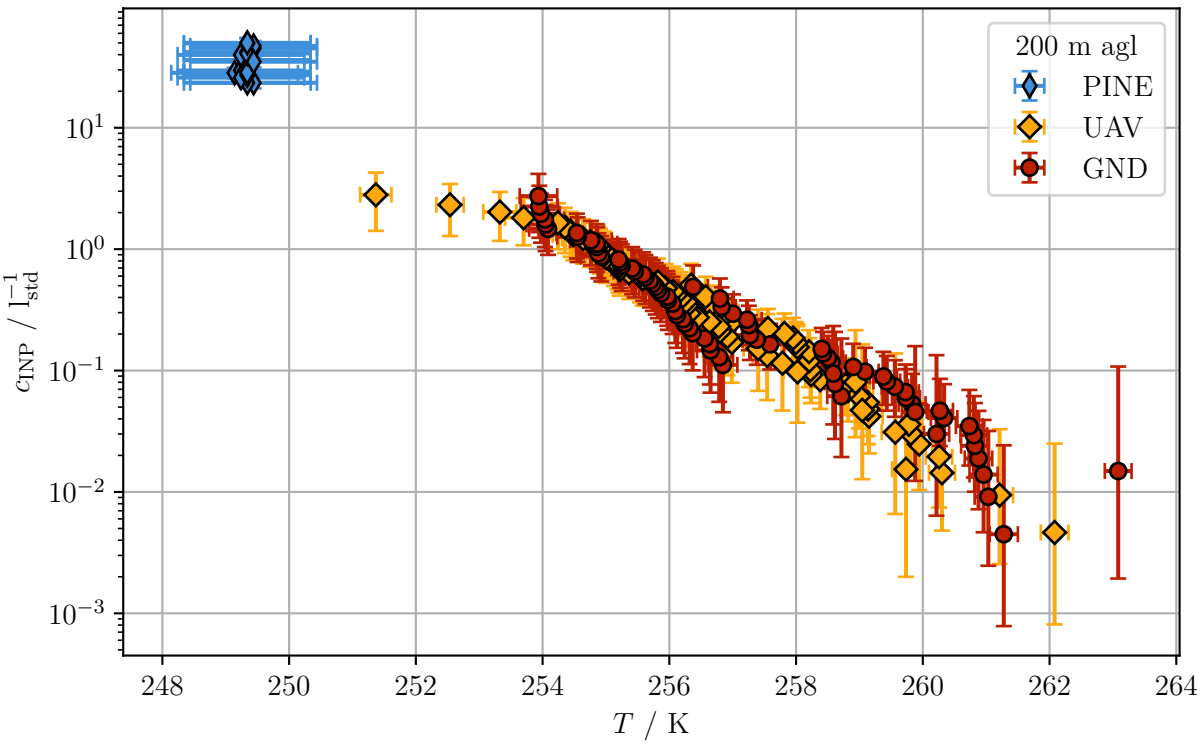

Figure C.9.: **Freezing spectra measured on the ground and at an altitude of** 200 m **agl at 11th October 2022 9.48 am GMT during PaCE 2022.**

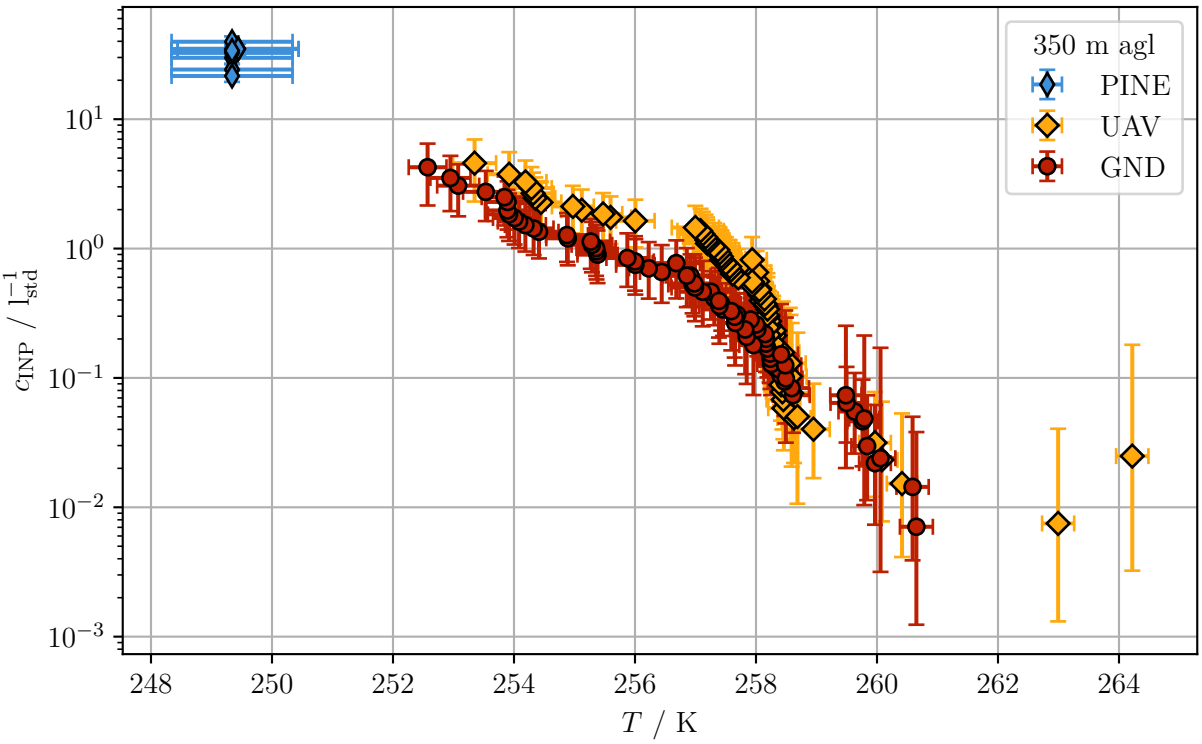

Figure C.10.: **Freezing spectra measured on the ground and at an altitude of** 350 m **agl at 11th October 2022 1.56 pm GMT during PaCE 2022.**

C.3. Filter collection during ExINP_GVB 2023 and 2024

Table C.1 contains information on the filters taken during ExINP_GVB 2023 and 2024 by Naruki Hiranuma, his team and personell of GVB.

Table C.1.: **Filters taken during ExINP_GVB 2023 and 2024.** All filters were analysed by WT-CRAFT and taken by Naruki Hiranuma, his team, and personell from GVB. Some filters were also analysed utilizing INSEKT for comparison. All aerosol suspensions were subjected to heat treatment for 20 min at 100 °C (see also section 3.2.1). Date and time expressed according to ISO 8601.

Samplename	Start time	Stop time	Duration / h
GVB27†	2023-03-13T08:57:00Z	2023-03-15T08:11:00Z	47.23
GVB28	2023-03-15T08:23:00Z	2023-03-16T09:03:00Z	24.67
GVB29	2023-03-16T09:07:00Z	2023-03-17T13:24:00Z	
GVB30	2023-03-17T13:31:00Z	2023-03-18T08:39:00Z	19.13
GVB31	2023-03-18T09:04:00Z	2023-03-19T10:31:00Z	25.45
GVB32	2023-03-19T10:38:00Z	2023-03-20T08:15:00Z	21.62
GVB33	2023-03-20T08:25:00Z	2023-03-21T08:51:00Z	24.43
GVB36	2023-03-21T09:04:00Z	2023-03-22T08:27:00Z	23.38
GVB37	2023-03-22T08:31:00Z	2023-03-23T09:44:00Z	25.22
GVB38	2023-03-23T09:47:00Z	2023-03-24T09:00:00Z	23.22
GVB39	2023-03-24T09:09:00Z	2023-03-25T12:01:00Z	26.87
GVB40†	2023-03-25T12:06:00Z	2023-03-27T07:25:00Z	43.32
GVB41	2023-03-27T07:30:00Z	2023-03-28T07:46:00Z	24.27
GVB42	2023-03-28T07:53:00Z	2023-03-29T12:08:00Z	28.25
GVB43	2023-03-29T12:31:00Z	2023-03-30T08:06:00Z	19.58
GVB44	2023-03-30T08:10:00Z	2023-03-31T12:06:00Z	27.93
GVB45	2023-03-31T12:12:00Z	2023-04-01T10:16:00Z	22.07
GVB46†	2023-04-01T10:21:00Z	2023-04-03T09:34:00Z	47.22
GVB47	2023-04-03T09:39:00Z	2023-04-04T07:52:00Z	22.22
GVB48†	2023-04-04T07:57:00Z	2023-04-05T08:43:00Z	24.77
GVB49†	2023-04-05T08:48:00Z	2023-04-06T11:28:00Z	26.67
GVB50†	2023-04-06T11:33:00Z	2023-04-07T14:08:00Z	26.58
GVB51	2023-04-07T14:19:00Z	2023-04-08T10:51:00Z	20.53
GVB52†	2023-04-08T10:55:00Z	2023-04-10T07:15:00Z	44.33
GVB53	2023-04-10T07:19:00Z	2023-04-11T07:52:00Z	24.55
GVB54	2023-04-11T07:57:00Z	2023-04-12T08:10:00Z	24.22
GVB55	2023-04-12T08:15:00Z	2023-04-13T07:09:00Z	22.90

Continued on next page

Table C.1.: **Filters taken during ExINP_GVB 2023 and 2024.** All filters were analysed by WT-CRAFT and taken by Naruki Hiranuma, his team, and personell from GVB. Some filters were also analysed utilizing INSEKT for comparison. All aerosol suspensions were subjected to heat treatment for 20 min at 100 °C (see also section 3.2.1). Date and time expressed according to ISO 8601. (Continued)

Samplename	Start time	Stop time	Duration / h
GVB56	2023-04-13T07:14:00Z	2023-04-14T07:50:00Z	24.60
GVB57	2023-04-14T07:54:00Z	2023-04-15T07:24:00Z	23.50
GVB58	2023-04-16T09:07:00Z	2023-04-17T13:24:00Z	28.28
GVB125	2024-03-03T12:23:00Z	2024-03-06T09:06:00Z	68.72
GVB126	2024-03-06T09:10:00Z	2024-03-09T08:43:00Z	71.55
GVB127	2024-03-09T08:43:00Z	2024-03-12T08:20:00Z	71.58
GVB128	2024-03-12T08:27:00Z	2024-03-13T08:49:00Z	24.37
GVB129	2024-03-13T08:55:00Z	2024-03-14T08:35:00Z	23.67
GVB130	2024-03-14T08:40:00Z	2024-03-15T09:44:00Z	25.07
GVB131	2024-03-15T09:49:00Z	2024-03-16T14:42:00Z	28.88
GVB132‡	2024-03-16T14:45:00Z	2024-03-16T14:48:00Z	
GVB133	2024-03-16T14:48:00Z	2024-03-17T10:44:00Z	19.98
GVB134	2024-03-17T10:50:00Z	2024-03-18T09:00:00Z	22.17
GVB135	2024-03-18T09:06:00Z	2024-03-19T08:13:00Z	23.12
GVB136	2024-03-19T08:25:00Z	2024-03-20T08:03:00Z	23.63
GVB137	2024-03-20T08:14:00Z	2024-03-21T09:00:00Z	24.77
GVB138	2024-03-21T09:10:00Z	2024-03-22T08:19:00Z	23.15
GVB139	2024-03-22T08:27:00Z	2024-03-23T07:43:00Z	23.27
GVB140	2024-03-23T07:52:00Z	2024-03-25T08:48:00Z	48.93
GVB141	2024-03-25T08:57:00Z	2024-03-26T07:54:00Z	22.95
GVB142‡	2024-03-26T08:06:00Z	2024-03-26T08:09:00Z	
GVB143	2024-03-26T08:17:00Z	2024-03-27T08:37:00Z	24.33
GVB144	2024-03-27T08:48:00Z	2024-03-28T08:49:00Z	24.02
GVB145	2024-03-28T08:58:00Z	2024-03-29T08:42:00Z	23.73
GVB146	2024-03-29T08:52:00Z	2024-03-30T08:43:00Z	23.85
GVB147	2024-03-30T08:53:00Z	2024-04-01T11:17:00Z	50.40
GVB148	2024-04-01T11:29:00Z	2024-04-02T06:43:00Z	19.23
GVB149	2024-04-02T06:53:00Z	2024-04-03T07:14:00Z	24.35
GVB150‡	2024-04-03T07:24:00Z	2024-04-03T07:27:00Z	
GVB151	2024-04-03T07:39:00Z	2024-04-04T07:49:00Z	24.17
GVB152‡	2024-04-04T07:57:00Z	2024-03-26T08:00:00Z	

Continued on next page

Table C.1.: **Filters taken during ExINP_GVB 2023 and 2024.** All filters were analysed by WT-CRAFT and taken by Naruki Hiranuma, his team, and personell from GVB. Some filters were also analysed utilizing INSEKT for comparison. All aerosol suspensions were subjected to heat treatment for 20 min at 100 °C (see also section 3.2.1). Date and time expressed according to ISO 8601. (Continued)

Samplename	Start time	Stop time	Duration / h
GVB153	2024-04-04T08:08:00Z	2024-04-05T07:31:00Z	23.38
GVB154	2024-04-05T07:40:00Z	2024-04-06T07:42:00Z	24.03
GVB155	2024-04-06T07:48:00Z	2024-04-09T08:26:00Z	72.63
GVB156	2024-04-09T08:32:00Z	2024-04-12T08:28:00Z	71.93
GVB157	2024-04-12T08:34:00Z	2024-04-15T09:31:00Z	72.95
GVB158	2024-04-15T09:36:00Z	2024-04-18T07:39:00Z	70.05
GVB159	2024-04-18T07:45:00Z	2024-04-22T09:21:00Z	97.60
GVB160	2024-04-22T09:24:00Z	2024-04-25T07:18:00Z	69.90
GVB161	2024-04-25T07:22:00Z	2024-04-28T16:30:00Z	81.13
GVB162	2024-04-28T16:36:00Z	2024-05-02T12:17:00Z	91.68
GVB163	2024-05-02T12:22:00Z	2024-05-05T14:50:00Z	74.47
GVB164	2024-05-05T14:55:00Z	2024-05-08T08:23:00Z	65.47
GVB165	2024-05-08T08:27:00Z	2024-05-11T10:46:00Z	74.32
GVB166	2024-05-11T10:50:00Z	2024-05-15T09:19:00Z	94.48
GVB167	2024-05-15T09:21:00Z	2024-05-20T08:48:00Z	119.45
GVB168	2024-05-20T08:51:00Z	2024-05-24T07:28:00Z	94.62
GVB169	2024-05-24T07:33:00Z	2024-05-28T08:51:00Z	97.30
GVB170	2024-05-28T08:54:00Z	2024-06-01T11:45:00Z	98.95
GVB171	2024-06-01T11:49:00Z	2024-06-05T12:47:00Z	96.97
GVB172	2024-06-05T12:50:00Z	2024-06-08T11:30:00Z	70.67
GVB173	2024-06-08T11:33:00Z	2024-06-11T08:01:00Z	68.47
GVB174	2024-06-11T08:03:00Z	2024-06-15T10:17:00Z	98.23
GVB175	2024-06-15T10:21:00Z	2024-06-19T07:54:00Z	93.55

† Analysed with WT-CRAFT and INSEKT.
‡ This filter is a handling blank.

C.3.1. Comparison of filter samples between INSEKT and WT-CRAFT

Some of these filters have been cut in half and where analysed by INSEKT as well. This is visualized in figures C.11 to C.17. The results are compared utilizing the normalized mean bias defined as

$$B_{\mathrm{n}} = \frac{2}{N} \sum_{i=1}^{N} \frac{a_i - b_i}{a_i + b_i} \tag{C.2}$$

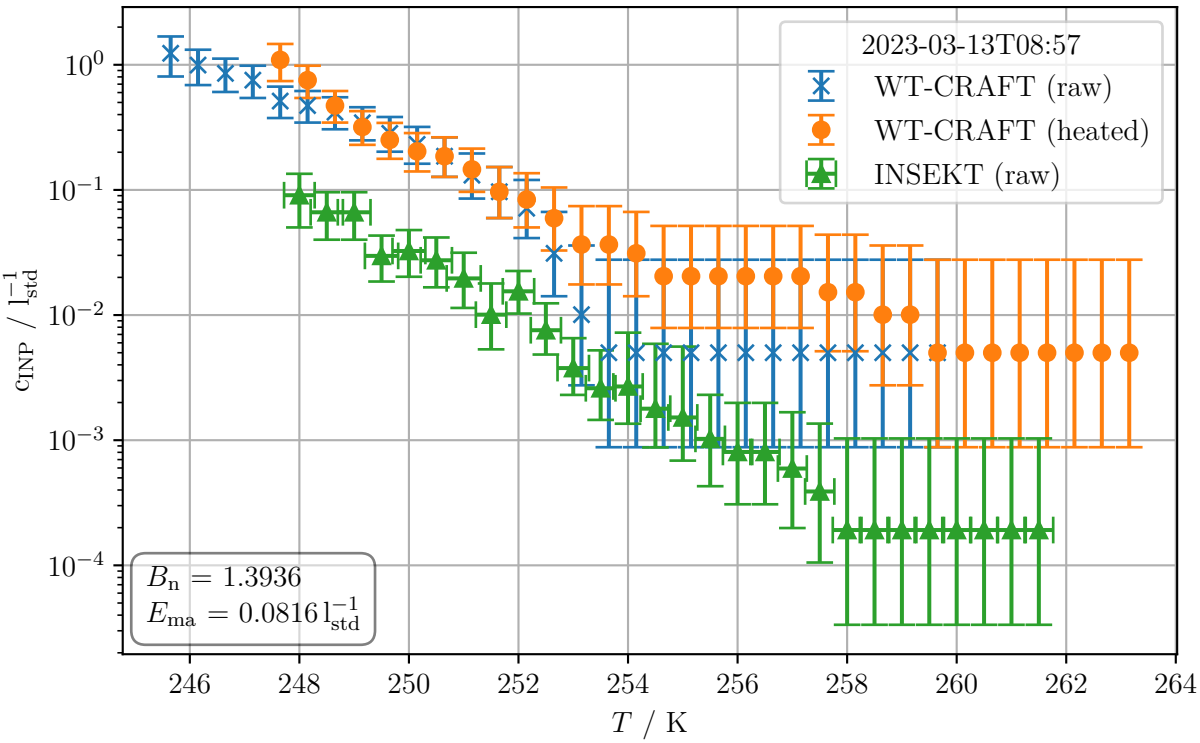

Figure C.11.: **Freezing spectra obtained from the same filter (GVB27) via WT-CRAFT and INSEKT.** The filters analyzed with INSEKT were stored for around six months at −20 °C. The normalized mean bias B_n and the mean absolute error E_{ma} are shown.

and the mean absolute error

$$E_{ma} = \frac{1}{N}\sum_{i=1}^{N} \mathrm{abs}(a_i - b_i) \ . \tag{C.3}$$

The normalized mean bias is zero if the two samples a and b are equal. It is positive if sample a is larger than sample b and negative if sample a is smaller than sample b. The mean absolute error is zero if the two samples a and b are equal. If grows larger if the two samples are not equal, the larger the mean absolute error, the larger the difference between sample a and sample b.

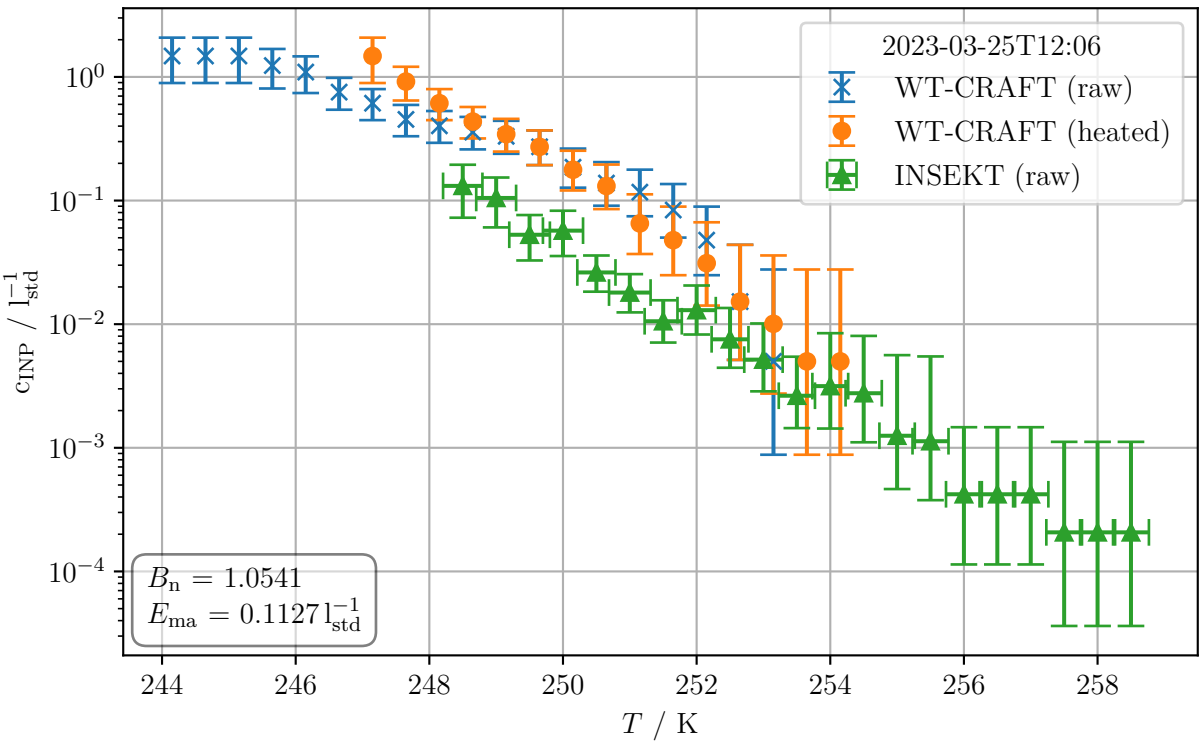

Figure C.12.: **Freezing spectra obtained from the same filter (GVB40) via WT-CRAFT and INSEKT.** The filters analyzed with INSEKT were stored for around six months at −20 °C. The normalized mean bias B_n and the mean absolute error E_{ma} are shown.

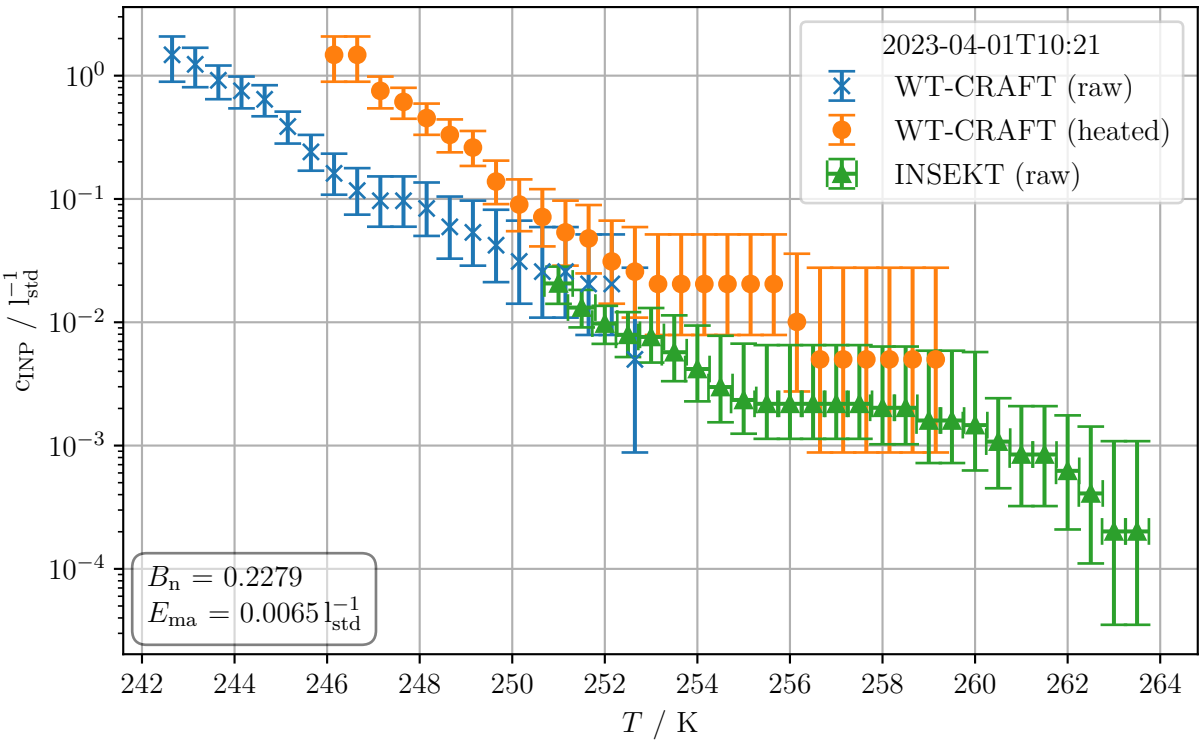

Figure C.13.: **Freezing spectra obtained from the same filter (GVB46) via WT-CRAFT and INSEKT.** The filters analyzed with INSEKT were stored for around six months at −20 °C. The normalized mean bias B_n and the mean absolute error E_{ma} are shown.

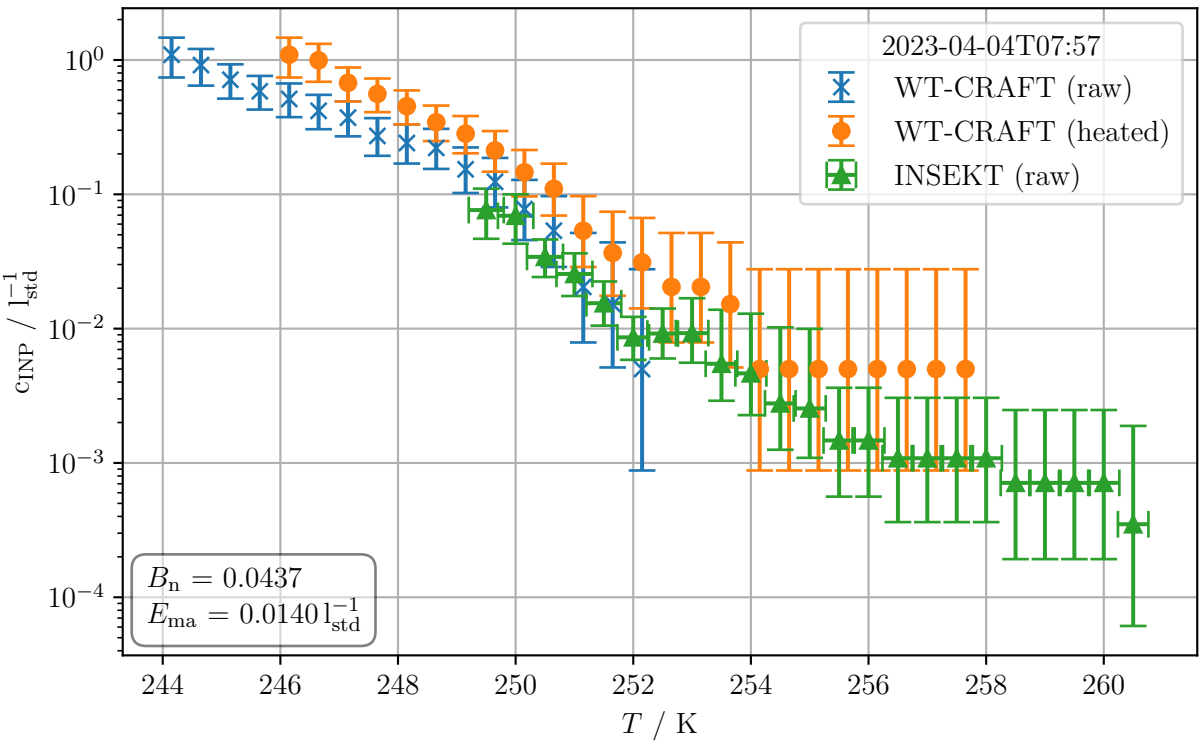

Figure C.14.: **Freezing spectra obtained from the same filter (GVB48) via WT-CRAFT and INSEKT.** The filters analyzed with INSEKT were stored for around six months at −20 °C. The normalized mean bias B_n and the mean absolute error E_{ma} are shown.

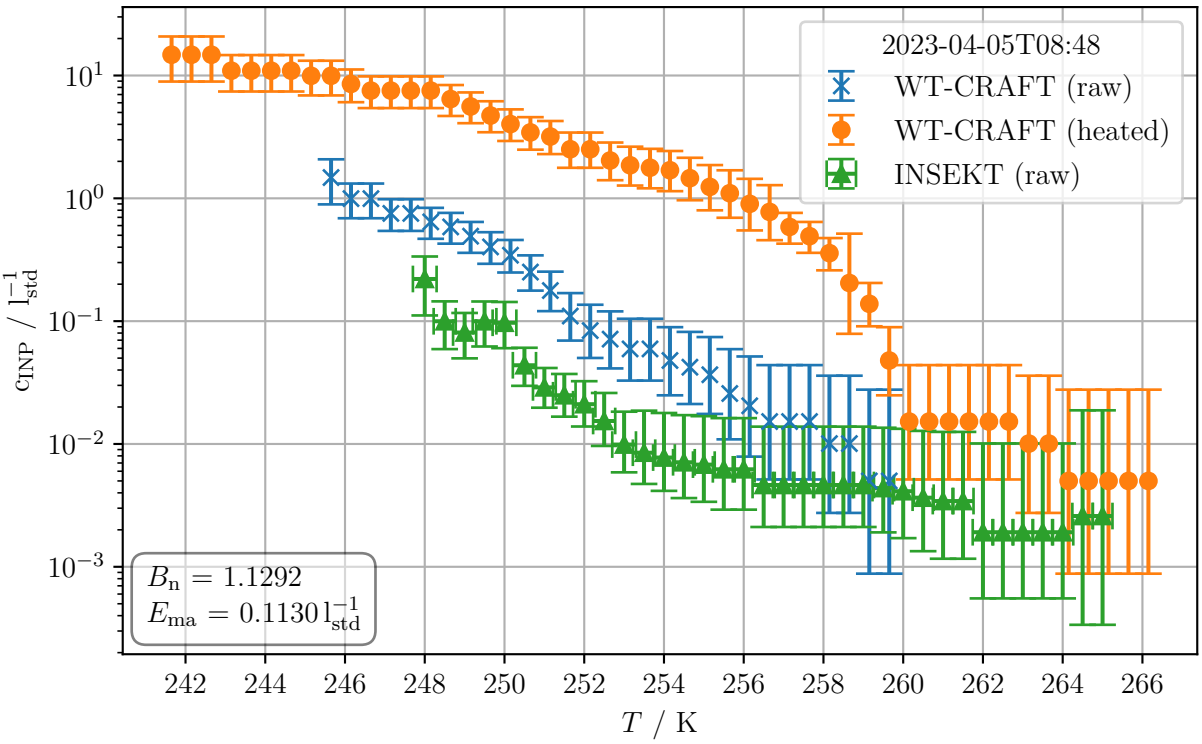

Figure C.15.: **Freezing spectra obtained from the same filter (GVB49) via WT-CRAFT and INSEKT.** The filters analyzed with INSEKT were stored for around six months at −20 °C. The normalized mean bias B_n and the mean absolute error E_{ma} are shown.

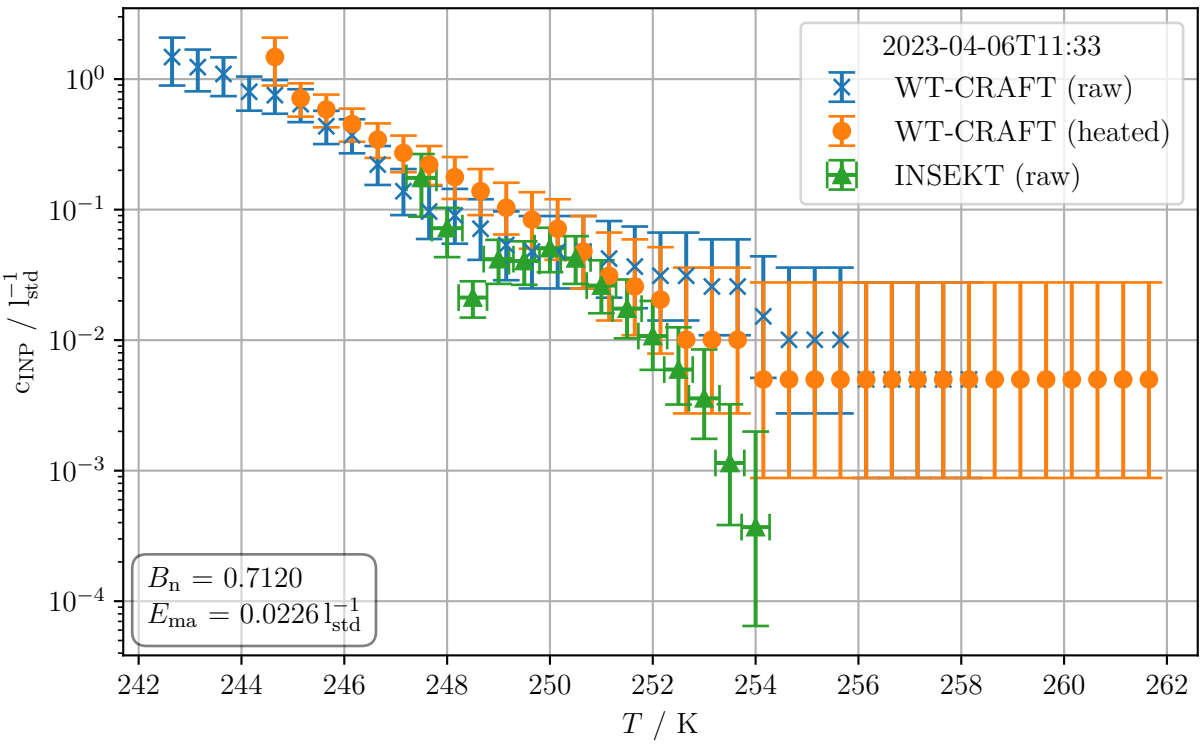

Figure C.16.: **Freezing spectra obtained from the same filter (GVB50) via WT-CRAFT and INSEKT.** The filters analyzed with INSEKT were stored for around six months at −20 °C. The normalized mean bias B_n and the mean absolute error E_{ma} are shown.

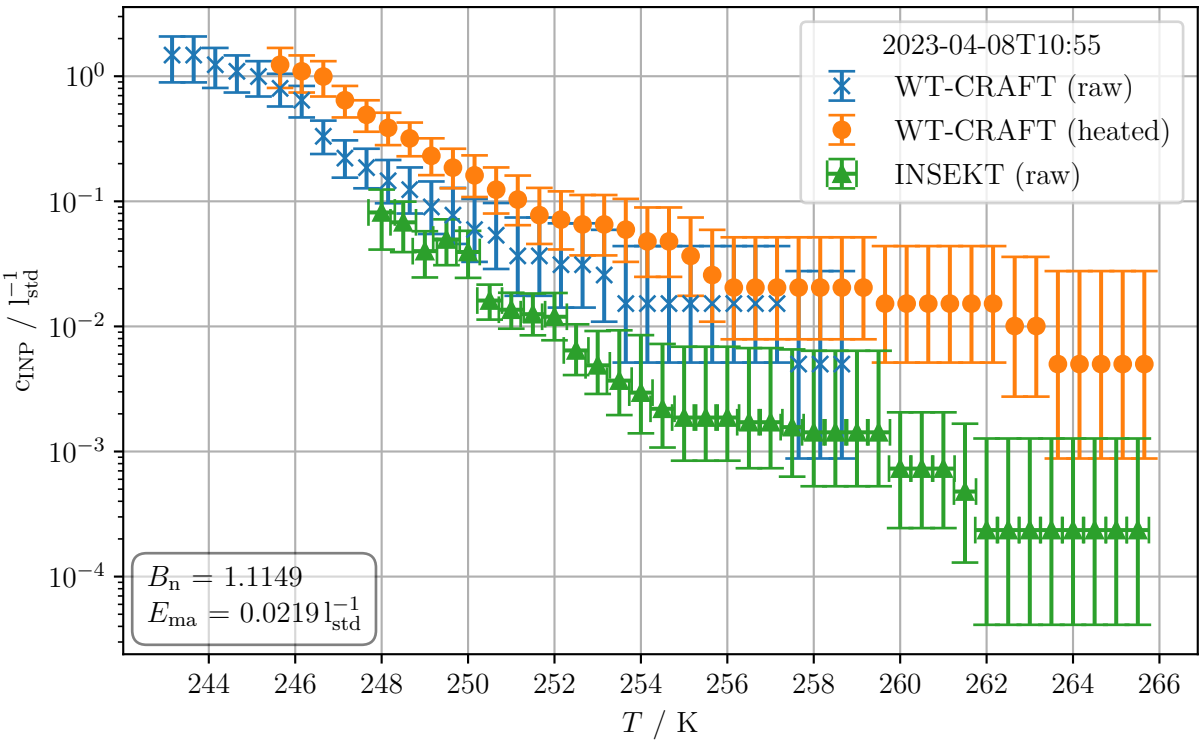

Figure C.17.: **Freezing spectra obtained from the same filter (GVB52) via WT-CRAFT and INSEKT.** The filters analyzed with INSEKT were stored for around six months at −20 °C. The normalized mean bias B_n and the mean absolute error E_{ma} are shown.

C.3.2. Integration error calculated for backwards trajectories

The relative integration error is used to assess the validity of backward trajectories calculated by HYSPLIT. The relative integration error is the loop closure distance divided by the total distance travelled by reverse and original trajectories and divided by two. The relative integration error is given in % and the frequency is shown in figure C.18 for the four altitudes 250 m, 500 m, 750 m and 1000 m agl. The trajectories are created using HYSPLIT (e.g., Draxler and Hess 1998; Stein et al. 2015) utilizing PySPLIT (Warner 2018) and data from Global Data Assimilation System (GDAS).

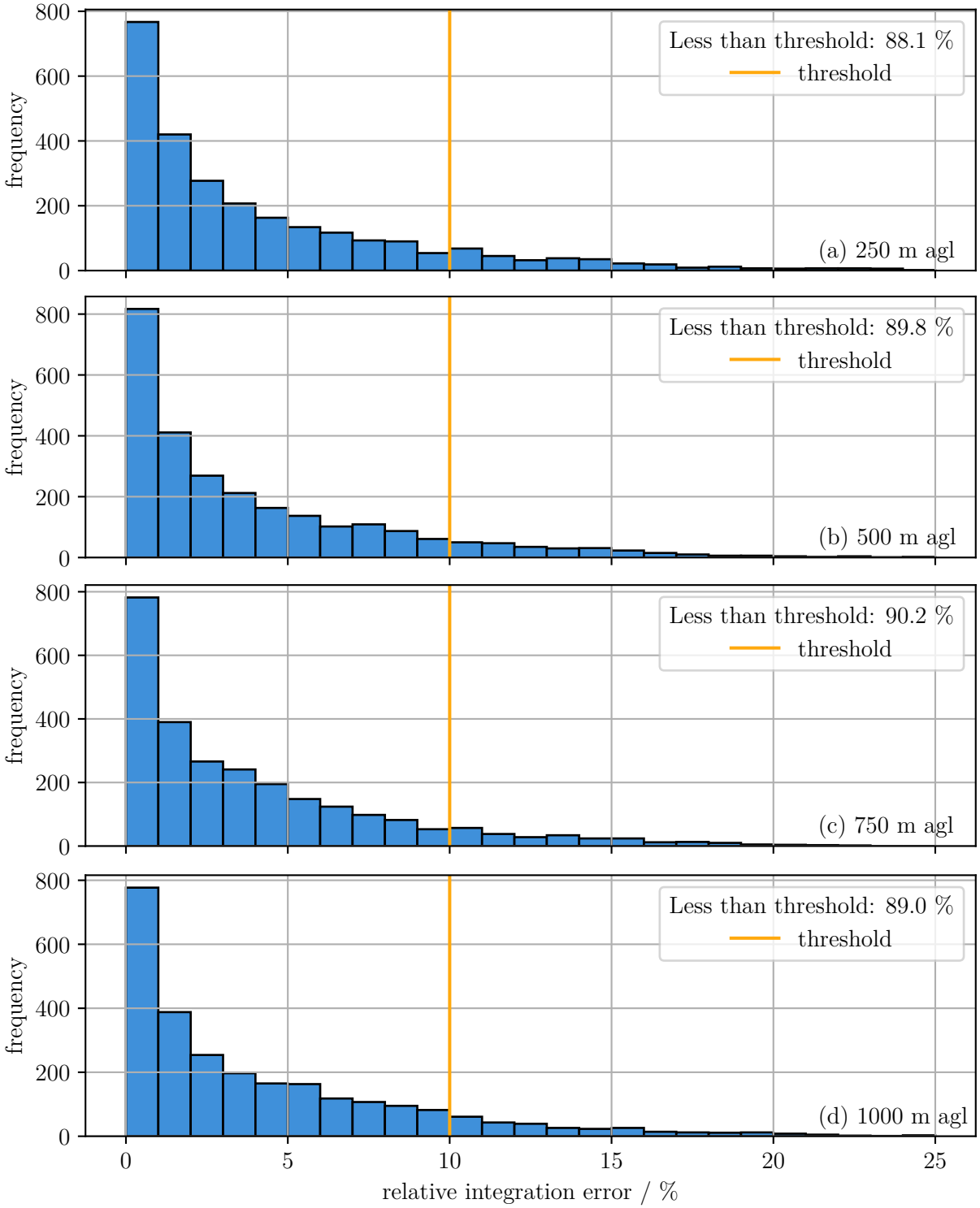

Figure C.18.: **Frequency of relative integration error calculated for backward trajectories calculated by HYSPLIT.** A threshold of 10 % is chosen as a threshold above which the trajectory is not used in the analysis. This corresponds to around 90 % valid trajectories per altitude.

C.4. Determination of lower and higher INAS density episodes

Lower and higher INAS density episodes are defined by calculating the first and third quartiles of the INAS density. Any data below the first quartile is considered 'low' and any data above the third quartile is considered 'high'. To obtain a managable number of lower and higher INAS density episodes, the dataset was split into daily datasets. If a single day contained more than $^3/_{24}$ of a 'low' INAS density, the whole day was considered to be part of an higher INAS density episode. The same approach is used for the lower INAS density episodes. A typical temperature ramp takes around 3 h, therefore this threshold is used for the daily datasets. This is done for the INAS density calculated for each nucleation temperature bin and results in the episodes listed in table C.2.

Table C.2.: **List of lower and higher INAS density episodes of the campaigns PaCE-2022, ExINP_GVB 2023, ExINP_GVB 2024 and ExINP_ZEP.** The temperatures represent the middle of the nucleation temperature bin.

Episode number	First day	Last day	Temperatures / K
lower episodes during PaCE-2022			
1	2022-09-24	2022-09-27	250
2	2022-10-09	2022-10-10	250
3	2022-10-12	2022-10-13	250
4	2022-10-13	2022-10-15	246
5	2022-11-01	2022-11-03	242, 246 and 248
6	2022-11-06	2022-11-09	242, 244, 246, 248 and 250
7	2022-11-14	2022-11-20	248
8	2022-11-23	2022-11-24	248
9	2022-12-05	2022-12-09	248 and 250
higher episodes during PaCE-2022			
1	2022-09-28	2022-09-29	248 and 250
2	2022-10-11	2022-10-12	250
3	2022-10-15	2022-10-16	246
4	2022-11-04	2022-11-05	240, 244, 246 and 248
5	2022-11-09	2022-11-10	246 and 248
6	2022-11-12	2022-11-13	248
7	2022-11-22	2022-11-23	248
8	2022-11-25	2022-11-29	248
9	2022-12-02	2022-12-05	248
10	2022-12-06	2022-12-07	248
11	2022-12-10	2022-12-11	248

Continued on next page

Table C.2.: **List of lower and higher INAS density episodes of the campaigns PaCE-2022, ExINP_GVB 2023, ExINP_GVB 2024 and ExINP_ZEP.** The temperatures represent the middle of the nucleation temperature bin. (Continued)

Episode number	First day	Last day	Temperatures / K
12	2022-12-14	2022-12-15	250
lower episodes during ExINP_GVB 2023			
1	2023-03-17	2023-03-23	242 and 244
higher episodes during ExINP_GVB 2023			
1	2023-03-23	2023-03-27	240, 242, 244 and 245
lower episodes during ExINP_GVB 2024			
1	2024-04-26	2024-04-28	239, 243 and 245
2	2024-05-02	2024-05-06	239, 241, 243, 245 and 249
3	2024-06-01	2024-06-04	241, 243, 245, 247 and 249
higher episodes during ExINP_GVB 2024			
1	2024-04-12	2024-04-16	239, 241, 243 and 245
2	2024-05-08	2024-05-10	243, 245 and 247
3	2024-05-16	2024-05-18	239, 241, 243, 245 and 247
lower episodes during ExINP_ZEP			
1	2023-05-22	2023-05-25	244, 246, 248 and 250
2	2023-06-03	2023-06-06	242 and 244
3	2023-06-09	2023-06-12	250
4	2023-06-26	2023-06-27	242
5	2023-07-07	2023-07-09	244 and 250
6	2023-09-01	2023-09-02	244
7	2023-09-05	2023-09-07	244
8	2023-09-22	2023-09-26	242, 244, 246, 248 and 250
9	2023-10-02	2023-10-05	242, 244, 246, 248 and 250
10	2023-10-07	2023-10-11	242, 244, 246, 248 and 250
11	2023-10-13	2023-10-14	250

Continued on next page

Table C.2.: **List of lower and higher INAS density episodes of the campaigns PaCE-2022, ExINP_GVB 2023, ExINP_GVB 2024 and ExINP_ZEP.** The temperatures represent the middle of the nucleation temperature bin. (Continued)

Episode number	First day	Last day	Temperatures / K
12	2023-10-17	2023-10-18	242 and 244
13	2023-10-20	2023-10-21	242, 244 and 246
14	2023-10-23	2023-10-29	242, 244, 246, 248 and 250
15	2023-11-10	2023-11-11	250
16	2023-12-11	2023-12-12	250
17	2023-12-14	2023-12-15	244
18	2024-01-04	2024-01-07	246, 248 and 250
19	2024-02-23	2024-02-24	250
higher episodes during ExINP_ZEP			
1	2023-05-29	2023-05-31	250
2	2023-06-22	2023-06-27	242, 244, 246, 248 and 250
3	2023-06-28	2023-06-29	242, 244, 246, 248 and 250
4	2023-08-18	2023-08-19	244
5	2023-08-30	2023-08-31	250
6	2023-09-02	2023-09-03	250
7	2023-09-05	2023-09-07	242
8	2023-09-09	2023-09-10	242, 244 and 248
9	2023-09-21	2023-09-22	248
10	2023-11-05	2023-11-06	244 and 246
11	2023-11-22	2023-11-23	248
12	2023-11-29	2023-11-30	244, 248 and 250
13	2023-12-20	2023-12-23	240, 242, 244 and 246
14	2024-01-02	2024-01-03	242
15	2024-01-09	2024-01-10	242, 244, 246, 248 and 250
16	2024-01-19	2024-01-20	242, 244, 246, 248 and 250
17	2024-01-22	2024-01-24	242, 244 and 246
18	2024-01-30	2024-01-31	246
19	2024-02-27	2024-02-28	242

Continued on next page

Table C.2.: **List of lower and higher INAS density episodes of the campaigns PaCE-2022, ExINP_GVB 2023, ExINP_GVB 2024 and ExINP_ZEP.** The temperatures represent the middle of the nucleation temperature bin. (Continued)

Episode number	First day	Last day	Temperatures / K
20	2024-03-15	2024-03-17	240 and 242
21	2024-03-20	2024-03-21	240, 244 and 250
22	2024-03-23	2024-03-26	244
23	2024-03-28	2024-03-31	240, 242 and 244

Appendix D.

Additional information on mobile filter setup

The transport efficiency of aerosol particles is calculated for the mobile filter setup deployed on the UAV during its three versions. The total transport efficiency is visualized in figure D.1.

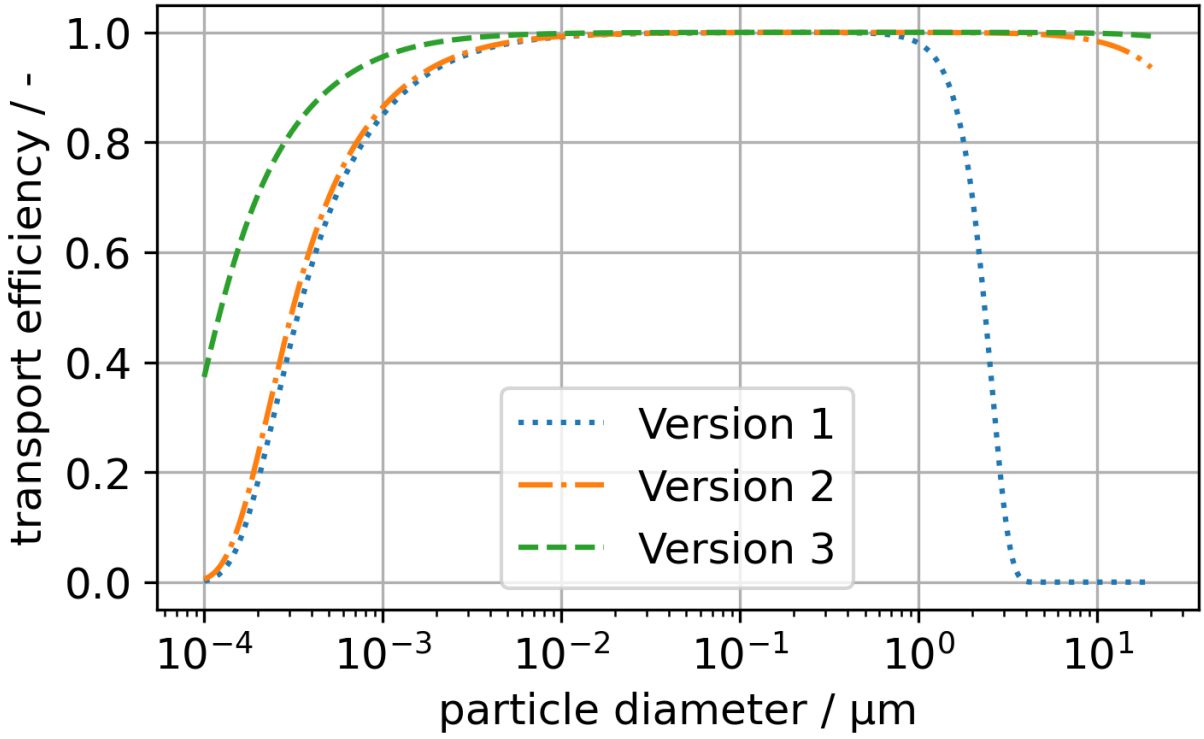

Figure D.1.: **Transport efficiency of mobile filter setup.** Transport efficiency calculated for the three versions described in section 3.3.2. All calculations are done using the as_tools software developed during this work. The software can be accessed at https://codebase.helmholtz.cloud/alexander.boehmlaender/as_tools.git, last accessed 2025-06-23.

Appendix E.

Parameterization formulas and classification of INAS episodes

This chapter presents the parameterizations for different aerosol samples. The valid temperature range and their references are given in table 2.3. All INAS densities are given in cm^{-2}.

A parameterization was developed by Ullrich et al. (2017) for dust aerosol:

$$n_\mathrm{s} = 10^{-4} \exp\left(0.517 \left(\frac{T}{\mathrm{K}} + 273.15\right) + 150.577\right) \ . \tag{E.1}$$

For illite, a parameterization was developed by Broadley et al. (2012):

$$\begin{aligned} n_\mathrm{s} = \exp\Bigg(& -4.822\,268 \times 10^{-3} \left(\frac{T}{\mathrm{K}} + 273.15\right)^3 \\ & + 3.446\,885\,376 \left(\frac{T}{\mathrm{K}} + 273.15\right)^2 \\ & + -8.215\,309 \times 10^{2} \left(\frac{T}{\mathrm{K}} + 273.15\right) \\ & + 6.530\,43 \times 10^{4} \Bigg) \ . \end{aligned} \tag{E.2}$$

A parameterization of soot was developed by Ullrich et al. (2017):

$$n_\mathrm{s} = 7.436 \times 10^{-4} \exp\left(-0.0101 \left(\frac{T}{\mathrm{K}}\right)^2 - 0.8525 \left(\frac{T}{\mathrm{K}}\right) + 0.7667\right) \ . \tag{E.3}$$

Data from volcanic ash measurements was used by Murray et al. (2012) to develop a parameterization:

$$n_\mathrm{s} = \exp\left(-0.02287 \left(\frac{T}{\mathrm{K}}\right)^2 - 1.87203 \left(\frac{T}{\mathrm{K}}\right) - 22.05302\right) \ . \tag{E.4}$$

Murray et al. (2012) also developed a parameterization for birch pollen:

$$n_\mathrm{s} = \exp\left(-0.0309 \left(\frac{T}{\mathrm{K}}\right)^3 - 1.9893 \left(\frac{T}{\mathrm{K}}\right)^2 - 42.938 \left(\frac{T}{\mathrm{K}}\right) - 297.26\right) \ . \tag{E.5}$$

A parameterization for *Cladosporidium* spores was devloped by Murray et al. (2012):

$$n_\mathrm{s} = \exp\left(-0.02934 \left(\frac{T}{\mathrm{K}}\right)^3 - 2.91415 \left(\frac{T}{\mathrm{K}}\right)^2 - 96.59842 \left(\frac{T}{\mathrm{K}}\right) - 1056.63326\right) \ . \tag{E.6}$$

The bacteria *Pseudonomas Syringae* follows the parameterization devloped by Murray et al. (2012):

$$n_{\mathrm{s}} = \exp\left(-0.4325\left(\frac{T}{\mathrm{K}}\right)^{2} - 5.1067\left(\frac{T}{\mathrm{K}}\right) - 10.399\right) \ . \tag{E.7}$$

The following three parameterizations were developed by Schneider et al. (2021) utilizing data collected in the boreal forest in southern Finland during summertime:

$$n_{\mathrm{s}} = 10^{-4}\exp\left(-0.543\left(\frac{T}{\mathrm{K}} + 273.15\right) + 154\right) \ , \tag{E.8}$$

during the trnasition period between summertime and wintertime:

$$n_{\mathrm{s}} = 10^{-4}\exp\left(-0.49\left(\frac{T}{\mathrm{K}} + 273.15\right) + 140\right) \ , \tag{E.9}$$

and during wintertime:

$$n_{\mathrm{s}} = 10^{-4}\exp\left(-0.495\left(\frac{T}{\mathrm{K}} + 273.15\right) + 141\right) \ . \tag{E.10}$$

Bibliography

Acosta Navarro, J. C., V. Varma, I. Riipinen, Ø. Seland, A. Kirkevåg, H. Struthers, T. Iversen, H.-C. Hansson and A. M. L. Ekman (2016). 'Amplification of Arctic warming by past air pollution reductions in Europe'. In: *Nature Geoscience* 9 (4), pp. 277–281. ISSN: 1752-0908. DOI: 10.1038/ngeo2673.

Agresti, A. and B. A. Coull (1998). 'Approximate is Better than "Exact" for Interval Estimation of Binomial Proportions'. In: *The American Statistician* 52 (2), pp. 119–126. DOI: 10.1080/00031305.1998.10480550.

Aliabadi, A. A., J. L. Thomas, A. B. Herber, R. M. Staebler, W. R. Leaitch, H. Schulz, K. S. Law, L. Marelle, J. Burkart, M. D. Willis, H. Bozem, P. M. Hoor, F. Köllner, J. Schneider, M. Levasseur and J. P. D. Abbatt (2016). 'Ship emissions measurement in the Arctic by plume intercepts of the Canadian Coast Guard icebreaker *Amundsen* from the *Polar* 6 aircraft platform'. In: *Atmospheric Chemistry and Physics* 16 (12), pp. 7899–7916. DOI: 10.5194/acp-16-7899-2016.

Alpert, P. A. and D. A. Knopf (2016). 'Analysis of isothermal and cooling-rate-dependent immersion freezing by a unifying stochastic ice nucleation model'. In: *Atmospheric Chemistry and Physics* 16 (4), pp. 2083–2107. ISSN: 1680-7324. DOI: 10.5194/acp-16-2083-2016.

Altstädter, B., A. Platis, M. Jähn, H. Baars, J. Lückerath, A. Held, A. Lampert, J. Bange, M. Hermann and B. Wehner (2018). 'Airborne observations of newly formed boundary layer aerosol particles under cloudy conditions'. In: *Atmospheric Chemistry and Physics* 18 (11), pp. 8249–8264. DOI: 10.5194/acp-18-8249-2018.

Amore, A., F. Giardi, S. Becagli, L. Caiazzo, M. Mazzola, M. Severi and R. Traversi (2022). 'Source apportionment of sulphate in the High Arctic by a 10 yr-long record from Gruvebadet Observatory (Ny-Ålesund, Svalbard Islands)'. In: *Atmospheric Environment* 270, p. 118890. ISSN: 1352-2310. DOI: 10.1016/j.atmosenv.2021.118890.

Andreas, E. L., K. F. Jones and C. W. Fairall (2010). 'Production velocity of sea spray droplets'. In: *Journal of Geophysical Research: Oceans* 115 (C12). ISSN: 0148-0227. DOI: 10.1029/2010jc006458.

Andreas, E. L. (1992). 'Sea spray and the turbulent air-sea heat fluxes'. In: *Journal of Geophysical Research: Oceans* 97 (C7), pp. 11429–11441. ISSN: 0148-0227. DOI: 10.1029/92jc00876.

Andreas, E. L. (1998). 'A New Sea Spray Generation Function for Wind Speeds up to $32\,\mathrm{m\,s^{-1}}$'. In: *Journal of Physical Oceanography* 28 (11), pp. 2175–2184. ISSN: 1520-0485. DOI: 10.1175/1520-0485(1998)028<2175:anssgf>2.0.co;2.

Anguelova, M., R. P. Barber and J. Wu (1999). 'Spume Drops Produced by the Wind Tearing of Wave Crests'. In: *Journal of Physical Oceanography* 29 (6), pp. 1156–1165. ISSN: 1520-0485. DOI: 10.1175/1520-0485(1999)029<1156:sdpbtw>2.0.co;2.

Anttila, T., D. Brus, A. Jaatinen, A.-P. Hyvärinen, N. Kivekäs, S. Romakkaniemi, M. Komppula and H. Lihavainen (2012). 'Relationships between particles, cloud condensation nuclei and

cloud droplet activation during the third Pallas Cloud Experiment'. In: *Atmospheric Chemistry and Physics* 12 (23), pp. 11435–11450. ISSN: 1680-7324. DOI: 10.5194/acp-12-11435-2012.

Anttila, T., P. Vaattovaara, M. Komppula, A.-P. Hyvärinen, H. Lihavainen, V.-M. Kerminen and A. Laaksonen (2009). 'Size-dependent activation of aerosols into cloud droplets at a subarctic background site during the second Pallas Cloud Experiment (2nd PaCE): method development and data evaluation'. In: *Atmospheric Chemistry and Physics* 9 (14), pp. 4841–4854. ISSN: 1680-7324. DOI: 10.5194/acp-9-4841-2009.

Ardyna, M., C. J. Mundy, N. Mayot, L. C. Matthes, L. Oziel, C. Horvat, E. Leu, P. Assmy, V. Hill, P. A. Matrai, M. Gale, I. A. Melnikov and K. R. Arrigo (2020). 'Under-Ice Phytoplankton Blooms: Shedding Light on the "Invisible" Part of Arctic Primary Production'. In: *Frontiers in Marine Science* 7. ISSN: 2296-7745. DOI: 10.3389/fmars.2020.608032.

Aristotle (2006). *Meteorology*. Ed. by E. W. Webster. ISBN: 9781425001025.

Arnalds, O. (2010). 'Dust sources and deposition of aeolian materials in Iceland'. In: *Icelandic Agricultural Science* 23 (2010), pp. 3–21.

Arnalds, O., P. Dagsson-Waldhauserova and H. Olafsson (2016). 'The Icelandic volcanic aeolian environment: Processes and impacts — A review'. In: *Aeolian Research* 20, pp. 176–195. DOI: 10.1016/j.aeolia.2016.01.004.

Asmi, A., A. Wiedensohler, P. Laj, A.-M. Fjaeraa, K. Sellegri, W. Birmili, E. Weingartner, U. Baltensperger, V. Zdimal, N. Zikova, J.-P. Putaud, A. Marinoni, P. Tunved, H.-C. Hansson, M. Fiebig, N. Kivekäs, H. Lihavainen, E. Asmi, V. Ulevicius, P. P. Aalto, E. Swietlicki, A. Kristensson, N. Mihalopoulos, N. Kalivitis, I. Kalapov, G. Kiss, G. de Leeuw, B. Henzing, R. M. Harrison, D. Beddows, C. O'Dowd, S. G. Jennings, H. Flentje, K. Weinhold, F. Meinhardt, L. Ries and M. Kulmala (2011). 'Number size distributions and seasonality of submicron particles in Europe 2008–2009'. In: *Atmospheric Chemistry and Physics* 11 (11), pp. 5505–5538. DOI: 10.5194/acp-11-5505-2011.

Asmi, E., J. Backman, H. Servomaa, A. Virkkula, M. I. Gini, K. Eleftheriadis, T. Müller, S. Ohata, Y. Kondo and A. Hyvärinen (2021). 'Absorption instruments inter-comparison campaign at the Arctic Pallas station'. In: *Atmospheric Measurement Techniques* 14 (8), pp. 5397–5413. ISSN: 1867-8548. DOI: 10.5194/amt-14-5397-2021.

Assmy, P., A. Cecilie Kvernvik, H. Hop, C. J. Hoppe, M. Chierici, D. David T., P. Duarte, A. Fransson, L. M. García, W. Patuła, S. Kwaśniewski, M. Maturilli, O. Pavlova, A. Tatarek, J. M. Wiktor, A. Wold, K. K. Wolf and A. Bailey (2023). 'Seasonal plankton dynamics in Kongsfjorden during two years of contrasting environmental conditions'. In: *Progress in Oceanography* 213, p. 102996. ISSN: 0079-6611. DOI: 10.1016/j.pocean.2023.102996.

Atkinson, J. D., B. J. Murray, M. T. Woodhouse, T. F. Whale, K. J. Baustian, K. S. Carslaw, S. Dobbie, D. O'Sullivan and T. L. Malkin (2013). 'The importance of feldspar for ice nucleation by mineral dust in mixed-phase clouds'. In: *Nature* 498 (7454), pp. 355–358. DOI: 10.1038/nature12278.

Baddock, M. C., T. Mockford, J. E. Bullard and T. Thorsteinsson (2017). 'Pathways of high-latitude dust in the North Atlantic'. In: *Earth and Planetary Science Letters* 459, pp. 170–182. DOI: 10.1016/j.epsl.2016.11.034.

Barahona, D. (2012). 'On the ice nucleation spectrum'. In: *Atmospheric Chemistry and Physics* 12 (8), pp. 3733–3752. ISSN: 1680-7324. DOI: 10.5194/acp-12-3733-2012.

Bärfuss, K., F. Pätzold, B. Altstädter, E. Kathe, S. Nowak, L. Bretschneider, U. Bestmann and A. Lampert (2018). 'New Setup of the UAS ALADINA for Measuring Boundary Layer Properties, Atmospheric Particles and Solar Radiation'. In: *Atmosphere* 9 (1). ISSN: 2073-4433. DOI: 10.3390/atmos9010028.

Barr, S. L., B. Wyld, J. B. McQuaid, R. R. Neely III and B. J. Murray (2023). 'Southern Alaska as a source of atmospheric mineral dust and ice-nucleating particles'. In: *Science Advances* 9 (33). ISSN: 2375-2548. DOI: 10.1126/sciadv.adg3708.

Barry, K. R., T. C. J. Hill, C. Jentzsch, B. F. Moffett, F. Stratmann and P. J. DeMott (2021). 'Pragmatic protocols for working cleanly when measuring ice nucleating particles'. In: *Atmospheric Research* 250, p. 105419. DOI: 10.1016/j.atmosres.2020.105419.

Bauer, S. E., S. Menon, D. Koch, T. C. Bond and K. Tsigaridis (2010). 'A global modeling study on carbonaceous aerosol microphysical characteristics and radiative effects'. In: *Atmospheric Chemistry and Physics* 10 (15), pp. 7439–7456. ISSN: 1680-7324. DOI: 10.5194/acp-10-7439-2010.

Baustian, K. J., D. J. Cziczo, M. E. Wise, K. A. Pratt, G. Kulkarni, A. G. Hallar and M. A. Tolbert (2012). 'Importance of aerosol composition, mixing state, and morphology for heterogeneous ice nucleation: A combined field and laboratory approach'. In: *Journal of Geophysical Research: Atmospheres* 117 (D6), p. D06217. DOI: 10.1029/2011JD016784.

Beer, E., I. Eisenman and T. J. W. Wagner (2020). 'Polar Amplification Due to Enhanced Heat Flux Across the Halocline'. In: *Geophysical Research Letters* 47 (4). ISSN: 1944-8007. DOI: 10.1029/2019gl086706.

Beine, H. J., S. Argentini, A. Maurizi, A. Viola and G. Mastrantonio (2001). 'The local wind field at Ny-Ålesund and the Zeppelin mountain at Svalbard'. In: *Meteorology and Atmospheric Physics* 78 (1–2), pp. 107–113. ISSN: 1436-5065. DOI: 10.1007/s007030170009.

Bellouin, N., J. Quaas, E. Gryspeerdt, S. Kinne, P. Stier, D. Watson-Parris, O. Boucher, K. S. Carslaw, M. Christensen, A.-L. Daniau, J.-L. Dufresne, G. Feingold, S. Fiedler, P. Forster, A. Gettelman, J. M. Haywood, U. Lohmann, F. Malavelle, T. Mauritsen, D. T. McCoy, G. Myhre, J. Mülmenstädt, D. Neubauer, A. Possner, M. Rugenstein, Y. Sato, M. Schulz, S. E. Schwartz, O. Sourdeval, T. Storelvmo, V. Toll, D. Winker and B. Stevens (2020). 'Bounding Global Aerosol Radiative Forcing of Climate Change'. In: *Reviews of Geophysics* 58 (1). DOI: 10.1029/2019rg000660.

Belmonte Rivas, M. and A. Stoffelen (2019). 'Characterizing ERA-Interim and ERA5 surface wind biases using ASCAT'. In: *Ocean Science* 15 (3), pp. 831–852. ISSN: 1812-0792. DOI: 10.5194/os-15-831-2019.

Ben-Yami, M., P. Good, L. C. Jackson, M. Crucifix, A. Hu, O. Saenko, D. Swingedouw and N. Boers (2024). 'Impacts of AMOC Collapse on Monsoon Rainfall: A Multi-Model Comparison'. In: *Earth's Future* 12 (9). ISSN: 2328-4277. DOI: 10.1029/2023ef003959.

Berezinski, N. A., G. V. Stepanov and V. G. Khorguani (1988). 'Ice-forming activity of atmospheric aerosol particles of different sizes'. In: *Atmospheric Aerosols and Nucleation*. Springer Berlin Heidelberg, pp. 709–712. ISBN: 9783540459248. DOI: 10.1007/3-540-50108-8_1167.

Bertozzi, B., R. Wagner, J. Song, K. Höhler, J. Pfeifer, H. Saathoff, T. Leisner and O. Möhler (2021). 'Ice nucleation ability of ammonium sulfate aerosol particles internally mixed with secondary organics'. In: *Atmospheric Chemistry and Physics* 21 (13), pp. 10779–10798. ISSN: 1680-7324. DOI: 10.5194/acp-21-10779-2021.

Bieber, P. and N. Borduas-Dedekind (2024). 'High-speed cryo-microscopy reveals that ice-nucleating proteins of *Pseudomonas syringae* trigger freezing at hydrophobic interfaces'. In: *Science Advances* 10 (27). ISSN: 2375-2548. DOI: 10.1126/sciadv.adn6606.

Bieber, P., T. M. Seifried, J. Burkart, J. Gratzl, A. Kasper-Giebl, D. G. Schmale and H. Grothe (2020). 'A Drone-Based Bioaerosol Sampling System to Monitor Ice Nucleation Particles in the Lower Atmosphere'. In: *Remote Sensing* 12 (3), p. 552. DOI: 10.3390/rs12030552.

Bigg, E. K. (1996). 'Ice forming nuclei in the high Arctic'. In: *Tellus B: Chemical and Physical Meteorology* 48 (2), pp. 223–233. DOI: 10.3402/tellusb.v48i2.15888.

Bintanja, R., R. G. Graversen and W. Hazeleger (2011). 'Arctic winter warming amplified by the thermal inversion and consequent low infrared cooling to space'. In: *Nature Geoscience* 4 (11), pp. 758–761. ISSN: 1752-0908. DOI: 10.1038/ngeo1285.

Bischof, K., P. Convey, P. Duarte, J.-P. Gattuso, M. Granberg, H. Hop, C. Hoppe, C. Jiménez, L. Lisitsyn, B. Martinez, M. Y. Roleda, P. Thor, J. M. Wiktor and G. W. Gabrielsen (2019). 'The Ecosystem of Kongsfjorden, Svalbard'. In: *The Ecosystem of Kongsfjorden, Svalbard*. Ed. by H. Hop and C. Wiencke. Vol. 2. Advances in Polar Ecology. Springer International Publishing. Chap. Kongsfjorden as Harbinger of the Future Arctic: Knowns, Unknowns and Research Priorities, pp. 537–562. ISBN: 9783319464251. DOI: 10.1007/978-3-319-46425-1_14.

Boggs, P. T. and J. E. Rogers (1990). 'Orthogonal Distance Regression'. In: *Statistical analysis of measurement error models and applications: proceedings of the AMS-IMS-SIAM joint summer research conference held June 10-16, 1989*. Vol. 112. Contemporary Mathematics, p. 186.

Böhmländer, A. (2021). 'A new Aerosol Payload for Unmanned Aerial Vehicles: Design and First Application for Ice-Nucleating Particle Measurements'. MA thesis. Karlsruhe Institute of Technology.

Böhmländer, A., L. Lacher, D. Brus, K.-M. Doulgeris, Z. Brasseur, M. Boyer, J. Kuula, T. Leisner and O. Möhler (2024). 'A novel aerosol filter sampler for measuring the vertical distribution of ice-nucleating particles via fixed-wing uncrewed aerial vehicles'. In: *Atmospheric Measurement Techniques* 18 (16), pp. 3959–3971. ISSN: 1867-8548. DOI: 10.5194/amt-18-3959-2025.

Böhmländer, A., L. Lacher, R. Fösig, N. Büttner, J. Nadolny, D. Brus, K.-M. Doulgeris and O. Möhler (2025a). 'Measurement of the ice-nucleating particle concentration with the Portable Ice Nucleation Experiment during the Pallas Cloud Experiment 2022 [dataset]'. In: *Earth System Science Data* 17 (11), pp. 6165–6171. ISSN: 1866-3516. DOI: 10.5194/essd-17-6165-2025.

Böhmländer, A., L. Lacher, K. Höhler, D. Brus, K.-M. Doulgeris, J. Girdwood, T. Leisner and O. Möhler (2025b). 'Measurement of the ice-nucleating particle concentration using a mobile filter-based sampler on-board of a fixed-wing uncrewed aerial vehicle during the Pallas Cloud Experiment 2022 [dataset]'. In: *Earth System Science Data* 17 (11), pp. 6157–6164. ISSN: 1866-3516. DOI: 10.5194/essd-17-6157-2025.

Boike, J., O. Ippisch, P. P. Overduin, B. Hagedorn and K. Roth (2008). 'Water, heat and solute dynamics of a mud boil, Spitsbergen'. In: *Geomorphology* 95 (1–2), pp. 61–73. ISSN: 0169-555X. DOI: 10.1016/j.geomorph.2006.07.033.

Boike, J., I. Juszak, S. Lange, S. Chadburn, E. Burke, P. P. Overduin, K. Roth, O. Ippisch, N. Bornemann, L. Stern, I. Gouttevin, E. Hauber and S. Westermann (2018). 'A 20-year record (1998–2017) of permafrost, active layer and meteorological conditions at a high Arctic permafrost research site (Bayelva, Spitsbergen)'. In: *Earth System Science Data* 10 (1), pp. 355–390. ISSN: 1866-3516. DOI: 10.5194/essd-10-355-2018.

Boose, Y., Z. A. Kanji, M. Kohn, B. Sierau, A. Zipori, I. Crawford, G. Lloyd, N. Bukowiecki, E. Herrmann, P. Kupiszewski, M. Steinbacher and U. Lohmann (2016). 'Ice Nucleating Particle Measurements at 241 K during Winter Months at 3580 m MSL in the Swiss Alps'. In: *Journal of the Atmospheric Sciences* 73 (5), pp. 2203–2228. DOI: 10.1175/JAS-D-15-0236.1.

Borys, R. D. (1989). 'Studies of ice nucleation by Arctic aerosol on AGASP-II'. In: *Journal of Atmospheric Chemistry* 9 (1), pp. 169–185. ISSN: 1573-0662. DOI: 10.1007/bf00052831.

Bosch (2020). *BME280 - Data sheet*. 1.9. BME280 sensor specifications. Bosch Sensortec.

Boucher, O., D. Randall, P. Artaxo, C. Bretherton, G. Feingold, P. Forster, V.-M. Kerminen, Y. Kondo, H. Liao, U. Lohmann, P. Rasch, S. K. Satheesh, S. Sherwood, B. Stevens and X. Y. Zhang (2013). 'Clouds and Aerosols'. In: *Climate Change 2013: The Physical Science Basis. Contribution of Working Group I to the Fifth Assessment Report of the Intergovernmental Panel on Climate Change*. Ed. by T. F. Stocker, D. Qin, G.-K. Plattner, M. Tignor, S. K. Allen, J. Boschung, A. Nauels, Y. Xia, V. Bex and P. M. Midgley. Cambridge, United Kingdom and New York, NY, USA: Cambridge University Press. Chap. 7, pp. 571–658. ISBN: 978-1-107-66182-0. DOI: 10.1017/CBO9781107415324.016.

Bozem, H., P. Hoor, D. Kunkel, F. Köllner, J. Schneider, A. Herber, H. Schulz, W. R. Leaitch, A. A. Aliabadi, M. D. Willis, J. Burkart and J. P. D. Abbatt (2019). 'Characterization of transport regimes and the polar dome during Arctic spring and summer using in situ aircraft measurements'. In: *Atmospheric Chemistry and Physics* 19 (23), pp. 15049–15071. DOI: 10.5194/acp-19-15049-2019.

Broadley, S. L., B. J. Murray, R. J. Herbert, J. D. Atkinson, S. Dobbie, T. L. Malkin, E. Condliffe and L. Neve (2012). 'Immersion mode heterogeneous ice nucleation by an illite rich powder representative of atmospheric mineral dust'. In: *Atmospheric Chemistry and Physics* 12 (1), pp. 287–307. ISSN: 1680-7324. DOI: 10.5194/acp-12-287-2012.

Brodowsky, C. V., T. Sukhodolov, G. Chiodo, V. Aquila, S. Bekki, S. S. Dhomse, M. Höpfner, A. Laakso, G. W. Mann, U. Niemeier, G. Pitari, I. Quaglia, E. Rozanov, A. Schmidt, T. Sekiya, S. Tilmes, C. Timmreck, S. Vattioni, D. Visioni, P. Yu, Y. Zhu and T. Peter (2024). 'Analysis of the global atmospheric background sulfur budget in a multi-model framework'. In: *Atmospheric Chemistry and Physics* 24 (9), pp. 5513–5548. ISSN: 1680-7324. DOI: 10.5194/acp-24-5513-2024.

Broecker, W. S. (1975). 'Climatic Change: Are We on the Brink of a Pronounced Global Warming?' In: *Science* 189 (4201), pp. 460–463. ISSN: 1095-9203. DOI: 10.1126/science.189.4201.460.

Brooks, S. D., K. Suter and L. Olivarez (2014). 'Effects of Chemical Aging on the Ice Nucleation Activity of Soot and Polycyclic Aromatic Hydrocarbon Aerosols'. In: *Journal of Physical Chemistry A* 118 (43), pp. 10036–10047. ISSN: 1089-5639. DOI: 10.1021/jp508809y.

Brus, D., K.-M. Doulgeris, G. Bagheri, E. Bodenschatz, R. Pohorsky, J. Schmale, A. Böhmländer, O. Möhler, L. Lacher, J. Girdwood, J. G. Gratzl, V. Kaikkonen, E. O'Connor, V. Le, J. Backman and H. Servomaa (2025). 'Data generated during the Pallas Cloud Experiment 2022 campaign: an introduction and overview'. In: *Earth System Science Data [preprint]*. In preparation.

Bullard, J. E., M. Baddock, T. Bradwell, J. Crusius, E. Darlington, D. Gaiero, S. Gassó, G. Gisladottir, R. Hodgkins, R. McCulloch, C. McKenna-Neuman, T. Mockford, H. Stewart and T. Thorsteinsson (2016). 'High-latitude dust in the Earth system'. In: *Reviews of Geophysics* 54 (2), pp. 447–485. DOI: 10.1002/2016rg000518.

Burrows, S. M., C. Hoose, U. Pöschl and M. G. Lawrence (2013). 'Ice nuclei in marine air: biogenic particles or dust?' In: *Atmospheric Chemistry and Physics* 13 (1), pp. 245–267. DOI: 10.5194/acp-13-245-2013.

Cai, Y., D. C. Montague, W. Mooiweer-Bryan and T. Deshler (2008). 'Performance characteristics of the ultra high sensitivity aerosol spectrometer for particles between 55 and 800 nm: Laboratory and field studies'. In: *Journal of Aerosol Science* 39 (9), pp. 759–769. ISSN: 0021-8502. DOI: 10.1016/j.jaerosci.2008.04.007.

Calvert, J. G. (1990). 'Glossary of atmospheric chemistry terms (Recommendations 1990)'. In: *Pure and Applied Chemistry* 62 (11), pp. 2167–2219. ISSN: 0033-4545. DOI: 10.1351/pac199062112167.

Carlsen, T. and R. O. David (2022). 'Spaceborne Evidence That Ice-Nucleating Particles Influence High-Latitude Cloud Phase'. In: *Geophysical Research Letters* 49 (14). ISSN: 1944-8007. DOI: 10.1029/2022gl098041.

Caroppo, C., P. Pagliara, F. Azzaro, S. Miserocchi and M. Azzaro (2017). 'Late Summer Phytoplankton Blooms in the Changing Polar Environment of the Kongsfjorden (Svalbard, Arctic)'. In: *Cryptogamie, Algologie* 38 (1), pp. 53–72. ISSN: 1776-0984. DOI: 10.7872/crya/v38.iss1.2017.53.

Charlson, R. J., J. Langner, H. Rodhe, C. B. Leovy and S. G. Warren (1991). 'Perturbation of the northern hemisphere radiative balance by backscattering from anthropogenic sulfate aerosols*'. In: *Tellus A* 43 (4). DOI: 10.3402/tellusa.v43i4.11944.

Chen, J., Z. Wu, S. Augustin-Bauditz, S. Grawe, M. Hartmann, X. Pei, Z. Liu, D. Ji and H. Wex (2018). 'Ice-nucleating particle concentrations unaffected by urban air pollution in Beijing, China'. In: *Atmospheric Chemistry and Physics* 18 (5), pp. 3523–3539. ISSN: 1680-7324. DOI: 10.5194/acp-18-3523-2018.

Chen, J.-P., A. Hazra and Z. Levin (2008). 'Parameterizing ice nucleation rates using contact angle and activation energy derived from laboratory data'. In: *Atmospheric Chemistry and Physics* 8 (24), pp. 7431–7449. DOI: 10.5194/acp-8-7431-2008.

Chen, J.-P. (1994). 'Theory of Deliquescence and Modified Köhler Curves'. In: *Journal of the Atmospheric Sciences* 51 (23), pp. 3505–3516.

Chen, Q., J. A. Mirrielees, S. Thanekar, N. A. Loeb, R. M. Kirpes, L. M. Upchurch, A. J. Barget, N. N. Lata, A. R. W. Raso, S. M. McNamara, S. China, P. K. Quinn, A. P. Ault, A. Kennedy, P. B. Shepson, J. D. Fuentes and K. A. Pratt (2022). 'Atmospheric particle abundance and sea salt aerosol observations in the springtime Arctic: a focus on blowing snow and leads'. In: *Atmospheric Chemistry and Physics* 22 (23), pp. 15263–15285. ISSN: 1680-7324. DOI: 10.5194/acp-22-15263-2022.

Chen, S.-C., Y. Hu, D. Y. H. Pui and J. Wang (2016). 'Explicit expressions for the minimum efficiency and most penetrating particle size of Nuclepore filters'. In: *Journal of Aerosol Science* 100, pp. 108–117. DOI: 10.1016/j.jaerosci.2016.07.008.

Chernoff, D. I. and A. K. Bertram (2010). 'Effects of sulfate coatings on the ice nucleation properties of a biological ice nucleus and several types of minerals'. In: *Journal of Geophysical Research: Atmospheres* 115 (D20). DOI: 10.1029/2010JD014254.

Chin, M., T. Diehl, O. Dubovik, T. F. Eck, B. N. Holben, A. Sinyuk and D. G. Streets (2009). 'Light absorption by pollution, dust, and biomass burning aerosols: a global model study and

evaluation with AERONET measurements'. In: *Annales Geophysicae* 27 (9), pp. 3439–3464. ISSN: 1432-0576. DOI: 10.5194/angeo-27-3439-2009.

Christner, B. C., R. Cai, C. E. Morris, K. S. McCarter, C. M. Foreman, M. L. Skidmore, S. N. Montross and D. C. Sands (2008). 'Geographic, seasonal, and precipitation chemistry influence on the abundance and activity of biological ice nucleators in rain and snow'. In: *Proceedings of the National Academy of Sciences* 105 (48), pp. 18854–18859. ISSN: 1091-6490. DOI: 10.1073/pnas.0809816105.

Ciemer, C., R. Winkelmann, J. Kurths and N. Boers (2021). 'Impact of an AMOC weakening on the stability of the southern Amazon rainforest'. In: *The European Physical Journal Special Topics* 230 (14–15), pp. 3065–3073. ISSN: 1951-6401. DOI: 10.1140/epjs/s11734-021-00186-x.

Conen, F., E. Stopelli and L. Zimmermann (2016). 'Clues that decaying leaves enrich Arctic air with ice nucleating particles'. In: *Atmospheric Environment* 129 (Supplement C), pp. 91–94. ISSN: 1352-2310. DOI: 10.1016/j.atmosenv.2016.01.027.

Connolly, P. J., O. Möhler, P. R. Field, H. Saathoff, R. Burgess, T. Choularton and M. Gallagher (2009). 'Studies of heterogeneous freezing by three different desert dust samples'. In: *Atmospheric Chemistry and Physics* 9 (8), pp. 2805–2824. ISSN: 1680-7324. DOI: 10.5194/acp-9-2805-2009.

Consiglio, A. N., Y. Ouyang, M. J. Powell-Palm and B. Rubinsky (2023). 'An extreme value statistics model of heterogeneous ice nucleation for quantifying the stability of supercooled aqueous systems'. In: *The Journal of Chemical Physics* 159 (6). ISSN: 1089-7690. DOI: 10.1063/5.0155494.

Cooper, W. A. (1974). 'A possible mechanism for contact nucleation'. In: *Journal of the Atmospheric Sciences* 31 (7), pp. 1832–1837. DOI: 10.1175/1520-0469(1974)031<1832:APMFCN>2.0.CO;2.

Cotton, W. R., G. J. Tripoli, R. M. Rauber and E. A. Mulvihill (1986). 'Numerical Simulation of the Effects of Varying Ice Crystal Nucleation Rates and Aggregation Processes on Orographic Snowfall'. In: *Journal of Climate and Applied Meteorology* 25 (11), pp. 1658–1680. ISSN: 0733-3021. DOI: 10.1175/1520-0450(1986)025<1658:nsoteo>2.0.co;2.

Creamean, J. M., J. N. Cross, R. Pickart, L. McRaven, P. Lin, A. Pacini, R. Hanlon, D. G. Schmale, J. Ceniceros, T. Aydell, N. Colombi, E. Bolger and P. J. DeMott (2019). 'Ice Nucleating Particles Carried From Below a Phytoplankton Bloom to the Arctic Atmosphere'. In: *Geophysical Research Letters* 46 (14), pp. 8572–8581. ISSN: 1944-8007. DOI: 10.1029/2019gl083039.

Creamean, J., T. Hill, C. Hume and T. Devadoss (2024). *Ice Nucleation Spectrometer (INS) Instrument Handbook*. Tech. rep. DOE/SC-ARM-TR-278. Richland, Washington: U.S. Department of Energy, Atmospheric Radiation Measurement user facility.

Creamean, J. M., T. C. J. Hill, P. J. DeMott, J. Uetake, S. Kreidenweis and T. A. Douglas (2020). 'Thawing permafrost: an overlooked source of seeds for Arctic cloud formation'. In: *Environmental Research Letters* 15 (8), p. 084022. ISSN: 1748-9326. DOI: 10.1088/1748-9326/ab87d3.

Creamean, J. M., K. Barry, T. C. J. Hill, C. Hume, P. J. DeMott, M. D. Shupe, S. Dahlke, S. Willmes, J. Schmale, I. Beck, C. J. M. Hoppe, A. Fong, E. Chamberlain, J. Bowman, R. Scharien and O. Persson (2022). 'Annual cycle observations of aerosols capable of ice formation in central Arctic clouds'. In: *Nature Communications* 13 (1). DOI: 10.1038/s41467-022-31182-x.

Creamean, J. M., G. de Boer, H. Telg, F. Mei, D. Dexheimer, M. D. Shupe, A. Solomon and A. McComiskey (2021). 'Assessing the vertical structure of Arctic aerosols using balloon-

borne measurements'. In: *Atmospheric Chemistry and Physics* 21 (3), pp. 1737–1757. DOI: 10.5194/acp-21-1737-2021.

Creamean, J. M., R. M. Kirpes, K. A. Pratt, N. J. Spada, M. Maahn, G. de Boer, R. C. Schnell and S. China (2018a). 'Marine and terrestrial influences on ice nucleating particles during continuous springtime measurements in an Arctic oilfield location'. In: *Atmospheric Chemistry and Physics* 18 (24), pp. 18023–18042. ISSN: 1680-7324. DOI: 10.5194/acp-18-18023-2018.

Creamean, J. M., K. M. Primm, M. A. Tolbert, E. G. Hall, J. Wendell, A. Jordan, P. J. Sheridan, J. Smith and R. C. Schnell (2018b). 'HOVERCAT: a novel aerial system for evaluation of aerosol–cloud interactions'. In: *Atmospheric Measurement Techniques* 11 (7), pp. 3969–3985. ISSN: 1867-8548. DOI: 10.5194/amt-11-3969-2018.

Creamean, J. M., K. J. Suski, D. Rosenfeld, A. Cazorla, P. J. DeMott, R. C. Sullivan, A. B. White, F. M. Ralph, P. Minnis, J. M. Comstock, J. M. Tomlinson and K. A. Prather (2013). 'Dust and Biological Aerosols from the Sahara and Asia Influence Precipitation in the Western U.S'. In: *Science* 339 (6127), pp. 1572–1578. DOI: 10.1126/science.1227279.

Dagsson-Waldhauserova, P., O. Arnalds and H. Olafsson (2013). 'Long-term frequency and characteristics of dust storm events in Northeast Iceland (1949–2011)'. In: *Atmospheric Environment* 77, pp. 117–127. DOI: 10.1016/j.atmosenv.2013.04.075.

Dagsson-Waldhauserova, P., O. Arnalds and H. Olafsson (2017). 'Long-term dust aerosol production from natural sources in Iceland'. In: *Journal of the Air & Waste Management Association* 67 (2), pp. 173–181. DOI: 10.1080/10962247.2013.805703.

Dai, A. (2022). 'Arctic amplification is the main cause of the Atlantic meridional overturning circulation weakening under large CO2 increases'. In: *Climate Dynamics* 58 (11–12), pp. 3243–3259. ISSN: 1432-0894. DOI: 10.1007/s00382-021-06096-x.

Dai, A. and M. T. Jenkins (2023). 'Relationships among Arctic warming, sea-ice loss, stability, lapse rate feedback, and Arctic amplification'. In: *Climate Dynamics* 61 (11–12), pp. 5217–5232. ISSN: 1432-0894. DOI: 10.1007/s00382-023-06848-x.

Dai, A., D. Luo, M. Song and J. Liu (2019). 'Arctic amplification is caused by sea-ice loss under increasing CO2'. In: *Nature Communications* 10 (1). ISSN: 2041-1723. DOI: 10.1038/s41467-018-07954-9.

Daily, M. I., M. D. Tarn, T. F. Whale and B. J. Murray (2022). 'An evaluation of the heat test for the ice-nucleating ability of minerals and biological material'. In: *Atmospheric Measurement Techniques* 15 (8), pp. 2635–2665. ISSN: 1867-8548. DOI: 10.5194/amt-15-2635-2022.

DallaValle, J. M., C. Orr and B. L. Hinkle (1954). 'The aggregation of aerosols'. In: *British Journal of Applied Physics* 5 (S3), S198–S206. ISSN: 0508-3443. DOI: 10.1088/0508-3443/5/s3/365.

David, R. O., C. Marcolli, J. Fahrni, Y. Qiu, Y. A. Perez Sirkin, V. Molinero, F. Mahrt, D. Brühwiler, U. Lohmann and Z. A. Kanji (2019). 'Pore condensation and freezing is responsible for ice formation below water saturation for porous particles'. In: *Proceedings of the National Academy of Sciences* 116 (17), pp. 8184–8189. DOI: 10.1073/pnas.1813647116.

Dee, D. P., S. M. Uppala, A. J. Simmons, P. Berrisford, P. Poli, S. Kobayashi, U. Andrae, M. A. Balmaseda, G. Balsamo, P. Bauer, P. Bechtold, A. C. M. Beljaars, L. van de Berg, J. Bidlot, N. Bormann, C. Delsol, R. Dragani, M. Fuentes, A. J. Geer, L. Haimberger, S. B. Healy, H. Hersbach, E. V. Hólm, L. Isaksen, P. Kållberg, M. Köhler, M. Matricardi, A. P. McNally, B. M. Monge-Sanz, J.-J. Morcrette, B.-K. Park, C. Peubey, P. de Rosnay, C. Tavolato, J.-N. Thépaut and F. Vitart (2011). 'The ERA-Interim reanalysis: configuration and performance

of the data assimilation system'. In: *Quarterly Journal of the Royal Meteorological Society* 137 (656), pp. 553–597. DOI: 10.1002/qj.828.

Dekhtyareva, A., K. Holmén, M. Maturilli, O. Hermansen and R. Graversen (2018). 'Effect of seasonal mesoscale and microscale meteorological conditions in Ny-Ålesund on results of monitoring of long-range transported pollution'. In: *Polar Research* 37 (1), p. 1508196. ISSN: 1751-8369. DOI: 10.1080/17518369.2018.1508196.

DeMott, P. J. (1995). 'Quantitative descriptions of ice formation mechanisms of silver iodide-type aerosols'. In: *Atmospheric Research* 38 (1), pp. 63–99. ISSN: 0169-8095. DOI: 10.1016/0169-8095(94)00088-U.

DeMott, P. J., T. C. J. Hill, M. D. Petters, A. K. Bertram, Y. Tobo, R. H. Mason, K. J. Suski, C. S. McCluskey, E. J. T. Levin, G. P. Schill, Y. Boose, A. M. Rauker, A. J. Miller, J. Zaragoza, K. Rocci, N. E. Rothfuss, H. P. Taylor, J. D. Hader, C. Chou, J. A. Huffman, U. Pöschl, A. J. Prenni and S. M. Kreidenweis (2017). 'Comparative measurements of ambient atmospheric concentrations of ice nucleating particles using multiple immersion freezing methods and a continuous flow diffusion chamber'. In: *Atmospheric Chemistry and Physics* 17 (18), pp. 11227–11245. ISSN: 1680-7324. DOI: 10.5194/acp-17-11227-2017.

DeMott, P. J., O. Möhler, D. J. Cziczo, N. Hiranuma, M. D. Petters, S. S. Petters, F. Belosi, H. G. Bingemer, S. D. Brooks, C. Budke, M. Burkert-Kohn, K. N. Collier, A. Danielczok, O. Eppers, L. Felgitsch, S. Garimella, H. Grothe, P. Herenz, T. C. J. Hill, K. Höhler, Z. A. Kanji, A. Kiselev, T. Koop, T. B. Kristensen, K. Krüger, G. Kulkarni, E. J. T. Levin, B. J. Murray, A. Nicosia, D. O'Sullivan, A. Peckhaus, M. J. Polen, H. C. Price, N. Reicher, D. A. Rothenberg, Y. Rudich, G. Santachiara, T. Schiebel, J. Schrod, T. M. Seifried, F. Stratmann, R. C. Sullivan, K. J. Suski, M. Szakáll, H. P. Taylor, R. Ullrich, J. Vergara-Temprado, R. Wagner, T. F. Whale, D. Weber, A. Welti, T. W. Wilson, M. J. Wolf and J. Zenker (2018). 'The Fifth International Workshop on Ice Nucleation phase 2 (FIN-02): laboratory intercomparison of ice nucleation measurements'. In: *Atmos. Meas. Tech.* 11 (11), pp. 6231–6257. ISSN: 1867-8548. DOI: 10.5194/amt-11-6231-2018.

DeMott, P. J., A. J. Prenni, G. R. McMeeking, R. C. Sullivan, M. D. Petters, Y. Tobo, M. Niemand, O. Möhler, J. R. Snider, Z. Wang and S. M. Kreidenweis (2015). 'Integrating laboratory and field data to quantify the immersion freezing ice nucleation activity of mineral dust particles'. In: *Atmospheric Chemistry and Physics* 15 (1), pp. 393–409. ISSN: 1680-7324. DOI: 10.5194/acp-15-393-2015.

DeMott, P. J., T. C. J. Hill, C. S. McCluskey, K. A. Prather, D. B. Collins, R. C. Sullivan, M. J. Ruppel, R. H. Mason, V. E. Irish, T. Lee, C. Y. Hwang, T. S. Rhee, J. R. Snider, G. R. McMeeking, S. Dhaniyala, E. R. Lewis, J. J. B. Wentzell, J. Abbatt, C. Lee, C. M. Sultana, A. P. Ault, J. L. Axson, M. D. Martinez, I. Venero, G. Santos-Figueroa, M. D. Stokes, G. B. Deane, O. L. Mayol-Bracero, V. H. Grassian, T. H. Bertram, A. K. Bertram, B. F. Moffett and G. D. Franc (2016). 'Sea spray aerosol as a unique source of ice nucleating particles'. In: *Proceedings of the National Academy of Sciences* 113 (21), pp. 5797–5803. DOI: 10.1073/pnas.1514034112.

DeMott, P. J., J. A. Mirrielees, S. S. Petters, D. J. Cziczo, M. D. Petters, H. G. Bingemer, T. C. J. Hill, K. Froyd, S. Garimella, A. G. Hallar, E. J. T. Levin, I. B. McCubbin, A. E. Perring, C. N. Rapp, T. Schiebel, J. Schrod, K. J. Suski, D. Weber, M. J. Wolf, M. Zawadowicz, J. Zenker, O. Möhler and S. D. Brooks (2025). 'Field intercomparison of ice nucleation measurements: the Fifth International Workshop on Ice Nucleation Phase 3 (FIN-03)'. In: *Atmospheric*

Measurement Techniques 18 (3), pp. 639–672. ISSN: 1867-8548. DOI: 10.5194/amt-18-639-2025.

DeMott, P. J., A. J. Prenni, X. Liu, S. M. Kreidenweis, M. D. Petters, C. H. Twohy, M. S. Richardson, T. Eidhammer and D. C. Rogers (2010). 'Predicting global atmospheric ice nuclei distributions and their impacts on climate'. In: *Proceedings of the National Academy of Sciences* 107 (25), pp. 11217–11222. DOI: 10.1073/pnas.0910818107.

Denbigh, K. G. (1981). *The principles of chemical equilibrium. With applications in chemistry and chemical engineering*. 3. ed. Literaturangaben. Cambridge: Univ. Press. 494 pp. ISBN: 0521096553.

Diehl, K. and S. Mitra (1998). 'A laboratory study of the effects of a kerosene-burner exhaust on ice nucleation and the evaporation rate of ice crystals'. In: *Atmospheric Environment* 32 (18), pp. 3145–3151. ISSN: 1352-2310. DOI: 10.1016/s1352-2310(97)00467-6.

Dietel, B., O. Sourdeval and C. Hoose (2024). 'Characterisation of low-base and mid-base clouds and their thermodynamic phase over the Southern Ocean and Arctic marine regions'. In: *Atmospheric Chemistry and Physics* 24 (12), pp. 7359–7383. ISSN: 1680-7324. DOI: 10.5194/acp-24-7359-2024.

Doulgeris, K.-M., M. Komppula, S. Romakkaniemi, A.-P. Hyvärinen, V.-M. Kerminen and D. Brus (2020). 'In-situ cloud ground based measurements in Finnish sub-Arctic: Intercomparison of three cloud spectrometers'. In: *Atmospheric Measurement Techniques*. DOI: 10.5194/amt-2020-3.

Doulgeris, K.-M., H. Lihavainen, A.-P. Hyvärinen, V.-M. Kerminen and D. Brus (2022). 'An extensive data set for in situ microphysical characterization of low-level clouds in a Finnish sub-Arctic site'. In: *Earth System Science Data* 14 (2), pp. 637–649. ISSN: 1866-3516. DOI: 10.5194/essd-14-637-2022.

Doulgeris, K.-M., V. Vakkari, E. J. O'Connor, V.-M. Kerminen, H. Lihavainen and D. Brus (2023). 'Influence of air mass origin on microphysical properties of low-level clouds in a subarctic environment'. In: *Atmospheric Chemistry and Physics* 23 (4), pp. 2483–2498. ISSN: 1680-7324. DOI: 10.5194/acp-23-2483-2023.

Draxler, R. R. and G. Hess (1998). 'An overview of the HYSPLIT_4 modelling system for trajectories'. In: *Australian meteorological magazine* 47 (4), pp. 295–308.

Dusek, U., G. P. Reischl and R. Hitzenberger (2006). 'CCN Activation of Pure and Coated Carbon Black Particles'. In: *Environmental Science & Technology* 40 (4), pp. 1223–1230. DOI: 10.1021/es0503478.

Eckhardt, S., O. Hermansen, H. Grythe, M. Fiebig, K. Stebel, M. Cassiani, A. Baecklund and A. Stohl (2013). 'The influence of cruise ship emissions on air pollution in Svalbard – a harbinger of a more polluted Arctic?' In: *Atmospheric Chemistry and Physics* 13 (16), pp. 8401–8409. ISSN: 1680-7324. DOI: 10.5194/acp-13-8401-2013.

Eidhammer, T., P. J. DeMott and S. M. Kreidenweis (2009). 'A comparison of heterogeneous ice nucleation parameterizations using a parcel model framework'. In: *Journal of Geophysical Research: Atmospheres* 114 (D6). ISSN: 2156-2202. DOI: 10.1029/2008JD011095.

Eleftheriadis, K., S. Vratolis and S. Nyeki (2009). 'Aerosol black carbon in the European Arctic: Measurements at Zeppelin station, Ny-Ålesund, Svalbard from 1998–2007'. In: *Geophysical Research Letters* 36 (2), p. L02809. ISSN: 1944-8007. DOI: 10.1029/2008GL035741.

Emmert, J. T., D. P. Drob, J. M. Picone, D. E. Siskind, M. Jones, M. G. Mlynczak, P. F. Bernath, X. Chu, E. Doornbos, B. Funke, L. P. Goncharenko, M. E. Hervig, M. J. Schwartz, P. E. Sheese, F. Vargas, B. P. Williams and T. Yuan (2021). 'NRLMSIS 2.0: A Whole-Atmosphere Empirical Model of Temperature and Neutral Species Densities'. In: *Earth and Space Science* 8 (3). ISSN: 2333-5084. DOI: 10.1029/2020ea001321.

Engelmann, R., A. Ansmann, K. Ohneiser, H. Griesche, M. Radenz, J. Hofer, D. Althausen, S. Dahlke, M. Maturilli, I. Veselovskii, C. Jimenez, R. Wiesen, H. Baars, J. Bühl, H. Gebauer, M. Haarig, P. Seifert, U. Wandinger and A. Macke (2021). 'Wildfire smoke, Arctic haze, and aerosol effects on mixed-phase and cirrus clouds over the North Pole region during MOSAiC: an introduction'. In: *Atmospheric Chemistry and Physics* 21 (17), pp. 13397–13423. ISSN: 1680-7324. DOI: 10.5194/acp-21-13397-2021.

Engvall, A.-C., R. Krejci, J. Ström, R. Treffeisen, R. Scheele, O. Hermansen and J. Paatero (2008). 'Changes in aerosol properties during spring-summer period in the Arctic troposphere'. In: *Atmospheric Chemistry and Physics* 8 (3), pp. 445–462. DOI: 10.5194/acp-8-445-2008.

Ervens, B. and G. Feingold (2013). 'Sensitivities of immersion freezing: Reconciling classical nucleation theory and deterministic expressions'. In: *Geophysical Research Letters* 40 (12), pp. 3320–3324. ISSN: 1944-8007. DOI: 10.1002/grl.50580.

Evans, L. F. (1965). 'Requirements of an Ice Nucleus'. In: *Nature* 206 (4986), pp. 822–822. DOI: 10.1038/206822a0.

Fahrbach, E., J. Meincke, S. Østerhus, G. Rohardt, U. Schauer, V. Tverberg and J. Verduin (2001). 'Direct measurements of volume transports through Fram Strait'. In: *Polar Research* 20 (2), pp. 217–224. ISSN: 1751-8369. DOI: 10.1111/j.1751-8369.2001.tb00059.x.

Fairall, C. W., M. L. Banner, W. L. Peirson, W. Asher and R. P. Morison (2009). 'Investigation of the physical scaling of sea spray spume droplet production'. In: *Journal of Geophysical Research: Oceans* 114 (C10). ISSN: 0148-0227. DOI: 10.1029/2008jc004918.

Field, P. R. and A. J. Heymsfield (2015). 'Importance of snow to global precipitation'. In: *Geophysical Research Letters* 42 (21), pp. 9512–9520. ISSN: 0094-8276. DOI: 10.1002/2015gl065497.

Field, P. R., R. P. Lawson, P. R. A. Brown, G. Lloyd, C. Westbrook, D. Moisseev, A. Miltenberger, A. Nenes, A. Blyth, T. Choularton, P. Connolly, J. Buehl, J. Crosier, Z. Cui, C. Dearden, P. DeMott, A. Flossmann, A. Heymsfield, Y. Huang, H. Kalesse, Z. A. Kanji, A. Korolev, A. Kirchgaessner, S. Lasher-Trapp, T. Leisner, G. McFarquhar, V. Phillips, J. Stith and S. Sullivan (2017). 'Secondary Ice Production: Current State of the Science and Recommendations for the Future'. In: *Meteorological Monographs* 58, pp. 71–720. DOI: 10.1175/amsmonographs-d-16-0014.1.

Filioglou, M., A. Nikandrova, S. Niemelä, H. Baars, T. Mielonen, A. Leskinen, D. Brus, S. Romakkaniemi, E. Giannakaki and M. Komppula (2017). 'Profiling water vapor mixing ratios in Finland by means of a Raman lidar, a satellite and a model'. In: *Atmospheric Measurement Techniques* 10 (11), pp. 4303–4316. ISSN: 1867-8548. DOI: 10.5194/amt-10-4303-2017.

Fischer, T. P., S. Arellano, S. Carn, A. Aiuppa, B. Galle, P. Allard, T. Lopez, H. Shinohara, P. Kelly, C. Werner, C. Cardellini and G. Chiodini (2019). 'The emissions of CO2 and other volatiles from the world's subaerial volcanoes'. In: *Scientific Reports* 9 (1). ISSN: 2045-2322. DOI: 10.1038/s41598-019-54682-1.

Fletcher, N. H. (1958). 'Size effect in heterogeneous nucleation'. In: *The Journal of chemical physics* 29 (3), pp. 572–576. DOI: 10.1063/1.1744540.

Fletcher, N. H. (1962). *The physics of rainclouds*. University Press.

Fornea, A. P., S. D. Brooks, J. B. Dooley and A. Saha (2009). 'Heterogeneous freezing of ice on atmospheric aerosols containing ash, soot, and soil'. In: *Journal of Geophysical Research* 114 (D13). ISSN: 2156-2202. DOI: 10.1029/2009jd011958.

Fountain, A. G. and T. Ohtake (1985). 'Concentrations and Source Areas of Ice Nuclei in the Alaskan Atmosphere'. In: *Journal of Applied Meteorology and Climatology* 24 (4), pp. 377–382. DOI: 10.1175/1520-0450(1985)024<0377:Casaoi>2.0.Co;2.

Friddle, R. W. and K. Thürmer (2019). 'How nanoscale surface steps promote ice growth on feldspar: microscopy observation of morphology-enhanced condensation and freezing'. In: *Nanoscale* 11 (44), pp. 21147–21154. ISSN: 2040-3372. DOI: 10.1039/c9nr08729j.

Friedman, B., G. Kulkarni, J. Beránek, A. Zelenyuk, J. A. Thornton and D. J. Cziczo (2011). 'Ice nucleation and droplet formation by bare and coated soot particles'. In: *Journal of Geophysical Research: Atmospheres* 116 (D17). ISSN: 2156-2202. DOI: 10.1029/2011JD015999.

Fuchs, N. A. (1963). 'On the stationary charge distribution on aerosol particles in a bipolar ionic atmosphere'. In: *Geofisica pura e applicata* 56 (1), pp. 185–193. ISSN: 0367-4355. DOI: 10.1007/bf01993343.

Fukuta, N. (1966). 'Experimental Studies of Organic Ice Nuclei'. In: *Journal of the Atmospheric Sciences* 23 (2), pp. 191–196. ISSN: 1520-0469. DOI: 10.1175/1520-0469(1966)023<0191:esooin>2.0.co;2.

Gabric, A., P. Matrai, G. Jones and J. Middleton (2018). 'The Nexus between Sea Ice and Polar Emissions of Marine Biogenic Aerosols'. In: *Bulletin of the American Meteorological Society* 99 (1), pp. 61–81. ISSN: 1520-0477. DOI: 10.1175/bams-d-16-0254.1.

Gallet, J.-C., M. Björkman, C. Borstad, A. Hodson, H.-W. Jacobi, C. Larose, B. Luks, A. Spolaor, T. Schuler, A. Urazgildeeva and C. Zdanowicz (2019). *Snow research in Svalbard: current status and knowledge gaps*. Tech. rep. State of Environment Science in Svalbard (SESS). DOI: 10.5281/ZENODO.4778366.

Garrett, T. J., S. Brattström, S. Sharma, D. E. J. Worthy and P. Novelli (2011). 'The role of scavenging in the seasonal transport of black carbon and sulfate to the Arctic'. In: *Geophysical Research Letters* 38 (16). DOI: 10.1029/2011GL048221.

Gaston, C. J. (2020). 'Re-examining Dust Chemical Aging and Its Impacts on Earth's Climate'. In: *Accounts of Chemical Research* 53 (5), pp. 1005–1013. ISSN: 1520-4898. DOI: 10.1021/acs.accounts.0c00102.

Gérard, V., B. Noziere, L. Fine, C. Ferronato, D. K. Singh, A. A. Frossard, R. C. Cohen, E. Asmi, H. Lihavainen, N. Kivekäs, M. Aurela, D. Brus, S. Frka and A. Cvitešić Kušan (2019). 'Concentrations and Adsorption Isotherms for Amphiphilic Surfactants in PM1 Aerosols from Different Regions of Europe'. In: *Environmental Science & Technology* 53 (21), pp. 12379–12388. ISSN: 1520-5851. DOI: 10.1021/acs.est.9b03386.

Gerber, F., V. Sharma and M. Lehning (2023). 'CRYOWRF—Model Evaluation and the Effect of Blowing Snow on the Antarctic Surface Mass Balance'. In: *Journal of Geophysical Research: Atmospheres* 128 (12). ISSN: 2169-8996. DOI: 10.1029/2022jd037744.

Gerland, S., O. Pavlova, D. Divine, J. Negrel, S. Dahlke, A. M. Johansson, M. Maturilli and M. Semmling (2020). *Long-term monitoring of landfast sea ice extent and thickness in Kongsfjorden,*

and related applications (FastIce). Ed. by F. V. den Heuvel, C. Hübner, M. Błaszczyk, M. Heimann and H. Lihavainen. Longyearbyen.

Ginoux, P., M. Chin, I. Tegen, J. M. Prospero, B. Holben, O. Dubovik and S.-J. Lin (2001). 'Sources and distributions of dust aerosols simulated with the GOCART model'. In: *Journal of Geophysical Research: Atmospheres* 106 (D17), pp. 20255–20273. ISSN: 0148-0227. DOI: 10.1029/2000jd000053.

Ginoux, P., J. M. Prospero, T. E. Gill, N. C. Hsu and M. Zhao (2012). 'Global-scale attribution of anthropogenic and natural dust sources and their emission rates based on MODIS Deep Blue aerosol products'. In: *Reviews of Geophysics* 50 (3). ISSN: 1944-9208. DOI: 10.1029/2012rg000388.

Girdwood, J., H. Smith, W. Stanley, Z. Ulanowski, C. Stopford, C. Chemel, K.-M. Doulgeris, D. Brus, D. Campbell and R. Mackenzie (2020). 'Design and field campaign validation of a multi-rotor unmanned aerial vehicle and optical particle counter'. In: *Atmospheric Measurement Techniques* 13 (12), pp. 6613–6630. DOI: 10.5194/amt-13-6613-2020.

Girdwood, J., W. Stanley, C. Stopford and D. Brus (2022). 'Simulation and field campaign evaluation of an optical particle counter on a fixed-wing UAV'. In: *Atmospheric Measurement Techniques* 15 (7), pp. 2061–2076. ISSN: 1867-8548. DOI: 10.5194/amt-15-2061-2022.

Goel, V., S. K. Mishra, P. Pal, A. Ahlawat, N. Vijayan, S. Jain and C. Sharma (2020). 'Influence of chemical aging on physico-chemical properties of mineral dust particles: A case study of 2016 dust storms over Delhi'. In: *Environmental Pollution* 267, p. 115338. ISSN: 0269-7491. DOI: 10.1016/j.envpol.2020.115338.

Gong, S. L., L. A. Barrie and J.-P. Blanchet (1997). 'Modeling sea-salt aerosols in the atmosphere: 1. Model development'. In: *Journal of Geophysical Research: Atmospheres* 102 (D3), pp. 3805–3818. ISSN: 0148-0227. DOI: 10.1029/96jd02953.

Gong, X., J. Zhang, B. Croft, X. Yang, M. M. Frey, N. Bergner, R. Y.-W. Chang, J. M. Creamean, C. Kuang, R. V. Martin, A. Ranjithkumar, A. J. Sedlacek, J. Uin, S. Willmes, M. A. Zawadowicz, J. R. Pierce, M. D. Shupe, J. Schmale and J. Wang (2023). 'Arctic warming by abundant fine sea salt aerosols from blowing snow'. In: *Nature Geoscience* 16 (9), pp. 768–774. ISSN: 1752-0908. DOI: 10.1038/s41561-023-01254-8.

Graham, R. M., S. R. Hudson and M. Maturilli (2019). 'Improved Performance of ERA5 in Arctic Gateway Relative to Four Global Atmospheric Reanalyses'. In: *Geophysical Research Letters* 46 (11), pp. 6138–6147. ISSN: 1944-8007. DOI: 10.1029/2019gl082781.

Graversen, R. G. and M. Burtu (2016). 'Arctic amplification enhanced by latent energy transport of atmospheric planetary waves'. In: *Quarterly Journal of the Royal Meteorological Society* 142 (698), pp. 2046–2054. ISSN: 1477-870X. DOI: 10.1002/qj.2802.

Groot Zwaaftink, C. D., H. Grythe, H. Skov and A. Stohl (2016). 'Substantial contribution of northern high-latitude sources to mineral dust in the Arctic'. In: *Journal of Geophysical Research: Atmospheres* 121 (22), pp. 13, 678–13, 697. DOI: 10.1002/2016JD025482.

Groot Zwaaftink, C., H. Grythe, O. Arnalds, P. Dagsson-Waldhauserova, H. Skov, T. Jóhannsson, S. Eckhardt and A. Stohl (2017). 'Contributions of Icelandic and other high-latitude sources to mineral dust in the Arctic'. In: *EGU General Assembly Conference Abstracts*. EGU General Assembly Conference Abstracts, p. 13502.

Grythe, H., J. Ström, R. Krejci, P. Quinn and A. Stohl (2014). 'A review of sea-spray aerosol source functions using a large global set of sea salt aerosol concentration measurements'. In:

Atmospheric Chemistry and Physics 14 (3), pp. 1277–1297. ISSN: 1680-7324. DOI: 10.5194/acp-14-1277-2014.

Hallett, J. and S. C. Mossop (1974). 'Production of secondary ice particles during the riming process'. In: *Nature* 249 (5452), pp. 26–28. DOI: 10.1038/249026a0.

Hansen, J., M. Sato, P. Kharecha and K. von Schuckmann (2011). 'Earth's energy imbalance and implications'. In: *Atmospheric Chemistry and Physics* 11 (24), pp. 13421–13449. ISSN: 1680-7324. DOI: 10.5194/acp-11-13421-2011.

Hara, K., T. Maki, M. Kakikawa, F. Kobayashi and A. Matsuki (2016). 'Effects of different temperature treatments on biological ice nuclei in snow samples'. In: *Atmospheric Environment* 140, pp. 415–419. ISSN: 1352-2310. DOI: 10.1016/j.atmosenv.2016.06.011.

Hartmann, M., K. Adachi, O. Eppers, C. Haas, A. Herber, R. Holzinger, A. Hünerbein, E. Jäkel, C. Jentzsch, M. Pinxteren, H. Wex, S. Willmes and F. Stratmann (2020). 'Wintertime Airborne Measurements of Ice Nucleating Particles in the High Arctic: A Hint to a Marine, Biogenic Source for Ice Nucleating Particles'. In: *Geophysical Research Letters* 47 (13). DOI: 10.1029/2020gl087770.

Hartmann, M., X. Gong, S. Kecorius, M. van Pinxteren, T. Vogl, A. Welti, H. Wex, S. Zeppenfeld, H. Herrmann, A. Wiedensohler and F. Stratmann (2021). 'Terrestrial or marine – indications towards the origin of ice-nucleating particles during melt season in the European Arctic up to 83.7° N'. In: *Atmospheric Chemistry and Physics* 21 (15), pp. 11613–11636. DOI: 10.5194/acp-21-11613-2021.

Hatakka, J., T. Aalto, V. Aaltonen, M. Aurela, H. Hakola, M. Komppula, T. Laurila, H. Lihavainen, J. Paatero, K. Salminen and Y. Viisanen (2003). 'Overview of the atmospheric research activities and results at Pallas GAW station'. In: *Boreal Environment Research* 8.

Hauglustaine, D. A., Y. Balkanski and M. Schulz (2014). 'A global model simulation of present and future nitrate aerosols and their direct radiative forcing of climate'. In: *Atmospheric Chemistry and Physics* 14 (20), pp. 11031–11063. ISSN: 1680-7324. DOI: 10.5194/acp-14-11031-2014.

He, M. and S. Dhaniyala (2013). 'A multiple charging correction algorithm for scanning electrical mobility spectrometer data'. In: *Journal of Aerosol Science* 61, pp. 13–26. ISSN: 0021-8502. DOI: 10.1016/j.jaerosci.2013.03.007.

Heintzenberg, J., C. Leck and P. Tunved (2015). 'Potential source regions and processes of aerosol in the summer Arctic'. In: *Atmospheric Chemistry and Physics* 15 (11), pp. 6487–6502. ISSN: 1680-7324. DOI: 10.5194/acp-15-6487-2015.

Hersbach, H., B. Bell, P. Berrisford, S. Hirahara, A. Horányi, J. Muñoz-Sabater, J. Nicolas, C. Peubey, R. Radu, D. Schepers, A. Simmons, C. Soci, S. Abdalla, X. Abellan, G. Balsamo, P. Bechtold, G. Biavati, J. Bidlot, M. Bonavita, G. De Chiara, P. Dahlgren, D. Dee, M. Diamantakis, R. Dragani, J. Flemming, R. Forbes, M. Fuentes, A. Geer, L. Haimberger, S. Healy, R. J. Hogan, E. Hólm, M. Janisková, S. Keeley, P. Laloyaux, P. Lopez, C. Lupu, G. Radnoti, P. de Rosnay, I. Rozum, F. Vamborg, S. Villaume and J.-N. Thépaut (2020). 'The ERA5 global reanalysis'. In: *Quarterly Journal of the Royal Meteorological Society* 146 (730), pp. 1999–2049. ISSN: 1477-870X. DOI: 10.1002/qj.3803.

Hersbach, H., P. de Rosnay, B. Bell, D. Schepers, A. Simmons, C. Soci, S. Abdalla, M. Alonso-Balmaseda, G. Balsamo, P. Bechtold, P. Berrisford, J.-R. Bidlot, E. de Boisséson, M. Bonavita, P. Browne, R. Buizza, P. Dahlgren, D. Dee, R. Dragani, M. Diamantakis, J. Flemming, R. Forbes, A. Geer, T. Haiden, E. Hólm, L. Haimberger, R. Hogan, A. Horányi, M. Janiskova,

P. Laloyaux, P. Lopez, J. Munoz-Sabater, C. Peubey, R. Radu, D. Richardson, J.-N. Thépaut, F. Vitart, X. Yang, E. Zsótér and H. Zuo (2018). 'Operational global reanalysis: progress, future directions and synergies with NWP'. In: *ERA Report Series* (27). DOI: 10.21957/tkic6g3wm.

Hertel, O., J. Christensen, E. H. Runge, W. A. Asman, R. Berkowicz, M. F. Hovmand and Ø. Hov (1995). 'Development and testing of a new variable scale air pollution model—ACDEP'. In: *Atmospheric Environment* 29 (11), pp. 1267–1290. ISSN: 1352-2310. DOI: 10.1016/1352-2310(95)00067-9.

Heymsfield, A. J., C. Schmitt, C.-C.-J. Chen, A. Bansemer, A. Gettelman, P. R. Field and C. Liu (2020). 'Contributions of the Liquid and Ice Phases to Global Surface Precipitation: Observations and Global Climate Modeling'. In: *Journal of the Atmospheric Sciences* 77 (8), pp. 2629–2648. DOI: 10.1175/jas-d-19-0352.1.

Hill, T. C. J., P. J. DeMott, Y. Tobo, J. Fröhlich-Nowoisky, B. F. Moffett, G. D. Franc and S. M. Kreidenweis (2016). 'Sources of organic ice nucleating particles in soils'. In: *Atmospheric Chemistry and Physics* 16 (11), pp. 7195–7211. DOI: 10.5194/acp-16-7195-2016.

Hings, S. S., W. C. Wrobel, E. S. Cross, D. R. Worsnop, P. Davidovits and T. B. Onasch (2008). 'CCN activation experiments with adipic acid: effect of particle phase and adipic acid coatings on soluble and insoluble particles'. In: *Atmospheric Chemistry and Physics* 8 (14), pp. 3735–3748. ISSN: 1680-7324. DOI: 10.5194/acp-8-3735-2008.

Hiranuma, N., S. Augustin-Bauditz, H. Bingemer, C. Budke, J. Curtius, A. Danielczok, K. Diehl, K. Dreischmeier, M. Ebert, F. Frank, N. Hoffmann, K. Kandler, A. Kiselev, T. Koop, T. Leisner, O. Möhler, B. Nillius, A. Peckhaus, D. Rose, S. Weinbruch, H. Wex, Y. Boose, P. J. DeMott, J. D. Hader, T. C. J. Hill, Z. A. Kanji, G. Kulkarni, E. J. T. Levin, C. S. McCluskey, M. Murakami, B. J. Murray, D. Niedermeier, M. D. Petters, D. O'Sullivan, A. Saito, G. P. Schill, T. Tajiri, M. A. Tolbert, A. Welti, T. F. Whale, T. P. Wright and K. Yamashita (2015). 'A comprehensive laboratory study on the immersion freezing behavior of illite NX particles: a comparison of 17 ice nucleation measurement techniques'. In: *Atmospheric Chemistry and Physics* 15 (5), pp. 2489–2518. ISSN: 1680-7324. DOI: 10.5194/acp-15-2489-2015.

Hiranuma, N., K. Adachi, D. M. Bell, F. Belosi, H. Beydoun, B. Bhaduri, H. Bingemer, C. Budke, H.-C. Clemen, F. Conen, K. M. Cory, J. Curtius, P. J. DeMott, O. Eppers, S. Grawe, S. Hartmann, N. Hoffmann, K. Höhler, E. Jantsch, A. Kiselev, T. Koop, G. Kulkarni, A. Mayer, M. Murakami, B. J. Murray, A. Nicosia, M. D. Petters, M. Piazza, M. Polen, N. Reicher, Y. Rudich, A. Saito, G. Santachiara, T. Schiebel, G. P. Schill, J. Schneider, L. Segev, E. Stopelli, R. C. Sullivan, K. Suski, M. Szakáll, T. Tajiri, H. Taylor, Y. Tobo, R. Ullrich, D. Weber, H. Wex, T. F. Whale, C. L. Whiteside, K. Yamashita, A. Zelenyuk and O. Möhler (2019). 'A comprehensive characterization of ice nucleation by three different types of cellulose particles immersed in water'. In: *Atmospheric Chemistry and Physics* 19 (7), pp. 4823–4849. DOI: 10.5194/acp-19-4823-2019.

Hodal, H., S. Falk-Petersen, H. Hop, S. Kristiansen and M. Reigstad (2011). 'Spring bloom dynamics in Kongsfjorden, Svalbard: nutrients, phytoplankton, protozoans and primary production'. In: *Polar Biology* 35 (2), pp. 191–203. ISSN: 1432-2056. DOI: 10.1007/s00300-011-1053-7.

Hoffmann, N., A. Kiselev, D. Rzesanke, D. Duft and T. Leisner (2013). 'Experimental quantification of contact freezing in an electrodynamic balance'. In: *Atmospheric Measurement Techniques* 6 (9), pp. 2373–2382. DOI: 10.5194/amt-6-2373-2013.

Holden, M. A., J. M. Campbell, F. C. Meldrum, B. J. Murray and H. K. Christenson (2021). 'Active sites for ice nucleation differ depending on nucleation mode'. In: *Proceedings of the National Academy of Sciences* 118 (18). DOI: 10.1073/pnas.2022859118.

Holden, M. A., T. F. Whale, M. D. Tarn, D. O'Sullivan, R. D. Walshaw, B. J. Murray, F. C. Meldrum and H. K. Christenson (2019). 'High-speed imaging of ice nucleation in water proves the existence of active sites'. In: *Science Advances* 5 (2), eaav4316. DOI: 10.1126/sciadv.aav4316.

Hoose, C. and O. Möhler (2012). 'Heterogeneous ice nucleation on atmospheric aerosols: a review of results from laboratory experiments'. In: *Atmospheric Chemistry and Physics* 12 (20), pp. 9817–9854. DOI: 10.5194/acp-12-9817-2012.

Hoose, C., J. E. Kristjánsson, J.-P. Chen and A. Hazra (2010). 'A Classical-Theory-Based Parameterization of Heterogeneous Ice Nucleation by Mineral Dust, Soot, and Biological Particles in a Global Climate Model'. In: *Journal of the Atmospheric Sciences* 67 (8), pp. 2483–2503. DOI: 10.1175/2010jas3425.1.

Hoppel, W. A., G. M. Frick and J. W. Fitzgerald (2002). 'Surface source function for sea-salt aerosol and aerosol dry deposition to the ocean surface'. In: *Journal of Geophysical Research: Atmospheres* 107 (D19). ISSN: 0148-0227. DOI: 10.1029/2001jd002014.

Hoyle, C. R., V. Pinti, A. Welti, B. Zobrist, C. Marcolli, B. Luo, Á. Höskuldsson, H. B. Mattsson, O. Stetzer, T. Thorsteinsson, G. Larsen and T. Peter (2011). 'Ice nucleation properties of volcanic ash from Eyjafjallajökull'. In: *Atmospheric Chemistry and Physics* 11 (18), pp. 9911–9926. ISSN: 1680-7324. DOI: 10.5194/acp-11-9911-2011.

Hudson, J. G. (1992). 'Cloud Condensation Nuclei'. In: *Journal of Applied Meteorology* 32, pp. 596–607. DOI: 10.1175/1520-0450(1993)032<0596:CCN>2.0.CO;2.

Humlum, O. (2005). 'Holocene permafrost aggradation in Svalbard'. In: *Geological Society, London, Special Publications* 242 (1), pp. 119–129. ISSN: 2041-4927. DOI: 10.1144/gsl.sp.2005.242.01.11.

Hussain, S. and A. Haji-Akbari (2021). 'Role of Nanoscale Interfacial Proximity in Contact Freezing in Water'. In: *Journal of the American Chemical Society* 143 (5), pp. 2272–2284. ISSN: 1520-5126. DOI: 10.1021/jacs.0c10663.

Iannone, R., D. I. Chernoff, A. Pringle, S. T. Martin and A. K. Bertram (2011). 'The ice nucleation ability of one of the most abundant types of fungal spores found in the atmosphere'. In: *Atmospheric Chemistry and Physics* 11 (3), pp. 1191–1201. ISSN: 1680-7324. DOI: 10.5194/acp-11-1191-2011.

Intrieri, J. M., C. W. Fairall, M. D. Shupe, P. O. G. Persson, E. L. Andreas, P. S. Guest and R. E. Moritz (2002). 'An annual cycle of Arctic surface cloud forcing at SHEBA'. In: *Journal of Geophysical Research: Oceans* 107 (C10), SHE 13–1–SHE 13–14. DOI: 10.1029/2000JC000439.

IPCC (2021). *Climate Change 2021: The Physical Science Basis. Contribution of Working Group 1 to the Sixth Assessment Report of the Intergovernmental Panel on Climate Change*. Ed. by V. Masson-Delmotte, P. Zhai, A. Pirani, S. L. Connors, C. Péan, S. Berger, N. Caud, Y. Chen, L. Goldfarb, M. I. Gomis, M. Huang, K. Leitzell, E. Lonnoy, J. B. R. Matthews, T. K. Maycock, T. Waterfield, O. Yelekçi, R. Yu and B. Zhou. In Press. Cambrige University Press.

IPCC (2022a). *Climate Change 2022 - Mitigation of Climate Change: Working Group III Contribution to the Sixth Assessment Report of the Intergovernmental Panel on Climate Change*. Cambridge University Press. ISBN: 9781009157926. DOI: 10.1017/9781009157926.

IPCC (2022b). *Climate Change 2022 – Impacts, Adaptation and Vulnerability: Working Group II Contribution to the Sixth Assessment Report of the Intergovernmental Panel on Climate Change*. Ed. by V. Masson-Delmotte, P. Zhai, A. Pirani, S. L. Connors, C. Péan, Y. Chen, L. Goldfarb, M. I. Gomis, J. B. R. Matthews, S. Berger, M. Huang, O. Yeclekçi, R. Yu, B. Zhou, E. Lonnoy, T. K. Maycock, T. Waterfield, K. Leitzell and N. Caud. Cambridge University Press. ISBN: 9781009325844. DOI: 10.1017/9781009325844.

Irish, V. E., P. Elizondo, J. Chen, C. Chou, J. Charette, M. Lizotte, L. A. Ladino, T. W. Wilson, M. Gosselin, B. J. Murray, E. Polishchuk, J. P. D. Abbatt, L. A. Miller and A. K. Bertram (2017). 'Ice-nucleating particles in Canadian Arctic sea-surface microlayer and bulk seawater'. In: *Atmospheric Chemistry and Physics* 17 (17), pp. 10583–10595. ISSN: 1680-7324. DOI: 10.5194/acp-17-10583-2017.

Irish, V. E., S. J. Hanna, M. D. Willis, S. China, J. L. Thomas, J. J. B. Wentzell, A. Cirisan, M. Si, W. R. Leaitch, J. G. Murphy, J. P. D. Abbatt, A. Laskin, E. Girard and A. K. Bertram (2019). 'Ice nucleating particles in the marine boundary layer in the Canadian Arctic during summer 2014'. In: *Atmospheric Chemistry and Physics* 19 (2), pp. 1027–1039. ISSN: 1680-7324. DOI: 10.5194/acp-19-1027-2019.

ISO 2533:1975 (1975). *Standard Atmosphere*. standard. International Organization for Standardization.

Iversen, T. and E. Joranger (1985). 'Arctic air pollution and large scale atmospheric flows'. In: *Atmospheric Environment (1967)* 19 (12), pp. 2099–2108. ISSN: 0004-6981. DOI: 10.1016/0004-6981(85)90117-9.

Jacob, D. J., J. H. Crawford, H. Maring, A. D. Clarke, J. E. Dibb, L. K. Emmons, R. A. Ferrare, C. A. Hostetler, P. B. Russell, H. B. Singh, A. M. Thompson, G. E. Shaw, E. McCauley, J. R. Pederson and J. A. Fisher (2010). 'The Arctic Research of the Composition of the Troposphere from Aircraft and Satellites (ARCTAS) mission: design, execution, and first results'. In: *Atmospheric Chemistry and Physics* 10 (11), pp. 5191–5212. DOI: 10.5194/acp-10-5191-2010.

Jahl, L. G., T. A. Brubaker, M. J. Polen, L. G. Jahn, K. P. Cain, B. B. Bowers, W. D. Fahy, S. Graves and R. C. Sullivan (2021). 'Atmospheric aging enhances the ice nucleation ability of biomass-burning aerosol'. In: *Science Advances* 7 (9). ISSN: 2375-2548. DOI: 10.1126/sciadv.abd3440.

Jakobsson, M., L. Mayer, B. Coakley, J. A. Dowdeswell, S. Forbes, B. Fridman, H. Hodnesdal, R. Noormets, R. Pedersen, M. Rebesco, H. W. Schenke, Y. Zarayskaya, D. Accettella, A. Armstrong, R. M. Anderson, P. Bienhoff, A. Camerlenghi, I. Church, M. Edwards, J. V. Gardner, J. K. Hall, B. Hell, O. Hestvik, Y. Kristoffersen, C. Marcussen, R. Mohammad, D. Mosher, S. V. Nghiem, M. T. Pedrosa, P. G. Travaglini and P. Weatherall (2012). 'The International Bathymetric Chart of the Arctic Ocean (IBCAO) Version 3.0'. In: *Geophysical Research Letters* 39 (12). ISSN: 1944-8007. DOI: 10.1029/2012gl052219.

Jenkins, M. and A. Dai (2021). 'The Impact of Sea-Ice Loss on Arctic Climate Feedbacks and Their Role for Arctic Amplification'. In: *Geophysical Research Letters* 48 (15). ISSN: 1944-8007. DOI: 10.1029/2021gl094599.

Jensen, L. Z., J. K. Simonsen, A. Pastor, C. Pearce, P. Nørnberg, L. C. Lund-Hansen, K. Finster and T. Šantl-Temkiv (2025). 'Linking biogenic high-temperature ice nucleating particles in Arctic soils and streams to their microbial producers'. In: *Aerosol Research* 3 (1), pp. 81–100. ISSN: 2940-3391. DOI: 10.5194/ar-3-81-2025.

Johnson, D. L., J. I. Rodriguez, B. A. Carroll, J. G. Bustamante, C. S. Kirkconnell, T. T. Luong, J. B. Murphy and M. F. Haley (2014). 'Integrated testing of the Thales LPT9510 pulse tube cooler and the iris LCCE electronics'. In: *AIP Conference Proceedings*. AIP Publishing LLC, pp. 1806–1813. DOI: 10.1063/1.4860927.

Jones, H. M., G. Young, T. W. Choularton, K. N. Bower, T. Lachlan-Cope, S. O'Shea, J. Dorsey, R. Ladkin, A. Kirchgaessner and A. Weiss (2018). 'Summertime Arctic Aircraft Measurements during ACCACIA'. In: *Atmospheric Chemistry and Physics Discussions*. Publisher: Copernicus GmbH, pp. 1–40. DOI: 10.5194/acp-2018-283.

Jurányi, Z., M. Zanatta, M. T. Lund, B. H. Samset, R. B. Skeie, S. Sharma, M. Wendisch and A. Herber (2023). 'Atmospheric concentrations of black carbon are substantially higher in spring than summer in the Arctic'. In: *Communications Earth & Environment* 4 (1). ISSN: 2662-4435. DOI: 10.1038/s43247-023-00749-x.

Kalverla, P. C., J. B. Duncan Jr., G.-J. Steeneveld and A. A. M. Holtslag (2019). 'Low-level jets over the North Sea based on ERA5 and observations: together they do better'. In: *Wind Energy Science* 4 (2), pp. 193–209. ISSN: 2366-7451. DOI: 10.5194/wes-4-193-2019.

Kandler, K., N. Benker, U. Bundke, E. Cuevas, M. Ebert, P. Knippertz, S. Rodríguez, L. Schütz and S. Weinbruch (2007). 'Chemical composition and complex refractive index of Saharan Mineral Dust at Izaña, Tenerife (Spain) derived by electron microscopy'. In: *Atmospheric Environment* 41 (37), pp. 8058–8074. ISSN: 1352-2310. DOI: 10.1016/j.atmosenv.2007.06.047.

Kanji, Z. A., L. A. Ladino, H. Wex, Y. Boose, M. Burkert-Kohn, D. J. Cziczo and M. Krämer (2017). 'Overview of Ice Nucleating Particles'. In: *Meteorological Monographs* 58, pp. 11–133. DOI: 10.1175/amsmonographs-d-16-0006.1.

Kanji, Z. A., R. C. Sullivan, M. Niemand, P. J. DeMott, A. J. Prenni, C. Chou, H. Saathoff and O. Möhler (2019). 'Heterogeneous ice nucleation properties of natural desert dust particles coated with a surrogate of secondary organic aerosol'. In: *Atmospheric Chemistry and Physics* 19 (7), pp. 5091–5110. ISSN: 1680-7324. DOI: 10.5194/acp-19-5091-2019.

Karg, E., S. Dua and J. Tschiersch (1991). 'Experimental counting efficiency of the TSI aerodynamic particle sizer in the submicron size range'. In: *Journal of Aerosol Science* 22, S351–S354. ISSN: 0021-8502. DOI: 10.1016/s0021-8502(05)80110-7.

Karlsson, L., R. Krejci, M. Koike, K. Ebell and P. Zieger (2021). 'A long-term study of cloud residuals from low-level Arctic clouds'. In: *Atmospheric Chemistry and Physics* 21 (11), pp. 8933–8959. DOI: 10.5194/acp-21-8933-2021.

Kaufmann, J. (2019). 'Long-term Measurements of Ice Nucleating Particles in a Boreal Forest during the Winter to Spring Transition'. MA thesis. Karlsruhe Institute of Technology.

Kezoudi, M., C. Keleshis, P. Antoniou, G. Biskos, M. Bronz, C. Constantinides, M. Desservettaz, R.-S. Gao, J. Girdwood, J. Harnetiaux, K. Kandler, A. Leonidou, Y. Liu, J. Lelieveld, F. Marenco, N. Mihalopoulos, G. Močnik, K. Neitola, J.-D. Paris, M. Pikridas, R. Sarda-Esteve, C. Stopford, F. Unga, M. Vrekoussis and J. Sciare (2021). 'The Unmanned Systems Research Laboratory (USRL): A New Facility for UAV-Based Atmospheric Observations'. In: *Atmosphere* 12 (8), p. 1042. DOI: 10.3390/atmos12081042.

Khvorostyanov, V. I. and J. A. Curry (2000). 'A new theory of heterogeneous ice nucleation for application in cloud and climate models'. In: *Geophysical Research Letters* 27 (24), pp. 4081–4084. ISSN: 1944-8007. DOI: 10.1029/1999gl011211.

Khvorostyanov, V. I. and J. A. Curry (2004). 'The Theory of Ice Nucleation by Heterogeneous Freezing of Deliquescent Mixed CCN. Part I: Critical Radius, Energy, and Nucleation Rate'. In: *Journal of the Atmospheric Sciences* 61 (22), pp. 2676–2691. DOI: 10.1175/jas3266.1.

Khvorostyanov, V. I. and J. A. Curry (2005). 'The Theory of Ice Nucleation by Heterogeneous Freezing of Deliquescent Mixed CCN. Part II: Parcel Model Simulation'. In: *Journal of the Atmospheric Sciences* 62 (2), pp. 261–285. ISSN: 0022-4928. DOI: 10.1175/jas-3367.1.

Kieft, T. L. (1988). 'Ice Nucleation Activity in Lichens'. In: *Applied and Environmental Microbiology* 54 (7), pp. 1678–1681. ISSN: 1098-5336. DOI: 10.1128/aem.54.7.1678-1681.1988.

Kim, B.-M., J.-Y. Hong, S.-Y. Jun, X. Zhang, H. Kwon, S.-J. Kim, J.-H. Kim, S.-W. Kim and H.-K. Kim (2017). 'Major cause of unprecedented Arctic warming in January 2016: Critical role of an Atlantic windstorm'. In: *Scientific Reports* 7 (1). ISSN: 2045-2322. DOI: 10.1038/srep40051.

Kiselev, A., F. Bachmann, P. Pedevilla, S. J. Cox, A. Michaelides, D. Gerthsen and T. Leisner (2017). 'Active sites in heterogeneous ice nucleation—the example of K-rich feldspars'. In: *Science* 355 (6323), pp. 367–371. DOI: 10.1126/science.aai8034.

Kivekäs, N., V.-M. Kerminen, T. Raatikainen, P. Vaattovaara, A. Laaksonen and H. Lihavainen (2009). 'Physical and chemical characteristics of aerosol particles and cloud-dropletactivation during the Second Pallas Cloud Experiment (Seconda PaCE)'. In: *Boreal Environment Research* 14, pp. 515–526.

Knopf, D. A. and P. A. Alpert (2023). 'Atmospheric ice nucleation'. In: *Nature Reviews Physics* 5 (4), pp. 203–217. ISSN: 2522-5820. DOI: 10.1038/s42254-023-00570-7.

Knopf, D. A., P. A. Alpert and B. Wang (2018). 'The Role of Organic Aerosol in Atmospheric Ice Nucleation: A Review'. In: *ACS Earth and Space Chemistry* 2 (3), pp. 168–202. ISSN: 2472-3452. DOI: 10.1021/acsearthspacechem.7b00120.

Knutson, E. and K. Whitby (1975). 'Aerosol classification by electric mobility: apparatus, theory, and applications'. In: *Journal of Aerosol Science* 6 (6), pp. 443–451. ISSN: 0021-8502. DOI: 10.1016/0021-8502(75)90060-9.

Köhler, H. (1936). 'The nucleus in and the growth of hygroscopic droplets'. In: *Transactions of the Faraday Society* 32 (0), pp. 1152–1161. ISSN: 0014-7672. DOI: 10.1039/TF9363201152.

Kok, J. F. (2011). 'A scaling theory for the size distribution of emitted dust aerosols suggests climate models underestimate the size of the global dust cycle'. In: *Proceedings of the National Academy of Sciences* 108 (3), pp. 1016–1021. ISSN: 1091-6490. DOI: 10.1073/pnas.1014798108.

Kok, J. F., A. A. Adebiyi, S. Albani, Y. Balkanski, R. Checa-Garcia, M. Chin, P. R. Colarco, D. S. Hamilton, Y. Huang, A. Ito, M. Klose, D. M. Leung, L. Li, N. M. Mahowald, R. L. Miller, V. Obiso, C. Pérez García-Pando, A. Rocha-Lima, J. S. Wan and C. A. Whicker (2021). 'Improved representation of the global dust cycle using observational constraints on dust properties and abundance'. In: *Atmospheric Chemistry and Physics* 21 (10), pp. 8127–8167. ISSN: 1680-7324. DOI: 10.5194/acp-21-8127-2021.

Kokhanovsky, A. and C. Tomasi, eds. (2020). *Physics and Chemistry of the Arctic Atmosphere*. Springer International Publishing. DOI: 10.1007/978-3-030-33566-3.

Komppula, M., H. Lihavainen, V.-M. Kerminen, M. Kulmala and Y. Viisanen (2005). 'Measurements of cloud droplet activation of aerosol particles at a clean subarctic background site'. In: *Journal of Geophysical Research: Atmospheres* 110 (D6). ISSN: 0148-0227. DOI: 10.1029/2004jd005200.

Koop, T. and B. Zobrist (2009). 'Parameterizations for ice nucleation in biological and atmospheric systems'. In: *Physical Chemistry Chemical Physics* 11 (46), p. 10839. ISSN: 1463-9084. DOI: 10.1039/b914289d.

Köppen, W. (2011). 'The thermal zones of the Earth according to the duration of hot, moderate and cold periods and to the impact of heat on the organic world'. In: *Meteorologische Zeitschrift* 20 (3), pp. 351–360. ISSN: 0941-2948. DOI: 10.1127/0941-2948/2011/105.

Korolev, A., I. Heckman, M. Wolde, A. S. Ackerman, A. M. Fridlind, L. A. Ladino, R. P. Lawson, J. Milbrandt and E. Williams (2020). 'A new look at the environmental conditions favorable to secondary ice production'. In: *Atmospheric Chemistry and Physics* 20 (3), pp. 1391–1429. DOI: 10.5194/acp-20-1391-2020.

Korolev, A. and T. Leisner (2020). 'Review of experimental studies of secondary ice production'. In: *Atmospheric Chemistry and Physics* 20 (20), pp. 11767–11797. DOI: 10.5194/acp-20-11767-2020.

Krishnan, S., A. M. L. Ekman, H.-C. Hansson, I. Riipinen, A. Lewinschal, L. J. Wilcox and T. Dallafior (2020). 'The Roles of the Atmosphere and Ocean in Driving Arctic Warming Due to European Aerosol Reductions'. In: *Geophysical Research Letters* 47 (7). ISSN: 1944-8007. DOI: 10.1029/2019gl086681.

Kulkarni, G., J. Fan, J. M. Comstock, X. Liu and M. Ovchinnikov (2012). 'Laboratory measurements and model sensitivity studies of dust deposition ice nucleation'. In: *Atmospheric Chemistry and Physics* 12 (16), pp. 7295–7308. ISSN: 1680-7324. DOI: 10.5194/acp-12-7295-2012.

Kulkarni, G., C. Sanders, K. Zhang, X. Liu and C. Zhao (2014). 'Ice nucleation of bare and sulfuric acid-coated mineral dust particles and implication for cloud properties'. In: *Journal of Geophysical Research: Atmospheres* 119 (16), pp. 9993–10011. ISSN: 2169-8996. DOI: 10.1002/2014JD021567.

Kulkarni, P. (2011). *Aerosol measurement : principles, techniques, and applications*. Ed. by P. Kulkarni, P. A. Baron and K. Willeke. Hoboken, N.J: Wiley. ISBN: 9780470387412.

Kvíderová, J., J. Hájek and R. M. Worland (2013). 'The Ice Nucleation Acticity of Extremophilic Algae'. In: *CryoLetters* 34 (2), pp. 137–148.

Kyrö, E.-M., T. Grönholm, H. Vuollekoski, A. Virkkula, M. Kulmala and L. Laakso (2009). 'Snow scavenging of ultrafine particles: field measurements and parameterization'. In: *Boreal Environment Research* 14, pp. 527–538. ISSN: 1797-2469.

Laakso, L., T. Grönholm, Ü. Rannik, M. Kosmale, V. Fiedler, H. Vehkamäki and M. Kulmala (2003). 'Ultrafine particle scavenging coefficients calculated from 6 years field measurements'. In: *Atmospheric Environment* 37 (25), pp. 3605–3613. ISSN: 1352-2310. DOI: 10.1016/s1352-2310(03)00326-1.

Lacher, L., M. P. Adams, K. Barry, B. Bertozzi, H. Bingemer, C. Boffo, Y. Bras, N. Büttner, D. Castarede, D. J. Cziczo, P. J. DeMott, R. Fösig, M. Goodell, K. Höhler, T. C. J. Hill, C. Jentzsch, L. A. Ladino, E. J. T. Levin, S. Mertes, O. Möhler, K. A. Moore, B. J. Murray, J. Nadolny, T. Pfeuffer, D. Picard, C. Ramírez-Romero, M. Ribeiro, S. Richter, J. Schrod, K. Sellegri, F. Stratmann, B. E. Swanson, E. S. Thomson, H. Wex, M. J. Wolf and E. Freney (2024). 'The Puy de Dôme ICe Nucleation Intercomparison Campaign (PICNIC): comparison between online and offline methods in ambient air'. In: *Atmospheric Chemistry and Physics* 24 (4), pp. 2651–2678. ISSN: 1680-7324. DOI: 10.5194/acp-24-2651-2024.

Ladino, L., O. Stetzer, F. Lüönd, A. Welti and U. Lohmann (2011). 'Contact freezing experiments of kaolinite particles with cloud droplets'. In: *Journal of Geophysical Research: Atmospheres* 116 (D22). ISSN: 2156-2202. DOI: 10.1029/2011JD015727.

Ladino Moreno, L. A., O. Stetzer and U. Lohmann (2013). 'Contact freezing: a review of experimental studies'. In: *Atmospheric Chemistry and Physics* 13 (19), pp. 9745–9769. ISSN: 1680-7324. DOI: 10.5194/acp-13-9745-2013.

Lamas, C. P., C. Vega and E. G. Noya (2022). 'Freezing point depression of salt aqueous solutions using the Madrid-2019 model'. In: *The Journal of Chemical Physics* 156 (13). ISSN: 1089-7690. DOI: 10.1063/5.0085051.

Lampert, A., B. Altstädter, K. Bärfuss, L. Bretschneider, J. Sandgaard, J. Michaelis, L. Lobitz, M. Asmussen, E. Damm, R. Käthner, T. Krüger, C. Lüpkes, S. Nowak, A. Peuker, T. Rausch, F. Reiser, A. Scholtz, D. Sotomayor Zakharov, D. Gaus, S. Bansmer, B. Wehner and F. Pätzold (2020). 'Unmanned Aerial Systems for Investigating the Polar Atmospheric Boundary Layer—Technical Challenges and Examples of Applications'. In: *Atmosphere* 11 (4). ISSN: 2073-4433. DOI: 10.3390/atmos11040416.

Laursen, P., J. Sommer-Larsen, B. Milvang-Jensen, J. P. U. Fynbo and A. O. Razoumov (2019). 'Lyman α-emitting galaxies in the epoch of reionization'. In: *Astronomy & Astrophysics* 627, A84. DOI: 10.1051/0004-6361/201833645.

Leaitch, W. R., S. Sharma, L. Huang, D. Toom-Sauntry, A. Chivulescu, A. M. Macdonald, K. von Salzen, J. R. Pierce, A. K. Bertram, J. C. Schroder, N. C. Shantz, R. Y.-W. Chang and A.-L. Norman (2013). 'Dimethyl sulfide control of the clean summertime Arctic aerosol and cloud'. In: *Elementa: Science of the Anthropocene* 1. Ed. by D. Helmig and J. Savarino. ISSN: 2325-1026. DOI: 10.12952/journal.elementa.000017.

Lee, H., K. Lee, C. R. Lunder, R. Krejci, W. Aas, J. Park, K.-T. Park, B. Y. Lee, Y. J. Yoon and K. Park (2020). 'Atmospheric new particle formation characteristics in the Arctic as measured at Mount Zeppelin, Svalbard, from 2016 to 2018'. In: *Atmospheric Chemistry and Physics* 20 (21), pp. 13425–13441. ISSN: 1680-7324. DOI: 10.5194/acp-20-13425-2020.

Leeuw, G. de, E. L. Andreas, M. D. Anguelova, C. W. Fairall, E. R. Lewis, C. O'Dowd, M. Schulz and S. E. Schwartz (2011). 'Production flux of sea spray aerosol'. In: *Rev. Geophys* 49 (2). ISSN: 1944-9208. DOI: 10.1029/2010RG000349.

Leu, E., C. Mundy, P. Assmy, K. Campbell, T. Gabrielsen, M. Gosselin, T. Juul-Pedersen and R. Gradinger (2015). 'Arctic spring awakening – Steering principles behind the phenology of vernal ice algal blooms'. In: *Progress in Oceanography* 139, pp. 151–170. ISSN: 0079-6611. DOI: 10.1016/j.pocean.2015.07.012.

Lewis, E. R. and S. E. Schwartz (2004). *Sea salt aerosol production: Mechanisms, Methods, Measurements and Models - A critical review*. Geophysical monograph 152. Washington, DC: American Geophysical Union. ISBN: 1118666054.

Lewis, S. L. and M. A. Maslin (2015). 'Defining the Anthropocene'. In: *Nature* 519 (7542), pp. 171–180. DOI: 10.1038/nature14258.

Li, G., J. Wieder, J. T. Pasquier, J. Henneberger and Z. A. Kanji (2022a). 'Predicting atmospheric background number concentration of ice-nucleating particles in the Arctic'. In: *Atmospheric Chemistry and Physics* 22 (21), pp. 14441–14454. ISSN: 1680-7324. DOI: 10.5194/acp-22-14441-2022.

Li, J., B. E. Carlson, Y. L. Yung, D. Lv, J. Hansen, J. E. Penner, H. Liao, V. Ramaswamy, R. A. Kahn, P. Zhang, O. Dubovik, A. Ding, A. A. Lacis, L. Zhang and Y. Dong (2022b). 'Scattering and absorbing aerosols in the climate system'. In: *Nature Reviews Earth & Environment* 3 (6), pp. 363–379. ISSN: 2662-138X. DOI: 10.1038/s43017-022-00296-7.

Li, L. and J. W. Pomeroy (1997). 'Probability of occurrence of blowing snow'. In: *Journal of Geophysical Research: Atmospheres* 102 (D18), pp. 21955–21964. ISSN: 0148-0227. DOI: 10.1029/97jd01522.

Lihavainen, H., V.-M. Kerminen, M. Komppula, A.-P. Hyvärinen, J. Laakia, S. Saarikoski, U. Makkonen, N. Kivekäs, R. Hillamo, M. Kulmala and Y. Viisanen (2008). 'Measurements of the relation between aerosol properties and microphysics and chemistry of low level liquid water clouds in Northern Finland'. In: *Atmospheric Chemistry and Physics* 8 (23), pp. 6925–6938. ISSN: 1680-7324. DOI: 10.5194/acp-8-6925-2008.

Lihavainen, H., V.-M. Kerminen and L. A. Remer (2010). 'Aerosol-cloud interaction determined by both in situ and satellite data over a northern high-latitude site'. In: *Atmospheric Chemistry and Physics* 10 (22), pp. 10987–10995. ISSN: 1680-7324. DOI: 10.5194/acp-10-10987-2010.

Ling, T. Y., J. Wang and D. Y. H. Pui (2011). 'Measurement of filtration efficiency of Nuclepore filters challenged with polystyrene latex nanoparticles: experiments and modeling'. In: *Journal of Nanoparticle Research* 13 (10), pp. 5415–5424. DOI: 10.1007/s11051-011-0529-2.

Lloyd, C. R., R. J. Harding, T. Friborg and M. Aurela (2001). 'Surface fluxes of heat and water vapour from sites in the European Arctic'. In: *Theoretical and Applied Climatology* 70 (1–4), pp. 19–33. ISSN: 1434-4483. DOI: 10.1007/s007040170003.

Loeb, N. G. and W. Su (2010). 'Direct Aerosol Radiative Forcing Uncertainty Based on a Radiative Perturbation Analysis'. In: *Journal of Climate* 23 (19), pp. 5288–5293. ISSN: 0894-8755. DOI: 10.1175/2010jcli3543.1.

Lohila, A., T. Penttilä, S. Jortikka, T. Aalto, P. Anttila, E. Asmi, M. Aurela, J. Hatakka, H. Hellén, H. Henttonen, P. Hänninen, J. Kilkki, K. Kyllönen, T. Laurila, A. Lepistö, H. Lihavainen, U. Makkonen, J. Paatero, M. Rask, R. Sutinen, J.-P. Tuovinen, J. Vuorenmaa and Y. Viisanen (2015). 'Preface to the special issue on integrated research of atmosphere, ecosystems and environment at Pallas'. In: *Boreal Environment Research*. Vol. 20. 4, pp. 431–454.

Lohmann, U., F. Lüönd and F. Mahrt (2016). *An Introduction to Clouds: From the Microscale to Climate*. Cambridge: Cambridge University Press. ISBN: 9781139087513.

Lüönd, F., O. Stetzer, A. Welti and U. Lohmann (2010). 'Experimental study on the ice nucleation ability of size-selected kaolinite particles in the immersion mode'. In: *Journal of Geophysical Research: Atmospheres* 115 (D14), pp. 2156–2202. DOI: 10.1029/2009JD012959.

Lupi, A., M. Busetto, S. Becagli, F. Giardi, C. Lanconelli, M. Mazzola, R. Udisti, H.-C. Hansson, T. Henning, B. Petkov, J. Ström, R. Krejci, P. Tunved, A. P. Viola and V. Vitale (2016). 'Multi-seasonal ultrafine aerosol particle number concentration measurements at the Gruvebadet observatory, Ny-Alesund, Svalbard Islands'. In: *Environmental Changes in Arctic* 27 (2016), pp. 59–71. DOI: 10.1007/s12210-016-0532-8.

Lv, C., N. T. Tsona and L. Du (2020). 'Sea spray aerosol formation: Results on the role of different parameters and organic concentrations from bubble bursting experiments'. In: *Chemosphere* 252, p. 126456. ISSN: 0045-6535. DOI: 10.1016/j.chemosphere.2020.126456.

Macdonald, K. M., S. Sharma, D. Toom, A. Chivulescu, S. Hanna, A. K. Bertram, A. Platt, M. Elsasser, L. Huang, D. Tarasick, N. Chellman, J. R. McConnell, H. Bozem, D. Kunkel, Y. D. Lei, G. J. Evans and J. P. D. Abbatt (2017). 'Observations of atmospheric chemical deposition to high Arctic snow'. In: *Atmospheric Chemistry and Physics* 17 (9). Publisher: Copernicus GmbH, pp. 5775–5788. DOI: 10.5194/acp-17-5775-2017.

MacKay, K. M. (2017). *Introduction to modern inorganic chemistry*. Ed. by R. A. MacKay and W. Henderson. 6th edition, first issued in hardback. Boca Raton: CRC Press. 610 pp. ISBN: 9781138435476.

Mackenzie, A. P. (1977). 'Non-equilibrium freezing behaviour of aqueous systems'. In: *Philosophical Transactions of the Royal Society of London. B, Biological Sciences* 278 (959), pp. 167–189. ISSN: 2054-0280. DOI: 10.1098/rstb.1977.0036.

MacLachlan, S. E., F. R. Cottier, W. E. N. Austin and J. A. Howe (2007). 'The salinity: δ^{18}O water relationship in Kongsfjorden, western Spitsbergen'. In: *Polar Research* 26 (2), pp. 160–167. ISSN: 1751-8369. DOI: 10.1111/j.1751-8369.2007.00016.x.

Mahrt, F., P. A. Alpert, J. Dou, P. Grönquist, P. C. Arroyo, M. Ammann, U. Lohmann and Z. A. Kanji (2020). 'Aging induced changes in ice nucleation activity of combustion aerosol as determined by near edge X-ray absorption fine structure (NEXAFS) spectroscopy'. In: *Environmental Science: Processes & Impacts* 22 (4), pp. 895–907. ISSN: 2050-7895. DOI: 10.1039/c9em00525k.

Maki, L. R., E. L. Galyan, M.-M. Chang-Chien and D. R. Caldwell (1974). 'Ice Nucleation Induced by *Pseudomonas syringae*'. In: *Applied Microbiology* 28 (3), pp. 456–459. ISSN: 0003-6919. DOI: 10.1128/am.28.3.456-459.1974.

Malkin, T. L., B. J. Murray, A. V. Brukhno, J. Anwar and C. G. Salzmann (2012). 'Structure of ice crystallized from supercooled water'. In: *Proceedings of the National Academy of Sciences* 109 (4), pp. 1041–1045. ISSN: 1091-6490. DOI: 10.1073/pnas.1113059109.

Marcolli, C., S. Gedamke, T. Peter and B. Zobrist (2007). 'Efficiency of immersion mode ice nucleation on surrogates of mineral dust'. In: *Atmospheric Chemistry and Physics* 7 (19), pp. 5081–5091. ISSN: 1680-7324. DOI: 10.5194/acp-7-5081-2007.

Marcolli, C., F. Mahrt and B. Kärcher (2021). 'Soot PCF: pore condensation and freezing framework for soot aggregates'. In: *Atmospheric Chemistry and Physics* 21 (10), pp. 7791–7843. ISSN: 1680-7324. DOI: 10.5194/acp-21-7791-2021.

Marinou, E., M. Tesche, A. Nenes, A. Ansmann, J. Schrod, D. Mamali, A. Tsekeri, M. Pikridas, H. Baars, R. Engelmann, K. A. Voudouri, S. Solomos, J. Sciare, S. Groß, F. Ewald and V. Amiridis (2019). 'Retrieval of ice-nucleating particle concentrations from lidar observations and comparison with UAV in situ measurements'. In: *Atmospheric Chemistry and Physics* 19 (17), pp. 11315–11342. ISSN: 1680-7324. DOI: 10.5194/acp-19-11315-2019.

Mårtensson, E. M., E. D. Nilsson, G. de Leeuw, L. H. Cohen and H.-C. Hansson (2003). 'Laboratory simulations and parameterization of the primary marine aerosol production'. In: *Journal of Geophysical Research: Atmospheres* 108 (D9). ISSN: 0148-0227. DOI: 10.1029/2002jd002263.

Mason, R. H., M. Si, C. Chou, V. E. Irish, R. Dickie, P. Elizondo, R. Wong, M. Brintnell, M. Elsasser, W. M. Lassar, K. M. Pierce, W. R. Leaitch, A. M. MacDonald, A. Platt, D. Toom-Sauntry, R. Sarda-Estève, C. L. Schiller, K. J. Suski, T. C. J. Hill, J. P. D. Abbatt, J. A. Huffman, P. J. DeMott and A. K. Bertram (2016). 'Size-resolved measurements of ice-nucleating

particles at six locations in North America and one in Europe'. In: *Atmospheric Chemistry and Physics* 16 (3), pp. 1637–1651. ISSN: 1680-7324. DOI: 10.5194/acp-16-1637-2016.

Matsoukas, T. and S. K. Friedlander (1991). 'Dynamics of aerosol agglomerate formation'. In: *Journal of Colloid and Interface Science* 146 (2), pp. 495–506. ISSN: 0021-9797. DOI: 10.1016/0021-9797(91)90213-r.

Matta, C. F., L. Massa, A. V. Gubskaya and E. Knoll (2010). 'Can One Take the Logarithm or the Sine of a Dimensioned Quantity or a Unit? Dimensional Analysis Involving Transcendental Functions'. In: *Journal of Chemical Education* 88 (1), pp. 67–70. ISSN: 1938-1328. DOI: 10.1021/ed1000476.

Maturilli, M., A. Herber and G. König-Langlo (2013). 'Climatology and time series of surface meteorology in Ny-Ålesund, Svalbard'. In: *Earth System Science Data* 5 (1), pp. 155–163. ISSN: 1866-3516. DOI: 10.5194/essd-5-155-2013.

May, N. W., P. K. Quinn, S. M. McNamara and K. A. Pratt (2016). 'Multiyear study of the dependence of sea salt aerosol on wind speed and sea ice conditions in the coastal Arctic'. In: *Journal of Geophysical Research: Atmospheres* 121 (15), pp. 9208–9219. ISSN: 2169-8996. DOI: 10.1002/2016jd025273.

McCluskey, C. S., T. C. J. Hill, R. S. Humphries, A. M. Rauker, S. Moreau, P. G. Strutton, S. D. Chambers, A. G. Williams, I. McRobert, J. Ward, M. D. Keywood, J. Harnwell, W. Ponsonby, Z. M. Loh, P. B. Krummel, A. Protat, S. M. Kreidenweis and P. J. DeMott (2018a). 'Observations of Ice Nucleating Particles Over Southern Ocean Waters'. In: *Geophys. Res. Lett.* 45 (21), pp. 11, 989–11, 997. ISSN: 0094-8276. DOI: 10.1029/2018gl079981.

McCluskey, C. S., T. C. J. Hill, F. Malfatti, C. M. Sultana, C. Lee, M. V. Santander, C. M. Beall, K. A. Moore, G. C. Cornwell, D. B. Collins, K. A. Prather, T. Jayarathne, E. A. Stone, F. Azam, S. M. Kreidenweis and P. J. DeMott (2017). 'A Dynamic Link between Ice Nucleating Particles Released in Nascent Sea Spray Aerosol and Oceanic Biological Activity during Two Mesocosm Experiments'. In: *Journal of the Atmospheric Sciences* 74 (1), pp. 151–166. DOI: 10.1175/jas-d-16-0087.1.

McCluskey, C. S., J. Ovadnevaite, M. Rinaldi, J. Atkinson, F. Belosi, D. Ceburnis, S. Marullo, T. C. J. Hill, U. Lohmann, Z. A. Kanji, C. O'Dowd, S. M. Kreidenweis and P. J. DeMott (2018b). 'Marine and Terrestrial Organic Ice-Nucleating Particles in Pristine Marine to Continentally Influenced Northeast Atlantic Air Masses'. In: *Journal of Geophysical Research: Atmospheres* 123 (11), pp. 6196–6212. ISSN: 2169-897X. DOI: 10.1029/2017jd028033.

McDonald, J. (1964). 'Cloud Nucleation on Insoluble Particles'. In: *Journal of the Atmospheric Sciences* 21 (1), pp. 109–116. ISSN: 1520-0469. DOI: 10.1175/1520-0469(1964)021<0109:cnoip>2.0.co;2.

McKinley, I. M., C. D. Hummel, B. W. Mueller, D. L. Johnson and J. I. Rodriguez (2024). 'Characterization testing of the Thales LPT9310-HP cryocooler'. In: *IOP Conference Series: Materials Science and Engineering* 1301 (1), p. 012022. ISSN: 1757-899X. DOI: 10.1088/1757-899x/1301/1/012022.

Meinander, O., P. Dagsson-Waldhauserova, P. Amosov, E. Aseyeva, C. Atkins, A. Baklanov, C. Baldo, S. L. Barr, B. Barzycka, L. G. Benning, B. Cvetkovic, P. Enchilik, D. Frolov, S. Gassó, K. Kandler, N. Kasimov, J. Kavan, J. King, T. Koroleva, V. Krupskaya, M. Kulmala, M. Kusiak, H. K. Lappalainen, M. Laska, J. Lasne, M. Lewandowski, B. Luks, J. B. McQuaid, B. Moroni, B. Murray, O. Möhler, A. Nawrot, S. Nickovic, N. T. O'Neill, G. Pejanovic, O. Popovicheva, K. Ranjbar, M. Romanias, O. Samonova, A. Sanchez-Marroquin, K. Schepanski,

I. Semenkov, A. Sharapova, E. Shevnina, Z. Shi, M. Sofiev, F. Thevenet, T. Thorsteinsson, M. Timofeev, N. S. Umo, A. Uppstu, D. Urupina, G. Varga, T. Werner, O. Arnalds and A. Vukovic Vimic (2022). 'Newly identified climatically and environmentally significant high-latitude dust sources'. In: *Atmospheric Chemistry and Physics* 22 (17), pp. 11889–11930. ISSN: 1680-7324. DOI: 10.5194/acp-22-11889-2022.

Meyers, M. P., P. J. DeMott and W. R. Cotton (1992). 'New Primary Ice-Nucleation Parameterizations in an Explicit Cloud Model'. In: *Journal of Applied Meteorology* 31 (7), pp. 708–721. DOI: 10.1175/1520-0450(1992)031<0708:npinpi>2.0.co;2.

Miller, N. B., M. D. Shupe, C. J. Cox, V. P. Walden, D. D. Turner and K. Steffen (2015). 'Cloud Radiative Forcing at Summit, Greenland'. In: *Journal of Climate* 28 (15), pp. 6267–6280. ISSN: 1520-0442. DOI: 10.1175/jcli-d-15-0076.1.

Mishchenko, M. I., L. D. Travis and A. Lacis (2002). *Scattering, absorption, and emission of light by small particles*. 1. publ. Cambridge [u.a.]: Cambridge Univ. Press. ISBN: 052178252X.

MIT (1972). 'Inadvertent climate modification: Report of the study of Man's impact on climate'. In: *Quarterly Journal of the Royal Meteorological Society* 98 (417), pp. 708–709. ISSN: 1477-870X. DOI: 10.1002/qj.49709841724.

Möhler, O., S. Büttner, C. Linke, M. Schnaiter, H. Saathoff, O. Stetzer, R. Wagner, M. Krämer, A. Mangold, V. Ebert and U. Schurath (2005). 'Effect of sulfuric acid coating on heterogeneous ice nucleation by soot aerosol particles'. In: *Journal of Geophysical Research: Atmospheres* 110 (D11). DOI: 10.1029/2004JD005169.

Möhler, O., P. R. Field, P. Connolly, S. Benz, H. Saathoff, M. Schnaiter, R. Wagner, R. Cotton, M. Krämer, A. Mangold and A. J. Heymsfield (2006). 'Efficiency of the deposition mode ice nucleation on mineral dust particles'. In: *Atmospheric Chemistry and Physics* 6 (10), pp. 3007–3021. ISSN: 1680-7324. DOI: 10.5194/acp-6-3007-2006.

Möhler, O., M. Adams, L. Lacher, F. Vogel, J. Nadolny, R. Ullrich, C. Boffo, T. Pfeuffer, A. Hobl, M. Weiß, H. S. K. Vepuri, N. Hiranuma and B. J. Murray (2021). 'The Portable Ice Nucleation Experiment (PINE): a new online instrument for laboratory studies and automated long-term field observations of ice-nucleating particles'. In: *Atmospheric Measurement Techniques* 14 (2), pp. 1143–1166. DOI: 10.5194/amt-14-1143-2021.

Möhler, O., S. Benz, H. Saathoff, M. Schnaiter, R. Wagner, J. Schneider, S. Walter, V. Ebert and S. Wagner (2008). 'The effect of organic coating on the heterogeneous ice nucleation efficiency of mineral dust aerosols'. In: *Environmental Research Letters* 3 (2), p. 025007. DOI: 10.1088/1748-9326/3/2/025007.

Monahan, E. C., O'Muircheartaigh and I. G. (1986). 'Whitecaps and the passive remote sensing of the ocean surface'. In: *International Journal of Remote Sensing* 7 (5), pp. 627–642. ISSN: 1366-5901. DOI: 10.1080/01431168608954716.

Monahan, E. C., A. Staniec and P. Vlahos (2017). 'Spume Drops: Their Potential Role in Air-Sea Gas Exchange'. In: *Journal of Geophysical Research: Oceans* 122 (12), pp. 9500–9517. ISSN: 2169-9291. DOI: 10.1002/2017jc013293.

Moore, R. H., E. B. Wiggins, A. T. Ahern, S. Zimmerman, L. Montgomery, P. C. Jost, C. E. Robinson, L. D. Ziemba, E. L. Winstead, B. E. Anderson, C. A. Brock, M. D. Brown, G. Chen, E. C. Crosbie, H. Guo, J. L. Jimenez, C. E. Jordan, M. Lyu, B. A. Nault, N. E. Rothfuss, K. J. Sanchez, M. Schueneman, T. J. Shingler, M. A. Shook, K. L. Thornhill, N. L. Wagner and J. Wang (2021). 'Sizing response of the Ultra-High Sensitivity Aerosol Spectrometer

(UHSAS) and Laser Aerosol Spectrometer (LAS) to changes in submicron aerosol composition and refractive index'. In: *Atmospheric Measurement Techniques* 14 (6), pp. 4517–4542. ISSN: 1867-8548. DOI: 10.5194/amt-14-4517-2021.

Morrison, H., G. de Boer, G. Feingold, J. Harrington, M. D. Shupe and K. Sulia (2011). 'Resilience of persistent Arctic mixed-phase clouds'. In: *Nature Geoscience* 5, p. 11. DOI: 10.1038/ngeo1332.

Mossop, S. C. (1976). 'Production of secondary ice particles during the growth of graupel by riming'. In: *Quarterly Journal of the Royal Meteorological Society* 102 (431), pp. 45–57. DOI: 10.1002/qj.49710243104.

Mülmenstädt, J., O. Sourdeval, J. Delanoë and J. Quaas (2015). 'Frequency of occurrence of rain from liquid-, mixed-, and ice-phase clouds derived from A-Train satellite retrievals'. In: *Geophys. Res. Lett.* 42 (15), pp. 6502–6509. ISSN: 1944-8007. DOI: 10.1002/2015GL064604.

Murray, B. J., S. L. Broadley, T. W. Wilson, J. D. Atkinson and R. H. Wills (2011). 'Heterogeneous freezing of water droplets containing kaolinite particles'. In: *Atmospheric Chemistry and Physics* 11 (9), pp. 4191–4207. ISSN: 1680-7324. DOI: 10.5194/acp-11-4191-2011.

Murray, B. J., D. O'Sullivan, J. D. Atkinson and M. E. Webb (2012). 'Ice nucleation by particles immersed in supercooled cloud droplets'. In: *Chemical Society Reviews* 41 (19), p. 6519. ISSN: 0306-0012. DOI: 10.1039/c2cs35200a.

Myhre, G., B. H. Samset, M. Schulz, Y. Balkanski, S. Bauer, T. K. Berntsen, H. Bian, N. Bellouin, M. Chin, T. Diehl, R. C. Easter, J. Feichter, S. J. Ghan, D. Hauglustaine, T. Iversen, S. Kinne, A. Kirkevåg, J.-F. Lamarque, G. Lin, X. Liu, M. T. Lund, G. Luo, X. Ma, T. van Noije, J. E. Penner, P. J. Rasch, A. Ruiz, ø. Seland, R. B. Skeie, P. Stier, T. Takemura, K. Tsigaridis, P. Wang, Z. Wang, L. Xu, H. Yu, F. Yu, J.-H. Yoon, K. Zhang, H. Zhang and C. Zhou (2013). 'Radiative forcing of the direct aerosol effect from AeroCom Phase II simulations'. In: *Atmospheric Chemistry and Physics* 13 (4), pp. 1853–1877. DOI: 10.5194/acp-13-1853-2013.

Niedermeier, D., S. Hartmann, R. A. Shaw, D. Covert, T. F. Mentel, J. Schneider, L. Poulain, P. Reitz, C. Spindler, T. Clauss, A. Kiselev, E. Hallbauer, H. Wex, K. Mildenberger and F. Stratmann (2010). 'Heterogeneous freezing of droplets with immersed mineral dust particles – measurements and parameterization'. In: *Atmospheric Chemistry and Physics* 10 (8), pp. 3601–3614. ISSN: 1680-7324. DOI: 10.5194/acp-10-3601-2010.

Niedermeier, D., R. A. Shaw, S. Hartmann, H. Wex, T. Clauss, J. Voigtländer and F. Stratmann (2011). 'Heterogeneous ice nucleation: exploring the transition from stochastic to singular freezing behavior'. In: *Atmospheric Chemistry and Physics* 11 (16), pp. 8767–8775. ISSN: 1680-7324. DOI: 10.5194/acp-11-8767-2011.

Niedermeier, D., S. Augustin-Bauditz, S. Hartmann, H. Wex, K. Ignatius and F. Stratmann (2015). 'Can we define an asymptotic value for the ice active surface site density for heterogeneous ice nucleation?' In: *Journal of Geophysical Research: Atmospheres* 120 (10), pp. 5036–5046. ISSN: 2169-8996. DOI: 10.1002/2014jd022814.

Niedermeier, D., B. Ervens, T. Clauss, J. Voigtländer, H. Wex, S. Hartmann and F. Stratmann (2014). 'A computationally efficient description of heterogeneous freezing: A simplified version of the Soccer ball model'. In: *Geophysical Research Letters* 41 (2), pp. 736–741. ISSN: 1944-8007. DOI: 10.1002/2013gl058684.

Niehaus, J., K. W. Bunker, S. China, A. Kostinski, C. Mazzoleni and W. Cantrell (2014). 'A Technique to Measure Ice Nuclei in the Contact Mode'. In: *Journal of Atmospheric and Oceanic Technology* 31 (4), pp. 913–922. ISSN: 1520-0426. DOI: 10.1175/jtech-d-13-00156.1.

Noël, A., G. Truchon, Y. Cloutier, M. Charbonneau, K. Maghni and R. Tardif (2016). 'Mass or total surface area with aerosol size distribution as exposure metrics for inflammatory, cytotoxic and oxidative lung responses in rats exposed to titanium dioxide nanoparticles'. In: *Toxicology and Industrial Health* 33 (4), pp. 351–364. ISSN: 1477-0393. DOI: 10.1177/0748233716651560.

Nomokonova, T., K. Ebell, U. Löhnert, M. Maturilli, C. Ritter and E. O'Connor (2019). 'Statistics on clouds and their relation to thermodynamic conditions at Ny-Alesund using ground-based sensor synergy'. In: *Atmospheric Chemistry and Physics* 19 (6). Publisher: Copernicus GmbH, pp. 4105–4126. DOI: 10.5194/acp-19-4105-2019.

O'Sullivan, D., B. J. Murray, T. L. Malkin, T. F. Whale, N. S. Umo, J. D. Atkinson, H. C. Price, K. J. Baustian, J. Browse and M. E. Webb (2014). 'Ice nucleation by fertile soil dusts: relative importance of mineral and biogenic components'. In: *Atmospheric Chemistry and Physics* 14 (4), pp. 1853–1867. DOI: 10.5194/acp-14-1853-2014.

Ogura, I., M. Kotake, H. Sakurai and K. Honda (2016). 'Surface-collection efficiency of Nuclepore filters for nanoparticles'. In: *Aerosol Science and Technology* 50 (8), pp. 846–856. DOI: 10.1080/02786826.2016.1200007.

Oh, H.-J., Y. Ma and J. Kim (2020). 'Human Inhalation Exposure to Aerosol and Health Effect: Aerosol Monitoring and Modelling Regional Deposited Doses'. In: *International Journal of Environmental Research and Public Health* 17 (6), p. 1923. ISSN: 1660-4601. DOI: 10.3390/ijerph17061923.

Ohtsuka, T., M. Adachi, M. Uchida and T. Nakatsubo (2006). 'Relationships between vegetation types and soil properties along a topographical gradient on the northern coast of the Brøgger Peninsula, Svalbard'. In: *Polar Bioscience* 19, pp. 63–72.

Olauson, J. (2018). 'ERA5: The new champion of wind power modelling?' In: *Renewable Energy* 126, pp. 322–331. ISSN: 0960-1481. DOI: 10.1016/j.renene.2018.03.056.

Ostwald, W. (1897). 'Studien über die Bildung und Umwandlung fester Körper: 1. Abhandlung: Übersättigung und Überkaltung'. In: *Zeitschrift für Physikalische Chemie* 22U (1), pp. 289–330. ISSN: 0942-9352. DOI: 10.1515/zpch-1897-2233.

Pach, E. and A. Verdaguer (2019). 'Pores Dominate Ice Nucleation on Feldspars'. In: *The Journal of Physical Chemistry C* 123 (34), pp. 20998–21004. ISSN: 1932-7455. DOI: 10.1021/acs.jpcc.9b05845.

Park, S.-G., H.-L. Kim, Y.-W. Ham and S.-H. Jung (2017). 'Comparative Evaluation of the OTT PARSIVEL2 Using a Collocated Two-Dimensional Video Disdrometer'. In: *Journal of Atmospheric and Oceanic Technology* 34 (9), pp. 2059–2082. ISSN: 1520-0426. DOI: 10.1175/jtech-d-16-0256.1.

Peckhaus, A., A. Kiselev, T. Hiron, M. Ebert and T. Leisner (2016). 'A comparative study of K-rich and Na/Ca-rich feldspar ice-nucleating particles in a nanoliter droplet freezing assay'. In: *Atmospheric Chemistry and Physics* 16 (18), pp. 11477–11496. DOI: 10.5194/acp-16-11477-2016.

Perkins, R. J., S. M. Gillette, T. C. J. Hill and P. J. DeMott (2019). 'The Labile Nature of Ice Nucleation by Arizona Test Dust'. In: *ACS Earth and Space Chemistry* 4 (1), pp. 133–141. ISSN: 2472-3452. DOI: 10.1021/acsearthspacechem.9b00304.

Pfeifer, S., T. Müller, K. Weinhold, N. Zikova, S. M. dos Santos, A. Marinoni, O. F. Bischof, C. Kykal, L. Ries, F. Meinhardt, P. Aalto, N. Mihalopoulos and A. Wiedensohler (2016). 'Intercomparison of 15 aerodynamic particle size spectrometers (APS 3321): uncertainties in particle sizing and number size distribution'. In: *Atmospheric Measurement Techniques* 9 (4), pp. 1545–1551. DOI: 10.5194/amt-9-1545-2016.

Philippi, P. C. (2024). *Thermodynamics: From Fundamentals to Multiphase and Multicomponent Systems*. Springer Nature Switzerland. ISBN: 9783031493577. DOI: 10.1007/978-3-031-49357-7.

Piedehierro, A. A., A. Welti, A. Buchholz, K. Korhonen, I. Pullinen, I. Summanen, A. Virtanen and A. Laaksonen (2021). 'Ice nucleation on surrogates of boreal forest SOA particles: effect of water content and oxidative age'. In: *Atmospheric Chemistry and Physics* 21 (14), pp. 11069–11078. ISSN: 1680-7324. DOI: 10.5194/acp-21-11069-2021.

Pilz, C., M. Lonardi, U. Egerer, H. Siebert, A. Ehrlich, A. J. Heymsfield, C. G. Schmitt, M. D. Shupe, B. Wehner and M. Wendisch (2023). 'Profile observations of the Arctic atmospheric boundary layer with the BELUGA tethered balloon during MOSAiC'. In: *Scientific Data* 10 (1). ISSN: 2052-4463. DOI: 10.1038/s41597-023-02423-5.

Pisso, I., E. Sollum, H. Grythe, N. I. Kristiansen, M. Cassiani, S. Eckhardt, D. Arnold, D. Morton, R. L. Thompson, C. D. Groot Zwaaftink, N. Evangeliou, H. Sodemann, L. Haimberger, S. Henne, D. Brunner, J. F. Burkhart, A. Fouilloux, J. Brioude, A. Philipp, P. Seibert and A. Stohl (2019). 'The Lagrangian particle dispersion model FLEXPART version 10.4'. In: *Geoscientific Model Development* 12 (12), pp. 4955–4997. ISSN: 1991-9603. DOI: 10.5194/gmd-12-4955-2019.

Pithan, F. and T. Mauritsen (2014). 'Arctic amplification dominated by temperature feedbacks in contemporary climate models'. In: *Nature Geoscience* 7, p. 181. DOI: 10.1038/ngeo2071.

Platt, S. M., Ø. Hov, T. Berg, K. Breivik, S. Eckhardt, K. Eleftheriadis, N. Evangeliou, M. Fiebig, R. Fisher, G. Hansen, H.-C. Hansson, J. Heintzenberg, O. Hermansen, D. Heslin-Rees, K. Holmén, S. Hudson, R. Kallenborn, R. Krejci, T. Krognes, S. Larssen, D. Lowry, C. L. Myhre, C. Lunder, E. Nisbet, P. B. Nizzetto, K.-T. Park, C. A. Pedersen, K. A. Pfaffhuber, T. Röckmann, N. Schmidbauer, S. Solberg, A. Stohl, J. Ström, T. Svendby, P. Tunved, K. Tørnkvist, C. van der Veen, S. Vratolis, Y. J. Yoon, K. E. Yttri, P. Zieger, W. Aas and K. Tørseth (2022). 'Atmospheric composition in the European Arctic and 30 years of the Zeppelin Observatory, Ny-Alesund'. In: *Atmospheric Chemistry & Physics* 22 (5), pp. 3321–3369. DOI: 10.5194/acp-22-3321-2022.

Porter, G. C. E., S. N. F. Sikora, M. P. Adams, U. Proske, A. D. Harrison, M. D. Tarn, I. M. Brooks and B. J. Murray (2020). 'Resolving the size of ice-nucleating particles with a balloon deployable aerosol sampler: the SHARK'. In: *Atmospheric Measurement Techniques* 13 (6), pp. 2905–2921. DOI: 10.5194/amt-13-2905-2020.

Prenni, A., P. DeMott, D. Rogers, S. M. Kreidenweis, G. M. McFarquhar, G. Zhang and M. R. Poellot (2009). 'Ice nuclei characteristics from M-PACE and their relation to ice formation in clouds'. In: *Tellus B: Chemical and Physical Meteorology* 61 (2), pp. 436–448. ISSN: 1600-0889. DOI: 10.1111/j.1600-0889.2008.00415.x.

Prospero, J. M., J. E. Bullard and R. Hodgkins (2012). 'High-Latitude Dust Over the North Atlantic: Inputs from Icelandic Proglacial Dust Storms'. In: *Science* 335 (6072). Publisher: American Association for the Advancement of Science Section: Report, pp. 1078–1082. DOI: 10.1126/science.1217447.

Prospero, J. M., P. Ginoux, O. Torres, S. E. Nicholson and T. E. Gill (2002). 'Environmental Characterization Of Global Sources Of Atmospheric Soil Dust Identified With The Nimbus 7 Total Ozone Mapping Spectrometer (TOMS) Absorbing Aerosol Product'. In: *Reviews of Geophysics* 40 (1). ISSN: 1944-9208. DOI: 10.1029/2000rg000095.

Pruppacher, H. R. and J. D. Klett (1997). *Microphysics of Clouds and Precipitation*. Kluwer Acad. Norwell, Mass.

Quinn, P. K., A. Stohl, A. Arneth, T. Berntsen, J. Burkhart, J. Christensen, M. Flanner, K. Kupiainen, H. Lihavainen, M. Shepherd, V. Shevchenko, H. Skov and V. Vestreng (2011). *The impact of black carbon on Arctic climate*. Ed. by A.-C. E. S. Kristine Aasarød. Oslo, Norway: Arctic Monitoring and Assessment Programme. ISBN: 9788279710691.

Raatz, W. E. (1984). 'Observations of "Arctic Haze" during the "Ptarmigan" weather reconnaissance flights, 1948-1961'. In: *Tellus B: Chemical and Physical Meteorology* 36 (2), p. 126. ISSN: 0280-6509. DOI: 10.3402/tellusb.v36i2.14882.

Radke, L. F., P. V. Hobbs and J. E. Pinnons (1976). 'Observations of Cloud Condensation Nuclei, Sodium-Containing Particles, Ice Nuclei and the Light-Scattering Coefficient Near Barrow, Alaska'. In: *Journal of Applied Meteorology* 15 (9), pp. 982–995. ISSN: 0021-8952. DOI: 10.1175/1520-0450(1976)015<0982:ooccns>2.0.co;2.

Rantanen, M., A. Y. Karpechko, A. Lipponen, K. Nordling, O. Hyvärinen, K. Ruosteenoja, T. Vihma and A. Laaksonen (2022). 'The Arctic has warmed nearly four times faster than the globe since 1979'. In: *Communications Earth & Environment* 3 (1). ISSN: 2662-4435. DOI: 10.1038/s43247-022-00498-3.

Raschke, E., S. Kinne, W. B. Rossow, P. W. Stackhouse and M. Wild (2015). 'Comparison of Radiative Energy Flows in Observational Datasets and Climate Modeling'. In: *Journal of Applied Meteorology and Climatology* 55 (1), pp. 93–117. DOI: 10.1175/JAMC-D-14-0281.1.

Rasmussen, D. H. (1982). 'Thermodynamics and nucleation phenomena — A set of experimental observations'. In: *Journal of Crystal Growth* 56 (1), pp. 56–66. ISSN: 0022-0248. DOI: 10.1016/0022-0248(82)90012-4.

Rinaldi, M., N. Hiranuma, G. Santachiara, M. Mazzola, K. Mansour, M. Paglione, C. A. Rodriguez, R. Traversi, S. Becagli, D. Cappelletti and F. Belosi (2021). 'Ice-nucleating particle concentration measurements from Ny-Alesund during the Arctic spring-summer in 2018'. In: *Atmospheric Chemistry & Physics* 21 (19), pp. 14725–14748. DOI: 10.5194/acp-21-14725-2021.

Roiger, A., J.-L. Thomas, H. Schlager, K. S. Law, J. Kim, A. Schäfler, B. Weinzierl, F. Dahlkötter, I. Krisch, L. Marelle, A. Minikin, J.-C. Raut, A. Reiter, M. Rose, M. Scheibe, P. Stock, R. Baumann, I. Bouarar, C. Clerbaux, M. George, T. Onishi and J. Flemming (2015). 'Quantifying Emerging Local Anthropogenic Emissions in the Arctic Region: The ACCESS Aircraft Campaign Experiment'. In: *Bulletin of the American Meteorological Society* 96 (3), pp. 441–460. DOI: 10.1175/bams-d-13-00169.1.

Rowe, P. M., M. Fergoda and S. Neshyba (2020). 'Temperature-Dependent Optical Properties of Liquid Water From 240 to 298 K'. In: *Journal of Geophysical Research: Atmospheres* 125 (17). ISSN: 2169-8996. DOI: 10.1029/2020jd032624.

Russell, L. M., R. H. Moore, S. M. Burrows and P. K. Quinn (2023). 'Ocean flux of salt, sulfate, and organic components to atmospheric aerosol'. In: *Earth-Science Reviews* 239, p. 104364. ISSN: 0012-8252. DOI: 10.1016/j.earscirev.2023.104364.

Saha, R., F. Y. Testik and M. C. Testik (2021). 'Assessment of OTT Pluvio2 Rain Intensity Measurements'. In: *Journal of Atmospheric and Oceanic Technology* 38 (4), pp. 897–908. ISSN: 1520-0426. DOI: 10.1175/jtech-d-19-0219.1.

Salam, A., U. Lohmann, B. Crenna, G. Lesins, P. Klages, D. Rogers, R. Irani, A. MacGillivray and M. Coffin (2006). 'Ice Nucleation Studies of Mineral Dust Particles with a New Continuous Flow Diffusion Chamber'. In: *Aerosol Science and Technology* 40 (2), pp. 134–143. DOI: 10.1080/02786820500444853.

Salzmann, C. G., P. G. Radaelli, B. Slater and J. L. Finney (2011). 'The polymorphism of ice: five unresolved questions'. In: *Physical Chemistry Chemical Physics* 13 (41), p. 18468. ISSN: 1463-9084. DOI: 10.1039/c1cp21712g.

Sanchez-Marroquin, A., S. L. Barr, I. T. Burke, J. B. McQuaid and B. J. Murray (2023). 'Aircraft ice-nucleating particle and aerosol composition measurements in the western North American Arctic'. In: *Atmospheric Chemistry and Physics* 23 (21), pp. 13819–13834. ISSN: 1680-7324. DOI: 10.5194/acp-23-13819-2023.

Santachiara, G., L. D. Matteo, F. Prodi and F. Belosi (2010). 'Atmospheric particles acting as Ice Forming Nuclei in different size ranges'. In: *Atmospheric Research* 96 (2–3), pp. 266–272. ISSN: 0169-8095. DOI: 10.1016/j.atmosres.2009.08.004.

Sassen, K. and K.-N. Liou (1979). 'Scattering of Polarized Laser Light by Water Droplet, Mixed-Phase and Ice Crystal Clouds. Part I: Angular Scattering Patterns'. In: *Journal of the Atmospheric Sciences* 36 (5), pp. 838–851. ISSN: 1520-0469. DOI: 10.1175/1520-0469(1979)036<0838:sopllb>2.0.co;2.

Satheesh, S. K. and K. K. Moorthy (2005). 'Radiative effects of natural aerosols: A review'. In: *Atmospheric Environment* 39 (11), pp. 2089–2110. ISSN: 1352-2310. DOI: 10.1016/j.atmosenv.2004.12.029.

Savre, J. and A. M. L. Ekman (2015). 'A theory-based parameterization for heterogeneous ice nucleation and implications for the simulation of ice processes in atmospheric models'. In: *Journal of Geophysical Research: Atmospheres* 120 (10), pp. 4937–4961. ISSN: 2169-8996. DOI: 10.1002/2014jd023000.

Schäfer, D., B. Palm, P. Lünenschloß, L. Schmidt, T. Schnicke and J. Bumberger (2024). *System for automated Quality Control - SaQC (v2.6.0)*. Zenodo. DOI: https://doi.org/10.5281/zenodo.5888547.

Scheuvens, D., L. Schütz, K. Kandler, M. Ebert and S. Weinbruch (2013). 'Bulk composition of northern African dust and its source sediments — A compilation'. In: *Earth-Science Reviews* 116, pp. 170–194. ISSN: 0012-8252. DOI: 10.1016/j.earscirev.2012.08.005.

Schiebel, T. (2017). 'Ice Nucleation Activity of Soil Dust Aerosols'. PhD thesis. Karlsruhe Institute of Technology. DOI: 10.5445/ir/1000076327.

Schmale, J., P. Zieger and A. M. L. Ekman (2021). 'Aerosols in current and future Arctic climate'. In: *Nature Climate Change* 11 (2), pp. 95–105. DOI: 10.1038/s41558-020-00969-5.

Schmidt, L., D. Schäfer, J. Geller, P. Lünenschloss, B. Palm, K. Rinke, C. Rebmann, M. Rode and J. Bumberger (2023). 'System for automated Quality Control (SaQC) to enable traceable and reproducible data streams in environmental science'. In: *Environmental Modelling & Software* 169, p. 105809. ISSN: 1364-8152. DOI: 10.1016/j.envsoft.2023.105809.

Schneider, J., K. Höhler, P. Heikkilä, J. Keskinen, B. Bertozzi, P. Bogert, T. Schorr, N. S. Umo, F. Vogel, Z. Brasseur, Y. Wu, S. Hakala, J. Duplissy, D. Moisseev, M. Kulmala, M. P. Adams, B. J. Murray, K. Korhonen, L. Hao, E. S. Thomson, D. Castarède, T. Leisner, T. Petäjä and O. Möhler (2021). 'The seasonal cycle of ice-nucleating particles linked to the abundance of biogenic aerosol in boreal forests'. In: *Atmospheric Chemistry and Physics* 21 (5), pp. 3899–3918. ISSN: 1680-7324. DOI: 10.5194/acp-21-3899-2021.

Schrod, J., D. Weber, J. Drücke, C. Keleshis, M. Pikridas, M. Ebert, B. Cvetkovic, S. Nickovic, E. Marinou, H. Baars, A. Ansmann, M. Vrekoussis, N. Mihalopoulos, J. Sciare, J. Curtius and H. G. Bingemer (2017). 'Ice nucleating particles over the Eastern Mediterranean measured by unmanned aircraft systems'. In: *Atmospheric Chemistry and Physics* 17 (7), pp. 4817–4835. DOI: 10.5194/acp-17-4817-2017.

Schulz, H., M. Zanatta, H. Bozem, W. R. Leaitch, A. B. Herber, J. Burkart, M. D. Willis, D. Kunkel, P. M. Hoor, J. P. D. Abbatt and R. Gerdes (2019). 'High Arctic aircraft measurements characterising black carbon vertical variability in spring and summer'. In: *Atmospheric Chemistry and Physics* 19 (4), pp. 2361–2384. DOI: 10.5194/acp-19-2361-2019.

Schulz, J. (2016). 'The optimal Berry-Esseen constant in the binomial case'. PhD thesis. Universität Trier.

Schulz, M., C. Textor, S. Kinne, Y. Balkanski, S. Bauer, T. Berntsen, T. Berglen, O. Boucher, F. Dentener, S. Guibert, I. S. A. Isaksen, T. Iversen, D. Koch, A. Kirkevåg, X. Liu, V. Montanaro, G. Myhre, J. E. Penner, G. Pitari, S. Reddy, Ø. Seland, P. Stier and T. Takemura (2006). 'Radiative forcing by aerosols as derived from the AeroCom present-day and pre-industrial simulations'. In: *Atmospheric Chemistry and Physics* 6 (12), pp. 5225–5246. DOI: 10.5194/acp-6-5225-2006.

Screen, J. A. and I. Simmonds (2010). 'The central role of diminishing sea ice in recent Arctic temperature amplification'. In: *Nature* 464 (7293), pp. 1334–1337. DOI: 10.1038/nature09051.

Seinfeld, J. H. and S. N. Pandis (2016). *Atmospheric chemistry and physics: from air pollution to climate change*. John Wiley & Sons. ISBN: 1118947401.

Seland, Ø., T. Iversen, A. Kirkevåg and T. Storelvmo (2008). 'Aerosol-climate interactions in the CAM-Oslo atmospheric GCM and investigation of associated basic shortcomings'. In: *Tellus A: Dynamic Meteorology and Oceanography* 60 (3), p. 459. ISSN: 1600-0870. DOI: 10.1111/j.1600-0870.2007.00318.x.

Sensirion (2013). *SFM4100 Series*. 1.3. Sensirion.

Sensirion (2021). *SHT4x*. 2nd ed. Sensirion.

Serreze, M. C. and J. A. Francis (2006). 'The Arctic Amplification Debate'. In: *Climatic Change* 76 (3), pp. 241–264. ISSN: 1573-1480. DOI: 10.1007/s10584-005-9017-y.

Shao, Y. and H. Lu (2000). 'A simple expression for wind erosion threshold friction velocity'. In: *Journal of Geophysical Research: Atmospheres* 105 (D17), pp. 22437–22443. ISSN: 0148-0227. DOI: 10.1029/2000jd900304.

Sharma, P. and K. Hanumantha Rao (2002). 'Analysis of different approaches for evaluation of surface energy of microbial cells by contact angle goniometry'. In: *Advances in Colloid and Interface Science* 98 (3), pp. 341–463. ISSN: 0001-8686. DOI: 10.1016/s0001-8686(02)00004-0.

Shaw, G. E. (1995). 'The Arctic Haze Phenomenon'. In: *Bulletin of the American Meteorological Society* 76 (12), pp. 2403–2414. DOI: 10.1175/1520-0477(1995)076<2403:Tahp>2.0.Co;2.

Shi, Y., X. Liu, M. Wu, X. Zhao, Z. Ke and H. Brown (2022). 'Relative importance of high-latitude local and long-range-transported dust for Arctic ice-nucleating particles and impacts on Arctic mixed-phase clouds'. In: *Atmospheric Chemistry and Physics* 22 (4), pp. 2909–2935. DOI: 10.5194/acp-22-2909-2022.

Shiraiwa, M., K. Ueda, A. Pozzer, G. Lammel, C. J. Kampf, A. Fushimi, S. Enami, A. M. Arangio, J. Fröhlich-Nowoisky, Y. Fujitani, A. Furuyama, P. S. J. Lakey, J. Lelieveld, K. Lucas, Y. Morino, U. Pöschl, S. Takahama, A. Takami, H. Tong, B. Weber, A. Yoshino and K. Sato (2017). 'Aerosol Health Effects from Molecular to Global Scales'. In: *Environmental Science & Technology* 51 (23), pp. 13545–13567. ISSN: 1520-5851. DOI: 10.1021/acs.est.7b04417.

Shupe, M. D. (2011). 'Clouds at Arctic Atmospheric Observatories. Part II: Thermodynamic Phase Characteristics'. In: *J. Appl. Meteorol. Climatol.* 50 (3), pp. 645–661. DOI: 10.1175/2010jamc2468.1.

Shupe, M. D. and J. M. Intrieri (2004). 'Cloud Radiative Forcing of the Arctic Surface: The Influence of Cloud Properties, Surface Albedo, and Solar Zenith Angle'. In: *Journal of Climate* 17 (3), pp. 616–628. DOI: 10.1175/1520-0442(2004)017<0616:crfota>2.0.co;2.

Shupe, M. D., S. Y. Matrosov and T. Uttal (2006). 'Arctic Mixed-Phase Cloud Properties Derived from Surface-Based Sensors at SHEBA'. In: *Journal of the Atmospheric Sciences* 63 (2), pp. 697–711. DOI: 10.1175/jas3659.1.

Shupe, M. D., M. Rex, B. Blomquist, P. O. G. Persson, J. Schmale, T. Uttal, D. Althausen, H. Angot, S. Archer, L. Bariteau, I. Beck, J. Bilberry, S. Bucci, C. Buck, M. Boyer, Z. Brasseur, I. M. Brooks, R. Calmer, J. Cassano, V. Castro, D. Chu, D. Costa, C. J. Cox, J. Creamean, S. Crewell, S. Dahlke, E. Damm, G. de Boer, H. Deckelmann, K. Dethloff, M. Dütsch, K. Ebell, A. Ehrlich, J. Ellis, R. Engelmann, A. A. Fong, M. M. Frey, M. R. Gallagher, L. Ganzeveld, R. Gradinger, J. Graeser, V. Greenamyer, H. Griesche, S. Griffiths, J. Hamilton, G. Heinemann, D. Helmig, A. Herber, C. Heuzé, J. Hofer, T. Houchens, D. Howard, J. Inoue, H.-W. Jacobi, R. Jaiser, T. Jokinen, O. Jourdan, G. Jozef, W. King, A. Kirchgaessner, M. Klingebiel, M. Krassovski, T. Krumpen, A. Lampert, W. Landing, T. Laurila, D. Lawrence, M. Lonardi, B. Loose, C. Lüpkes, M. Maahn, A. Macke, W. Maslowski, C. Marsay, M. Maturilli, M. Mech, S. Morris, M. Moser, M. Nicolaus, P. Ortega, J. Osborn, F. Pätzold, D. K. Perovich, T. Petäjä, C. Pilz, R. Pirazzini, K. Posman, H. Powers, K. A. Pratt, A. Preußer, L. Quéléver, M. Radenz, B. Rabe, A. Rinke, T. Sachs, A. Schulz, H. Siebert, T. Silva, A. Solomon, A. Sommerfeld, G. Spreen, M. Stephens, A. Stohl, G. Svensson, J. Uin, J. Viegas, C. Voigt, P. von der Gathen, B. Wehner, J. M. Welker, M. Wendisch, M. Werner, Z. Xie and F. Yue (2022). 'Overview of the MOSAiC expedition: Atmosphere'. In: *Elementa: Science of the Anthropocene* 10 (1). ISSN: 2325-1026. DOI: 10.1525/elementa.2021.00060.

Shupe, M. D., T. Uttal and S. Y. Matrosov (2005). 'Arctic Cloud Microphysics Retrievals from Surface-Based Remote Sensors at SHEBA'. In: *Journal of Applied Meteorology* 44 (10), pp. 1544–1562. DOI: 10.1175/jam2297.1.

Silva, M. T., J. L. Guerrero-Rascado, A. L. Correia, D. A. Gouveia and H. M. J. Barbosa (2022). 'On the Sensitivity of a Ground-Based Tropospheric Lidar to Aitken Mode Particles in the Upper Troposphere'. In: *Remote Sensing* 14 (19), p. 4913. ISSN: 2072-4292. DOI: 10.3390/rs14194913.

Smart, L. E., L. E. Smart and E. A. Moore (2005). *Solid state chemistry. An introduction.* Ed. by E. Moore. 3. ed. Includes bibliographical references and index. Boca Raton, Fla. [u.a.]: Taylor & Francis, CRC. 407 pp. ISBN: 9780748775163.

Smith, M. H., P. M. Park and I. E. Consterdine (1993). 'Marine aerosol concentrations and estimated fluxes over the sea'. In: *Quarterly Journal of the Royal Meteorological Society* 119 (512), pp. 809–824. ISSN: 1477-870X. DOI: 10.1002/qj.49711951211.

Sodemann, H., T. M. Lai, F. Marenco, C. L. Ryder, C. Flamant, P. Knippertz, P. Rosenberg, M. Bart and J. B. McQuaid (2015). 'Lagrangian dust model simulations for a case of moist convective dust emission and transport in the western Sahara region during Fennec/LADUNEX'. In: *Journal of Geophysical Research: Atmospheres* 120 (12), pp. 6117–6144. ISSN: 2169-8996. DOI: 10.1002/2015jd023283.

Sokolik, I., A. Andronova and T. C. Johnson (1993). 'Complex refractive index of atmospheric dust aerosols'. In: *Atmospheric Environment. Part A. General Topics* 27 (16), pp. 2495–2502. ISSN: 0960-1686. DOI: 10.1016/0960-1686(93)90021-p.

Song, A., J. Li, N. T. Tsona and L. Du (2023). 'Parameterizations for sea spray aerosol production flux'. In: *Applied Geochemistry* 157, p. 105776. ISSN: 0883-2927. DOI: 10.1016/j.apgeochem.2023.105776.

Stanelle, T., I. Bey, T. Raddatz, C. Reick and I. Tegen (2014). 'Anthropogenically induced changes in twentieth century mineral dust burden and the associated impact on radiative forcing'. In: *Journal of Geophysical Research: Atmospheres* 119 (23). ISSN: 2169-8996. DOI: 10.1002/2014jd022062.

Stein, A. F., R. R. Draxler, G. D. Rolph, B. J. B. Stunder, M. D. Cohen and F. Ngan (2015). 'NOAA's HYSPLIT Atmospheric Transport and Dispersion Modeling System'. In: *Bull. Am. Meteorol. Soc.* 96 (12), pp. 2059–2077. DOI: 10.1175/bams-d-14-00110.1.

Steinke, I., O. Möhler, A. Kiselev, M. Niemand, H. Saathoff, M. Schnaiter, J. Skrotzki, C. Hoose and T. Leisner (2011). 'Ice nucleation properties of fine ash particles from the Eyjafjallajökull eruption in April 2010'. In: *Atmospheric Chemistry and Physics* 11 (24), pp. 12945–12958. ISSN: 1680-7324. DOI: 10.5194/acp-11-12945-2011.

Steinke, I. and S. M. Burrows (2022). 'Sensitivity of ice nucleation parameterizations to the variability in underlying ice nucleation rate coefficients'. In: *Environmental Science: Atmospheres* 2 (5), pp. 1101–1107. ISSN: 2634-3606. DOI: 10.1039/d2ea00019a.

Stephens, G. L. and T. L'Ecuyer (2015). 'The Earth's energy balance'. In: *Atmospheric Research* 166, pp. 195–203. ISSN: 0169-8095. DOI: 10.1016/j.atmosres.2015.06.024.

Stephens, G. L., J. Li, M. Wild, C. A. Clayson, N. Loeb, S. Kato, T. L'Ecuyer, P. W. Stackhouse, M. Lebsock and T. Andrews (2012). 'An update on Earth's energy balance in light of the latest global observations'. In: *Nature Geoscience* 5 (10), pp. 691–696. ISSN: 1752-0908. DOI: 10.1038/ngeo1580.

Stier, P., J. Feichter, S. Kinne, S. Kloster, E. Vignati, J. Wilson, L. Ganzeveld, I. Tegen, M. Werner, Y. Balkanski, M. Schulz, O. Boucher, A. Minikin and A. Petzold (2005). 'The aerosol-climate model ECHAM5-HAM'. In: *Atmospheric Chemistry and Physics* 5 (4), pp. 1125–1156. ISSN: 1680-7324. DOI: 10.5194/acp-5-1125-2005.

Stjern, C. W., B. H. Samset, G. Myhre, P. M. Forster, Ø. Hodnebrog, T. Andrews, O. Boucher, G. Faluvegi, T. Iversen, M. Kasoar, V. Kharin, A. Kirkevåg, J.-F. Lamarque, D. Olivié, T. Richardson, D. Shawki, D. Shindell, C. J. Smith, T. Takemura and A. Voulgarakis (2017). 'Rapid Adjustments Cause Weak Surface Temperature Response to Increased Black Carbon Concentrations'. In: *Journal of Geophysical Research: Atmospheres* 122 (21), pp. 11462–11481. DOI: 10.1002/2017JD027326.

Stohl, A. (2006). 'Characteristics of atmospheric transport into the Arctic troposphere'. In: *Journal of Geophysical Research: Atmospheres* 111 (D11). ISSN: 0148-0227. DOI: 10.1029/2005jd006888.

Stramler, K., A. D. Del Genio and W. B. Rossow (2011). 'Synoptically Driven Arctic Winter States'. In: *Journal of Climate* 24 (6), pp. 1747–1762. ISSN: 0894-8755. DOI: 10.1175/2010jcli3817.1.

Ström, J., J. Umegård, K. Tørseth, P. Tunved, H. C. Hansson, K. Holmén, V. Wismann, A. Herber and G. König-Langlo (2003). 'One year of particle size distribution and aerosol chemical composition measurements at the Zeppelin Station, Svalbard, March 2000–March 2001'. In: *Physics and Chemistry of the Earth, Parts A/B/C* 28 (28), pp. 1181–1190. ISSN: 1474-7065. DOI: 10.1016/j.pce.2003.08.058.

Ström, J., A. C. Engvall, F. Delbart, R. Krejci and R. Treffeisen (2009). 'On small particles in the Arctic summer boundary layer: observations at two different heights near Ny-Ålesund, Svalbard'. In: *Tellus B: Chemical and Physical Meteorology* 61 (2), pp. 473–482. DOI: 10.1111/j.1600-0889.2009.00412.x.

Student (1908). 'The Probable Error of a Mean'. In: *Biometrika* 6 (1), pp. 1–25. ISSN: 0006-3444. DOI: 10.2307/2331554.

Stuecker, M. F., C. M. Bitz, K. C. Armour, C. Proistosescu, S. M. Kang, S.-P. Xie, D. Kim, S. McGregor, W. Zhang, S. Zhao, W. Cai, Y. Dong and F.-F. Jin (2018). 'Polar amplification dominated by local forcing and feedbacks'. In: *Nature Climate Change* 8 (12), pp. 1076–1081. ISSN: 1758-6798. DOI: 10.1038/s41558-018-0339-y.

Sullivan, S. C., C. Hoose and A. Nenes (2017). 'Investigating the contribution of secondary ice production to in-cloud ice crystal numbers'. In: *Journal of Geophysical Research: Atmospheres* 122 (17), pp. 9391–9412. DOI: 10.1002/2017jd026546.

Sullivan, S. C., C. Hoose, A. Kiselev, T. Leisner and A. Nenes (2018). 'Initiation of secondary ice production in clouds'. In: *Atmospheric Chemistry and Physics* 18 (3), pp. 1593–1610. DOI: 10.5194/acp-18-1593-2018.

Sun, J. and P. A. Ariya (2006). 'Atmospheric organic and bio-aerosols as cloud condensation nuclei (CCN): A review'. In: *Atmospheric Environment* 40 (5), pp. 795–820. ISSN: 1352-2310. DOI: 10.1016/j.atmosenv.2005.05.052.

Sutinen, R., M. Kuoppamaa, P. Hänninen, M. Middleton, P. Närhi, S. Vartiainen and M.-L. Sutinen (2010). 'Tree species distribution on mafic and felsic fells in Finnish Lapland'. In: *Scandinavian Journal of Forest Research* 26 (1), pp. 11–20. ISSN: 1651-1891. DOI: 10.1080/02827581.2010.534109.

Sutinen, R., P. NÄrhi, M. Middleton, P. HÄnninen, M. Timonen and M.-L. Sutinen (2012). 'Advance of Norway spruce (Picea abies) onto mafic Lommoltunturi fell in Finnish Lapland during the last 200 years'. In: *Boreas* 41 (3), pp. 367–378. ISSN: 1502-3885. DOI: 10.1111/j.1502-3885.2011.00238.x.

Takemura, T., T. Nakajima, O. Dubovik, B. N. Holben and S. Kinne (2002). 'Single-Scattering Albedo and Radiative Forcing of Various Aerosol Species with a Global Three-Dimensional Model'. In: *Journal of Climate* 15 (4), pp. 333–352. DOI: 10.1175/1520-0442(2002)015<0333:SSAARF>2.0.CO;2.

Tarek, M., F. P. Brissette and R. Arsenault (2020). 'Evaluation of the ERA5 reanalysis as a potential reference dataset for hydrological modelling over North America'. In: *Hydrology and Earth System Sciences* 24 (5), pp. 2527–2544. DOI: 10.5194/hess-24-2527-2020.

Tavolato, C. and L. Isaksen (2014). 'On the use of a Huber norm for observation quality control in the ECMWF 4D-Var'. In: *Quarterly Journal of the Royal Meteorological Society* 141 (690), pp. 1514–1527. ISSN: 1477-870X. DOI: 10.1002/qj.2440.

Taylor, P. C., M. Cai, A. Hu, J. Meehl, W. Washington and G. J. Zhang (2013). 'A Decomposition of Feedback Contributions to Polar Warming Amplification'. In: *Journal of Climate* 26 (18), pp. 7023–7043. ISSN: 1520-0442. DOI: 10.1175/jcli-d-12-00696.1.

Terrenoire, E., D. A. Hauglustaine, Y. Cohen, A. Cozic, R. Valorso, F. Lefèvre and S. Matthes (2022). 'Impact of present and future aircraft NOxand aerosol emissions on atmospheric composition and associated direct radiative forcing of climate'. In: *Atmospheric Chemistry and Physics* 22 (18), pp. 11987–12023. ISSN: 1680-7324. DOI: 10.5194/acp-22-11987-2022.

Tesson, S. V. M. and T. Šantl-Temkiv (2018). 'Ice Nucleation Activity and Aeolian Dispersal Success in Airborne and Aquatic Microalgae'. In: *Frontiers in Microbiology* 9. ISSN: 1664-302X. DOI: 10.3389/fmicb.2018.02681.

Tetzner, D., E. Thomas and C. Allen (2019). 'A Validation of ERA5 Reanalysis Data in the Southern Antarctic Peninsula—Ellsworth Land Region, and Its Implications for Ice Core Studies'. In: *Geosciences* 9 (7), p. 289. ISSN: 2076-3263. DOI: 10.3390/geosciences9070289.

Thackeray, C. W. and A. Hall (2019). 'An emergent constraint on future Arctic sea-ice albedo feedback'. In: *Nature Climate Change* 9 (12), pp. 972–978. ISSN: 1758-6798. DOI: 10.1038/s41558-019-0619-1.

Thomson, D. J. (1987). 'Criteria for the selection of stochastic models of particle trajectories in turbulent flows'. In: *Journal of Fluid Mechanics* 180 (1), p. 529. ISSN: 1469-7645. DOI: 10.1017/s0022112087001940.

Tobo, Y., K. Adachi, P. J. DeMott, T. C. J. Hill, D. S. Hamilton, N. M. Mahowald, N. Nagatsuka, S. Ohata, J. Uetake, Y. Kondo and M. Koike (2019). 'Glacially sourced dust as a potentially significant source of ice nucleating particles'. In: *Nature Geoscience* 12 (4), pp. 253–258. DOI: 10.1038/s41561-019-0314-x.

Tobo, Y., K. Adachi, K. Kawai, H. Matsui, S. Ohata, N. Oshima, Y. Kondo, O. Hermansen, M. Uchida, J. Inoue and M. Koike (2024). 'Surface warming in Svalbard may have led to increases in highly active ice-nucleating particles'. In: *Communications Earth & Environment* 5 (1). ISSN: 2662-4435. DOI: 10.1038/s43247-024-01677-0.

Tsigaridis, K., M. Krol, F. J. Dentener, Y. Balkanski, J. Lathière, S. Metzger, D. A. Hauglustaine and M. Kanakidou (2006). 'Change in global aerosol composition since preindustrial times'. In: *Atmospheric Chemistry and Physics* 6 (12), pp. 5143–5162. ISSN: 1680-7324. DOI: 10.5194/acp-6-5143-2006.

Tunved, P., J. Ström and R. Krejci (2013). 'Arctic aerosol life cycle: linking aerosol size distributions observed between 2000 and 2010 with air mass transport and precipitation at Zeppelin station, Ny-Alesund, Svalbard'. In: *Atmospheric Chemistry and Physics* 13 (7), pp. 3643–3660. DOI: 10.5194/acp-13-3643-2013.

Twomey, S. (1959). 'The nuclei of natural cloud formation part 1: The chemical diffusion method and its application to atmospheric nuclei'. In: *Geofisica pura e applicata* 43, pp. 227–242. DOI: 10.1007/BF01993559.

Uchida, M., T. Nakatsubo, H. Kanda and H. Koizumi (2006). 'Estimation of the annual primary production of the lichen Cetrariella delisei in a glacier foreland in the High Arctic, Ny-Ølesund,

Svalbard'. In: *Polar Research* 25 (1), pp. 39–49. ISSN: 1751-8369. DOI: 10.3402/polar.v25i1.6237.

Uin, J. (2024). *Ultra-High-Sensitivity Aerosol Spectrometer (UHSAS) Instrument Handbook*. Tech. rep. DOE/SC-ARM-TR-163. DOE Office of Science Atmospheric Radiation Measurement Program (United States). DOI: 10.2172/1251410.

Ullrich, R., C. Hoose, O. Möhler, M. Niemand, R. Wagner, K. Höhler, N. Hiranuma, H. Saathoff and T. Leisner (2017). 'A New Ice Nucleation Active Site Parameterization for Desert Dust and Soot'. In: *Journal of the Atmospheric Sciences* 74 (3), pp. 699–717. DOI: 10.1175/jas-d-16-0074.1.

Vali, G. (1971). 'Quantitative Evaluation of Experimental Results an the Heterogeneous Freezing Nucleation of Supercooled Liquids'. In: *Journal of the Atmospheric Sciences* 28 (3), pp. 402–409. DOI: 10.1175/1520-0469(1971)028<0402:qeoera>2.0.co;2.

Vali, G. (1994). 'Freezing Rate Due to Heterogeneous Nucleation'. In: *Journal of the Atmospheric Sciences* 51 (13), pp. 1843–1856. ISSN: 1520-0469. DOI: 10.1175/1520-0469(1994)051<1843:frdthn>2.0.co;2.

Van Santen, R. A. (1984). 'The Ostwald step rule'. In: *The Journal of Physical Chemistry* 88 (24), pp. 5768–5769. ISSN: 1541-5740. DOI: 10.1021/j150668a002.

Vepuri, H. S. K., C. A. Rodriguez, D. G. Georgakopoulos, D. Hume, J. Webb, G. D. Mayer and N. Hiranuma (2021). 'Ice-nucleating particles in precipitation samples from the Texas Panhandle'. In: *Atmospheric Chemistry and Physics* 21 (6), pp. 4503–4520. ISSN: 1680-7324. DOI: 10.5194/acp-21-4503-2021.

Vergara-Temprado, J., A. K. Miltenberger, K. Furtado, D. P. Grosvenor, B. J. Shipway, A. A. Hill, J. M. Wilkinson, P. R. Field, B. J. Murray and K. S. Carslaw (2018). 'Strong control of Southern Ocean cloud reflectivity by ice-nucleating particles'. In: *Proc. Natl. Acad. Sci.* 115 (11), pp. 2687–2692. DOI: 10.1073/pnas.1721627115.

Veron, F. (2015). 'Ocean Spray'. In: *Annual Review of Fluid Mechanics* 47 (1), pp. 507–538. ISSN: 1545-4479. DOI: 10.1146/annurev-fluid-010814-014651.

Vihtakari, M. (2019). 'PlotSvalbard: PlotSvalbard-Plot research data from Svalbard on maps'. In: *R package version 0.8* 5.

Villa, T., F. Gonzalez, B. Miljievic, Z. Ristovski and L. Morawska (2016). 'An Overview of Small Unmanned Aerial Vehicles for Air Quality Measurements: Present Applications and Future Prospectives'. In: *Sensors* 16 (7), p. 1072. DOI: 10.3390/s16071072.

Vogel, F., L. Lacher, J. Nadolny, H. Saathoff, T. Leisner and O. Möhler (2022). 'Development and validation of a new cloud simulation experiment for lab-based aerosol–cloud studies'. In: *Review of Scientific Instruments* 93 (9). ISSN: 1089-7623. DOI: 10.1063/5.0098777.

Vonnegut, B. (1947). 'The Nucleation of Ice Formation by Silver Iodide'. In: *Journal of Applied Physics* 18 (7), pp. 593–595. DOI: 10.1063/1.1697813.

Wagner, P. E. (1982). 'Aerosol Growth by Condensation'. In: *Aerosol Microphysics II*. Springer Berlin Heidelberg, pp. 129–178. ISBN: 9783642818059. DOI: 10.1007/978-3-642-81805-9_5.

Wagner, R., H. Bunz, C. Linke, O. Möhler, K.-H. Naumann, H. Saathoff, M. Schnaiter and U. Schurath (2006). 'Chamber Simulations of Cloud Chemistry: The AIDA Chamber'. In: *Nato Science Series: IV: Earth and Environmental Science*. Kluwer Academic Publishers, pp. 67–82. DOI: 10.1007/1-4020-4232-9_5.

Wagner, R., A. Kiselev, O. Möhler, H. Saathoff and I. Steinke (2016). 'Pre-activation of ice-nucleating particles by the pore condensation and freezing mechanism'. In: *Atmospheric Chemistry and Physics* 16 (4), pp. 2025–2042. ISSN: 1680-7324. DOI: 10.5194/acp-16-2025-2016.

Wall, C. J., J. R. Norris, A. Possner, D. T. McCoy, I. L. McCoy and N. J. Lutsko (2022). 'Assessing effective radiative forcing from aerosol–cloud interactions over the global ocean'. In: *Proceedings of the National Academy of Sciences* 119 (46). ISSN: 1091-6490. DOI: 10.1073/pnas.2210481119.

Wallis, S. (2013). 'Binomial Confidence Intervals and Contingency Tests: Mathematical Fundamentals and the Evaluation of Alternative Methods'. In: *Journal of Quantitative Linguistics* 20 (3), pp. 178–208. DOI: 10.1080/09296174.2013.799918.

Wang, Q., D. J. Jacob, J. A. Fisher, J. Mao, E. M. Leibensperger, C. C. Carouge, P. Le Sager, Y. Kondo, J. L. Jimenez, M. J. Cubison and S. J. Doherty (2011). 'Sources of carbonaceous aerosols and deposited black carbon in the Arctic in winter-spring: implications for radiative forcing'. In: *Atmospheric Chemistry and Physics* 11 (23), pp. 12453–12473. DOI: 10.5194/acp-11-12453-2011.

Warner, M. S. C. (2018). 'Introduction to PySPLIT: A Python Toolkit for NOAA ARL's HYSPLIT Model'. In: *Computing in Science & Engineering* 20 (5), pp. 47–62. DOI: 10.1109/mcse.2017.3301549.

Welker, R. W. (2012). 'Developments in Surface Contamination and Cleaning'. In: *Developments in Surface Contamination and Cleaning*. Ed. by R. Kohli and K. Mittal. Elsevier. Chap. 4, pp. 179–213. ISBN: 9781437778830. DOI: 10.1016/b978-1-4377-7883-0.00004-3.

Welti, A., Z. A. Kanji, F. Lüönd, O. Stetzer and U. Lohmann (2014). 'Exploring the mechanisms of ice nucleation on kaolinite: from deposition nucleation to condensation freezing'. In: *Journal of the Atmospheric Sciences* 71, pp. 16–36. DOI: 10.1175/JAS-D-12-0252.1.

Welti, A., F. Lüönd, Z. A. Kanji, O. Stetzer and U. Lohmann (2012). 'Time dependence of immersion freezing: an experimental study on size selected kaolinite particles'. In: *Atmospheric Chemistry and Physics* 12 (20), pp. 9893–9907. ISSN: 1680-7324. DOI: 10.5194/acp-12-9893-2012.

Welti, A., F. Lüönd, O. Stetzer and U. Lohmann (2009). 'Influence of particle size on the ice nucleating ability of mineral dusts'. In: *Atmospheric Chemistry and Physics* 9 (18), pp. 6705–6715. ISSN: 1680-7324. DOI: 10.5194/acp-9-6705-2009.

Wendisch, M., A. Macke, A. Ehrlich, C. Lüpkes, M. Mech, D. Chechin, K. Dethloff, C. B. Velasco, H. Bozem, M. Brückner, H.-C. Clemen, S. Crewell, T. Donth, R. Dupuy, K. Ebell, U. Egerer, R. Engelmann, C. Engler, O. Eppers, M. Gehrmann, X. Gong, M. Gottschalk, C. Gourbeyre, H. Griesche, J. Hartmann, M. Hartmann, B. Heinold, A. Herber, H. Herrmann, G. Heygster, P. Hoor, S. Jafariserajehlou, E. Jäkel, E. Järvinen, O. Jourdan, U. Kästner, S. Kecorius, E. M. Knudsen, F. Köllner, J. Kretzschmar, L. Lelli, D. Leroy, M. Maturilli, L. Mei, S. Mertes, G. Mioche, R. Neuber, M. Nicolaus, T. Nomokonova, J. Notholt, M. Palm, M. van Pinxteren, J. Quaas, P. Richter, E. Ruiz-Donoso, M. Schäfer, K. Schmieder, M. Schnaiter, J. Schneider, A. Schwarzenböck, P. Seifert, M. D. Shupe, H. Siebert, G. Spreen, J. Stapf, F. Stratmann, T. Vogl, A. Welti, H. Wex, A. Wiedensohler, M. Zanatta and S. Zeppenfeld (2019). 'The Arctic Cloud Puzzle: Using ACLOUD/PASCAL Multiplatform Observations to Unravel the Role of Clouds and Aerosol Particles in Arctic Amplification'. In: *Bulletin of the American Meteorological Society* 100 (5), pp. 841–871. DOI: 10.1175/bams-d-18-0072.1.

Weng, H., J. Lin, R. Martin, D. B. Millet, L. Jaeglé, D. Ridley, C. Keller, C. Li, M. Du and J. Meng (2020). 'Global high-resolution emissions of soil NOx, sea salt aerosols, and biogenic volatile organic compounds'. In: *Scientific Data* 7 (1). ISSN: 2052-4463. DOI: 10.1038/s41597-020-0488-5.

Westervelt, D. M., A. J. Conley, A. M. Fiore, J.-F. Lamarque, D. T. Shindell, M. Previdi, N. R. Mascioli, G. Faluvegi, G. Correa and L. W. Horowitz (2018). 'Connecting regional aerosol emissions reductions to local and remote precipitation responses'. In: *Atmospheric Chemistry and Physics* 18 (16), pp. 12461–12475. ISSN: 1680-7324. DOI: 10.5194/acp-18-12461-2018.

Wex, H., S. Augustin-Bauditz, Y. Boose, C. Budke, J. Curtius, K. Diehl, A. Dreyer, F. Frank, S. Hartmann, N. Hiranuma, E. Jantsch, Z. A. Kanji, A. Kiselev, T. Koop, O. Möhler, D. Niedermeier, B. Nillius, M. Rösch, D. Rose, C. Schmidt, I. Steinke and F. Stratmann (2015). 'Intercomparing different devices for the investigation of ice nucleating particles using Snomax® as test substance'. In: *Atmospheric Chemistry and Physics* 15 (3). Publisher: Copernicus GmbH, pp. 1463–1485. DOI: 10.5194/acp-15-1463-2015.

Wex, H., L. Huang, W. Zhang, H. Hung, R. Traversi, S. Becagli, R. J. Sheesley, C. E. Moffett, T. E. Barrett, R. Bossi, H. Skov, A. Hünerbein, J. Lubitz, M. Löffler, O. Linke, M. Hartmann, P. Herenz and F. Stratmann (2019). 'Annual variability of ice-nucleating particle concentrations at different Arctic locations'. In: *Atmospheric Chemistry and Physics* 19 (7), pp. 5293–5311. ISSN: 1680-7324. DOI: 10.5194/acp-19-5293-2019.

Wheeler, M. J. and A. K. Bertram (2012). 'Deposition nucleation on mineral dust particles: a case against classical nucleation theory with the assumption of a single contact angle'. In: *Atmospheric Chemistry and Physics* 12 (2), pp. 1189–1201. ISSN: 1680-7324. DOI: 10.5194/acp-12-1189-2012.

Wheeler, M. J., R. H. Mason, K. Steunenberg, M. Wagstaff, C. Chou and A. K. Bertram (2014). 'Immersion Freezing of Supermicron Mineral Dust Particles: Freezing Results, Testing Different Schemes for Describing Ice Nucleation, and Ice Nucleation Active Site Densities'. In: *The Journal of Physical Chemistry A* 119 (19), pp. 4358–4372. ISSN: 1520-5215. DOI: 10.1021/jp507875q.

Whitby, K., W. Clark, V. Marple, G. Sverdrup, G. Sem, K. Willeke, B. Liu and D. Pui (1975). 'Characterization of California aerosols—I. Size distributions of freeway aerosol'. In: *Atmospheric Environment (1967)* 9 (5), pp. 463–482. ISSN: 0004-6981. DOI: 10.1016/0004-6981(75)90107-9.

Wiacek, A., T. Peter and U. Lohmann (2010). 'The potential influence of Asian and African mineral dust on ice, mixed-phase and liquid water clouds'. In: *Atmospheric Chemistry and Physics* 10 (18), pp. 8649–8667. DOI: 10.5194/acp-10-8649-2010.

Wieber, C., M. Rosenhøj Jeppesen, K. Finster, C. Melvad and T. Šantl-Temkiv (2024). 'Micro-PINGUIN: microtiter-plate-based instrument for ice nucleation detection in gallium with an infrared camera'. In: *Atmospheric Measurement Techniques* 17 (9), pp. 2707–2719. ISSN: 1867-8548. DOI: 10.5194/amt-17-2707-2024.

Wiedensohler, A. (1988). 'An approximation of the bipolar charge distribution for particles in the submicron size range'. In: *Journal of Aerosol Science* 19 (3), pp. 387–389. ISSN: 0021-8502. DOI: 10.1016/0021-8502(88)90278-9.

Wientjes, I. G. M., R. S. W. Van de Wal, G. J. Reichart, A. Sluijs and J. Oerlemans (2011). 'Dust from the dark region in the western ablation zone of the Greenland ice sheet'. In: *The Cryosphere* 5 (3), pp. 589–601. ISSN: 1994-0424. DOI: 10.5194/tc-5-589-2011.

Wilbourn, E. K., D. C. O. Thornton, C. Ott, J. Graff, P. K. Quinn, T. S. Bates, R. Betha, L. M. Russell, M. J. Behrenfeld and S. D. Brooks (2020). 'Ice Nucleation by Marine Aerosols Over the North Atlantic Ocean in Late Spring'. In: *Journal of Geophysical Research: Atmospheres* 125 (4). ISSN: 2169-8996. DOI: 10.1029/2019jd030913.

Wilkinson, M. D., M. Dumontier, I. J. Aalbersberg, G. Appleton, M. Axton, A. Baak, N. Blomberg, J.-W. Boiten, L. B. da Silva Santos, P. E. Bourne, J. Bouwman, A. J. Brookes, T. Clark, M. Crosas, I. Dillo, O. Dumon, S. Edmunds, C. T. Evelo, R. Finkers, A. Gonzalez-Beltran, A. J. Gray, P. Groth, C. Goble, J. S. Grethe, J. Heringa, P. A. 't Hoen, R. Hooft, T. Kuhn, R. Kok, J. Kok, S. J. Lusher, M. E. Martone, A. Mons, A. L. Packer, B. Persson, P. Rocca-Serra, M. Roos, R. van Schaik, S.-A. Sansone, E. Schultes, T. Sengstag, T. Slater, G. Strawn, M. A. Swertz, M. Thompson, J. van der Lei, E. van Mulligen, J. Velterop, A. Waagmeester, P. Wittenburg, K. Wolstencroft, J. Zhao and B. Mons (2016). 'The FAIR Guiding Principles for scientific data management and stewardship'. In: *Scientific Data* 3 (1). ISSN: 2052-4463. DOI: 10.1038/sdata.2016.18.

Williams, J., M. de Reus, R. Krejci, H. Fischer and J. Ström (2002). 'Application of the variability-size relationship to atmospheric aerosol studies: estimating aerosol lifetimes and ages'. In: *Atmospheric Chemistry and Physics* 2 (2), pp. 133–145. DOI: 10.5194/acp-2-133-2002.

Willis, M. D., H. Bozem, D. Kunkel, A. K. Y. Lee, H. Schulz, J. Burkart, A. A. Aliabadi, A. B. Herber, W. R. Leaitch and J. P. D. Abbatt (2019). 'Aircraft-based measurements of High Arctic springtime aerosol show evidence for vertically varying sources, transport and composition'. In: *Atmospheric Chemistry and Physics* 19 (1), pp. 57–76. DOI: 10.5194/acp-19-57-2019.

Wilson, E. B. (1927). 'Probable Inference, the Law of Succession, and Statistical Inference'. In: *Journal of the American Statistical Association* 22 (158), pp. 209–212. DOI: 10.1080/01621459.1927.10502953.

Wilson, T. W., L. A. Ladino, P. A. Alpert, M. N. Breckels, I. M. Brooks, J. Browse, S. M. Burrows, K. S. Carslaw, J. A. Huffman, C. Judd, W. P. Kilthau, R. H. Mason, G. McFiggans, L. A. Miller, J. J. Najera, E. Polishchuk, S. Rae, C. L. Schiller, M. Si, J. V. Temprado, T. F. Whale, J. P. S. Wong, O. Wurl, J. D. Yakobi-Hancock, J. P. D. Abbatt, J. Y. Aller, A. K. Bertram, D. A. Knopf and B. J. Murray (2015). 'A marine biogenic source of atmospheric ice-nucleating particles'. In: *Nature* 525 (7568), pp. 234–238. ISSN: 0028-0836. DOI: 10.1038/nature14986.

Wittmann, M., C. D. Groot Zwaaftink, L. Steffensen Schmidt, S. Guðmundsson, F. Pálsson, O. Arnalds, H. Björnsson, T. Thorsteinsson and A. Stohl (2017). 'Impact of dust deposition on the albedo of Vatnajökull ice cap, Iceland'. In: *The Cryosphere* 11 (2), pp. 741–754. ISSN: 1994-0424. DOI: 10.5194/tc-11-741-2017.

Woods, C. and R. Caballero (2016). 'The Role of Moist Intrusions in Winter Arctic Warming and Sea Ice Decline'. In: *Journal of Climate* 29 (12), pp. 4473–4485. ISSN: 1520-0442. DOI: 10.1175/jcli-d-15-0773.1.

Woolf, D. K., P. A. Bowyer and E. C. Monahan (1987). 'Discriminating between the film drops and jet drops produced by a simulated whitecap'. In: *Journal of Geophysical Research: Oceans* 92 (C5), pp. 5142–5150. ISSN: 0148-0227. DOI: 10.1029/jc092ic05p05142.

Wriedt, T. (2012). 'Mie Theory: A Review'. In: *The Mie Theory*. Springer Berlin Heidelberg, pp. 53–71. ISBN: 9783642287381. DOI: 10.1007/978-3-642-28738-1_2.

Wu, J. (1992). 'Bubble flux and marine aerosol spectra under various wind velocities'. In: *Journal of Geophysical Research: Oceans* 97 (C2), pp. 2327–2333. ISSN: 0148-0227. DOI: 10.1029/91jc02568.

Wu, J. (1993). 'Production of spume drops by the wind tearing of wave crests: The search for quantification'. In: *Journal of Geophysical Research: Oceans* 98 (C10), pp. 18221–18227. ISSN: 0148-0227. DOI: 10.1029/93jc01834.

Xi, X. and I. N. Sokolik (2016). 'Quantifying the anthropogenic dust emission from agricultural land use and desiccation of the Aral Sea in Central Asia'. In: *Journal of Geophysical Research: Atmospheres* 121 (20). ISSN: 2169-8996. DOI: 10.1002/2016jd025556.

Xi, Y., C. Xu, A. Downey, R. Stevens, J. O. Bachelder, J. King, P. L. Hayes and A. K. Bertram (2022). 'Ice nucleating properties of airborne dust from an actively retreating glacier in Yukon, Canada'. In: *Environmental Science: Atmospheres* 2 (4), pp. 714–726. ISSN: 2634-3606. DOI: 10.1039/d1ea00101a.

Xiang, M., M. Morgeneyer, F. Philippe, M. Manokaran and C. Bressot (2020). 'Comparative review of efficiency analysis for airborne solid submicrometer particle sampling by nuclepore filters'. In: *Chemical Engineering Research and Design* 164, pp. 338–351. DOI: 10.1016/j.cherd.2020.10.009.

Xu, H., Y. Ren, W. Zhang, W. Meng, X. Yun, X. Yu, J. Li, Y. Zhang, G. Shen, J. Ma, B. Li, H. Cheng, X. Wang, Y. Wan and S. Tao (2021). 'Updated Global Black Carbon Emissions from 1960 to 2017: Improvements, Trends, and Drivers'. In: *Environmental Science & Technology* 55 (12), pp. 7869–7879. ISSN: 1520-5851. DOI: 10.1021/acs.est.1c03117.

Xu, J.-W., R. V. Martin, A. Morrow, S. Sharma, L. Huang, W. R. Leaitch, J. Burkart, H. Schulz, M. Zanatta, M. D. Willis, D. K. Henze, C. J. Lee, A. B. Herber and J. P. D. Abbatt (2017). 'Source attribution of Arctic black carbon constrained by aircraft and surface measurements'. In: *Atmospheric Chemistry and Physics* 17 (19), pp. 11971–11989. DOI: 10.5194/acp-17-11971-2017.

Xu, X., S. K. Frey, A. Boluwade, A. R. Erler, O. Khader, D. R. Lapen and E. Sudicky (2019). 'Evaluation of variability among different precipitation products in the Northern Great Plains'. In: *Journal of Hydrology: Regional Studies* 24, p. 100608. ISSN: 2214-5818. DOI: 10.1016/j.ejrh.2019.100608.

Yankofsky, S. A., Z. Levin, T. Bertold and N. Sandlerman (1981). 'Some Basic Characteristics of Bacterial Freezing Nuclei'. In: *Journal of Applied Meteorology* 20 (9), pp. 1013–1019. ISSN: 0021-8952. DOI: 10.1175/1520-0450(1981)020<1013:sbcobf>2.0.co;2.

Yoshida, T., Y. Kousaka and K. Okuyama (1976). 'Growth of Aerosol Particles by Condensation'. In: *Industrial & Engineering Chemistry Fundamentals* 15 (1), pp. 37–41. ISSN: 1541-4833. DOI: 10.1021/i160057a007.

Yu, F., Y. Liu, L. Fan, L. Li, Y. Han and G. Chen (2017). 'Design and implementation of atmospheric multi-parameter sensor for UAV-based aerosol distribution detection'. In: *Sensor Review* 37 (2), pp. 196–210. DOI: 10.1108/sr-09-2016-0199.

Yu, H., Y. J. Kaufman, M. Chin, G. Feingold, L. A. Remer, T. L. Anderson, Y. Balkanski, N. Bellouin, O. Boucher, S. Christopher, P. DeCola, R. Kahn, D. Koch, N. Loeb, M. S. Reddy, M. Schulz, T. Takemura and M. Zhou (2006). 'A review of measurement-based assessments of the aerosol direct radiative effect and forcing'. In: *Atmospheric Chemistry and Physics* 6 (3), pp. 613–666. ISSN: 1680-7324. DOI: 10.5194/acp-6-613-2006.

Zamora, L. M., R. A. Kahn, M. J. Cubison, G. S. Diskin, J. L. Jimenez, Y. Kondo, G. M. McFarquhar, A. Nenes, K. L. Thornhill, A. Wisthaler, A. Zelenyuk and L. D. Ziemba (2016). 'Aircraft-measured indirect cloud effects from biomass burning smoke in the Arctic and

subarctic'. In: *Atmospheric Chemistry and Physics* 16 (2), pp. 715–738. DOI: 10.5194/acp-16-715-2016.

Zender, C. S. (2003). 'Mineral Dust Entrainment and Deposition (DEAD) model: Description and 1990s dust climatology'. In: *Journal of Geophysical Research: Atmospheress* 108 (D14). DOI: 10.1029/2002jd002775.

Zobrist, B., C. Marcolli, T. Peter and T. Koop (2008). 'Heterogeneous Ice Nucleation in Aqueous Solutions: the Role of Water Activity'. In: *The Journal of Physical Chemistry A* 112 (17), pp. 3965–3975. ISSN: 1520-5215. DOI: 10.1021/jp7112208.

Zolles, T., J. Burkart, T. Häusler, B. Pummer, R. Hitzenberger and H. Grother (2015). 'Identification of Ice Nucleation Active Sites on Feldspar Dust Particles'. In: *Journal of Physical Chemistry A* 119 (11), pp. 2692–2700. DOI: 10.1021/jp509839x.

Acknowledgments

I would first of all like to thank my supervisors Prof. Dr. Thomas Leisner and Prof. Dr. Corinna Hoose for giving me the opportunity to work on my dissertation at the IMKAAF. This has been a long time in the making and I am grateful for this opportunity and for getting to know the many facets of physics outside particle physics.

Secondly, I definitely have to give a great thanks to my supervisors at IMKAAF, Dr. Larissa Lacher and Dr. Ottmar Möhler, who were always open for fruitful discussions about science, work and additional opportunities that might present themselves. Larissa, I am very grateful for all the discussions we had and for all the help you offered me, be it the planning of a field campaign, reading over my thesis, or my abstracts for conferences. This would have not been such a good time without you! To Ottmar, I am happy and grateful, that you always had an open mind for new ideas, while still keeping a focus on the scientific aspects at hand. You both helped me through this thesis and I hope I was and am able to live up to it!

There are many people that were somehow involved in this thesis and my work at AAF, therefore I would generally thank the whole institute for providing a good and fun work environment, which featured many hours of coffee drinking inside as well as outside in the sun. Some people, however, I would like to name, since they provided support in many ways. I would like to thank Olga Dombrowski and her team of HiWis, who helped with lots of the analysis of the filters, the snow samples and the ocean samples. Thanks also to Steffen Vogt, who helped me understand that shipping things outside the EU is a very unfun business. Here, I would also like to use the opportunity to thank Jens Nadolny for developing the PINE software and always having an open ear for many different needs and wishes, as well as a fantastic developer of light magic on PhD hats! Many thanks to Nicole Büttner and Dr. Romy Fösig, who developed the PIA software to analyse the PINE data and always had an open ear to help with writing this thesis and discussing various issues with CF-conventions that I had. In general, a big thanks to the whole PINE community, from Dr. Franziska Vogel, Dr. Pia Bogert and Dr. Larissa Lacher for teaching me about your instrument! To Tillia Gädeke my thanks for analyzing the snow samples and showing me how the cold stage works.

I would also like to thank some additional people who proof-read my thesis and provided me with useful comments that shaped this thesis. Thanks to Dr. Marco Zanatta, who read through the Arctic part of this thesis and helped me refine this section. Thanks to Dr. Kristina Höhler, who read through the INSEKT section and also read through the result chapter to provide me with a good feeling for both! Thanks to Nicole Büttner and Dr. Romy Fösig who gave me helpful tips to the PINE chapter, especially to Nicole who also read through the result chapter and had a good eye for the details. Thank you to Dr. Tobias Schorr, who gave me comments and helpful additions to numerous parts, especially for looking at the accuracy of my statements. Also thanks to Johanna Seidel, who read through the cold stage section and provided me additional information and help with the setup.

During my many campaigns, I met a bunch of wonderful and fascinating people, some of which I am grateful to call friends. Thanks to David and Kostas for accepting me into the little UAV community at Pallas, thanks to Jess, who shared her excitement of Star Trek and electronics with me. Thanks to all the people in Ny-Ålesund, who made living in the nothernmost permanent settlement an experience, that I had the privilege to experience twice. Thanks to my master students Tim Lippmann and Miriam Bentke, who joined me during both visits and were both a great source of scientific discussions.

To all my friends, who supported me through this time, I am grateful! Thank you Mark, Tobi and Eugen for starting this long journey of studying physics together and finally finishing it. Thanks to Pia, Tobi, Nicole, Jens, Marco, Steph, Johanna and Franzi, who always made the institute life fun! Thanks to Tobi and Yaqiong, my office mates, for accepting (begrudgingly) my messy work place. I will not promise that I will tidy it up, but I will promise to try my best!

Thanks to my parents. You were always there for me and always supported me and there are no words that can described my gratitude.